Are the Moons of Jupiter Unique?
Thermochemical Disk Modeling of Moon Formation

Oberg, N.O.

DOI
10.4233/uuid:4b5044b3-3718-42e6-ba31-f27c9b984c15

Publication date
2023

Document Version
Final published version

Citation (APA)
Oberg, N. O. (2023). *Are the Moons of Jupiter Unique? Thermochemical Disk Modeling of Moon Formation*. [Dissertation (TU Delft), Delft University of Technology]. https://doi.org/10.4233/uuid:4b5044b3-3718-42e6-ba31-f27c9b984c15

Are the Moons of Jupiter Unique?

Thermochemical Disk Modeling of Moon Formation

Dissertation

for the purpose of obtaining the degree of doctor
at Delft University of Technology
by the authority of the Rector Magnificus, prof.dr.ir. T.H.J.J. van der Hagen,
Chair of the Board for Doctorates
to be defended publicly on
Monday 5 June 2023 at 12:30 o'clock

by

Nickolas Oliver OBERG
MSc., University of Groningen, The Netherlands
born in Antwerp (Wilrijk), Belgium

This dissertation has been approved by the promotors.

Composition of the doctoral committee:

Rector Magnificus	chairperson
Prof. dr. L.L.A. Vermeersen	Delft University of Technology, *promotor*
Prof. dr. I.E.E. Kamp	University of Groningen, *promotor*
Dr. S.M. Cazaux	Delft University of Technology, *copromotor*

Independent members:

Prof. dr. B.R. Brandl	Delft University of Technology
Prof. dr. P. Caselli	Max Planck Institute for Extraterrestrial Physics, Germany
Prof. dr. T. Guillot	Laboratoire Lagrange, CNRS, Observatoire de la Cote d'Azur, France
Dr. S. Raymond	Laboratoire d'Astrophysique de Bordeaux, France
Prof. dr. ir. P.N.A.M. Visser	Delft University of Technology, reserve member

The doctoral research has been carried out in the context of an agreement on joint doctoral supervision between the University of Groningen, the Netherlands, and Delft University of Technology, the Netherlands.

NWO Nederlandse Organisatie voor Wetenschappelijk Onderzoek

NOVA

Zijn de Manen van Jupiter Uniek?

Thermochemische Schijfmodellering van Maanvorming

Proefschrift

ter verkrijging van de graad van doctor
aan de Technische Universiteit Delft,
op gezag van de Rector Magnificus, prof.dr.ir. T.H.J.J. van der Hagen,
voorzitter van het College voor Promoties,
in het openbaar te verdedigen op
maandag 5 Juni 2023 om 12:30 uur

door

Nickolas Oliver OBERG
MSc., Rijksuniversiteit Groningen, Nederland
geboren te Antwerpen (Wilrijk), België

Dit proefschrift is goedgekeurd door de promotoren.

Samenstelling promotiecommissie bestaat uit:

Rector Magnificus	voorzitter
Prof. dr. L.L.A. Vermeersen	Technische Universiteit Delft, *promotor*
Prof. dr. I.E.E. Kamp	Rijksuniversiteit Groningen, *promotor*
Dr. S.M. Cazaux	Technische Universiteit Delft, *copromotor*

Onafhankelijke leden:

Prof. dr. B.R. Brandl	Technische Universiteit Delft
Prof. dr. P. Caselli	Max Planck Institute for Extraterrestrial Physics, Duitsland
Prof. dr. T. Guillot	Laboratoire Lagrange, CNRS, Observatoire de la Cote d'Azur, Frankrijk
Dr. S. Raymond	Laboratoire d'Astrophysique de Bordeaux, Frankrijk
Prof. dr. ir. P.N.A.M. Visser	Technische Universiteit Delft, reservelid

Het promotieonderzoek is uitgevoerd in het kader van een overeenkomst inzake gezamenlijke promotiebegeleiding tussen de Rijksuniversiteit Groningen en de Technische Universiteit Delft.

NWO Nederlandse Organisatie voor Wetenschappelijk Onderzoek

NOVA

To Yvi and Dennis.

Contents

Summary

The practice of astronomy is in many ways an intrinsically introspective endeavour. A significant fraction of astronomical motivation is derived from the desire to understand whether a habitable planet such as the Earth is a unique object, and, by extension, whether the inhabitants of the Earth themselves collectively represent a unique phenomenon. By definition, a world is considered potentially habitable if it is theoretically capable of supporting liquid water at its surface. But by focusing solely on strictly Earth-like planets, we risk overlooking other potentially habitable options. In fact, the majority of the worlds known to host liquid water oceans in the solar system are not Earth-like at all. These other worlds do however share a singular defining characteristic: they are the icy moons that orbit the gas giant planets. Their oceans are concealed below kilometers of frozen crust. In the solar system at least three moons are known to host an ocean with a high degree of confidence (Europa, Enceladus, and Titan), and another four are suspected (Ganymede, Callisto, Mimas, and Dione). Hence, any hope of answering the question as to how unique the phenomena of life on Earth really is may hinge predominantly on answering a seemingly unrelated question: how unique are the icy moons?

The formation of gas giants appears to be accompanied by the formation of moons, as, at least in the solar system, the two appear inseparable. The gaseous planets Jupiter, Saturn, and Uranus, are each attended by a retinue of moons both regular and irregular. The regular satellites tend to orbit in a single plane, in the same direction, and on nearly circular paths. These peculiar properties are also exhibited by the planets, and hence it is considered likely that some similar process has been at play to form them both. That process is the formation within a swirling disk of gas and dust. Planets form within disks that surrounded a star (a circum*stellar* disk) while the moons would have formed within a disk surrounding their planet (a circum*planetary* disk, or CPD).

The last decade of strides made in the observation of circumstellar disks has revolutionized our understanding of the planet formation process. To what extent might the moon and planet formation process be similar? To what extent might we be able to extrapolate our understanding of circumstellar disks down to the scales characteristic of circumplanetary disks? Is there a smooth continuum in physical processes, connecting the formation of large moons, with the formation of the smallest planets? In this work we have extended the theoretical tools used to explore planet formation down into this new regime. On the observational side, as the scale of the astrophysical object shrinks, the capabilities of the instrument must rise commensurately to observe it. We are now at the earliest possible stage of directly observing CPDs to gain insights beyond the theoretical into how giant planet moon formation actually proceeds.

Chapter 2: Photoevaporation of the Jovian Circumplanetary Disk

The planetary architecture of the solar system has provided several clues as to the sort of environment it may have formed in. Perhaps a gravitational encounter with a nearby star

Figure i: Illustration of a circumstellar and circumplanetary disk evaporating under intense external UV radiation from the nearby high-mass star forming region.

truncated the outer solar system, removing planets beyond Neptune and stirring up distant objects in the Kuiper belt and Oort cloud. Or perhaps, as the Sun probably formed in a relatively large stellar cluster, a massive nearby star irradiated the circumstellar disk with ultraviolet radiation. If the disk was externally irradiated by sufficiently intense UV light, gas in the disk can be heated until its motion overcomes its gravitational binding energy to the star. In that case the gas escapes, and is blown away from the surface of the disk. Small dust grains that are well-coupled to the gas will be entrained in the flow. Given that the most weakly bound gas is the first to escape, the outer regions of the disk are evaporated and the disk shrinks. Such evaporating disks are observed today in the Orion Nebula where they can be seen shedding long dramatic tails of gas.

The architecture of Jupiter's Galilean moon system is peculiar in that no major satellite orbits beyond Callisto despite there being ample space within the planet's Hill

sphere to fit many additional large moons. Could the CPD in which the moons formed also have been truncated in a way similar to the solar system? Jupiter is a sufficiently massive planet that it would have been able to sweep clean an empty gap in the circumstellar disk. Such a gap, or annulus, if sufficiently empty, would expose the planet and its CPD directly to the external radiation. In Chapter 1 we explore the consequences that such high-mass stellar cluster environment might have on the process of giant planet moon formation. To that end we built a model stellar cluster representative of the one in which the Sun formed, and calculated the motion of the stars within it over several million years. For each potential sun, or sun-like star in the cluster, we determined the total incident magnitude of UV radiation contributed by all other members of the stellar cluster. This allowed us to derive the time-variable UV flux on the putative young solar system.

Our model CPD was then irradiated with varying levels of background UV such that we were able to derive a relationship for how its temperature would increase as a function of the UV flux. This allowed us to calculate the level of background UV at which point gas would be sufficiently heated to become gravitationally unbound from the circumplanetary disk. Normally the CPD is fed by fresh gas and dust falling onto it from the surrounding disk. Later this gas escapes, either falling into the planet or beyond the outer edge of the CPD. The balance between inflow and outflow allows the CPD to exist in steady-state. With the additional evaporation of gas, the new balance results in a disk with a smaller size. The faster the disk loses gas and evaporates, the smaller the size it will have in equilibrium. For each potential solar system in the cluster we were thus able to study the plausible range of sizes to which the CPDs might be shrunk by evaporation.

Interestingly, we found that the majority of CPDs in our stellar cluster tended to have their new outer radii (their truncation radii) clustered around a single value. This new outer radius happens to coincide with the orbit of the outermost regular satellite of Jupiter, Callisto. It appears that photoevaporation of the CPD can offer one explanation as to why the satellite system of Jupiter is not larger than it is - because it lacked the material to form icy moons beyond this orbit. As Saturn and the ice giants were likely not massive enough to open their own dust-free gaps in the circumstellar disks, their CPDs would not have been exposed to comparable levels of UV radiation.

Chapter 3: Ice formation in circumplanetary disks

One striking characteristic of Jupiter's Galilean moon system is its so-called "compositional gradient". As the distance from the planet increases, the iciness of the moons increases as well. The innermost Galilean moon Io is entirely ice-free, while the outermost Callisto consists of nearly equal parts ice and rock. Broadly speaking there are two ways in which this may have occurred. The first possibility is that it occurred after moon's formation, through e.g. bombardment of the moons by asteroids and comets which could have heated the moons until their ices melted and then escaped via an atmosphere. The second is that the gradient may be primordial, in that it reflects the con-

Figure ii: Artist's impression of a "snowline" comprised of icy particles in a circumplanetary disk.

ditions in which the moons formed. For the gradient to be primordial, the solids from which the moons formed must already have exhibited the property of increasing iciness with distance from Jupiter. This idea is appealing, as the CPD from which the moons formed was likely hotter near the luminous planet and colder further away. Hence at some distance from the planet the disk should have become cold enough for volatiles like water to freeze out onto grains.

If we assume that the gradient was primordial, we may place a novel constraint on moon formation: ice must form in the outer CPD but not the inner CPD. This is interesting because the time available to form ices is limited by a key physical parameter that describes the disk evolution: the so-called viscosity. The viscosity parameterizes how efficiently the disk spreads outwards due to the radial exchange of angular momentum by turbulent self-interaction at small scales. In only a few thousand years most of

the gas that has fallen onto a CPD may spread outwards and far away enough from the planet that it is lost beyond its gravitational influence. The disk thus has a short "viscous timescale". Can ices form within this viscous timescale? The viscous timescale must be at least as long as the ice formation timescale.

We tested a grid of plausible CPD models to determine how, when, and where ices form inside the CPD. Ices may be “inherited" from the surrounding circumstellar disk, or they may form in-situ. If the ices are "reset", sublimating during the accretion process, they will need to re-freeze onto dust grains.

The timescale of ice formation after a reset was found to be very short (less than one year) such that it was not possible to place a meaningful constraint on the disk viscosity. This demonstrates that even a high-mass gas giant (with 10× the mass of Jupiter) could still form icy moons. The gravitational pull of such massive planets would accelerate infalling material and form strong accretion shocks causing ices to be sublimated, but significant quantities of ice are able to form again afterwards.

However, we found that a CPD with a relatively low viscosity is most closely able to reproduce the compositional gradient of the Galilean moons. The iceline (the distance from the planet at which ices are able to form) can then form between the present day position of Europa and Ganymede. This is where the iceline might be expected to form in the event that the compositional gradient was primordial.

If the host planet is massive enough, its magnetic field can truncate the inner CPD and prevent moons from falling into the planet. An inwardly migrating moon is prevented from migrating into the planet at the CPD inner edge. If additional satellites drift inwards they can enter a resonant orbital configuration with the innermost moon and are also prevented from drifting further inwards. The moons are then resonantly locked in place, accreting drifting pebbles on either side of the iceline, accordingly becoming either predominantly rocky or predominantly icy.

Furthermore we were able to constrain the maximum amount of solids in the disk, realizing that the solid (rocky) mass must be reduced by a factor 20 to explain the composition of the outermost moons. This factor corresponds very closely with the expected loss of pebbles to inwards aerodynamic drift - supporting the idea that large grains are quickly lost by falling into the planet and that smaller grains go on to build moons.

Chapter 4: Ice composition in circumplanetary disks

While we know that several icy moons in the solar system contain liquid water oceans, we do not know whether these oceans are truly habitable environments. Whether or not an ocean is truly habitable depends on its composition and longevity. A subsurface ocean that contains significant quantities of ammonia, for example, is able to resist freezing - and thus might be able to survive for geological timescales even when heating mechanisms, such as tidal or radiogenic heating, diminish.

In the cold, dense midplane of the CPD, ices of various types are able to form. Chemistry in this context proceeds in large parts on the surface of grains. Molecules, initially floating freely in the gas, temporarily stick to a dust grain surface. The molecules

Figure iii: Artist's impression of a variety of differing icy and rocky particles coalescing somewhere inside a circumplanetary disk.

then tend to wander around the surface of the dust grain, hopping from one sticking-site to another. When two molecules encounter each other during their hopping, they may react to form new products. We refer to this as grain-surface chemistry. To understand the composition of ices that can form in the CPD we must be able to model grain surface chemistry. As far as we are aware, grain-surface chemistry has not been employed previously in the literature to study the formation of ices in CPDs. We therefore included surface chemistry in our model to study the formation and evolution of ices in CPDs.

In the previous section we discussed the possibility that ices from the circumstellar disk may either be inherited by the CPD or they may be reset: shock-heated, destroyed, and returned to the gas (sublimated) as atoms. But this initial condition is not necessarily binary. A partial reset is also possible, in which only the ices sublimate, and the rest of the gas and dust is inherited. A partial reset is what we expect to occur specifically

to gas and ice falling onto a CPD surrounding a planet such as Jupiter. We investigated the consequences of all three of these initial conditions: reset, partial reset, and inheritance to see what sort of ice compositions might arise and what it can tell us about the composition of Jupiter's moons.

We find that in a partial reset scenario, ammonia ice can be accreted and destroyed. After it is sublimated the released nitrogen tends to find its way into N_2 molecules. Once the nitrogen is locked into the N_2 it tends to stay there, as N_2 molecules can effectively shield themselves from the damaging UV radiation. Ammonia ice can survive however if the accretion shock is weak enough such that the CPD inherits circumstellar disk material directly. Material falling onto the CPD of a lower mass planet such as Saturn is less likely to be shock-heated during accretion. The Saturnian moon Titan has a thick nitrogen atmosphere that may have originated from the photochemical or impact-induced destruction of ammonia ice inherited from the circumstellar disk. The loss of ammonia ice in the Jovian CPD implies any forming moons may not have had the nitrogen reservoir available to later develop a dense N_2 atmosphere like Titan's. Likewise, subsurface oceans of the Galilean satellites would lack ammonia in solution, where it could act as a powerful antifreeze.

While we found that Jupiter's moons may be nitrogen poor, we do infer the presence of a substantial CO_2 ice component. This could explain the origin of the CO_2 observed on Callisto where it is dug up by impact craters. Ganymede may have formed free of CO_2, as it is found to orbit interior to the CO_2 iceline in the CPD.

In general, we find the chemistry in the CPD is very different from that of the circumstellar disk as the very high gas densities at relatively cold temperatures enable new chemical pathways that rely on three-body reactions to occur efficiently.

Chapter 5: Modeling Circumplanetary Dust Emission in the Mid-Infrared

Transition disks are planet-forming disks in which a cavity depleted in dust and gas has appeared around the star. These disks represent a transient stage prior to the full dispersal of the gas disk. Massive planets accreting circumstellar disk material are implicated in the formation of these cavities. A pre-transition disk still contains an inner disk, and its annular cavity is typically referred to as a gap. One of the most well-studied disks with a gap is the HD 100546 system. This system is host to several claimed exoplanet detections, both inside and outside the gap, but none of them have been definitively confirmed. This system and five other young stars were selected to be observed with VISIR (VLT Imager and Spectrograph for the mid-InfraRed) and NEAR (Near Earths in the AlphaCen Region).

VISIR and its upgrade NEAR are instruments on the European Very Large Telescope (VLT). With VISIR and NEAR we performed observations of six young stars with (pre-)transition disks suspected to host planets, in search of these planets and their circumplanetary disks. The observations were more sensitive at Mid-infrared (MIR) wavelengths and the exposure time was longer than in previous studies. The use of

adaptive optics on the VLT improved the angular resolution of the observations such that the disks could be resolved. MIR wavelengths trace dust at temperature near 150 K. Massive Herbig Ae/Be stars are able to heat dust grains in their circumstellar disks out to great distance. The dust re-radiates in the infrared and its properties can thus be studied by observation in the MIR. The detectability of a planet could also be enhanced by the presence of warm dust in its CPD.

No new companion objects were detected in this series of observations. However, the non-detection of companions allowed us to place limits on the luminosity of any theoretical planets and CPDs in these systems. A planet orbiting within the gap of the HD 100546 system would be spatially unresolved, and could only be detected by the presence of excess emission associated with the star and inner disk. The maximum modeled companion flux is not sufficient to disentangle from the inner disk flux uncertainty. For planets at greater separation we are able to place a limit on their brightness. Outside of 180 au (astronomical units) planets with a luminosity of 0.0028 $L_\odot$ (solar luminosity) are ruled out. Companions with a luminosity comparable to an M-dwarf star with 1% of the Sun's luminosity were ruled out at distances $a > 60$ au in the TW Hydra system, $a > 110$ au in HD 169142, $a > 150$ au in HD 163296, and $a > 160$ au in HD 36112.

Chapter 6: Observing circumplanetary disks in the future with METIS

Actual detections of CPDs remain rare, and in each case it is difficult to distinguish a true disk surrounding a planet from a large spherical envelope of dust. One candidate CPD has been observed in the PDS 70 system. The PDS 70 system is a disk with a large empty gap in which at least two gas giant exoplanets orbit. One of these planets appears to be surrounded by dust. Hitherto no other disk system with a gap has been found to unambiguously contain a planet, despite that the leading hypothesis for gap formation implicates the presence of planets. As mentioned in the previous section the HD 100546 system is host to a disk with a conspicuous gap in which several planet candidates are suspected to orbit.

Perhaps most interestingly, the presence of a gaseous CPD within the gap has been inferred from the observation of spectral lines emitted by carbon monoxide (CO). The CO spectral lines have been observed to change over time, shifting in wavelength as if the source of the CO were orbiting the star at the predicted position of a planet. Today, it remains difficult to confirm that this planet and its CPD really exists.

The upcoming 39-meter Extremely Large Telescope (ELT) holds promise to make this detection. The METIS instrument on the ELT will be able to observe the mid-infrared wavelengths at which carbon monoxide signals can be detected. However, METIS is so capable compared to previous instruments that it may not only be able to detect the spectral signal, but to simultaneously spatially resolve the emission and verify that it is indeed not originating from the circumstellar disk. To this end we constructed a model combining the emission we expect to see from a CPD with that of the circumstellar disk, and passed it through an instrument simulator. This allowed us to analyze the synthetic observations to determine whether or not we can expect METIS

Figure iv: Artist's impression of the HD 100546 system with circumstellar disk gap and planet candidate.

to detect a CPD in the HD 100546 system or similar systems.

We found that the detectability of a CPD relies quite strongly on the level of background radiation. As we found in Chapter 1, a CPD in a transparent "optically thin" gap can be exposed to significant external irradiation. The HD 100546 star, in particular, is very massive and very luminous, emitting much more UV than does the Sun. The CPD of a planet in orbit around HD 100546 might thus be exposed to nearly 1000 times as much radiation as Jupiter's CPD was exposed to. If the surface layers of the CPD are heated by this UV, the gas begins to emit the carbon monoxide spectral signals very strongly. With our default assumptions, we find that the signal of the CPD can easily be detected by METIS.

The picture is complicated by uncertainties regarding the size of the CPD. If the CPD is much smaller than we expect, this might impact our ability to detect it. A

reduction in radius by a factor 3 - possible due to tidal interactions with the star - would reduce the surface area of the CPD by a factor of nearly 10, and the emitting area of the spectral lines would be correspondingly smaller.

Also, given the close link that was found between external irradiation of the CPD and its resulting detectability, it was important to determine if the stellar UV radiation could really enter the gap and strike the CPD. Small dust grains floating into the gap might effectively block this UV, or obscure the CPD signal by their own thermal emission. The gap region is effectively shadowed by an inner disk that reduces the amount of incident stellar radiation. The majority (90%) of the UV radiation reaching the CPD is however originating from back-scattering off the outer edge of the gap region. And even if the disk gap would be filled with enough dust so as to make it effectively no longer a gap, we found it would still be sufficiently transparent at the relevant wavelengths to allow a CPD to be detected.

Conclusion

Are Jupiter's moons unique? In certain aspects they are, and in others perhaps not. The Sun itself appears to have formed in proximity to many other high-mass stars, unlike the planet-forming disks we study in detail in nearby Taurus. This particular formation environment may have limited the size of the Jovian satellite system by radiatively stripping Jupiter's circumplanetary disk of gas, restricting it to form only as many satellites as could be packed within the orbit of Callisto. Much larger satellite systems may be able to accumulate around planets in more benign radiative environments.

The stark contrast between the inner and relatively dry Io and Europa and the outer, icy and massive Ganymede and Callisto may be a typical consequence of moon formation in a gaseous disk around Jupiter-mass planets. Regardless of initial (chemical) conditions, an iceline forms in the CPD and does so quickly, and is not easily erased by the inwards aerodynamic drift of dust. If moons are prevented from migrating by e.g. being resonantly anchored to the moon at the CPD inner edge, they continue to accrete radially drifting pebbles in-situ. Moons then become either predominantly rocky or consist of an ice-rock mixture depending on their position within the CPD.

In terms of chemical composition, the mass of the planet may also play a pivotal role, with three distinct categories of icy moon composition corresponding to the "inheritance", "partial reset", and "reset" case initial conditions. In that sense the composition of the moons of Saturn-like planets may reflect that of their surrounding circumstellar disk, while those of Super-Jupiters will be chemically distinct and nitrogen-poor. The moons of Jupiter mass planets may lie somewhere in between, nitrogen-poor but also enhanced in carbon content.

Soon, 40-meter class ground-based observatories such as the ELT will allow for the study of moon formation around distant exoplanets. While moon-forming disks may remain challenging to detect by the thermal emission of their minimal dust content, spectral observations of molecular gas may prove to be a more powerful tool to detect and characterize them. Together with the arrival of JUICE and Europa Clipper at the

Jupiter system over the next decade, our understanding of moon formation will surely be propelled to new heights.

Samenvatting

Sterrenkunde is in veel opzichten een introspectieve bezigheid. Een belangrijk deel van de astronomische motivatie komt voort uit de wens te begrijpen of een bewoonbare planeet zoals de aarde een uniek object is, en, in het verlengde daarvan, of de bewoners van de aarde zelf collectief een uniek fenomeen vertegenwoordigen. Per definitie wordt een wereld als potentieel bewoonbaar beschouwd als zij theoretisch in staat is vloeibaar water aan haar oppervlak te bevatten. Maar als we alleen focussen op aarde-achtige planeten riskeren we andere potentieel bewoonbare planeten over het hoofd te zien. De meeste werelden in het zonnestelsel waarvan bekend is dat ze oceanen met vloeibaar water herbergen, lijken namelijk helemaal niet op de aarde. Deze andere werelden hebben echter één kenmerk gemeen: het zijn de ijzige manen die rond gasreuzen draaien. Hun oceanen zitten verborgen onder kilometers bevroren korst. Van ten minste drie manen in het zonnestelsel is met grote zekerheid bekend dat ze een oceaan herbergen (Europa, Enceladus, and Titan), en van nog eens vier wordt vermoed (Ganymedes, Callisto, Mimas, and Dione). Daarom hangt elke hoop op antwoord op de vraag hoe uniek het leven op aarde is af van een schijnbaar ongerelateerde vraag: hoe uniek zijn de ijzige manen?

De vorming van gasreuzen lijkt gepaard te gaan met de vorming van manen, althans, in het zonnestelsel lijken die twee onlosmakelijk met elkaar verbonden. De gasplaneten Jupiter, Saturnus en Uranus worden elk omcirkeld door een reeks regelmatige en onregelmatige manen. De regelmatige satellieten draaien in één vlak, in dezelfde richting en op bijna cirkelvormige banen. Deze bijzondere eigenschappen worden ook door de planeten vertoond, en daarom wordt het waarschijnlijk geacht dat er een soortgelijk proces aan te pas is gekomen om ze te vormen. Dat proces vond waarschijnlijk plaats in een wervelende schijf van gas en stof. Planeten ontstaan in schijven die een ster omgeven (een circum*stellaire* schijf), terwijl de manen ontstaan zijn in een schijf die hun planeet omringd (een circum*planetaire* schijf).

Het laatste decennium van vooruitgang in de observatie van circumstellaire schijven heeft ons begrip van het proces van planeetvorming radicaal veranderd. In hoeverre is het proces van maan- en planeetvorming vergelijkbaar? In hoeverre kunnen we ons begrip van circumstellaire schijven extrapoleren naar de kleinere schalen die kenmerkend zijn voor circumplanetaire schijven? Is er een naadloos continuüm in fysische processen, dat de vorming van grote manen verbindt met de vorming van de kleinste planeten? In dit onderzoek hebben we de theoretische tools uitgebreid zodat we planeetvorming kunnen verkennen binnen dit nieuwe regime. Naarmate de schaal van het proces kleiner wordt, moeten de capaciteiten van een instrument evenredig toenemen om ze waar te nemen. Wij bevinden ons nu in het vroegst mogelijke stadium van rechtstreekse waarneming van CPD's om meer dan alleen theoretische inzichten te krijgen in hoe de vorming van ijzige manen in werkelijkheid verloopt.

Hoofdstuk 2 - Photoevaporatie van de joviaanse circumplanetaire schijf

De planetaire architectuur van het zonnestelsel geeft ons verschillende aanwijzingen over de soort omgeving waarin het gevormd zou kunnen zijn. Misschien werd de buitenste regio van het zonnestelsel door een ontmoeting met een nabije ster afgeknot, waardoor planeten voorbij Neptunus verdwenen en de Kuiper- en Oort-wolk van verre objecten in opschudding kwamen. Of misschien, omdat de zon waarschijnlijk in een relatief grote stellaire cluster is gevormd, heeft een massieve nabije ster de circumstellaire schijf bestraald met ultraviolette (UV) straling. Als de schijf extern werd bestraald door voldoende intens UV-licht, kan het gas in de schijf worden verhit totdat zijn beweging de zwaartekrachtbindingsenergie met de ster overwint. In dat geval ontsnapt het gas, en wordt het weggeblazen van het oppervlak van de schijf. Kleine stofkorrels die sterk gebonden zijn aan het gas worden in de stroom meegevoerd. Aangezien het zwakst gebonden gas als eerste ontsnapt, verdampen de buitenste regionen en krimpt de schijf. Dergelijke verdampende schijven worden tegenwoordig waargenomen in de Orionnevel, en kan men zien hoe gas in lange dramatische staarten wordt afgeworpen.

Het eigenaardige aan de architectuur van het Galileïsche maansysteem is dat er, ondanks dat er voldoende ruimte is in de “Hill sphere" van de planeet, geen grote satelliet bestaat voorbij Callisto. Zou de CPD waarin de manen gevormd zijn, afgekapt kunnen zijn op een vergelijkbare manier als het zonnenstelsel? Jupiter is een voldoende massief planeet om een lege kloof in de circumstellaire schijf schoon te vegen. Zo’n kloof, of annulus, kan, indien voldoende leeg, de planeet en zijn CPD direct blootstellen aan de externe straling. In hoofdstuk 1 hebben wij onderzocht welke gevolgen een dergelijke stellaire geboorteomgeving zou kunnen hebben voor het proces van de vorming van manen. Daartoe hebben wij een model van een sterrenhoop gebouwd die volgens ons representatief is voor diegene waarin de zon is ontstaan, en de beweging van de sterren daarin over enkele miljoenen jaren berekend. Voor elke potentiële zon, of zonachtige ster in de sterrenhoop, bepaalden we de totale invallende magnitude van de UV-straling die door alle andere leden van de sterrenhoop wordt bijgedragen. Zo konden we de tijdvariabele UV-flux op het vermoedelijke jonge zonnestelsel afleiden.

Onze model-CPD werd vervolgens bestraald met verschillende niveaus van achtergrond -UV totdat we een verband konden afleiden met de temperatuurstijging. Zo konden we het UV-achtergrondniveau berekenen waarop het gas voldoende verhit zou zijn om zich gravitationeel los te maken van de CPD. Normaal gesproken wordt de CPD gevoed door vers gas en stof dat er vanuit de omringende nevel op valt. Later ontsnapt dit gas en valt het in de planeet of verspreidt zich voorbij de buitenrand van de schijf. Door het evenwicht tussen in- en uitstroom kan de CPD in een stationaire toestand bestaan. Met de extra verdamping van gas onstaat een nieuwe evenwicht tussen in- en uitstroom, met als resultaat een schijf met een kleinere omvang. Hoe sneller de schijf gas verliest en verdampt, hoe kleiner hij in evenwicht zou zijn. Voor elk niveau van achtergrondstraling in de cluster konden wij dus een plausibele CPD-buitenstraal (afgekapte straal) afleiden.

Interessant is dat de meeste CPD's in onze sterrenhoop de neiging hebben hun nieuwe buitenstraal rond één waarde te concentreren. Deze nieuwe buitenstraal valt toevallig samen met de baan van de buitenste regelmatige satelliet van Jupiter: Callisto. Het lijkt er op dat fotoevaporatie een mogelijke verklaring kan bieden waarom het satellietsysteem van Jupiter niet groter is dan het is - er ontbrak materiaal om ijzige manen te kunnen vormen verder dan deze baan. Aangezien Saturnus en de ijsreuzen waarschijnlijk niet groot genoeg waren om hun eigen stof-vrije kloof in de circumstellaire schijven te openen, konden hun CPD's niet blootgesteld worden aan vergelijkbare hoeveelheden UV-straling.

Hoofdstuk 3 - IJsvorming in circumplanetaire schijven

Een frappant kenmerk van het Galileïsche maansysteem van Jupiter is de zogenaamde "compositiegradiënt". Naarmate de afstand tot de planeet toeneemt, neemt ook de ijzigheid van de manen toe. De binnenste Galileïsche maan Io is geheel ijsvrij, terwijl de buitenste maan Callisto uit bijna gelijke delen ijs en rots bestaat. In grote lijnen zijn er twee manieren waarop dit kan gebeurd zijn. De eerste mogelijkheid is dat dit na de vorming van de manen is gebeurd. Bijvoorbeeld, door bombardementen door asteroïden en kometen die de manen hebben verhit totdat hun ijs smolt en vervolgens via een atmosfeer ontsnapte. De tweede is dat de gradiënt primordiaal kan zijn, in die zin dat deze de omstandigheden weerspiegelt waarin de manen werden gevormd. Om de gradiënt primordiaal te laten zijn, moeten de vaste stoffen waaruit de manen zijn opgebouwd al de eigenschap vertonen dat de ijzigheid toeneemt met de afstand tot Jupiter. Dit idee is aanlokkelijk, omdat de CPD waaruit de manen zijn ontstaan waarschijnlijk heter was nabij de gloeiende planeet en kouder verder weg. Op een zekere afstand van de planeet moet de schijf dus koud genoeg zijn geworden om vluchtige stoffen zoals water op stofkorrels te laten bevriezen.

Als we aannemen dat de gradiënt primordiaal was, kunnen we een nieuwe beperking stellen aan het proces van maanvorming: er moet ijs kunnen vormen in de buitenste regio van een CPD, maar niet in de binnenste. Dit is interessant omdat de beschikbare tijd om ijs te vormen wordt beperkt door een belangrijke fysische parameter die de evolutie van de schijf bepaalt: de zogenaamde viscositeit. De viscositeit bepaalt hoe stroperig de schijf zich gedraagt, die zich naar buiten verspreidt door de radiale uitwisseling van impulsmoment door turbulente zelfinteractie op kleine schaal. Binnen slechts een paar duizend jaar kan het meeste gas dat op een CPD is gevallen zich naar buiten verspreiden en ver genoeg van de planeet verwijderd zijn zodat het buiten zijn gravitatie-invloed verdwijnt. De schijf heeft dus een korte "viskeuze tijdschaal". Kan er binnen deze viskeuze tijdschaal ijs vormen? De viskeuze tijdschaal moet minstens even lang zijn als de tijdschaal voor ijsvorming.

Wij hebben een reeks van plausibele CPD-modellen getest om te bepalen hoe, wanneer en waar zich binnen de CPD ijs vormt. Ijs kan worden geërfd van de omringende circumstellaire schijf, of kan ter plaatse worden gevormd. Als de verschillende soorten ijs worden "gereset" en dus tijdens het accretieproces sublimeren, moeten ze opnieuw

bevriezen op stofkorrels.

De tijdschaal van ijsvorming na een reset bleek zeer kort te zijn (minder dan 1 jaar), zodat het niet mogelijk was een zinvolle beperking te stellen aan de schijfviscositeit. Dit toont aan dat zelfs een gasreus met een hoge massa (een “super-Jupiter" met een massa van 10 Jupiters) nog steeds ijzige manen kan vormen. De zwaartekracht van zo’n massive planeten kan het instromende materiaal versnellen, waarbij sterke accretieschokken ijs sublimeren - toch kunnen significante hoeveelheden ijs achteraf opnieuw gevormd worden.

We vonden echter dat een CPD met een relatief lage viscositeit het dichtste de compositiegradient van de Galileïsche manen kan benaderen, en dat de ijslijn (de afstand van de planeet waarbij ijs kan vormen) zich kan plaatsen tussen de huidige positie van Europa en Ganymedes. Dit is waar de ijslijn naar verwachting zou ontstaan als de compositiegradiënt primordiaal was.

Als de planeet massief genoeg is, kan haar magnetisch veld de binnenste CPD afkappen, en dat voorkomt dat manen in de planeet vallen. Een maan die naar binnen toe migreert, zal niet verder migreren dan de CPD’s binnenrand. Als meerdere satellieten naar binnen toe drijven, kunnen ze een resonante configuratie vormen met de binnenste maan, en zullen ze daardoor verhinderd zijn om verder naar binnen te drijven. De manen zijn vergrendeld op hun plaats door hun resonantie, slokken aan beide zijden van de ijslijn rondzwervende steentjes op en bestaan navenant ofwel hoofdzakelijk uit rots of een mengsel van ijs en rots.

Bovendien hebben wij de maximale hoeveelheid vaste (rotsachtige) stoffen in de schijf kunnen vaststellen: de vaste massa moet met een factor 20 worden verminderd om de samenstelling van de buitenste manen te verklaren. Deze factor komt zeer goed overeen met het verwachte verlies van rotsachtige korrels door inwaartse aërodynamische drift - wat het idee ondersteunt dat grote korrels snel verloren gaan in CPD’s en dat kleine korrels verder gaan om manen te bouwen.

Hoofdstuk 4 - IJssamenstelling in circumplanetaire schijven

Hoewel we weten dat verschillende ijzige manen in het zonnestelsel oceanen met vloeibaar water bevatten, weten we niet of deze oceanen echt bewoonbaar zijn. Of een oceaan echt bewoonbaar is, hangt af van zijn samenstelling en levensduur. Een ondergrondse oceaan die grote hoeveelheden ammoniak bevat, is bijvoorbeeld bestand tegen bevriezing - en kan dus wellicht gedurende geologische tijdschalen overleven, zelfs wanneer mechanismen die voor verwarming zorgen, zoals getijden- of radiogene verwarming, afnemen.

In het koude, dichte middenvlak van de CPD kunnen zich verschillende soorten ijs vormen. De chemische reacties vinden in deze context grotendeels aan het oppervlak van de stofkorrels plaats. Moleculen, die aanvankelijk vrij in het gas zweven, kleven tijdelijk aan het oppervlak van een stofkorrel. De moleculen hebben dan de neiging om rond het oppervlak van de stofkorrel te hoppen, van de ene hechtplaats naar de andere. Wanneer twee moleculen elkaar tijdens het hoppen tegenkomen, kunnen zij een reactie ondergaan en nieuwe moleculen vormen. Wij noemen dit korrel-oppervlak

chemie. Om de samenstelling van de ijssoorten die zich in de CPD kunnen vormen te doorgronden, moeten we de chemie aan het korreloppervlak kunnen modelleren. De chemie van het korreloppervlak is nog niet eerder gebruikt om de vorming van ijs in CPD's te bestuderen.

Eerder bespraken we de mogelijkheid dat ijs van de circumstellaire schijf ofwel door de CPD wordt geërfd, of wordt gereset: verhit door schokken, vernietigd en terug naar het gas gevoerd, gesublimeerd tot atomen. Maar deze begintoestand is niet noodzakelijkerwijs binair. Een gedeeltelijke reset is ook mogelijk, waarbij alleen de ijzen sublimeren en de rest van het moleculaire gas en het stof wordt geërfd. Een gedeeltelijke reset is specifiek wat we verwachten in het geval van een Jupiter-achtige planeet. Wij hebben de gevolgen van alledrie deze beginvoorwaarden onderzocht: reset, gedeeltelijke reset en overerving, om te zien welk soort ijssamenstelling zou kunnen ontstaan en wat die ons zou kunnen vertellen over de samenstelling van Jupiters manen.

Wij stellen vast dat in het scenario van gedeeltelijke reset, ammoniakijs kan worden geaccumuleerd en vernietigd. Na sublimatie heeft vrijgekomen stikstof de tendens zijn weg te vinden naar de N2-moleculen. Zodra stikstof in N2 is opgesloten, blijft het daar, omdat N2-moleculen zich effectief kunnen beschermen tegen de schadelijke UV-straling. Ammonia-ijs kan echter blijven bestaan als de accretieschok zo zwak is dat de CPD rechtsreeks materiaal van de circumstellaire schijf erft. Materiaal dat op de CPD van een planeet met een lagere massa valt, zoals op Saturnus, heeft minder kans op schokverhitting tijdens de accretie. Titan, maan van Saturnus, heeft een dikke atmosfeer van stikstof die mogelijk is ontstaan door de (fotochemische of impact-geïnduceerde) vernietiging van ammoniakijs, geërfd van de circumstellaire schijf. Het verlies van ammoniakijs in de Joviaanse CPD impliceert dat eventuele vormende manen mogelijk geen stikstofreservoir hadden om later een dichte N2-atmosfeer te ontwikkelen zoals die van Titan. Net zoals de ondergrondse oceanen van de Galileïsche satellieten geen ammoniak in oplossing hebben, waar het als krachtig antivriesmiddel zou kunnen dienen.

Hoewel we hebben vastgesteld dat de manen van Jupiter mogelijk stikstofarm zijn, leiden we wel de aanwezigheid van een aanzienlijke CO_2-ijscomponent af. Dit zou de oorsprong van de CO_2 op Callisto kunnen verklaren, die er wordt opgegraven door inslag van meteorieten. Ganymedes kan zich zonder CO_2 gevormd hebben, aangezien zijn baan binnen de CO_2-ijslijn van de CPD ligt.

In het algemeen vinden we dat de chemie in de CPD vrij uniek is ten opzichte van de circumstellaire schijf, omdat de zeer hoge gasdichtheid bij relatief koude temperaturen nieuwe chemische routes mogelijk maakt die afhankelijk zijn van drielichamenreacties.

Hoofdstuk 5 - Modellering van circumplanetaire stofemissie in het midden-infrarood

Overgangsschijven zijn planeetvormende schijven waarin een holte met weinig stof en gas rond de ster is ontstaan. Deze schijven representeren een voorbijgaande fase voorafgaand aan de volledige verspreiding van de gasschijf. Bij de vorming van deze holtes

zijn massieve planeten betrokken die materiaal van de circumstellaire schijf opnemen. Een pre-overgangsschijf bevat nog een binnenschijf, en de ringvormige holte daarvan wordt doorgaans een kloof genoemd. Een van de best bestudeerde schijven met een kloof is het HD 100546-systeem. In dit systeem zijn verschillende beweerde waarnemingen van exoplaneten gedaan, zowel binnen als buiten de kloof, maar geen daarvan is definitief bevestigd. Dit stelsel en vijf andere jonge sterren zijn geselecteerd om te worden geobserveerd met VISIR (VLT Imager and Spectrograph for the mid-InfraRed) en NEAR (Near Earths in the AlphaCen Region).

VISIR en zijn upgrade NEAR zijn instrumenten op de Europese Very Large Telescope (VLT). Met VISIR en NEAR hebben we observaties uitgevoerd van zes jonge sterren met (pre-)overgangsschijven waarvan vermoed wordt dat ze planeten herbergen, op zoek naar deze planeten en hun circumplanetaire schijven. De observaties waren gevoeliger bij mid-infrarood (MIR) golflengten en de belichtingstijd was langer dan in eerdere studies. Het gebruik van adaptieve optiek op de VLT verbeterde de hoekresolutie van de waarnemingen, zodat de structuur van de schijven zichtbaar wordt. Met MIR-golflengten kan stof met een temperatuur van rond de 150 K worden opgespoord. Massieve Herbig Ae/Be-sterren kunnen tot op grote afstand stofkorrels in hun circumstellaire schijven verhitten. Het stof straalt dan uit in het infrarood en de eigenschappen ervan kunnen dus worden bestudeerd door observatie in het MIR. De detecteerbaarheid van een planeet kan ook worden vergroot door de aanwezigheid van warm stof in zijn CPD.

In deze reeks waarnemingen zijn geen nieuwe planeten of planeetachtige objecten ontdekt. Door het niet detecteren van zulke companions konden we echter grenzen stellen aan de helderheid van eventuele theoretische planeten en CPD's in deze systemen. Een planeet die in de kloof van de HD 100546-schijf draait, zou niet kunnen worden onderscheiden van de binnenschijf en ster en zou alleen kunnen worden gedetecteerd door de aanwezigheid van overtollige emissie die niet kan toegekend worden aan de binnenschijf en ster. De maximale gemodelleerde companionflux is niet groot genoeg om hem te kunnen ontwarren uit de onzekerheid van de flux van de binnenschijf. Voor planeten op grotere afstand kunnen we wel een limiet stellen aan hun mogelijke helderheid. Buiten 180 au (astronomische eenheden) zijn planeten met een helderheid van 0,0028 $L_{\odot}$ (veelheid van de helderheid van de zon) uitgesloten. Planeten-met-CPDs met een helderheid die vergelijkbaar is met die van een M-dwergster met 1% van de zon zijn uitgesloten op afstanden $a > 60$ au in het TW Hydra-systeem, $a > 110$ au in HD 169142, $a > 150$ au in HD 163296, en $a > 160$ au in HD 36112.

Hoofdstuk 6 - Toekomstige observatie van circumplanetaire schijven met METIS

Waarnemingen van CPD's blijven zeldzaam, en het is in elk geval moeilijk om een echte schijf rond een planeet te onderscheiden van een grote bolvormige stofmantel. Eén kandidaat CPD is waargenomen in het PDS 70-systeem. Het PDS 70-systeem is een schijf met een grote lege ruimte waarin ten minste twee exoplaneten draaien. Een van deze

planeten lijkt door stof omgeven te zijn. Van geen enkel ander schijfsysteem met een holte is ondubbelzinnig vastgesteld dat het een planeet bevat, hoewel de aanwezigheid van planeten wordt geïmpliceerd in de leidende hypothese van holtevorming. Zoals in de vorige paragraaf is vermeld, herbergt het HD 100546-systeem een schijf met een opvallend holte waarin verschillende planeetkandidaten worden vermoedelijk ronddraaien

Een van de best bestudeerde schijven met een kloof is het HD 100546-systeem. In dit systeem zijn bijna een dozijn vermeende exoplaneetdetecties gedaan, zowel binnen als buiten de kloof, maar geen daarvan is definitief. Wellicht het meest interessant is dat de aanwezigheid van een CPD afgeleid kan worden uit de waarneming van spectraallijnen van koolmonoxide (CO). Men heeft waargenomen dat de CO-spectraallijn afkomstig van dit systeem verandert en in golflengte verschuift in de loop der tijd, wat overeenkomt met de verwachte beweging van een planeet (en het gas in zijn CPD) die mogelijk rond de ster zou draaien. Vandaag blijft het moeilijk om te bevestigen dat er werkelijk een planeet en CPD aanwezig zijn.

De verwachte 39-meter Extremely Large Telescope (ELT) belooft deze detectie mogelijk te maken. Het METIS-instrument op de ELT zal de mid-infrarode golflengten kunnen waarnemen waarop koolmonoxidesignalen kunnen worden gedetecteerd. METIS is echter zo krachtig in vergelijking met eerdere instrumenten dat het misschien niet alleen het spectrale signaal kan detecteren, maar ook de emissie ruimtelijk kan onderscheiden en kan nagaan of deze inderdaad niet afkomstig is van de circumstellaire schijf. Daartoe hebben we een model geconstrueerd dat de verwachte emissie van een CPD combineert met die van de circumstellaire schijf, en dat door een instrumentensimulator gehaald. Zo konden we de synthetische waarnemingen analyseren om te bepalen of we al dan niet kunnen verwachten dat METIS een CPD kan detecteren in het HD 100546-systeem of soortgelijke systemen.

We ontdekten dat de detecteerbaarheid van een CPD sterk afhangt van het achtergrondstralingsniveau. Zoals we in hoofdstuk 1 hebben vastgesteld, kan een CPD in een transparante kloof worden blootgesteld aan aanzienlijke externe straling. Met name de ster HD 100546 is zeer massief en zeer helder, en zendt veel meer UV-straling uit dan de zon. De CPD van een planeet in een baan rond HD 100546 zou dus aan bijna 1000x zoveel straling kunnen worden blootgesteld als de CPD van Jupiter. Als de oppervlaktelagen van de CPD door deze straling worden verhit, begint het gas de koolmonoxidespectrale signalen zeer sterk uit te zenden. Met onze standaardaannames vinden we dat het signaal van de CPD gemakkelijk door METIS kan worden gedetecteerd.

Het scenario wordt gecompliceerd door onzekerheden over de grootte van de CPD. Als de CPD veel kleiner is dan we verwachten, kan dit gevolgen hebben voor ons vermogen om hem waar te nemen. Een vermindering van de straal met een factor 3 - mogelijk door getijdeninteracties met de ster - zou het oppervlak van de CPD met een factor van bijna 10 verkleinen, en het uitstralingsgebied van de spectraallijnen zou navenant kleiner zijn.

Gezien het nauwe verband dat is gevonden tussen externe bestraling van de CPD en de daaruit voortvloeiende detecteerbaarheid, was het van groot belang om vast te stellen of het klopt dat de stellaire UV-straling werkelijk de kloof kan binnendringen en

de CPD kan treffen. Kleine stofkorrels die in de kloof drijven zouden deze UV-straling effectief kunnen blokkeren, of het CPD-signaal kunnen belemmeren door hun eigen thermische emissie. De kloof wordt effectief overschaduwd door een binnenschijf die de hoeveelheid invallende stellaire straling vermindert. Het grootste deel (90 %) van de UV-straling die de CPD bereikt, is echter afkomstig van verstrooiing van de buitenrand van de kloof. En zelfs als de kloof in de schijf zou worden opgevuld met voldoende stof, waardoor het effectief geen kloof meer is, zou hij bij de relevante golflengten nog steeds transparant genoeg zijn om een CPD te detecteren.

Conclusie

Zijn Jupiters manen uniek? In sommige opzichten wel, in andere misschien niet. De zon lijkt zelf op een relatief ongewone manier te zijn gevormd, omgeven door een dichte cluster van vele hoog-massa sterren, in tegenstelling tot de planeetvormende schijven die we in detail bestuderen in het nabijgelegen Taurus. Deze eigenaardige vormingsomgeving kan de omvang van een potentieel massiever Joviaans satellietsysteem hebben beperkt door Jupiters planetaire schijf te strippen van gas, waardoor deze slechts zoveel satellieten kan vormen als er in de baan van Callisto passen. Mogelijk kunnen er veel grotere satellietsystemen gevormd worden in meer gunstige stralingsomstandigheden.

Het scherpe contrast tussen het relatief droge Io en Europa aan de binnenzijde, en de massieve, ijzige Ganymede en Callisto aan de buitenkant, zou een typische consequentie kunnen zijn van maanvorming binnen een gasschijf schijf rondom planeten met Jupitermassa. Ongeacht de (chemische) beginvoorwaarden verschijnt een ijslijn en doet dat snel, en wordt niet gemakkelijk uitgewist door de inwaartse aerodynamische drift van stofkorrels. Als manen door een orbitale resonantie verankererd worden aan een maan aan de binnenrand van de CPD, blijven ze ter plaatse radiaal drijvende steentjes opslokken. Manen worden dan overwegend rotsachtig of bestaan uit een mengsel van ijs en rots, afhankelijk van hun positie binnen de CPD.

De massa van de planeet kan echter een centrale rol spelen voor de chemische samenstelling van de manen, die we in drie afzonderlijke categorieën opdelen op basis van hun beginvoorwaarden: "overerving", "gedeeltelijke reset" en "reset". In dat opzicht weerspiegelen de composities van de manen van Saturnus-achtige planeten mogelijk die van hun omringende circumstellaire schijf, terwijl Super-Jupiters eerder chemisch verschillend en stikstofarm zullen zijn. De manen van Jupiter-achtige planeten liggen mogelijk ergens tussenin, stikstofarm maar met een verhoogd koolstofgehalte.

Binnenkort zullen de observatoria in de klasse van 40 meter zoals de ELT het mogelijk maken de maanvorming rond verre exoplaneten te bestuderen. Terwijl het een uitdaging blijft om maanvormende schijven te detecteren aan de thermische emissie van hun minimale stofgehalte, kunnen spectrale waarnemingen van moleculair gas een krachtiger instrument blijken om ze te detecteren en te karakteriseren. Samen met de aankomst van JUICE en Europa Clipper in het Jupiter-systeem in het komende decennium zal ons begrip van maanvorming naar nieuwe hoogten worden gestuwd.

1 Introduction

Suppose those infinite worlds are unlike ours.

- Johannes Kepler,
Kepler's Conversation with Galileo's Sidereal Messenger

One hour after sunset on the evening of January 7th 1610, Jupiter happened to lie between the two horns of Taurus. Intending to document hitherto invisible stars within the constellation by means of a novel telescope of his own construction, Galileo was temporarily distracted by the planet. He serendipitously observed three 'little stars' curiously arranged 'exactly in a straight line, parallel to the ecliptic' near Jupiter which he believed to be fixed stars (Galilei, 1610). After being led 'by some fatality' to observe the planet again the following night he encountered a curious development. Jupiter, in contradiction to the available ephemerides, was now to be found to the East of the stars. Fearful that the planet had deviated inexplicably from its stately proper motion in some kind of celestial tack, Galileo began to monitor the system regularly. Within days it became clear that there were four 'stars', and they accompanied the planet wherever it went.

Galileo successfully reasoned that the four lights were satellites of Jupiter and for their wandering labelled them 'planets'. The moons were independently discovered by Simon Marius a day later (Marius, 1614). It was Marius, on Kepler's suggestion, who assigned the names which would be widely adopted only in the latter half of the 20th century; Io, Europa, Ganymede, and Callisto (Lynn, 1903). The discovery of the satellites would have profound scientific, mathematical, and philosophical implications. Combined with the discovery of Venusian phases they effectively ended support for the geocentric model of the solar system (Johnson, 1978; Wootton, 2015). Periodic variations in eclipse timing of the moons would provide the first observational evidence of the finite speed of light (Rømer, 1677). Analysis of the moons' mutual gravitational perturbations led to the discovery and description of orbital resonance by Lagrange and later Laplace (de Sitter, 1931).

This "Galilean system" represented to contemporaneous thinkers a solar system in miniature. The physical diversity of the satellites, rivaling that of the terrestrial planets, came as a surprise after the first robotic missions visited the Jovian system in the 20th century. While the moons were expected by many to be geologically dead worlds they instead displayed a striking variety. Observed features ranged from sulphurous volcanic eruptions to signs of subsurface oceans, and from traces of world-girdling resurfacing events to craters nearly as ancient as the solar system itself (Smith et al., 1979).

Many unanswered but fundamental questions remain despite decades of remote and in-situ observation: Why are the Galilean moons as massive as they are? What process led to the significant compositional dichotomy between the inner and outer two satellites? How did their orbits evolve into a Laplace resonance? Were other moons of Jupiter once formed and lost? Why does the Jovian satellite system differ from those of Saturn or Uranus? Is there a fundamental connection between planet and regular satel-

Figure 1.1: Reproduction of Galileo's discovery sketches of the Galilean satellites from *Sidereus Nuncius*. On the first night Io and Europa were spatially unresolved near conjunction. On the second night, Callisto's position was not recorded. On January 9th the night sky was clouded. On January 10th Europa and Ganymede were spatially unresolved while Io was lost in Jupiter's glare.

lite formation? This multitude of questions can be synthesized into one: Are Jupiter's moons unique? No analog to the Jovian system has yet been found beyond the solar system, although this is largely due to instrumental limitations that preclude their detection.

The formation of the massive regular satellites of the solar system was likely a byproduct of the planet formation process (Lunine and Stevenson, 1982), a phenomenon now known to occur ubiquitously (Winn and Fabrycky, 2015; Winn, 2018; Zhu and Dong, 2021). Moons that orbit extrasolar planets may be habitable (Williams et al., 1997), and may even be the most common form of potentially habitable worlds (Kohler, 2018) if giant planets are found to host more than one massive satellite each (Hill et al., 2018). While the detection of exomoon systems similar to Jupiter's remains elusive (Teachey et al., 2018), the veil surrounding the anticipated but theoretical moon-forming circumplanetary disks (CPDs) has begun to lift (Reggiani et al., 2018; Isella et al., 2019; Benisty et al., 2021; Keppler et al., 2019; Bae et al., 2022).

1.1 Satellites of the Solar System

The natural satellites of the solar system planets are divided into “regular" and “irregular" dynamical categories. Regular satellites orbit their primary prograde, in its equatorial plane, with low eccentricity, and with low mutual inclinations between moons. The properties of regular satellites are consistent with formation in a disk in orbit around their primary. Irregular satellites may instead have been captured, and typically orbit in high inclinations with larger eccentricities. Some regular satellites accreted sufficient mass to overcome the tensile strength of their bulk composition and rounded to approach hydrostatic equilibrium. Of the regular satellites of the gas giants, 16 are sufficiently massive to have become rounded. Gravitationally rounded satellites are referred to as “major", while irregularly shaped satellites are referred to as “minor" regardless of their orbital parameters.

Jupiter has four major satellites: the Galilean moons Io, Europa, Ganymede, Callisto, and four minor regular satellites in the Amalthea group. The Amalthea group lies tightly confined to a common plane. The bulk density of Amalthea itself is below that of water suggesting that it contains a substantial fraction of ice, and is therefore suspected to have been captured rather than formed in-situ (Anderson et al., 2005). At first glance the Jovian regular satellite system has a superficial architectural similarity with the solar system planets: the four inner satellites of the Amalthea group, close-in to Jupiter and compactly spaced, mirror the four inner terrestrial planets, while the four outer massive Galilean satellites mirror the four outer massive gas and ice giant planets of the solar system.

Other regular satellites systems in the solar system are suspected to have formed in a disk similarly to the Jovian moons (Peale and Canup, 2015; Szulágyi et al., 2018). Saturn has seven spheroidal regular satellites (Mimas, Enceladus, Tethys, Dione, Rhea, Titan, and Iapetus). Unlike the Jovian system, the Saturnian satellites are dominated by the largest moon Titan, which contains 96% of the Saturnian satellite system total mass and is larger than the planet Mercury (Thomas, 2010). Unlike the Galilean satellites, Saturn’s inner regular satellites and Titan may not have formed simultaneously. The inner moons may instead have formed one-by-one from a viscously spreading ring system once sufficient matter drifted beyond the Saturnian Roche limit (Charnoz et al., 2011; Crida and Charnoz, 2012). Uranus has five rounded regular satellites (Miranda, Ariel, Umbriel, Titania, Oberon). The mass-period relation diagram of all the minor and major regular satellites of the solar system gas and ice giants can be found in Fig. 1.2. The distribution of the intermediate-mass moons of Saturn and Uranus in mass-period space appears suggestive of a potential common formation mechanism, while Titan and the Galilean moons are significant outliers from this trend.

Neptune, despite its only major satellite being captured into an irregular orbit, still hosts an array of minor satellites (Naiad, Thalassa, Despina, Galatea, Larissa, Hippocamp, and Proteus) that may have survived a chaotic capture process (Goldreich et al., 1989). The regular satellite systems of Jupiter, Saturn, and Uranus all have similar mass ratios with their planet; the ratio of the total satellite to planet mass $M_{\rm sat}/M_{\rm p} = 2 \times 10^{-4}$

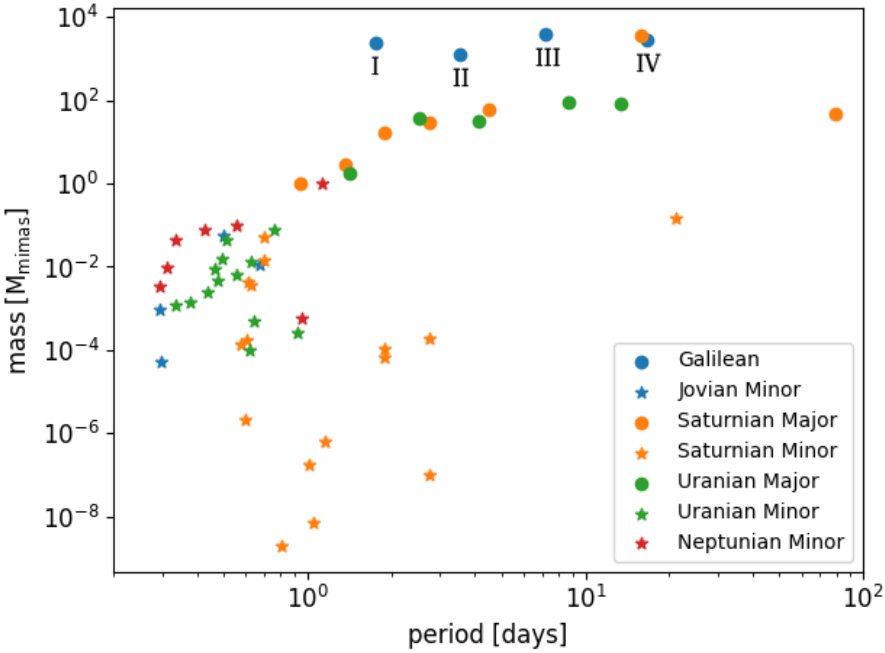

Figure 1.2: Select orbital and physical properties of the regular satellites of the solar system gas and ice giants (de Pater and Lissauer, 2010). The Galilean moons are labeled I (Io), II (Europa), III (Ganymede) and IV (Callisto). Mass is expressed in units of the mass of Mimas, the smallest gravitationally rounded satellite in the solar system.

for Jupiter, 2.5×10^{-4} for Saturn, and 10^{-4} for Uranus. The similarity of these regular satellite systems to compact exoplanet systems in terms of relative size and semi-major axes has not gone unnoticed (Kane et al., 2013).

1.1.1 The Galilean Moons

The Galilean moons were the first bodies found to be unambiguously in orbit around an object other than the Sun or the Earth. For contemporary thinkers they represented a solar system in miniature, albeit one advancing at an accelerated pace (with orbital periods ranging between 1.7 and 16.7 days) relative to the comparatively stately orbits of the planets (Johnson, 1978). This enabled the study of subtle gravitational effects that might otherwise require many decades to become apparent on the orbital timescale of the planets. The orbit of the inner three Galilean moons were quickly determined to be in a mean-motion resonance now known as the Laplace resonance. The orbital periods of Io, Europa, and Ganymede are approximately related by the ratio 1:2:4, while Callisto

does not participate in the resonance. In the Laplace resonance, the orbital phase of the satellites is locked via the relation

$$\Psi_L = \lambda_{\mathrm{I}} - 3\lambda_{\mathrm{E}} + 2\lambda_{\mathrm{G}} = 180^\circ, \quad (1)$$

where λ_I, λ_E, and λ_G are the mean longitudes of Io, Europa, and Ganymede. Outside of the solar system, a Laplace resonance is also found in the extrasolar planetary system Gliese 876, although its particular configuration does not prevent triple conjunctions (Martí et al., 2013). Laplace determined the Galilean moon masses to be only a fraction of Jupiter's mass through the study of their mutual perturbations, accurate to within 15% of modern values for Europa and Ganymede (Pappalardo et al., 2009). Estimates of their radii accurate to within 6-12% were made by the use of filar micrometers (Barnard, 1895). Atmospheric seeing prevented detailed observation of their surface features, although periodic brightness variations revealed that the moons rotated synchronously (Lyot, 1953). Even into the 20th century it was claimed erroneously that the moons had a pronounced prolateness, were egg-shaped, or that they consisted of a swarm of meteors or dust (Antoniadi, 1898; Pickering and Shapley, 1937); however generally they were believed to be similar in size and composition to the Earth's moon (de Sitter, 1931). The first suggestion that their bulk composition may be explained by water or carbon dioxide ice was made by Jeffreys (1923)

The first direct measurement of the composition of the Galilean system was made with infrared spectroscopy revealing ice-like absorption features on the outer moons (Pilcher et al., 1972). Early robotic exploration revealed that the Galilean moons were in general dissimilar to the Earth's moon, as none of them were both siliceous and geologically dead. The *Voyager* spacecraft revealed Io to be an actively volcanic world (Morabito et al., 1979), which had been predicted three days prior to closest approach (Peale et al., 1979). The surfaces of Europa and Ganymede were revealed to be younger than expected, having been resurfaced at some point after their initial formation, and also host to possible subsurface oceans (Cassen et al., 1979; Squyres et al., 1982). Lacking tectonism and being uniformly cratered, the properties of the outermost Galilean moon Callisto were more consistent with pre-robotic expectations. Measurements made by the *Galileo* spacecraft determined the axial moment of inertia of the moons, demonstrating that Callisto was likely only partially differentiated (Anderson et al., 2001). The orbital configuration, bulk composition, and internal differentiation state of the satellites became the most important constraints to understand their formation history.

Io

Io is the innermost of the Galilean satellites, and is the only massive Jovian satellite entirely free of volatile ices. The bulk density 3.53 g/cm^3 is similar to that of Mars and the Earth's Moon. Measurements of the moon's quadrupole gravitational coefficients by the Galileo spacecraft have been used to determine that the interior is differentiated into a silicate mantle and iron core (Anderson et al., 1996). Models of the interior suggest that the mantle is composed of 75% Forsterite, with a bulk composition similar

Parameter	Unit	Io	Europa	Ganymede	Callisto
Mean Radius	km	1821	1565	2631	2410
Mass	10^{23}kg	0.893	0.480	1.482	1.076
Density	$\rho_\oplus$	0.641	0.547	0.351	0.334
ice fraction	%	0	6-8	45	56
C/MR^2	-	0.375	0.346	0.311	0.359
a	R_J	5.9	9.40	14.97	26.33
p	days	1.77	3.55	7.15	16.68
i	degrees	0.04	0.47	0.18	0.19
e	-	0.004	0.009	0.001	0.007

Table 1: Galilean satellite physical and orbital properties (Schubert et al., 2004). Density is expressed in terms of the bulk density of the earth $\rho_\oplus$. a is the semi-major axis, p is the orbital period, i is the inclination, and e is the eccentricity. The semi-major axis is expressed in multiples of the Jupiter radius R_J.

to L-chondrites (Schubert et al., 2004). Its short orbital period and orbital eccentricity generate significant tidal heating (Peale et al., 1979; Yoder and Peale, 1981) and accordingly its surface is the most geologically active in the solar system. Around 400 active volcanoes are expected to be found on the surface at any given time, producing plumes of sulfur and sulfur dioxide (Lopes et al., 2004). Io's participation in the Laplace resonance is partially responsible for maintaining a non-zero orbital eccentricity, which would otherwise be circularized by the tidal dissipation and cause Io to migrate outwards (McKinnon, 2007). The dissipative heating is several hundred times as great as the heating produced by radiogenic decay (Bierson and Steinbrügge, 2021).

Io's primordial atmosphere has been lost either to thermal escape, XUV driven photoevaporation, bombardment driven loss, or stripping by Jupiter's magnetosphere (Heller et al., 2015). Further insights into Io's bulk composition can be derived from its volcanic emission and outgassing. A tenuous steady state atmosphere of SO_2, SO, NaCl, S, and O exists due to continuous replenishment by volcanoes and sublimation of SO_2 frost and interaction with Jupiter's magnetic field which removes 10^3 kg of gas per second (Moullet et al., 2010).

Europa

Europa is the next satellite orbiting exterior to Io. Its bulk density of 3.013±0.005 g/cm^3 lies below that of Io but above that of ice-rich Ganymede and Callisto (see Table.1), implying that it consists of a mixture of predominantly iron and rock with an external ice and water shell. It is the least massive Galilean satellite and also the one with the smallest radius. Measurements of its axial moment of inertia by the Galileo spacecraft imply its interior is differentiated (D Anderson et al., 1998). The surface composition appears to consist primarily of water ice and trace hydrated salt minerals (Calvin et al., 1995;

Dalton III et al., 2012; Trumbo et al., 2019). Its orbital eccentricity is sufficient to cause enough tidal heating to maintain a layer of liquid water beneath an ice shell (Ojakangas and Stevenson, 1989). Presence of the liquid shell is inferred from measurements of the induced magnetic moment of the moon which indicate a layer of electrically conductive material in the interior. The paucity of craters indicates that the surface is likely only 10 Myr old (Zahnle et al., 1998; Smith et al., 1979), and at least less than 200 million years old likely due to resurfacing (Pappalardo et al., 2009). The relatively low ice mass fraction of Europa ($\sim 6\%$) compared to Ganymede and Callisto is an interesting characteristic with the potential to inform formation scenarios (Canup and Ward, 2009; Ronnet et al., 2017).

Ganymede

Ganymede is the most massive Galilean satellite, the most massive satellite in the solar system, the only satellite with a substantial intrinsic magnetic field (Gurnett et al., 1996; Kivelson et al., 1996), and the primary target of the JUICE mission (Grasset et al., 2013). It is the outermost satellite of the Laplace resonance. Ganymede, like Callisto, contains a much higher mass fraction of ice than Europa, consisting of a silicate and iron core overlaid by an icy mantle (Schubert et al., 2004). It has the lowest observed axial moment of inertia of any solar system body, implying that its interior is fully differentiated. The surface appears to exhibit two types of terrain; 40% of the surface resembles an older more heavily cratered terrain similar to Callisto, while the remainder is a lighter grooved terrain relatively free of craters, evidencing some resurfacing process seems to have occurred post formation of the darker terrain (Smith et al., 1979). The stresses required to have tectonized Ganymede's surface to the observed degree could be explained by a past orbital resonance which drove tidal heating and flexing (Lucchitta, 1980; Showman et al., 1997, 2004), giving some clue as to possible pathways to evolve into the Laplace resonance.

Callisto

Callisto is the only Galilean satellite not taking part in the Laplace resonance. It is the outermost Galilean satellite with a semi-major axis of 26.33 R_J. Most strikingly Callisto appears to have undergone no significant resurfacing since its initial bombardment phase that saturated the surface with craters (Smith et al., 1979). Furthermore it stands out in that it is the only Galilean satellite which appears to be only partially or fully undifferentiated given the axial moment of inertia $C/MR^2 = 0.359 \pm 0.005$ measured by the Galileo spacecraft (McKinnon, 1997; Anderson et al., 1997; Anderson et al., 2001). However, heterogeneous mass distributions within a differentiated Callisto could also cause similar values (McKinnon, 1997; Kuskov and Kronrod, 2005). Crater relaxation indicates that at least the outer 10 km is mechanically dominated by ice (McKinnon, 1997). The potential state of partial-differentiation provides a powerful constraint on formation theories, requiring that Callisto did not accrete too quickly lest it be melted

and thoroughly differentiated (Canup and Ward, 2002; Moore et al., 2004).

1.2 Setting the stage: The Formation of Jupiter

Three main competing theories exist to explain the formation of giant gaseous planets. In the core accretion scenario, once Jupiter's core reached a mass of 5-20 $M_\oplus$ it began a process of runaway gas accretion (Pollack et al., 1996; Mordasini, 2013). This requires that it formed prior to the dispersal of the gas component of the protoplanetary disk (PPD) and thus within 1-10 Myr of the formation of the solar system (Haisch et al., 2001). In the first stage a planet core begins to form via planetesimal collision and accretion. Objects of size 100-1000 km collide until the core exhausts its feeding zone of further solid material, reaching its isolation mass. For core accretion to occur a critical mass of $\sim 2-10$ $M_\oplus$ must be reached (Ikoma et al., 2001) . As gas slowly accretes onto the core its feeding zone is correspondingly enlarged, allowing for the further accretion of solid material. Eventually the envelope becomes optically thick, and the accretion rate is limited by the envelope's thermal pressure. The envelope must radiate away the accretion energy before it can contract. Initially the planetary radius extends out to its Hill radius

$$R_{\rm H} = a(1-e)\left(\frac{M_{\rm p}}{3M_*}\right)^{1/3} \tag{2}$$

where a is the planet semi-major axis, e is the orbital eccentricity, $M_{\rm p}$ is the planet mass, and M_* is the stellar mass (Hill, 1877). The crossover mass is reached when the core and envelope mass become equal, at which point the envelope begins to contract under its own gravity. This begins the phase of runaway gas accretion. The limiting gas accretion rate is reached shortly after the onset of runaway accretion, set by the maximum rate at which the disk can supply new gas or can pass gas over a gap formed by the planet (Pollack et al., 1996). Eventually the planet radius contracts to be much smaller than the Hill sphere, and its radius is determined by the accretion shock of matter falling in from beyond the Hill radius. Different Jupiter formation scenarios result in different initial temperature and luminosity evolution tracks, although this is further complicated by the properties of the gas reservoir from which Jupiter pulls material, resulting in the so-called 'Hot-start' and 'Cold-start' scenarios (Spiegel and Burrows, 2012).

In the alternative "gravitational instability" induced direct collapse scenario, Jupiter-like planets form on a dynamical timescale from the prompt collapse of a fragment of protoplanetary disk material into a gravitationally bound object (Boss, 1997). The fragmentation of the disk can only occur if the disk is sufficiently cool and massive, where the self-gravity of the disk must dominate locally over the gravitational attraction of the star. A disk becomes unstable if the Toomre Q parameter

$$Q = \frac{c_{\rm s}\Omega}{\pi G\Sigma} < 1, \tag{3}$$

where c_s is the speed of sound in the disk, Ω is the epicyclic frequency, G is the gravitational constant and Σ is the surface density (Toomre, 1964). Non-axisymmetric perturbations such as spiral waves will begin to grow prior to the Q parameter decreasing below unity. Once a fragment forms it must collapse more quickly that the shearing timescale on which it would be disrupted by differential orbital motion (Gammie, 2001).

The required conditions of disk mass and disk temperature for a gravitational instability to occur conflict within the inner regions of a protoplanetary disk, where the disk surface density can be too large to cool quickly enough. As a result, direct collapse is unlikely to form planets inside of 40-100 au distance from the star. The results of radiative hydrodynamical models produce both fragmenting and non-fragmenting results from nearly initial conditions. To form Jupiter via direct gravitational collapse at its current orbital radius the gas surface density must be ~10 times greater than suggested by the Hayashi Minimum Mass Solar Nebula (Hayashi, 1981).

The third and most modern theory is that of pebble accretion. Pebble accretion is discussed in greater detail in Section 1.3.2. While similar to core accretion in that Jupiter would begin to rapidly accrete gas once a critical mass of its core was reached, in pebble accretion the core itself grows from the steady build up of small "pebbles" coupled to the gas on the orbital timescale (Lambrechts and Johansen, 2012) rather than planetesimals. One line of evidence that supports a pebble accretion origin for Jupiter's core is its chemical composition. Jupiter's atmosphere is enriched in various volatile gases relative to solar abundances by a factor 3-4 (Niemann et al., 1996). This enrichment can be the result of the accretion of ices, in particular a substantial reservoir of the highly volatile N_2 ice (Owen et al., 1999) which would normally be found at temperature below 30 K in the outer disk. Radial grain drift in a viscous disk may supply volatile-enriched solids to the inner disk (Booth et al., 2017), allowing Jupiter to accrete its envelope anywhere between 0.5-20 au (Mousis et al., 2019). Alternatively Jupiter may have formed further out by pebble accretion beyond 30 au (Bosman et al., 2019; Öberg and Wordsworth, 2019). However, Jupiter may still have formed closer in if a highly optically thick inner disk region would shadow the region beyond 3 au, reducing temperatures locally to below 30 K and allowing for the formation of N_2 ice (Ohno and Ueda, 2021). Given the timescale of the formation of mm to cm sized grains, pebble accretion circumvents several of the issues that face the core accretion model.

Giant Planet Luminosity Evolution

The composition, physical extent, and dynamical evolution of a circumplanetary disk may be closely tied to the luminosity of its primary, the planet. For wide-separation CPDs, the planet will be the dominant source of radiative heating. The hitherto directly imaged exoplanets are generally young and thus overly luminous compared to an evolved planet closer to equilibrium temperature with its stellar radiation field (Marois et al., 2008; Lagrange et al., 2010). The giant planets must radiate away their heat of formation during Kevin-Helmholtz contraction, potentially acting as source of heating for any CPD (Fortney and Nettelmann, 2010; Mordasini, 2013). Differing "Hot Start"

and "Cold Start" scenarios predict an initial temperature for a Jupiter mass planet at 1 Myr age to be between 500-1000 K (Spiegel and Burrows, 2012). Constraining the precise luminosity of the young Jupiter is challenging, with theoretical models predicting a spread of more than two orders of magnitude, and are sensitive to the accretion shock through which planetary mass is processed (Marley et al., 2007; Mordasini, 2013). The young Jupiter's luminosity varies over 5 orders of magnitude within the first 3 Myr after the start of the growth of a solid core in the core accretion scenario (Hubickyj et al., 2005). In the initial stages of runaway solids accretion, a peak of 10^{-5} $L_\odot$ is reached after less than 0.5 Myr. A second rapid increase in luminosity occurs some 2-3 Myr later, up to 10^{-2}-10^{-1} $L_\odot$ driven by runaway gas accretion. The peak luminosity is reached when accreting gas falling into the planet from near the Hill radius arrives at the shock interface and radiates away the majority of its gravitational potential energy. Afterwards the gas accretion becomes rate-limited and the young Jupiter begins to contract inside the effective accretion radius. Finally the luminosity drops until the isolation stage is reached after $\sim$ 2.5 Myr at 10^{-5} $L_\odot$. The planet continues to contract and cool until the present day, with a luminosity of 10^{-6} $L_\odot$ being reached after 10 Myr (Hubickyj et al., 2005).

1.2.1 Planet-disk interactions

Gap Opening

Annular gaps in protoplanetary disks have been suspected to exist for decades (Marsh and Mahoney, 1992; Calvet et al., 2005) and have long been suspected to be caused by the presence of forming planets (Kley and Nelson, 2012; Garufi et al., 2013; van der Marel et al., 2016; Zhang et al., 2018; Andrews, 2020). The diversity and ubiquity of radial structure in protoplanetary disks has been dramatically revealed by high angular resolution sub-mm observations of dust continuum emission, with results suggesting planet-disk interactions as the origin of the structure (Andrews et al., 2018; Huang et al., 2018). Several gap opening criteria have been formulated. Lin and Papaloizou (1993) proposed the pressure stability criterion

$$H \leq a \sqrt[3]{\frac{M_\mathrm{p}}{3M_*}} = R_\mathrm{H}, \tag{4}$$

where the pressure scale height of the disk H at the radius coincident with the planet's semi-major axis a is less than or equal to the planet's Hill radius, for a planet of mass M_p and a star of mass $M_\star$. The disk viscosity must also be sufficiently low such that viscous spreading does not overcome the rate at which the planet can sweep material from its gap (Crida et al., 2006) and that the planet migratory timescale is much shorter than its gap clearing timescale (Hourigan and Ward, 1984). Combining these requirements into one constraint, Crida et al. (2006) formulated the P criterion

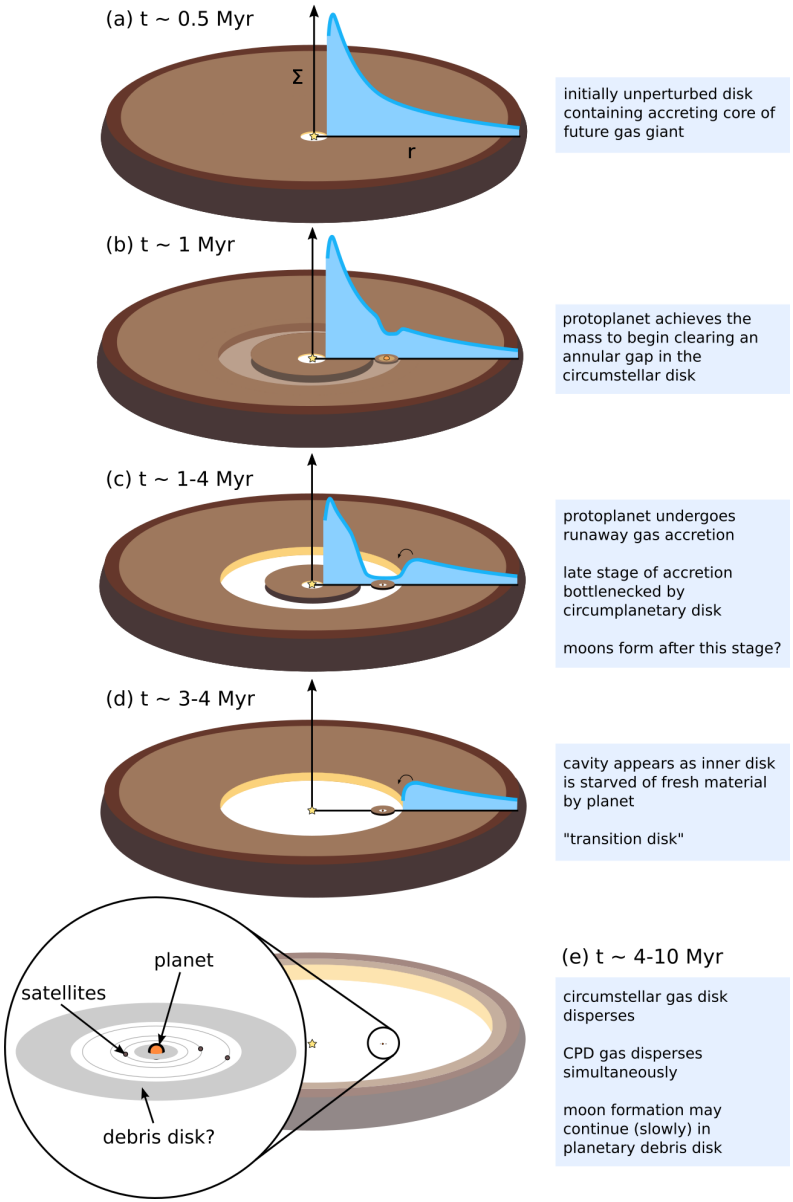

Figure 1.3: Moon formation in the context of planet-disk interaction and the evolution of the circumstellar disk surface density profile. The timing of events corresponds to the formation of Jupiter scenario described by Kruijer et al. (2017). Processes such as planetary migration and multiple planet formation are not depicted.

$$P = \frac{3}{4}\frac{H}{R_{\rm H}} + \frac{50}{q\mathrm{Re}}, \tag{5}$$

where q is the planet-star mass ratio mass, and Re is the Reynolds number, such that a value of $P \gtrsim 1$ will lead to gap opening.

In this paradigm once Jupiter reached a mass on the order of its present mass, gravitational interaction with the circumstellar disk resulted in the opening of an annular gap (Lin and Papaloizou, 1986, 1993; Morbidelli and Nesvorny, 2012), in which the surface density was reduced relative to the surrounding circumstellar disk by a factor $\sim 10^2 - 10^4$ (Kley, 1999; Szulágyi, 2017). Jupiter's core may have formed as early as 1 Myr (Kruijer et al., 2017). An early gap opening would likely have exposed a CPD to stellar and interstellar radiation fields dependant on the optical depth of the gap region (Turner et al., 2010). However, paleomagnetic measurements of asteroids suggest Jupiter's formation may have divided the solar system solid reservoir into distinct populations at $\sim 3 - 4$ Myr (Weiss and Bottke, 2021). After gap opening, accretion of material from the circumstellar disk material onto Jupiter through the gap continues (Kley, 1999). Gas has been shown in hydrodynamical simulations to flow into the planet's Hill sphere via the L1 and L2 points, colliding to form a shocked region from which material then falls inwards towards the planet and CPD (Lubow et al., 1999; D'Angelo et al., 2002).

Migration of the giant planet

51 Pegasi b is the first planet found orbiting a main sequence star other than the sun, and is the archetype of the Hot Jupiter class of exoplanets (Mayor and Queloz, 1995). Hot Jupiters are worlds of Jovian mass with very short orbital periods (P $\lesssim$ 10 days). The discovery of such an object was puzzling, as the mass required to construct a Jovian planet should not be found in the vicinity of the star. This posed a problem to any in-situ planet formation scenario. Planet migration within a circumstellar disk had been theoretically predicted (Goldreich and Tremaine, 1980) but the discovery of 51 Pegasi b refocused planet formation theories to emphasize the role of planetary migration during formation. The planet could instead have formed at a larger physical separation, possibly at or beyond the iceline where a sufficient reservoir of solid material exists to build up a core, and later migrate inwards towards its final position. Theories including migration were later able to explain several key dynamical and compositional features of the solar system. The Nice model (Gomes et al., 2005) and the Grand Tack (Walsh et al., 2011) are models which invoke dynamical re-arrangement of the solar system giant planets to explain their current orbital distribution, the mass of Mars, the composition of the asteroid belt, and other dynamical peculiarities of the solar system. Jupiter's excursion towards the Sun during the possible Grand Tack scenario requires that the Galilean moons formed prior to a theoretical Grand-Tack movement of Jupiter beyond 4.5±0.5 au (Heller et al., 2015).

Migration occurs because of gravitational interaction between the planet and protoplanetary disk (Kley and Nelson, 2012). The planet forms density waves in the disk ma-

terial, both trailing and leading the planet in its orbit. The leading density concentration pulls the planet forward, accelerating it along its orbit and thus increasing its semi-major axis. A trailing density enhancement causes the reverse effect, but the torques imposed on the planet by the density waves do not necessarily sum to zero. If the torques do not cancel each other out, the planet angular momentum must change. Angular momentum is conserved by the opposing migration of disk material, outwards in the case of an inwardly migrating planet.

If the gap opening criterion of Crida et al. (2006) is not satisfied such that $P > 1$, the resulting migration is known as Type I, which could cause low mass planets to spiral inwards. In Type II migration, $P < 1$, a gap has been opened and the net balance of torques causes migration depending on the planet's position relative to the gap edge and the disk viscosity - independently of the planet mass. Migration can have both positive and deleterious effects on the efficiency of planet formation. The formation timescale of planets can be reduced by migration, as a core which may already have reached its isolation mass can be moved into a new feeding zone by viscous disk evolution. However if the migration timescale is shorter than the planet formation timescale, the planet can spiral inwards and fall into the star. The same phenomena poses significant challenges to moon formation theories as the orbital decay timescales inside a CPD are expected to be very short (Canup and Ward, 2002).

1.3 Moon Formation in a Circumplanetary Disk

At some point during the interplay of Jupiter's runaway accretion, gap opening, migration, and contraction, a circumplanetary disk formed. Although whether a rotationally supported disk or extended envelope forms is still a matter of debate (Szulágyi et al., 2016). CPD formation pathways can roughly be divided into four categories:

1. Accretion disk: a CPD which forms by the accretion of material from the surrounding circumstellar disk during or after the Jupiter's runaway gas accretion phase (Canup and Ward, 2002).

2. Spin-out disk: a CPD which forms when Jupiter's contraction and angular momentum conservation causes material around its equator to be centrifugally ejected (Korycansky et al., 1991).

3. Impact generated: Material which is thrown out of Jupiter in a massive collision re-forms into a CPD (Boynton, 1983).

4. Co-accretion: In which a gaseous disk and/or circumJovian envelope is penetrated by planetesimals which are ablated, causing their material to join with the disk matter via gas drag and contribute solid material for satellite formation (Mosqueira and Estrada, 2003a).

Modern theories of moon formation tend to have adopted the accretion disk scenario, although variants of the co-accretion scenario have also proven useful (Ronnet

and Johansen, 2019). But independent of how the CPD comes to be, its relation with the surrounding circumstellar disk may be more relevant for its continued evolution and properties. CPDs either remain essentially isolated and static, evolving independently from the circumstellar disk material (Lunine and Stevenson, 1982), or continue to accrete or be enriched by material from their surroundings (Canup and Ward, 2002; Mosqueira and Estrada, 2003a).

1.3.1 History

The history of giant planet moon formation research can be roughly divided into four phases. These phases correspond largely to increases in technical capability. Observations were at first limited to ground-based facilities, but were followed by fly-by spacecraft, and eventually dedicated orbiters like *Galileo* and *Cassini*. A concurrent revolution in planet formation theory, sparked by the discovery of exoplanets and the advent of sub-mm interferometry, spilled over into moon formation theory.

Early speculation and ground-based measurements (1796-1974)

The earliest work, when ground-based observations were the only available data, was in general speculative and qualitative. Pierre-Simon Laplace proposed a theoretical near-simultaneous and common formation mechanism to explain the prograde motion and low mutual inclinations of the planets and regular satellites, a concept which is still considered the most likely scenario to the present day (Aitken, 1906; Kuiper, 1951). Based on the predicted temperatures within the proto-solar nebula it was suggested that small bodies of the outer solar system would be mixtures of rock and ice (Jeffreys, 1923; Lewis, 1972). This conclusion was supported by spectroscopic detection of water ice features on Europe, Ganymede, and Callisto (Kuiper, 1957; Moroz, 1966; Pilcher et al., 1972). Analysis of moon-moon mutual perturbations likewise determined that the three outer Galilean moons had densities incompatible with an Earth-like iron-silicate composition (de Sitter, 1931; Fink et al., 1973).

One of the earliest theoretical frameworks specifically addressing giant planet moon formation was made by Ruskol (1961) in which it was suggested that giant planet regular satellites formed by inelastic collision of satellite swarms in the vicinity of the planets. In this model the resulting collisional debris would form a disk from which moons would form by gravitational instability. Studies of the contraction history of Jupiter were carried out (Grossman et al., 1972), suggesting that Jupiter's initial luminosity was far in excess of that observed in the present epoch. Once the moon's bulk densities were more confidently determined (Kovalevsky, 1970; Morrison, 1973) the first theory dedicated to Galilean moon formation was formulated (Pollack and Reynolds, 1974). The authors attempted to explain the compositional density gradient observed in the four moons as a result of Jupiter's initial luminosity, setting constraints on the formation timescale of the moons, but did not describe in detail the cloud of material from which the moons must have coalesced.

Fly-by observations (1974-1995)

Confluent developments in planet formation theory and in-situ observation generated further interest and research in moon formation during the second phase (1974-1995). More mature theoretical models of planet formation in disks had taken shape, explaining lingering problems regarding angular momentum transfer by allowing disks to viscously spread (Hoyle, 1960; Safronov, 1972; Lynden-Bell and Pringle, 1974) with obvious implications for regular satellite formation. Additionally, the *Pioneer* 10 & 11 spacecraft were launched to study the properties of the interplanetary medium in 1972 and 1973 respectively, performing the first in-situ observations of Jupiter and its moons (Miles, 1973). Five years later the *Voyager* spacecraft dramatically revealed the diversity of the Galilean system (Smith et al., 1979). Attempts to unify the formation of all regular satellites into a single framework continued; in Harris and Kaula (1975) the planet's tidal dissipation factor was suggested to be the origin of the primary-secondary mass ratios of the terrestrial and Jovian satellite systems ($\sim 10^{-2}$ and $\sim 2\times10^{-4}$ respectively), wherein tidal friction prompts the inwards migration of satellites. Attempts to explain the evolution into the Laplace resonance were also made: in Wen-sai (1978) it was suggested that the Galilean moons initially formed from a circumplanetary disk embedded within a gaseous envelope from which Jupiter was continuously accreting. The increasing mass of Jupiter led to a steadily increasing gravitational attraction, causing the regular satellites to migrate inwards to their present position. Alternative models that invoked catastrophic restructuring of the satellite system were also proposed; Boynton (1982) posited that a single initial massive moon coeval with Jupiter was tidally disrupted, forming an accretion disk from which the current generation of moons formed as a secondary population. It was at this point that the first modern theory of Galilean moon formation came about: the Minimum Mass subNebula (MMsN) (Lunine and Stevenson, 1982).

Prior to the introduction of the minimum-mass subNebula (MMsN) model it was generally agreed upon that the Galilean satellites formed from a disk around Jupiter during or shortly after the formation of the planet itself. The MMsN also assumes that the Galilean moons formed from such a dense gaseous disk surrounding Jupiter. The model was constructed to explain the observed radial density gradient of the moons as well as the contrast in internal differentiation states between Ganymede and Callisto. Initially, in-fall of gas via Jupiter's Lagrange points allows for the accumulation of massive static disk driven by a weak turbulent regime. Within the gaseous disk the satellites were suggested to form quickly ($10^2 - 10^4$ yr) and become surrounded by optically thick primordial atmospheres saturated with water. The total mass of silicate solid material in the satellites (2.6×10^{26} g) and the ratio between rocky material and hydrogen/helium (6×10^{-3}) sets the 'minimum' mass from which the observed solid mass of the moons could form.

If the CPD mass were spread uniformly over a disk extending just beyond the orbit of Callisto to 30 R_J, the average surface density becomes 3×10^5 g cm^{-2}, far in excess of that found within comparable models of the solar nebula 10^3 g cm^{-2} (Hayashi, 1981), resulting in a CPD which is highly optically thick. Considering only the Rosseland

mean gas opacity, the vertical optical depth to the midplane is thus ~30 and radially $\tau \sim 600$. The resulting temperature profile of the disk midplane is taken for simplicity as adiabatic, for an ideal gas resulting in a drop-off linearly with radius as

$$T = 3600(R_J/R)\,\mathrm{K}, \tag{6}$$

such that ice would be able to condense at the present-day orbit of Ganymede. It is assumed that the MMsN is static over the formation time of the Galilean satellites and that the orbits of the satellites do not significantly change over their formation timescale. During the initial accretion phase, viscously driven turbulence prevents moon formation until cessation of gas infall onto disk. No mass inflow or viscous radial transport occurs thereafter, justified by the proposed satellite accretion time being much shorter than cooling time of disk. However, keeping temperatures low enough to allow the formation of ice-rich Ganymede requires a nearly inviscid disk.

Exoplanets and Dedicated Spacecraft (1995-2012)

The third phase followed the arrival of the *Galileo* spacecraft at Jupiter. This dedicated spacecraft mission led to great advances in the understanding of the interior structure of the Galilean satellites (Kivelson et al., 1996; Carr et al., 1998; Kivelson et al., 2000; Sohl et al., 2002) which appeared to be in tension with the MMsN model. The near simultaneous discovery of exoplanets, and in particular close-in Hot Jupiters, launched a renaissance in planet formation theory which would spill over into moon formation (Mayor and Queloz, 1995). In particular, the role of orbital migration was brought to the forefront as part of the effort to explain the emerging population of Hot Jupiters. Developments in 2D (Kley, 1999; Lubow et al., 1999; Bryden et al., 1999; Lubow and D'Angelo, 2006) and 3D (Kley et al., 2001; Lubow et al., 2003) modeling showed that if a massive planet opens a gap in its circumstellar disk, accretion should continue across the gap. This, in combination with several fundamental problems with a massive and static disk, led to the development of actively-fed accretion disk CPD models (Makalkin et al., 1999; Canup and Ward, 2002). Rather than containing all the solids required to form the Galilean moon system, this disk continually accretes fresh circumstellar material and allows for the build-up of solids in an otherwise cool disk. Such a model is referred to as a 'gas starved disk' (GSD) for its low instantaneous gas mass. In Canup and Ward (2002) the authors argue that the massive, static MMsN has several difficulties which cannot be reconciled by modification:

1. Callisto's partially differentiated state implies an accretion time $> 10^5$ years, while the MMsN satellites accrete in $\leq 10^3$ years, liberating sufficient energy to fully melt and differentiate Callisto.

2. The MMsN CPD must be almost inviscid, with a viscosity $\alpha \leq 10^{-6}$ for temperatures to be low enough for ices to be able to condense in the region beyond the current orbit of Ganymede.

3. Satellites in the MMsN decay very fast via Type I migration (10^2 years) and gas drag (10^3 years).

4. A Galilean-sized satellite imposes viscosity on the disk by density wave interactions implying $\alpha = 10^{-4} - 10^{-3}$.

5. Jupiter's obliquity is taken as evidence against the long term existence of a massive disk. If the CPD were present after dissipation of the solar nebula, resonance involving spin precession rate would force obliquity above 3°.

In the MMsN model the Kelvin-Helmholtz cooling time is a few x10^4 longer than the Safronov accretion time of the satellites (10-10^3 years) making it difficult for icy or rocky satellites to form. Due to the two orders of magnitude reduction in surface density of the GSD model, the cooling times are less than 10^3 yr. Within the MMsN the gas drag timescale for the infalling of small bodies is too short to allow for satellite formation. Type I and II migration timescale are also too short to allow for massive satellite formation in the MMsN unless viscosity is very low $\alpha < 10^6$.

Canup and Ward (2002) instead propose that the satellites form during the final stages of planetary gas accretion. A mass similar to the MMsN disk mass is still processed through the CPD integrated across the disk lifetime, but at a slow rate of inflow 2×10^{-7} M_J per year. In this case streams of material flow in via the L1 and L2 points, colliding to form two shocked regions at 100-200 R_J. Gas spirals inward after losing specific angular momentum and forms a prograde CPD. Mass accretion is modeled to flow onto the disk inside of a critical radius $r_c = 30$ R_J and viscously spread in- and outwards. Beyond the disk outer edge at 150 R_J disk material is lost to the surroundings. The CPD is than at any given moment orders of magnitude less massive than the MMsN. The low mass-inflow rate allows for sufficiently low disk temperatures to form icy moons, as well as relatively slow satellites accretion times ($\geq 10^5$ years) to prevent total differentiation of Callisto.

Disk temperature is estimated from the balance between accretion heating, viscous dissipation, Jupiter's luminosity heating, and disk surface radiative cooling. The dominant energy source is assumed to be viscous dissipation. Within the centrifugal radius (the radius where the specific angular momentum is equal to the average of the infalling material) the disk temperature $T_d \propto r^{-3/4}$. Orbital migration and decay of (proto-)satellites orbits still occurs within this disk. It is assumed that the existence of satellites indicates that at least one generation of moons could survive orbital decay and aerodynamic gas drag in the disk. Conditions in the disk must allow for an accretion timescale for Callisto longer than 10^5 years to prevent surface temperatures from exceeding 270 K.

The accreting gas is assumed to contain meter-sized rock and ice particles coupled to the gas in the Stokes flow regime. Solids grow into bodies large enough to become decoupled from the gas flow, possibly via Goldreich-Ward instability. Bodies decay by Type I migration and several Galilean mass satellites may be lost into Jupiter during this time, enriching the planet with metals. The reservoir of material is exhausted or

swept away and satellite growth stops. Satellites still in the dissipating CPD are the final generation to be formed. It is expected that Jupiter's luminosity is $\leq 10^{-4} L_{\odot}$ at this stage such that Ganymede and Callisto's surfaces reach the freezing point of water.

N-body simulations based on the GSD paradigm have suggested that the balance of mass-inflow onto the disk and accretion onto the planet creates a steady state instantaneous CPD mass which limits the total possible satellite system mass to $\sim 10^{-4}$ of the primary mass (Canup and Ward, 2006). In the solar system, the ratio of the mass of Jupiter, Saturn, and Uranus to their respective regular satellite systems are found to lie within a narrow range of $1.1 \times 10^{-4} - 2.5 \times 10^{-4}$. A fascinating implication is that the mass of the moons of the maximum-mass planetary (near the Deuterium-burning limit at 13 $M_{\rm J}$) would be approximately Martian (Heller and Pudritz, 2015).

Resolved planet-forming disk substructure and pebble accretion (2012-present)

Observations of planet forming disks with ALMA (Zhu et al., 2012; Dong et al., 2015a; Zhang et al., 2015; ALMA Partnership et al., 2015; Andrews et al., 2018), the advent of pebble accretion theory (Wahlberg Jansson and Johansen, 2014; Johansen and Lambrechts, 2017; Ormel et al., 2017b), and powerful 3D hydrodynamical simulations (Morbidelli et al., 2014; Szulágyi et al., 2016, 2022) characterize the most recent stage of theoretical work in gas giant moon formation. In this phase research on satellite formation research has substantially accelerated, in part due to the potential imminent detection of extrasolar moons, the detection of several candidate circumplanetary disks, and interest in the prevalence and habitability of exomoons (Hill et al., 2018; Teachey et al., 2018; Teachey and Kipping, 2018; Bae et al., 2022; Kipping et al., 2022). Advances and open questions characteristic of this phase are discussed in the following section.

1.3.2 Recent Developments and Open Questions

While a low-mass actively-fed disk CPD model allows for the formation and survival of icy satellites, several important questions remain. Perhaps most significantly, the origin, growth, and retention of solid matter in the CPD is still a matter of ongoing debate. Previously it was believed that the CPD could accrete sub-meter sized solids from the circumstellar disk which would grow to become large bodies (Canup and Ward, 2002, 2006; Sasaki et al., 2010). However it is now known that some form of instability is required to trigger this large body formation (Johansen et al., 2014). Key to this debate is the theory of pebble accretion. Developments in planetary accretion theory indicate that an efficient mechanism to grow planets is via the settling of small particles onto large bodies in a gas-rich environment as an alternative to planetesimal-driven growth (Johansen and Lambrechts, 2017; Ormel et al., 2017b). In pebble accretion, the effective collisional cross section of an accreting body is much larger than in a ballistic, gas-free regime. The particles are of gravitationally negligible mass while being small enough that their aerodynamic properties are highly relevant to their behaviour. For particles to play a role in pebble accretion they must be tightly coupled to the gas. The level of gas

coupling is quantified with the stopping time

$$t_{\text{stop}} = \frac{mv}{F_{\text{D}}} \tag{7}$$

where m is the particle mass, v is its velocity relative to the gas, and F_{D} is the force of gas drag (Whipple, 1972). The stopping time is thus a function of the size and density of the particle and the density of the gas. If the stopping time is small relatively to the inverse of the Keplerian orbital frequency Ω_{K} the particle is well coupled to the gas. This can be expressed as $\tau_{\text{s}} = \Omega_{\text{K}} t_{\text{stop}} < 1$. When $\sim 10^{-3} < \tau_{\text{s}} < 1$, we are in the "pebble" regime (Ormel et al., 2017b).

Origin of solids in the CPD

In a gas-starved disk paradigm, the CPD must continually accrete new solids in the form of dust and ice from the surrounding circumstellar disk. Recent findings regarding the interaction of dust grains with gas disk radial pressure inhomogeneities have challenged this scenario. Pebbles approaching the gas giant feeding zone are very sensitive to aerodynamic gas drag and pressure perturbations in the protoplanetary disk. A pressure bump at the gap outer edge can effectively trap and filter grains by size (Paardekooper, 2007; Morbidelli and Nesvorny, 2012; Pinilla et al., 2012; Lambrechts and Johansen, 2014). Hydrodynamic simulations show that gas flowing into the gap towards the circumplanetary region originates from above the circumstellar disk midplane at approximately one disk pressure scale height (Machida et al., 2008; Szulágyi et al., 2014). The oscillatory vertical motion of larger grains is damped by gas drag, causing them to settle towards the disk midplane. Larger pebbles efficiently settled into the midplane would thus be unable to join the accretion flow onto the CPD, depriving the CPD of a large fraction of the available solid material. Only particles below 10 μm in size could accrete onto the CPD once the Jovian gap is open (Paardekooper, 2007). This filtering by grain size makes it challenging for a gas-starved disk to accumulate the solid mass required to form the Galilean satellites.

An alternative possibility to deliver solids to the CPD is in the form of planetesimals that have already formed in the circumstellar disk (Estrada et al., 2009; Mosqueira et al., 2010; Fujita et al., 2013; D'Angelo and Podolak, 2015; Homma et al., 2020). These planetesimals could then pass through the CPD gas disk and experience a drag force, eventually being captured. Passage through the CPD would be energetic, and lead to the ablation of solid material which would seed the CPD (Ronnet and Johansen, 2020). The solid material in the inner region of the CPD may be dominated by captured planetesimals if their random velocity is small and a deep gap is not opened by the planet, in which case planetesimals can contribute significantly to the growth of the regular satellites (Suetsugu and Ohtsuki, 2017). Ronnet et al. (2018) theorizes that Saturn's core may have grown in the reservoir of pebbles at the pressure bump exterior to Jupiter's orbit. The formation of this core would scatter the trapped solids towards and into the Jovian CPD. Gas drag would then act to damp the planetesimal orbits until they circularized and became incorporated into growing satellites. The capture and

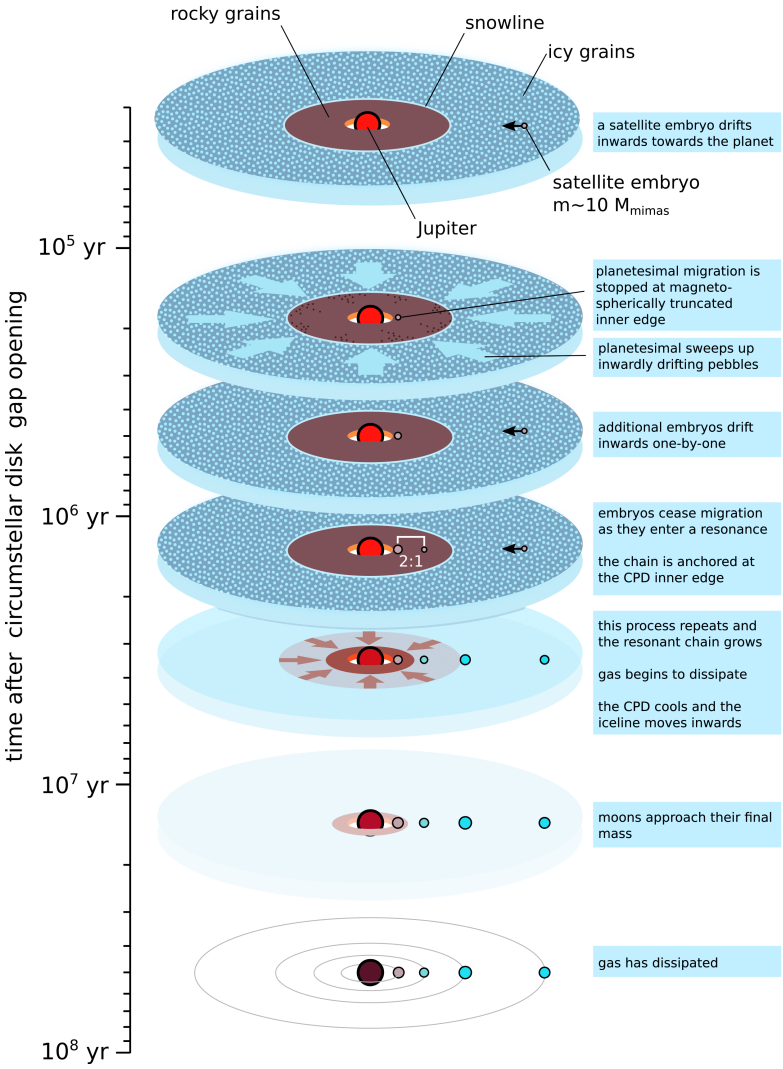

Figure 1.4: Illustration of the slow pebble accretion scenario described in (Shibaike et al., 2019). The innermost moon is prevented from falling into the planet by an inner edge of the gas disk. Additional moon embryos pile up in a resonant chain. Later, the iceline moves inwards as the disk loses gas and becomes colder. A late veneer of ice is deposited on Europa. The CPD gas disk dissipates entirely by 30 Myr.

ablation of planetesimals could then set the stage for a pebble accretion scenario that may produce a formation scenario similar in many ways to that of compact multiplanet (and resonant) systems such as TRAPPIST-1 (Ormel et al., 2017b; Izidoro et al., 2017; Lambrechts et al., 2019; Schoonenberg et al., 2019; Izidoro et al., 2021)

Alternatively, the presence of a massive planet in the gap may lead naturally to the vigorous vertical stirring of dust at the circumstellar disk midplane exterior to the planet orbit (Binkert et al., 2021) effectively negating the settling process. 3D dust+gas radiative hydrodynamic simulations of this so-called meridional circulation show that even mm-sized grains are prevented from settling by the planet (Szulágyi et al., 2022). In this case the dust-to-gas ratio of material at high altitudes in the circumstellar disk could be significantly enhanced, even exceeding the canonical value in the circumplanetary region and leading to vigorous delivery of solids to the CPD.

Dust depletion and traps within the CPD

An additional problem concerning the growth of solid material in CPDs is the rapid loss of dust to orbital decay. The formation of planetesimals within the CPD necessitates a local increase in the dust-to-gas ratio to near unity and sufficiently large grains to allow for e.g. the streaming instability to form km+ size objects (Youdin and Goodman, 2005; Johansen et al., 2007; Bai and Stone, 2010). In a steady-state accretion disk the radial momentum conservation equation for steady-state flow is

$$v_{\rm r}\frac{\partial v_{\rm r}}{\partial r} - \frac{v_\phi^2}{r} + \frac{1}{\rho_{\rm gas}}\frac{\partial P}{\partial r} + \frac{GM}{r^2} = 0 \tag{8}$$

where r is the radius, $v_{\rm r}$ is the gas radial velocity, v_ϕ is the gas circular velocity, M is the mass of the central object, P is the gas pressure and $\rho_{\rm gas}$ is the gas density (Armitage, 2010). As pressure is expected to decrease with increasing radius the pressure term is negative, and the velocity of the gas is sub-Keplerian. Dust grains on Keplerian orbits thus feel a headwind from the surrounding sub-Keplerian gas. This drag force causes the grains to lose angular momentum and spiral inwards towards the planet. The timescale of the radial dust drift in small disks is theorized to be short owing to very steep radial pressure gradients (Pinilla et al., 2013; Shibaike et al., 2017; Zhu et al., 2018; Rab et al., 2019). A CPD could lose mm-size grains within only 10^2-10^3 yr to radial drift. If the CPD would accrete gas with the canonical dust-to-gas ratio of 10^{-2} this could rapidly be reduced to $< 10^{-3}$ (Zhu et al., 2018; Rab et al., 2019). The fast radial drift of dust grains poses a serious problem to the in-situ formation of planetesimals and moons in the CPD (Shibaike et al., 2017).

There are several proposed solutions to this problem. One possibility is that dust is somehow trapped within the CPD until a sufficient accumulation allows for gravitational instability and subsequent planetesimal formation. Dust could be prevented from drifting into the planet if a gas-free cavity exists between the planet and the CPD inner edge. A gas-free cavity could form as the result of planetary magnetospheric interaction with ionized CPD gas. If Jupiter's magnetic field strength at the time of moon formation

was ∼ 40 Gauss, a cavity could be opened as soon as Jupiter itself opens a gap in the circumstellar disk (Shibaike et al., 2019). Solids would then pile up at this cavity edge until the local dust-to-gas ratio would reach a critical value at which instabilities and large body formation could occur. The presence of a cavity is also able to halt the gas-driven migration of entire moons into the planet (Sasaki et al., 2010; Ogihara and Ida, 2012). However it is not generally agreed upon that a cavity would in fact be opened (Owen and Menou, 2016; Cilibrasi et al., 2018).

Alternatively, outwards radial gas flow structure of the disk could lead to a hydrodynamic trap for intermediately sized grains in the outer part of the disk (Shibaike et al., 2017; Drążkowska and Szulágyi, 2018; Batygin and Morbidelli, 2020). Outwards flow of gas in a CPD is seen in several hydrodynamical models (Machida et al., 2010; Tanigawa et al., 2012; Szulágyi et al., 2014; Fung and Chiang, 2016; Szulágyi et al., 2017). In the results of Szulágyi (2017), large portions of the CPD midplane flow outwards with significant (∼ 100 m/s) velocity due to viscous stress and pressure from the hot planet. For a grain of a given size the inwards drift force is balanced at some radius by the outwards advection force of decreting gas. The dust mass of the CPD would then grow until successive episodes of instability and growth produce planetesimals which could then be incorporated into proto-moons (Batygin and Morbidelli, 2020). The loss of the remaining gas component of the CPD at the end of the circumstellar disk lifetime could trigger an additional round of planetesimal formation (Throop and Bally, 2005; Batygin and Morbidelli, 2020). The remaining gas-free debris disk would collisionally grow larger bodies but on a much longer timescale than in the presence of a gas disk, a scenario supported by the necessarily slow accretion of Callisto (Batygin and Morbidelli, 2020).

Migration of proto-moons and resonance

A very characteristic feature of the Galilean moon system is the Laplace mean-motion resonance of the inner three moons. How the satellites entered this configuration is still uncertain, although generally it is thought to be the result of orbital migration (Peale and Lee, 2002; Ogihara and Ida, 2012; Moraes et al., 2018). While Yoder and Peale (1981) argued that the system evolved into resonance via the outwards migration of Io, Peale and Lee (2002) argued instead for an inwards Type I migration of Ganymede which results in the capture of Io and Europa into the Laplace resonance. Inward migration is a natural result of satellites forming in a dense and viscously evolving CPD, and proto-satellite masses are insufficient to open gaps for reasonably viscous disks to drive Type II migration. Continuous mass inflow post gap-opening may even have resulted in the loss of tens of pre-Galilean satellites after they spiralled rapidly into Jupiter via Type I migration (Canup and Ward, 2002). The presence of a truncated inner gap (or hole) between Jupiter and the CPD may have been sufficient to prevent Io's migration into the Jovian Roche sphere. To investigate the orbital evolution of the satellites Moraes et al. (2018) investigated a hydrodynamical and N-body simulation within the framework of the classical static MMsN model. The authors found that the final orbital configuration

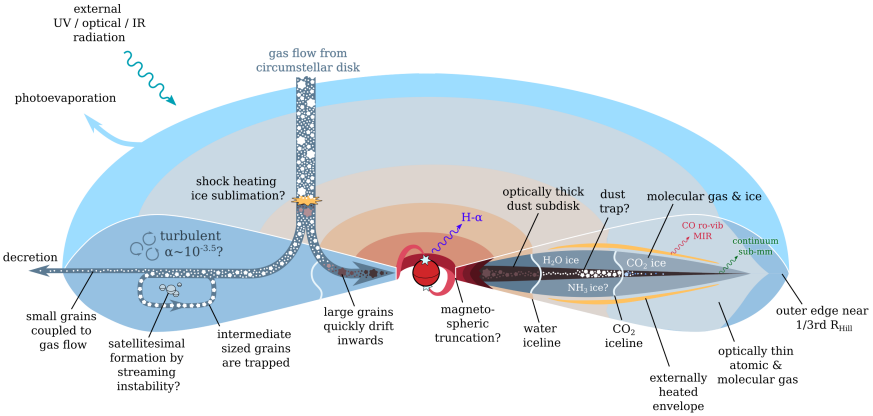

Figure 1.5: Illustration of various properties of the CPD and processes occurring within. The gas flow through the CPD and how it interacts with grains of differing sizes is shown on the left hand side. As gas in the CPD orbits with sub-Keplerian velocity, dust grains feel a drag force. The orbit of large grains decays quickly. Intermediate sized grains may become trapped where the drag force is equal to the force of advection by gas. Planetesimal (satellitesimal) formation may occur at these traps. Small grains remain well coupled to the gas and are lost together with it where it escapes the disk. The thermal, chemical, and physical structure of the CPD is represented on the right. External UV radiation heats a thin layer of gas from which molecular line emission may originate.

can consist of multiple satellites close to the planet locked into a resonant chain after the dissipation of the gas. Hence the Galilean satellites and close-in super Earths may form through a similar process. Similarly the seven-planet resonant chain of the TRAPPIST-1 system may have formed by inwards migration and pile-up (Ormel et al., 2017a; Unterborn et al., 2018), possibly explaining the inferred ice-rich compositions in regions where they could not have formed in-situ.

The compositional gradient and snowline

The most striking feature of the Galilean moon system is perhaps its compositional gradient, illustrated in Fig. 1.6. The two inner moons are smaller, either free of ice or with minor ice component, while the outer two are large and contain upwards of 50% ice by mass (Anderson et al., 1998; Sohl et al., 2002; Schubert et al., 2004). The origin of this gradient has been in dispute for several decades. Three possibilities are

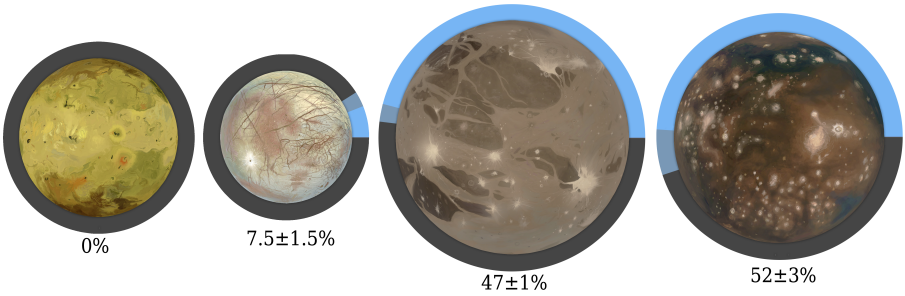

Figure 1.6: Illustration of the compositional gradient of ice mass fraction in the four Galilean satellites Io, Europa, Ganymede, and Callisto. The ice mass fraction is represented by the blue bar wrapped around each moon, with partially shaded regions indicating the range of uncertainty. The values and uncertainty range correspond to the estimated ice mass fractions of Kuskov and Kronrod (2005).

generally entertained: it is due to the ambient conditions during formation (Lunine and Stevenson, 1982; Pollack and Fanale, 1982; Canup and Ward, 2002; Mosqueira and Estrada, 2003a), due to the process of accretion (Nimmo and Korycansky, 2012), or due to a post-formation mechanism such as tidal heating (Dwyer et al., 2013). If the compositional gradient is primordial it may place the most powerful constraint on the history of the formation of the moons. Perhaps the simplest explanation is that the gradient is the result of the presence of an iceline in the CPD. In this scenario Ganymede and Callisto were able to accrete significant amounts of icy solids outside of the iceline. However, it is possible that Io and Europa initially accreted ice-rich mantles similar to those of Ganymede and Callisto which were later lost. While impact-driven escape and tidal heating do not seem like plausible avenues to dehydrate the inner moons (Bierson and Steinbrügge, 2021), hydrodynamic escape (vapor loss driven by accretional heating) does (Kuramoto and Matsui, 1994; Bierson and Nimmo, 2020).

Europa's intermediate degree of iciness provides additional constraints on the formation process. In general an iceline is predicted to be relatively discrete, and in this context the formation of an intermediately icy satellite is difficult. Inwards and rapid drift of icy grains has been considered a plausible origin (Ronnet et al., 2017). Sufficiently large icy bodies, i.e. meter-size, are able to retain their volatile content while drifting inwards due to aerodynamic drag, taking them inside of the iceline. At that location they accrete onto Europa and once embedded within the surface may be able to retain these ices for geological timescales. Alternatively, if the CPD energy balance continually evolves, the disk may cool significantly during the moon formation process. A cooling disk will cause the iceline to drift inwards. An inwardly drifting iceline could result in the final stages of moon accretion being relatively more abundant in ice. Hence if the tail end of Europa's accretion occurred only after an iceline swept inwards past its location, it could have accreted a thin veneer of ice (Shibaike et al., 2019). The pre-

cise determination of where the snowline may have been found is complicated by the possible orbital migration of the satellites post formation.

Heller et al. (2015) construct a semi-analytical model for CPD structure and evolution, including the effects of viscous heating, accretion heating, stellar irradiation, and irradiation by the young and luminous Jupiter to study the evolution of the iceline. They also consider the effects of the migration of Jupiter during the so-called 'Grand Tack' where Jupiter briefly approaches as close as 1.5 au to the sun. In their model, moons are constructed during the ongoing post-gap opening accretion stage. The presence of an inner cavity blocks the in-spiralling loss of satellites to type I migration. The iceline moves inwards radially on 10^5 yr timescale. This approach results in Io's migration being stopped at a truncated inner edge, and it does not lose its water via tidal heating but is instead primordially arid. In Heller and Pudritz (2015) a more general approach is taken considering theoretical exomoon systems around super-Jovian planets in the circumstellar habitable zone. It is found that the loss of satellites via type I migration in a gas fed accretion disk can be prevented by the density bump present at the CPD iceline, and not only at the CPD inner edge.

Viscosity in the CPD

A vital property of CPDs that regulates their energy balance, lifetime, and dynamics is the rate at which angular momentum can be transported radially in the disk. While the mechanism that drives this angular momentum transport is unknown, its efficiency is quantified by its dimensionless viscosity α. A viscous force causes disk gas to self-interact. As angular momentum is exchanged between two radially adjacent parcels of gas, the outer parcel gains momentum while the inner parcel loses it. This leads to a spreading of the disk (Lynden-Bell and Pringle, 1974). Material that spreads inwards may be accreted onto the planet, while material that spreads outwards may be lost beyond the planetary gravitational sphere of influence.

The molecular viscosity in protoplanetary disks is known to be too low to drive viscous evolution of the disk. Turbulence within the disk can however act effectively as a form of viscosity. This is described by the α-disk model of Shakura and Sunyaev (1973);

$$\nu = \alpha \frac{c_s^2}{\Omega_K}, \tag{9}$$

where ν is the viscosity, c_s is the isothermal sound speed, k is the Boltzmann constant, Ω_K is the Keplerian angular frequency and α is the dimensionless viscosity parameter. The disk is thus heated by friction as a function of the mass accretion rate $\dot{M}$ and Ω_K. Given that mass flow onto the CPD has shown numerically to occur post gap-opening, viscous heating could act as a source of heating for the dense, rapidly rotating CPD (Lubow et al., 1999).

The initial motivation for the development of the gas-starved disk has waned as the validity of the viscously-heated disk model has been questioned in recent years (Turner

et al., 2014; Gressel et al., 2015; Bai, 2017). Non-ideal magnetohydrodynamic (MHD) effects (Ohmic diffusion, Hall effect, ambipolar diffusion (Wardle, 2007; Bai, 2011)) suppress turbulent viscosity, limiting magneto-rotational instability induced turbulence to a thin surface layer (Hirose and Turner, 2011), and leading to inefficient midplane heating (Fujii et al., 2014, 2017; Mori et al., 2019) Hence, a CPD could be much denser and colder than envisioned by Canup and Ward (2002). In this case the low densities of the gas-starved disk may not be necessary to prevent “overheating" of the disk.

External radiation fields

Near the end of Jupiter's formation the young Sun had an excess X-Ray and UV flux of a factor $10^2 - 10^3$ over the present day (Zahnle and Walker, 1982; Ribas et al., 2005). A rapid migration of Jupiter and its CPD to 1.5 au during a ‘Grand Tack’ scenario (Walsh et al., 2011) may have resulted in a sufficiently high solar X-ray and UV flux to deplete the CPD of volatiles, implying the formation of Ganymede and Callisto occurred prior to the inwards migration. (Heller et al., 2015). If volatiles in the CPD are lost prior to the formation of satellites, we can infer that satellite formation must have occurred rapidly and prior to the gap opening or in the presence of a sufficiently massive CPD. While a pre-gap opening CPD is shielded effectively by the optically thick circumstellar disk midplane, photons may scatter into a gap from the Sun or may impinge directly from interstellar space. If the CPD is radiatively depleted of volatiles prior to the formation of the Galilean satellites, it must later be enhanced in volatile content by a dust or planetesimal capturing process or continued mass accretion from the circumstellar disk across the gap to explain the satellite compositions (Canup and Ward, 2006; Mosqueira et al., 2010; Ronnet et al., 2018).

Several lines of evidence suggest that the Sun was formed in a cluster environment with other stars (Adams, 2010). Isotopic abundances in meteorites indicate the presence of short-lived radioactive isotopes (Lee et al., 1976) possibly produced by a supernova explosion near the solar circumstellar disk (Chevalier, 2000). The truncation of the mass distribution in the solar system beyond 30 AU may have been caused by close stellar encounters in the birth cluster of 2000-10000 stars (Portegies Zwart, 2009). Photons with energy $h\nu \geq 13.6$ eV are ionizing photons known as EUV and efficiently drive photoevaporation. Photons of energy $6 < h\nu < 13.6$ eV are known as FUV. While more efficient at driving photoevaporation, EUV is emitted primarily by OB type stars which are comparatively rare. Hence FUV radiation often dominates the photoevaporation in moderately sized clusters. Supernovae explosions within the solar birth cluster have also been shown to truncate, heat, and tilt protoplanetary disks (Portegies Zwart et al., 2018), with potential deleterious effects for a CPD exposed by gap-opening. The chemistry, lifetime, and physical extent of the CPD may thus hinge directly on the unique formation conditions of the solar system. The prevalence of various moon system architectures could thus be tied to these conditions.

Bringing it all together: Population Synthesis Models

Population synthesis models are a statistical approach to reproducing observed populations of e.g. satellites by combining the physics relevant to their formation and analysing the properties of the resulting systems. The first population synthesis of satellite systems was performed by Sasaki et al. (2010) in an attempt to explain the differing architectures of the Jovian and Saturnian satellite systems. The authors employed a semi-analytical model with 1D viscous evolution to describe the growth and migration of proto-satellites in an accreting CPD based on the GSD. They assume that the cut-off of accretion onto Jupiter and its CPD is very rapid after gap opening, while for Saturn the tailing-off of accretion is much slower. They find that type I migration timescales are much longer than the Jovian disk viscous diffusion timescales and hence the satellites configuration is 'frozen' at the time of gap opening. Jupiter's disk is inferred to have had an inner magnetospheric truncation while Saturn's did not based on observations of Classical and Weak Line T-Tauri stars and their respective levels of magnetic coupling to disks. The resulting simulation produces 4-5 Galilean mass satellites for Jupiter in 80% of cases, with the inner satellites tending to be locked into a mean-motion resonance. Simultaneously they successfully recreate a single large, icy, satellite for Saturn in 70% of cases, concluding that the difference in architectures is largely due to the rate of decline of mass accretion and the presence or absence of an inner truncated CPD.

Miguel and Ida (2016) performed a semi-analytical population synthesis within a static and massive MMsN and found that massive satellites as large as Ganymede and Callisto were difficult to form against the very rapid migration brought on by high gas density. While in the GSD model considered by Sasaki et al. (2010) the maximum surface density of the disk is $\sim$ 100 g/cm^2, the viscosity $\alpha = 10^{-2} - 10^{-3}$, and the disk lifetime is (3-5)$\times 10^6$ years, the MMsN considered by the authors has a maximum surface density $\sim 10^5$ g/cm^2, $\alpha = 10^{-4} - 10^{-6}$, and the disk lifetime is $10^4 - 10^7$ years. They conclude that the rapid gas drag efficiently removes small planetesimals (satellitesimals) from the disk, requiring the initial embryo size to be larger than 30 km to reach a solids disk lifetime of 10^3 years. Rapid pebble accretion is invoked to bring the embryos up to 1000 km in size instantaneously. The authors conclude that while massive static disks are favored in circumstellar disk simulations, they may not be the most suited to explain the formation of the Galilean satellites.

Cilibrasi et al. (2018) perform a population synthesis of the Galilean moons in an accretion disk. CPD initial conditions are derived from fully 3D hydrodynamical models of gas density and temperature structure (Szulágyi, 2017). Satellites embryos grow via streaming instability in a dust trap, inferred to exist from the velocity profiles from the hydrodynamical simulations. The concentration of solids leads to rapid satellite formation in only 10^4 years, and many are lost to type I migration into Jupiter. On average 15 $M_\oplus$ of satellites are lost into Jupiter. The final satellites form very late in the CPD lifetime when it is reduced to only 2% of its initial mass. At this point it has cooled sufficiently that water ice can condense in the region of the dust trap at $\sim$ 80 R_J and 85% of the satellites formed are icy. Systems very similar to the Galileans were

found to form when disks had long dispersion timescale and high dust-to-gas ratios.

1.4 Observational Evidence

1.4.1 ...for circumplanetary disks

Several candidate CPDs have been identified, often via accretion tracers, such as the object embedded within a gap of the LkCa15 transitional disk (Kraus and Ireland, 2012), in the inner cavity of the transitional disk of HD 169142 (Reggiani et al., 2014), inside the gap of PDS70 (Keppler et al., 2019), and at a separation of 20 au from the Herbig A5 star MWC 758 (Reggiani et al., 2018). Other CPDs candidates been detected outside of gaps, such as around CS Cha c (Ginski et al., 2018) and GSC 6214-210 (Bowler et al., 2015). Debris disks or rings around unseen companions have also been detected in transit in the PDS 110 system (Osborn et al., 2017) and 1SWASP J140747 (V1400 Centauri) (Mamajek et al., 2012).

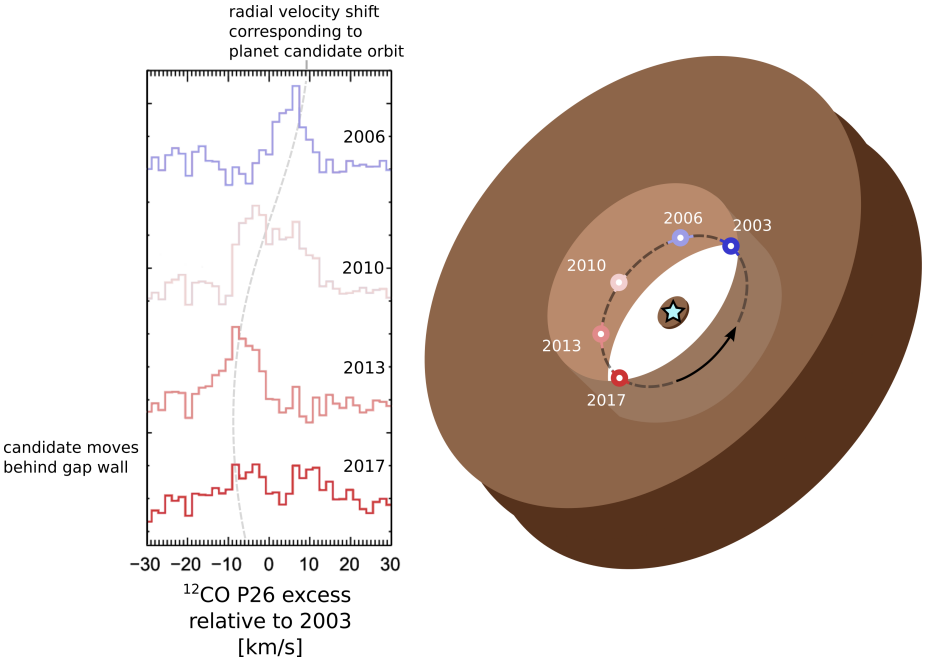

Figure 1.7: Reproduction and adaptation of Fig. 1 and 4 in (Brittain et al., 2019). On the left is the excess ^{12}CO (v=1-0) P26 emission (4.92 μm) relative to the observed 2003 spectrum. On the right is the planet+CPD position and orbital motion corresponding to the evolving line asymmetry. Around 2017 the planet+CPD candidate moves behind the gap near-wall and disappears.

The HD 100546 circumstellar disk is split by a gap depleted of dust and gas be-

tween ~1-20 au (Bouwman et al., 2003; Grady et al., 2005; Brittain et al., 2009; Avenhaus et al., 2014; Fedele et al., 2015; Jamialahmadi et al., 2018; Pineda et al., 2019). Hydrodynamical simulations suggest a planet of several Jupiter masses orbits within the gap at 10-15 au to produce the radial dust structure observed in mm-wave continuum emission (Pinilla et al., 2015; Pyerin et al., 2021; Fedele et al., 2021). CO ro-vibrational line asymmetries traced over more than a decade suggest a source of excess emission is orbiting the star on a timescale corresponding to a planet near the gap outer edge (Brittain et al., 2013, 2014). This phenomenon is illustrated in Fig. 1.7. The excess ^{12}CO (v=1-0) P26 emission vanishes as the predicted position of the planet moves behind the near-side of the gap outer edge (Brittain et al., 2019). A lack of compact dust continuum emission from the CPD candidate favors a low mass optically thin disk (Pineda et al., 2019).

PDS 70

The PDS 70 circumstellar disk has a wide gap (Hashimoto et al., 2012) containing at least two planets (Keppler et al., 2018; Müller et al., 2018; Wagner et al., 2018; Haffert et al., 2019). The planet PDS 70 c was discovered by the H-α emission associated with ongoing accretion (Haffert et al., 2019). Observations with the ALMA have detected unresolved sub-mm thermal emission co-located with this planet, interpreted as originating from a dusty CPD (Isella et al., 2019; Benisty et al., 2021). 3D radiative transfer modeling of the circumstellar and circumplanetary disk suggests that the CPD is optically thick with a dust mass upper limit of 0.7 $M_\oplus$ (Portilla-Revelo et al., 2022).

AS 209

An additional candidate CPD has been detected in the AS 209 disk by ^{13}CO J=2-1 gas line emission (Bae et al., 2022). The AS 209 disk is finely radially structured, with a dusty inner core and two rings seen in dust continuum emission at 62 and 103 au (Fedele et al., 2018). The CPD candidate lies exterior to the outer dust ring at 200 au. The candidate is embedded within a gap seen in the ^{12}CO emission. Despite being a gap, this region is optically thick in ^{12}CO and hence there is no counterpart detection in ^{12}CO. However, a perturbation in the velocity field of the ^{12}CO gas further supports the interpretation of a planet+CPD. The CPD temperature is measured to be 35 K, higher than the local 22 K of the circumstellar disk, suggesting a localized source of heating. Assuming a standard ^{13}CO abundance the gas mass is estimated to be 30 $M_\oplus$. Given the non-detection of associated continuum emission the dust mass of the CPD must be < 0.027 $M_\oplus$, suggesting a dust-to-gas ratio $< 9 \times 10^{-4}$, in line with prediction of rapid dust depletion of wide separation CPDs (Rab et al., 2019).

1.4.2 ...for exomoons

Analysis of Kepler photometric light curves of exo-Jupiters has hitherto failed to detect Galilean-like satellites around so-called 'warm' Jupiters (Teachey et al., 2018). The au-

thors stacked 6096 transits of 284 validated Kepler planets to create an ensemble 'grand light curve' to investigate satellite populations in bulk. Only a marginally significant signal corresponding to a population of super-Ios (R = 0.2-1 $R_\oplus$ at separations 5-15 R_P) was found. Given that the formation zone of the warm Jupiters is expected to be further out than their final orbits, these potential satellite systems may have migrated inwards with their planet, in which case they may have lost their outer satellites as the Hill radius reduced and the satellite orbits became unstable (Namouni, 2010). Planet-planet scattering events may also cause the loss of less tightly bound satellites (Gong et al., 2013; Hong et al., 2018), and the moons of closer-in planets have intrinsically less stable orbits (Dobos et al., 2021).

The exomoon candidate Kepler 1625b-i was found by transit light curve analysis orbiting a 12 $R_\oplus$ and 10M_J gas giant near the Deuterium-burning limit. The planet Kepler 1625b orbits at 0.811 au with an equilibrium temperature of 350 K, but most strikingly the satellite candidate has a predicted mass on the order of Neptune's. While such a satellite-primary mass ratio is large compared to the Galilean system, it represents the upper limit of CPD-formed satellites in numerical population synthesis models (Cilibrasi et al., 2018; Teachey and Kipping, 2018). A second candidate was identified in Kepler transit data, Kepler 1708 b-i, a 2.6 $R_\odot$ moon orbiting a Jupiter-sized planet (<4.6 M_J) at stellocentric distance 1.6 au (Kipping et al., 2022). However, given the significant period of the planet (737.1 d) only two transits have been recorded. Nevertheless the authors calculate a false-positive probability of $1^{+0.7}_{-1}\%$. It should be noted that the sensitivity of current instruments will bias the earliest detections to the largest moons orbiting the shortest-period planets, similarly to the initial exoplanet detections of close-in Hot Jupiters (Mayor and Queloz, 1995; Butler et al., 1997). Hence these early candidates are likely to be poorly representative of the overall population of exomoons and may even represent relatively unique formation scenarios.

1.5 This Work

How can we go about answering the question of whether Jupiter's moons are unique? In this work I bring to bear the last decade's worth of transformative developments in planet formation theory. I consider the context of the formation of the Galilean moons - where the solar system itself formed, and how that formation environment influenced their orbital architecture. I demonstrate how their most characteristic physical property - the compositional gradient - can arise in a circumplanetary disk despite the dynamical radial transport of dust and gas. I reveal how planets of differing masses chemically influence the process of moon formation, by the varying degrees to which they cause shock-heating of ices falling onto the moon-forming disks. Finally, I demonstrate the capability of a next-generation astronomical instrument to detect moon-forming disks around other stars.

Chapter 2

Photoevaporation of the Jovian Circumplanetary Disk

N. Oberg, I. Kamp, S. Cazaux & Ch. Rab

Abstract

Context: The Galilean satellites are thought to have formed from a circumplanetary disk (CPD) surrounding Jupiter. When it reached a critical mass, Jupiter opened an annular gap in the solar protoplanetary disk (PPD) that might have exposed the CPD to radiation from the young Sun or from the stellar cluster in which the Solar System formed.
Aims: We investigate the radiation field to which the Jovian CPD was exposed during the process of satellite formation. The resulting photoevaporation of the CPD is studied in this context to constrain possible formation scenarios for the Galilean satellites and explain architectural features of the Galilean system.
Methods: We constructed a model for the stellar birth cluster to determine the intracluster far-ultraviolet (FUV) radiation field. We employed analytical annular gap profiles informed by hydrodynamical simulations to investigate a range of plausible geometries for the Jovian gap. We used the radiation thermochemical code ProDiMo to evaluate the incident radiation field in the Jovian gap and the photoevaporation of an embedded 2D axisymmetric CPD.
Results: We derive the time-dependent intracluster FUV radiation field for the solar birth cluster over 10 Myr. We find that intracluster photoevaporation can cause significant truncation of the Jovian CPD. We determine steady-state truncation radii for possible CPDs, finding that the outer radius is proportional to the accretion rate $\dot{M}^{0.4}$. For CPD accretion rates $\dot{M} < 10^{-12} M_{\odot}$ yr^{-1}, photoevaporative truncation explains the lack of additional satellites outside the orbit of Callisto. For CPDs of mass $M_{\rm CPD} < 10^{-6.2} M_{\odot}$, photoevaporation can disperse the disk before Callisto is able to migrate into the Laplace resonance. This explains why Callisto is the only massive satellite that is excluded from the resonance.

N.Oberg et al. 2020 *Photoevaporation of the Jovian circumplanetary disk*, A&A 638, A135

2.1 Introduction

We consider the question whether the Galilean moon system is representative of satellite systems of extrasolar giant planets. The Galilean satellites were formed in a Jovian circumplanetary disk (CPD) (Lunine and Stevenson, 1982; Canup and Ward, 2002; Mosqueira and Estrada, 2003a) near the end of the formation of Jupiter (Cilibrasi et al., 2018). While direct detection of extrasolar Galilean analogs has thus far been unsuccessful (Teachey et al., 2018), several candidate moon-forming CPDs have been identified. The most robust CPD detections are associated with the PDS 70 system; the 5.4 ± 1 Myr old system contains two accreting planets at 23 and 35 au within a cavity (Wagner et al., 2018; Müller et al., 2018; Haffert et al., 2019). The inner planet PDS 70b has been detected in near-infrared photometry with an inferred mass of 5-9 $M_{\rm J}$ (Keppler et al., 2018) and a derived upper limit on circumplanetary dust mass lower than $\sim 0.01 M_{\oplus}$ (Keppler et al., 2019). K-band observations with VLT/SINFONI found a planetary spectral energy distribution (SED) best explained by the presence of a CPD (Christiaens et al., 2019). Observations with ALMA at 855 μm found continuum emission associated with a CPD around PDS 70c, with a dust mass $2 \times 10^{-3} - 4.2 \times 10^{-3} M_{\oplus}$ and an additional submillimeter point source spatially coincident but still offset from PDS 70b (Isella et al., 2019). Additional CPD candidates have been identified in a wide-orbit around CS Cha (Ginski et al., 2018), around MWC 758 (Reggiani et al., 2018), and in the inner cavity of the transitional disk of HD 169142 (Reggiani et al., 2014). Because potentially habitable exomoons may outnumber small terrestrial worlds in their respective habitable zones, the prevalence of massive satellites is a question of pertinent astrobiological interest (Heller et al., 2014).

The core-accretion model suggests that when the core of Jupiter reached a mass of 5-20 $M_{\oplus}$ it began a process of runaway gas accretion (Pollack et al., 1996; Mordasini, 2013), requiring that it formed prior to the dispersal of the gas component of the protoplanetary disk and thus within $\sim$10 Myr of the formation of the Solar System (Haisch et al., 2001). Gravitational interaction between Jupiter and the circumstellar disk possibly resulted in the rapid opening of an annular gap (Lin and Papaloizou, 1986, 1993; Edgar et al., 2007; Sasaki et al., 2010; Morbidelli and Nesvorny, 2012) in which the surface density was reduced relative to the surrounding protoplanetary disk (PPD) by a factor $\sim 10^2 - 10^4$ (Kley, 1999; Szulágyi, 2017). The timescale of the gap opening has been constrained by isotopic analysis of iron meteorites, which suggests that two distinct nebular reservoirs existed within the solar PPD, where the Jupiter gap acted to partially isolate the two reservoirs (Lambrechts and Johansen, 2014; Kruijer et al., 2017). In this case, the Jupiter core reached a mass of 20 $M_{\oplus}$ within <1 Myr and then grew to 50 $M_{\oplus}$ over 3-4 Myr, which is more slowly than predicted in the classical core-accretion scenario (Kruijer et al., 2017).

The accretion of gas onto Jupiter most likely led to the formation of a circumplanetary disk (Machida et al., 2008). The precise characteristics of the circumplanetary disk are still unclear, and several competing models are still considered. One possibility is a massive ($\sim 10^{-5} M_{\odot}$) static disk of low viscosity, which either initially contained or

was later enriched by sufficient solid material to form the Galilean satellites (Lunine and Stevenson, 1982; Mosqueira and Estrada, 2003a; Moraes et al., 2018). Alternatively, a family of accretion disk models has been postulated, in which the disks were fed by the continuous inflow of material from the surrounding PPD (Canup and Ward, 2002; Alibert et al., 2005; Canup and Ward, 2006, 2009). Even after the formation of a low-density annular gap, PPD material is expected to continue to flow across the gap and onto the planet and its CPD (Lubow and D'Angelo, 2006). Population synthesis models suggest that an accretion disk can successfully produce a Galilean-like retinue of satellites (Sasaki et al., 2010; Cilibrasi et al., 2018). After an optically thin gap is opened, solar photons may scatter onto the CPD or may impinge directly from interstellar space.

When a gaseous disk is exposed to an external UV radiation field as is present within a stellar cluster, a thin surface layer of gas can be heated such that the local sound speed of gas exceeds the gravitational escape velocity and the gas becomes unbound. This launches a thermal wind of escaping gas and entrained dust from the disk surface and outer edge (Hollenbach et al., 1994; Richling and Yorke, 2000). If the mass-loss rate caused by the photoevaporative flow is greater than the radial mass transport by viscous evolution, the disk can become truncated (Clarke, 2007). Photons of energy $6 < h\nu < 13.6$ eV are known as far-ultraviolet (FUV) photons and are expected to dominate photoevaporation in moderately sized clusters (Adams et al., 2004).

If the exposed Jovian CPD is depleted of volatiles or disrupted by photoevaporative processes prior to the formation of the Galilean satellites, it must afterward be enhanced in volatiles by a dust- or planetesimal-capturing process, or by continued mass accretion across the gap to explain the satellite compositions (Lubow et al., 1999; Canup and Ward, 2006; Mosqueira et al., 2010; Ronnet et al., 2018). While it is possible that satellite formation terminated prior to the stage of the Jovian gap opening (Sasaki et al., 2010), we consider models where the formation of the (final generation of) satellites occurs after the gap opening, in the case of either an optically thick massive and static disk or of a slow-inflow accretion disk (Lubow et al., 1999; Kley, 1999; Canup and Ward, 2002; Ronnet et al., 2018).

Several lines of evidence suggest that the Sun was formed in a stellar cluster (Adams, 2010) with a virial radius $r_{\rm vir} = 0.75 \pm 0.25$ pc and number of stars $N = 2500 \pm 300$ (Portegies Zwart, 2019). The short-lived radio-isotope (SLR) ^{26}Al in meteorites may have been produced by the enrichment of the solar PPD by winds from a nearby massive Wolf-Rayet star (Lee et al., 1976; Tang and Dauphas, 2012; Portegies Zwart, 2019). The truncation of the mass distribution in the Solar System beyond 45 au may have been caused by close stellar encounters in the birth cluster, UV-driven photoevaporation by nearby massive stars, or ram-pressure stripping by a supernova blast wave (Adams et al., 2004; Portegies Zwart, 2009; Adams, 2010). The cluster was likely an OB association in which a close stellar encounter occurred within 2 Myr and the probability of further close encounters became negligible after 5 Myr (Pfalzner, 2013). The Solar System was therefore likely bathed in an intense FUV radiation field while Jupiter was forming. The cluster would eventually have dispersed within some 10 to 100 million years (Hartmann et al., 2001).

The radiation environment inside the gap and around the circumjovian disk has been studied previously. Turner et al. (2012) used a Monte Carlo radiative transfer method to study the intragap radiation produced by a 10 $L_\odot$ star at time $t = 0.3$ Myr, motivated by the very rapid gap opening of a Jupiter formed in the gravitational instability scenario. Hydrostatic disk flaring in the gap exterior results in an illuminated outer edge of the gap that absorbs stellar radiation and reradiates it into the gap, resulting in a hot (> 150 K) gap that is inconsistent with an early formation of satellites (Durisen et al., 2007). Photoevaporation of the circumjovian disk has also been considered analytically in the context of a fixed CPD surface temperature (Mitchell and Stewart, 2011). In a 1D simulation that considered viscous evolution, accretion, and photoevaporation of the CPD, Mitchell and Stewart (2011) found that the CPD is radiatively truncated to a fraction of the Hill radius 0.16 r_H, in contrast to tidal forces, which have been suggested to truncate the CPD to 0.4 r_H (Martin and Lubow, 2011). The young Sun had an excess X-ray and UV flux $10^2 - 10^4$ times greater than at the present day (Zahnle and Walker, 1982; Feigelson et al., 2002; Preibisch et al., 2005; Ribas et al., 2005). A rapid migration of Jupiter and its disk to 1.5 au during a possible 'Grand Tack' scenario (Walsh et al., 2011) results in a sufficiently high solar irradiation to sublimate the CPD volatile reservoir, implying that the formation of Ganymede and Callisto occurred prior to any inward migration (Heller et al., 2015).

Several characteristics of the Galilean satellite system remain to be explained. Callisto is the only Galilean satellite that does not lie within the Laplace resonance, and no additional regular satellites exist beyond the orbit of Callisto. This might be indicative of an event that abruptly removed the gas content of the CPD to prevent further gas-driven migration by Callisto and to prevent the in situ formation of additional satellites at radii beyond 30 R_J. Previously, a rapid dispersal of the Jovian CPD has been invoked to explain the difference in the architectures between the Jovian and Saturnian regular satellite systems (Sasaki et al., 2010). We aim to improve our understanding of the formation of the Galilean satellites by modeling CPD truncation in the presence of external, and in particular, intracluster, FUV radiation. As a first application, we explore in this paper the conditions under which photoevaporation might explain the lack of massive satellites outside the orbit of Callisto and how it might have prevented Callisto from entering the Laplace resonance.

2.2 Methods

To capture the relevant physics of cluster-driven circumplanetary disk photoevaporation across nine orders of magnitude in spatial scale (from tens of Jovian radii to several parsecs) and four orders of magnitude in temporal resolution (from 1 kyr to 10 Myr) we model the evolution of the stellar cluster, Solar System, and Jovian circumplanetary disk independently. The general method of this approach is thus outlined in three parts. A diagram illustrating the systems modeled is shown in Fig. 2.1.

1) In Sect. 2.2.1 we simulate the evolution of an analog to the Sun-forming stellar

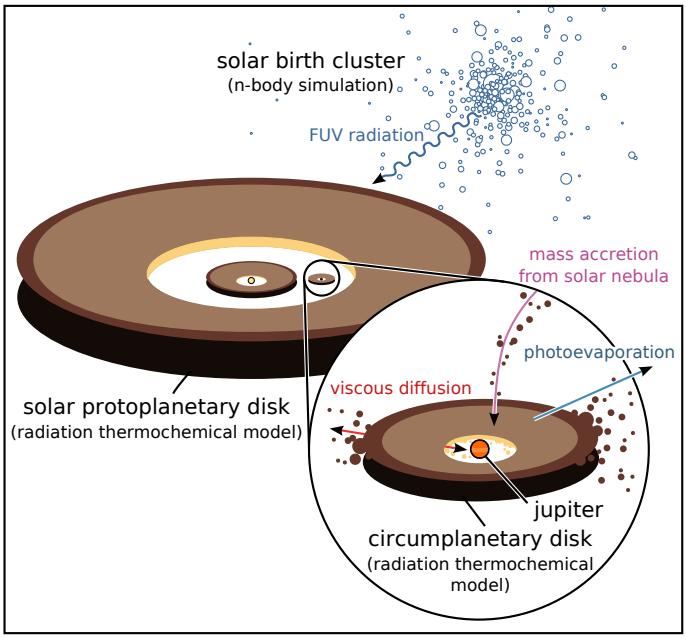

Figure 2.1: Illustration of the systems we modeled. The solar birth cluster n-body provides the background radiation field for the solar protoplanetary disk in the model. The protoplanetary disk model is used to determine the fraction of radiation incident on the circumplanetary disk. Mass in- and outflow to the CPD is calculated to derive steady-state truncation radii.

cluster to determine the time-varying FUV radiation field to which the Sun-like cluster stars are exposed over a typical PPD lifetime of $\sim$ 10 Myr (Pascucci and Tachibana, 2010). Each cluster star is sampled from a Kroupa initial mass function (IMF) (Kroupa, 2002) and a stellar FUV luminosity corresponding to its mass is calculated. Because the precise location of the Solar System inside the birth cluster is not known, we consider the radiation field incident on all cluster stars. This allows us to study 2500 Jovian CPD analogs simultaneously and to investigate the resulting distribution of incident FUV radiation fields as a function of time and stellar mass.

2) In Sect. 2.2.2 we construct a radiation thermochemical disk model of the protoplanetary disk of the Sun and introduce an annular gap of width 1-2 au in the surface density profile to investigate the penetration of the stellar and interstellar FUV radiation of the disk midplane and quantify the intragap radiation field.

3) In Sect. 2.2.3 the derived intragap radiation field is then applied as a background to a grid of disk models representing plausible Jovian CPDs. The resulting gas temperature structure and photoevaporative mass loss of the CPD are studied as a function of time. The truncation radii of the CPDs are calculated, and the evolution of the outer radius as a function of decreasing mass accretion is studied.

2.2.1 Interstellar radiation field and cluster environment

To determine the UV radiation field that an arbitrary cluster star is exposed to, we created a model of the solar birth environment. For the mass distribution of the cluster, we adopted a simple Plummer sphere (Plummer, 1911) and initialized it into virial equilibrium. The cluster was given a number of stars $N = 2500$ and a virial radius 0.75 pc (Portegies Zwart, 2019). The spatial distribution, mass, and temperature of the cluster stars are shown in Fig. 2.2. We sampled the stellar masses from the Kroupa IMF (Kroupa, 2002) with a lower mass limit of 0.08 $M_\odot$ and an upper mass of 150 $M_\odot$ (Weidner and Kroupa, 2006). An arbitrary resampling of 2500 stars from the Kroupa IMF resulted on average in 2.9±1.5 stars of mass greater than 20 $M_\odot$ in the cluster that dominate the cluster FUV emission. The resulting cluster mass is typically ~ 1000 $M_\odot$. The cluster simulation was then integrated over 10 Myr using the REBOUND n-body code (Rein and Liu, 2012).

In our disk modeling code ProDiMo (described in Sect. 2.2.2), the intensity of the external UV radiation field is parameterized by the so-called unit Draine field, χ, which is defined as

$$\chi = \frac{\int_{205\mathrm{nm}}^{91.2\mathrm{nm}} \lambda u_\lambda d\lambda}{\int_{205\mathrm{nm}}^{91.2\mathrm{nm}} \lambda u_\lambda^{\mathrm{Draine}} d\lambda}, \tag{10}$$

where λu_λ is the spectral flux density, and $\lambda u_\lambda^{\mathrm{Draine}}$ is the UV spectral flux density of the ISM (Draine, 1978; Röllig et al., 2007; Woitke et al., 2009). For $\chi = 1$, the dimensionless Habing unit of energy density $G_0 \approx 1.71$, and when it is integrated from 6-13.6 eV, $G_0 = 1$ corresponds to a UV flux $F_{\mathrm{UV}} = 1.6 \times 10^{-3}$ erg s^{-1} cm^{-2} (Draine and Bertoldi, 1996). In the radiative transfer, the external FUV radiation field is approximated as the sum of an isotropic diluted blackbody (20000 K) and the cosmic microwave background (CMB) (2.7 K),

$$I_\nu = \chi 1.71 W_{\mathrm{dil}} B_\nu(20000K) + B_\nu(2.7K), \tag{11}$$

where $W_{\mathrm{dil}} = 9.85357{\times}10^{-17}$ is the normalization factor for $\chi = 1$ (Woitke et al., 2009). The integration boundaries bracket radiation intensities that drive important photoionization and photodissociation processes in protoplanetary disks (van Dishoeck et al., 2006). The upper integral boundary of 91.2 nm is the Lyman limit. In ProDiMo, χ is a

free parameter. We can thus investigate the exposure of the CPD to variable FUV flux levels derived from the stellar cluster model.

Each star in the cluster was taken to be an ideal blackbody with a luminosity determined by the mass-luminosity relation $L \propto M^{3.5}$. We derived the stellar temperature and computed the resulting Planck function (Salaris and Cassisi, 2005). We integrated the Planck function over the FUV wavelength range specified in Eq. 11 to determine the photospheric FUV luminosity per star. T Tauri stars exhibit FUV excess in part because of strong Lyα (10.2 eV) emission, which can contribute $\sim$ 90% of the FUV flux (Ribas et al., 2005; Schindhelm et al., 2012). We therefore applied a correction factor to our T Tauri cluster stars ($M_* < 8\ M_\odot$) by scaling the UV luminosity relative to the bolometric luminosity $L_{\rm bol}$ to satisfy $L_{\rm UV} \sim 10^{-2.75\pm0.65} L_{\rm bol}$ for classical T Tauris (Yang et al., 2012). To reflect the large scatter in this relation, we drew 2500 samples from a normal distribution with standard deviation of the quoted uncertainty and applied to the cluster stars. The combined effect over the cluster is a FUV luminosity increase by a factor $\sim$ 60.

We then calculated for each star within the cluster the resulting incident FUV flux that originated from all others cluster stars for each time step. The behavior of the photoevaporative mass-loss rates described in Sect. 2.2.3 was then determined as a function of the time-variable FUV intra-cluster radiation field. We also considered that the CPDs are partially shielded by the surrounding disk material exterior to the gap and that the interstellar FUV flux must be reduced by a fraction corresponding to this opening angle. We here considered six surface density profiles to represent the disk evolution as a function of time. The profiles are shown in Fig. 2.3.

Two phenomena act to reduce flux incident on the CPD. The first is shielding from the surrounding protoplanetary disk material external to the gap. The second is the orientation of the system relative to the primary source of FUV radiation, which are the B stars in the cluster central region. Because we did not monitor the inclination of the PPDs during the cluster simulation, we averaged over all possible disk inclinations to account for the projected area and shielding from the PPD.

For each profile we measured the opening angle over which the planet has an optically thin line of sight to the exterior. We find visual extinction $A_V < 1$ opening angles for the six profiles in Fig. 2.3. These correspond to shielding of isotropic incident flux by a factor 0.5, 0.33, and 0.2 for t = 1 Myr, $\alpha = 10^{-3}, 10^{-4}$, and 10^{-5} , respectively, and 0.12, 0.06, and 0.03 for t = 5 Myr, $\alpha = 10^{-3}, 10^{-4}$, and 10^{-5} , respectively. We smoothly interpolated this shielding factor from the maximum to the minimum for the assumed α-viscosities over the first 5 Myr of the simulation to represent the evolution of the disk surface density. The effective projected area of a disk averaged across all possible orientations in three dimensions is half of its true area. At t = 1 Myr, the flux incident on the CPDs is thus diluted by a factor 4 at most, independently of extinction of normally incident rays. When instantaneous snapshots of the FUV flux distribution were extracted (as in Fig. 2.4), we convolved a random distribution of disk inclinations with the flux distribution to compensate for the effect of the averaged incidence angle.

Because the cluster includes short-lived massive ($M > 20\ M_\odot$) stars that contribute

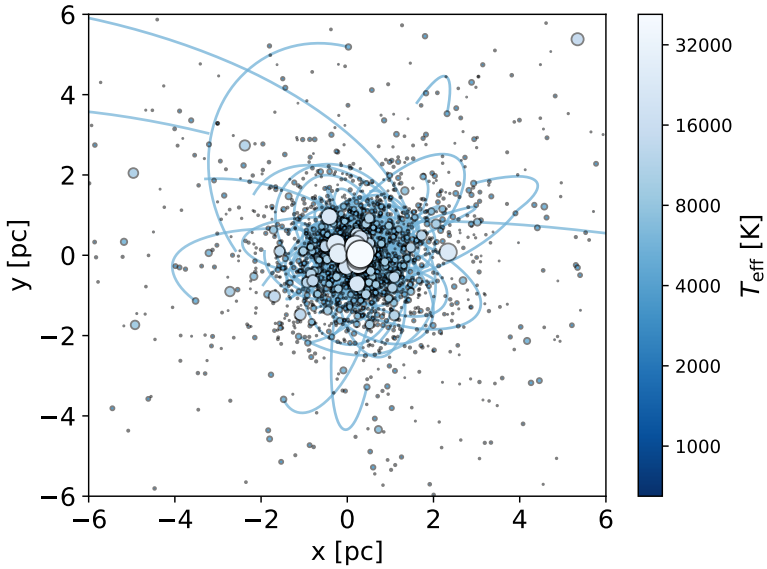

Figure 2.2: Projected x-y plane distribution of stars in the solar birth cluster at t = 5 Myr. Marker size and color indicate stellar mass. Trajectories of stars with mass corresponding to G-type stars are traced for 5 Myr.

to the total cluster FUV luminosity, it is worthwhile to discuss the possibility and implication of supernovae explosions that might occur within the cluster. While a supernova in the vicinity of the Sun may be required to explain r-process anomalies in Ca-Al inclusions, such an event would have occurred during the earliest formation stages of the Solar System (Brennecka et al., 2013) and it is therefore not relevant for the satellite formation process of Jupiter. However, the lifetime of massive stars greater than 20 $M_{\odot}$ is ≤ 8 Myr (Schaller et al., 1992), and it is therefore possible that other stars ended their main-sequence lifetime during the 10 Myr time span considered in our simulation. We find that when we populate our model cluster by sampling stellar masses from the Kroupa IMF, the population of stars of $M > 20\ M_{\odot}$ typically contribute $\sim$ 75% of the integrated cluster FUV luminosity, with the individual massive stars contributing $\sim$ 25% each to the total cluster FUV. The effect of the satellite formation process is thus contingent on whether the most massive stars formed early or late in the stellar formation history of the cluster. In clusters of $10^3 - 10^4$ members, the majority of star formation is expected to occur contemporaneously; in Orion, it is estimated that 53% of cluster stars formed within the last 1 Myr and 97% within the last 5 Myr (Palla and Stahler, 2000). The apparent ejection of several high-mass stars from Orion 2.5 Myr ago and the current ongoing massive star formation implies that both early and late formation of

massive stars are possible (Hoogerwerf et al., 2001; Beuther et al., 2007). We expect satellite formation to have occurred no earlier than 4 Myr after the formation of the Ca-Al inclusions to satisfy the constraint of the internal differentiation state of Callisto and no later than the dispersal of the gas component of the solar PPD after ~ 5 Myr (Canup and Ward, 2002; Barr and Canup, 2008; Mamajek, 2009). If the massive star formation rate is independent of the cluster age and the overall star formation rate accelerates, as observed in Orion, there is a 90-95% probability that a 20 $M_\odot$ star will not explode prior to the stage of satellite formation.

In the eventual case of one or more supernovae, we expect an abrupt reduction in cluster FUV luminosity by 25-75%. By resampling from our adopted IMF and reinitializing the initial positions of cluster members, we find that a cluster with 70% lower FUV flux than our fiducial case is still 1σ consistent with the resulting spread in cluster FUV luminosities. While the Solar System might be ram-pressure stripped by supernovae explosions (Portegies Zwart et al., 2018), the CPD is an actively supplied accretion disk whose mass and steady-state radius depend on the accretion rate, and we therefore expect CPDs to rebound to steady state within some 10^3 yr after accretion is resumed.

2.2.2 Disk modeling with ProDiMo

We used the radiation thermochemical disk model ProDiMo [1] (protoplanetary disk model) to simulate the solar nebula at the stage before the gap opening of Jupiter (Woitke et al., 2009; Kamp et al., 2010b; Thi et al., 2011). ProDiMo calculates the thermochemical structure of disks using a frequency-dependent 2D dust continuum radiative transfer, gas-phase and photochemistry, ice formation, and nonlocal thermal equilibrium (NLTE) heating and cooling mechanisms to self-consistently and iteratively determine the physical, chemical, and radiative conditions within a disk. ProDiMo performs a full 2D ray-based wavelength-dependent continuum radiative transfer at every grid point in the disk to calculate the local continuous radiation field $J_\nu(r, z)$ (Woitke et al., 2009). Rays are traced backward from each grid point along their direction of propagation while the radiative transfer equation is solved assuming LTE and coherent isotropic scattering. For a full description of the radiative transfer method, see Woitke et al. (2009). We adopted the standard DIANA dust opacities [2] for a mixture of amorphous silicates, amorphous carbon, and vacuum (Woitke et al., 2016; Min et al., 2016a).

Solar protoplanetary disk

To construct our protosolar nebula, we used a modified Hayashi minimum mass Solar nebula (MMSN) surface density profile (Hayashi, 1981) combined with an analytical gap structure approximation based on a generalized normal (Subbotin) distribution, with a characteristic flat bottom and Gaussian wings (Subbotin, 1923). The unperturbed surface density Σ at a radius r is thus described by

[1] https://www.astro.rug.nl/ prodimo/

[2] https://dianaproject.wp.st-andrews.ac.uk/data-results-downloads/fortran-package/

$$\Sigma(r) = \Sigma_{1\mathrm{au}}\left(\frac{r}{1\ \mathrm{au}}\right)^{-3/2}\ \mathrm{g\ cm^{-2}}, \tag{12}$$

where $\Sigma_{1\mathrm{au}}$ is the surface density at $r = 1$ au, and the gap structure D at a radius r is defined by

$$D(r) = X\frac{a}{2b\Gamma(\frac{1}{a})}\exp\left(-\left|\frac{r - r_\mathrm{p}}{b}\right|^a\right), \tag{13}$$

where b is the standard deviation of the Gaussian component of the gap, r_p is the radial location of the gap-opening planet, a is a shape parameter, Γ is the gamma function, and the gap depth is controlled by a normalization function X that scales the gap depth relative to the unperturbed surface density profile. The final perturbed surface density profile is thus defined as $\Sigma(\mathrm{r}) \cdot D(\mathrm{r})$, with a total mass of 0.02 $M_\odot$ out to 100 au for a surface density at 1 au $\Sigma_{1\mathrm{au}}$ of 1700 g cm^{-2} and a shape parameter $a = 8$. The semi-major axis of Jupiter at the stage of gap opening is poorly constrained because Jupiter may have migrated to its present location by gravitational interaction, with the protosolar nebula leading to short periods of dynamical instability (Tsiganis et al., 2005; Walsh et al., 2011). To make as few assumptions as possible, we therefore placed Jupiter at its current location of $r_\mathrm{p} = 5.2$ au. Our gap dimensions are informed by the analytical gap-scaling relation derived from hydrodynamical simulations of Kanagawa et al. (2016) for Jupiter-mass planets where the intragap minimum surface density Σ_gap and unperturbed surface density Σ_0 are related by $\Sigma_\mathrm{gap}/\Sigma_0 = (1{+}0.04\ K)^{-1}$, with K defined as

$$K = \left(\frac{M_\mathrm{p}}{M_*}\right)^2\left(\frac{H_\mathrm{p}}{r_\mathrm{p}}\right)^{-5}\alpha^{-1}. \tag{14}$$

Here H_p is the disk scale height at the radial location of the planet r_p, and α is the viscosity. To determine $H_\mathrm{p}/r_\mathrm{p}$, we first ran a single ProDiMo model of the unperturbed solar nebula. The heating-cooling balance of the disk was iteratively calculated until the disk structure converged to a vertical hydrostatic equilibrium, from which we extracted the radial scale height profile. Similarly, we employed the formula for the gap width at half-depth of Kanagawa et al. (2016), where

$$\frac{\Delta_\mathrm{gap}}{r_\mathrm{p}} = 0.41\left(\frac{M_\mathrm{p}}{M_*}\right)^{1/2}\left(\frac{H_\mathrm{p}}{r_\mathrm{p}}\right)^{-5}\alpha^{-1/4}, \tag{15}$$

where Δ_gap is the gap depth. We adopted two cases for the planet mass M_p (0.1 and 1 M_J) owing to the continuing accretion of Jupiter after the gap opening. We also considered that the total disk mass was reduced over the course of 5 Myr. Numerical simulations of accreting planets in gaseous disks show that the circumstellar disk is reduced to 60% of its unperturbed mass by the time of the Jovian gap opening, and to only 5% when the planet has reached its final mass of 1 M_J (D'Angelo, 2010). We first considered a gap profile at the time of gap opening $t \sim 1$ Myr when Jupiter has reached 10% of its final mass, or $\sim$ 30 $M_\oplus$ (Dong and Fung, 2017), and second, a gap profile for when

Jupiter approaches its final mass at $t \sim 5$ Myr. The resulting surface density profiles are shown in Fig. 2.3. Based on an initial Hayashi MMSN mass of $\sim 0.02 M_\odot$, we adopted total protosolar disk masses of 0.012 $M_\odot$ and 0.001 $M_\odot$ for the 1 and 5 Myr stages, respectively (D'Angelo, 2010). These values are in general agreement with the observed exponential decrease of the inner disk fraction with time $e^{-t/\tau_{\rm disk}}$ with a disk e-folding time $\tau_{\rm disk} = 2.5$ Myr (Mamajek, 2009). This suggests gas disk masses of 0.67 and 0.13 of the initial mass at 1 and 5 Myr, respectively. Finally, because of the uncertainty in the viscosity, we considered a range of possible PPD α viscosities from $10^{-5} - 10^{-3}$ (Shakura and Sunyaev, 1973; Kanagawa et al., 2015; Rafikov, 2017). The resulting surface density profiles for all self-consistent combinations of planet mass, disk mass, and disk viscosity are plotted in Fig. 2.3, and they result in a variation of approximately six orders of magnitude in the intragap surface density.

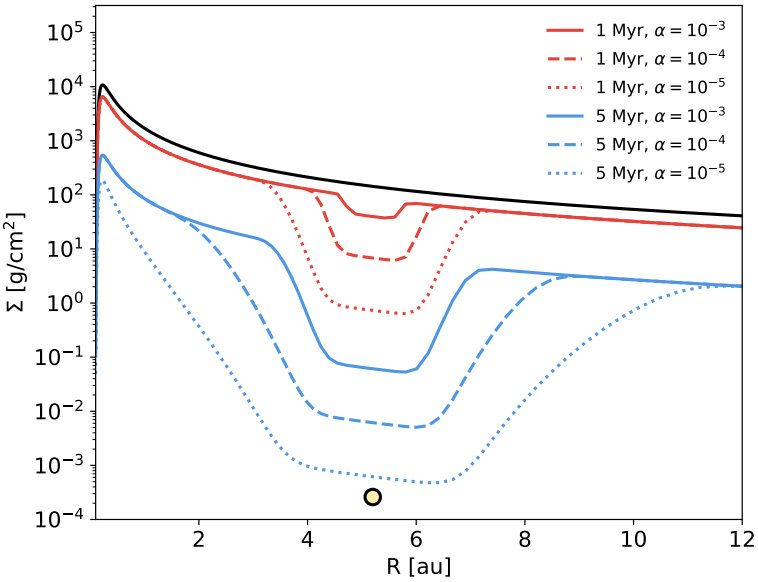

Figure 2.3: Surface density profiles of the solar protoplanetary disk. The red profiles show the earliest gap-opening phase when $M_{\rm p} = 0.1\ M_{\rm J}$ case at $t = 1$Myr when the disk has been reduced to 60% of its initial mass. The blue profiles show the $M_{\rm p} = 1 M_{\rm J}$ case where the remaining disk mass is 5% of the initial mass. The black line plots the unperturbed disk surface density at t_0 with a total mass of $0.02 M_\odot$. The orange dot indicates the radial location of Jupiter.

Solar luminosity and temperature were selected from the evolutionary tracks from

Parameter	Symbol	Value
Stellar mass	M_*	1.0 $M_\odot$
Stellar luminosity	L_*	2.335, 0.7032 $L_\odot$
Effective temperature	$T_{\rm eff}$	4278, 4245 K
UV luminosity	$L_{\rm UV,*}$	0.01 $L_\odot$
X-ray luminosity	$L_{\rm X}$	10^{30} erg s^{-1}
Interstellar UV field	χ	$10^1 - 10^7$
Disk mass	$M_{\rm disk}$	0.012, 0.001 $M_\odot$
Disk inner radius	$R_{\rm in}$	0.1 au
Disk outer radius	$R_{\rm out}$	100 au
Minimum dust size	$a_{\rm min}$	0.05 μm
Maximum dust size	$a_{\rm max}$	3000 μm
Dust size power law	p	3.5
Dust-to-gas ratio	d/g	10^{-2}
Dust composition:		
$Mg_{0.7}Fe_{0.3}SiO_3$		60 %
Amorphous carbon		15%
Vacuum		25%
Viscosity	α	$10^{-3}, 10^{-4}, 10^{-5}$

Table 2: ProDiMo model parameters for the solar protoplanetary disk at ages t = 1 Myr and 5 Myr. Stellar temperature and luminosity are selected from the pre-main-sequence stellar evolutionary tracks of Siess et al. (2000). Stellar UV and X-ray luminosities are adopted from Woitke et al. (2016).

the Grenoble stellar evolution code for pre-main-sequence stars (Siess et al., 2000). For the Sun, we adopted a 1 $M_\odot$ star with metallicity Z = 0.02 at ages of 1 Myr and 5 Myr to reflect the stages of gap opening and when the mass of Jupiter reaches $\sim$ 1 $M_{\rm J}$. We used the PHOENIX library of stellar atmospheric spectra (Brott and Hauschildt, 2005; Husser et al., 2013). All parameters of the solar protoplanetary disk are listed in Table 2.

Circumplanetary disk

Jovian CPD models can be roughly sorted into two categories. The first is a CPD analogous to the MMSN that contains sufficient solid matter to construct the Galilean satellites (Lunine and Stevenson, 1982; Mosqueira and Estrada, 2003a; Moraes et al., 2018). Assuming a canonical dust-to-gas mass ratio of 0.01, the resulting disk has a gas mass of $M_{\rm disk} \approx 2 \times 10^{-5} M_\odot$. To prevent rapid radial migration and loss of the satellites, the disk must be highly inviscid with $\alpha \leq 10^{-6}$ (Canup and Ward, 2002). We refer to this class of CPD as the "static" CPD. The second class of CPD models considers an accretion disk fed by a continuous flow of material from the surrounding

circumstellar disk (Canup and Ward, 2002; Alibert et al., 2005; Canup and Ward, 2009). In this class, the instantaneous mass of this CPD is a function of the mass-inflow rate and disk viscosity, and it can be sufficiently low to become optically thin. We therefore consider CPD masses in the range $10^{-5} - 10^{-9} M_{\odot}$ (Canup and Ward, 2006). We refer to this class of CPD as the "accretion" CPD.

To determine the temperature structure and hence photoevaporation rate of the accretion CPD, we considered the effects of viscous heating through dissipation. ProDiMo includes the parametrization for viscous heating of D'Alessio et al. (1998). We specified the viscous heating rate with a mass accretion rate $\dot{M}$. We assumed that the gravitational energy released is converted into heat. For a steady-state disk, the mass flux $\dot{M}$ is constant between all annuli. The half-column heating rate is

$$F_{\rm vis}(r) = \frac{3GM_{\rm p}\dot{M}}{8\pi r^3}(1 - \sqrt{r_p/r})\ \text{erg cm}^{-2}\text{s}^{-1}, \tag{16}$$

where G is the gravitational constant, $M_{\rm p}$ is the planetary mass, r is the distance to the planet in cylindrical coordinates, and $r_{\rm p}$ is the planetary radius. We must make an assumption about how heat is distributed within the column as a function of height z, converted into heating rate per volume by the relation

$$\Gamma_{\rm vis}(r,z) = F_{\rm vis}(r)\frac{\rho^P(r,z)}{\int \rho^P(r,z')dz'}\text{erg cm}^{-3}\text{s}^{-1}, \tag{17}$$

where ρ is the volume density at radial position r and height z, and P is a constant equal to 1.5 to avoid unphysical heating at low volume densities. Accordingly, most of the dissipative heating occurs in the CPD midplane.

The CPD is also heated directly by the radiation of Jupiter. The early luminosity of Jupiter spans five orders of magnitude over 3 Myr (Marley et al., 2007). In our CPD model we considered the Jupiter luminosity $L_{\rm p}$ after the runaway-gas-accretion phase when it briefly peaked at $L_{\rm p} > 10^{-3} L_{\odot}$ and then declined to $\sim 10^{-5} L_{\odot}$ and below. The surface temperature of Jupiter was likely 500-1000 K at this stage (Canup and Ward, 2002; Spiegel and Burrows, 2012). For the Jovian SED we adopted the DRIFT-PHOENIX model spectra for a body of $t = 1000$ K and surface gravity $2.55{\times}10^3$ cm s^{-2} (Helling et al., 2008).

We followed the steady-state surface density formulation of Canup and Ward (2002), which relates $\Sigma \propto \dot{M}/\alpha$. Because we explored five orders of magnitude of CPD mass and three orders of magnitude of mass accretion rate onto the CPD, each combination of CPD surface density Σ and accretion rate $\dot{M}$ corresponds to a unique value of α. Hence we explored CPD α viscosities from $2.5 \times 10^{-6} - 2.5 \times 10^{-1}$. Because the mechanism that causes viscosity in the PPD and CPD may not be the same, we considered that the two can have differing α-viscosities. The case of the CPD with a mass of $10^{-9} M_{\odot}$ and an accretion rate of $10^{-9} M_{\odot}$ yr^{-1} is thus rendered unphysical because $\alpha > 1$ is required.

In selecting a range of dust-to-gas ratios, we considered that dust can either quickly coagulate into satellitesimals through the streaming instability (Drążkowska and Szulágyi, 2018), or quickly settle into the midplane and be viscously transported into the

Parameter	Symbol	Value
Planet mass	$M_{\rm p}$	1.0 $M_{\rm J}$
Planetary luminosity	$L_{\rm p}$	$10^{-5} L_{\odot}$
Effective temperature	$T_{\rm eff,p}$	1000 K
UV luminosity	$L_{\rm UV,p}$	0.01,0.1 $L_{\rm p}$
Interstellar UV field	χ	$10^{1} - 10^{7}$
Background temperature	$T_{\rm back}$	70 K
Disk mass	$M_{\rm cpd}$	$10^{-5} - 10^{-9} M_{\odot}$
Disk inner radius	$R_{\rm in,cpd}$	0.0015 au
Disk outer radius	$R_{\rm out,cpd}$	0.2 au
Column density power index	β_{Σ}	1.0
Maximum dust size	$a_{\rm max}$	10, 3000 μm
Dust-to-gas ratio	d/g	$10^{-2}, 10^{-3}, 10^{-4}$
Flaring index	β	1.15
Reference scale height	$H_{0.1{\rm au}}$	0.01 au
Accretion rate	$\dot{M}$	$10^{-12} - 10^{-9} M_{\odot}$ yr^{-1}

Table 3: ProDiMo model parameters for models of the Jovian circumplanetary disk. The ranges of CPD mass and accretion rate are subdivided in steps of 10. Where not specified, the CPD parameters are identical to those listed in Table 2.

planet on short timescales. In either case, the amount of material stored in dust grains is rapidly depleted. Therefore we considered cases in which the dust-to-gas ratio is $10^{-2} - 10^{-4}$. Parameters for the static and accretion CPDs are listed in Table 3.

We considered five CPD steady-state masses in combination with four CPD mass accretion rates for a total of 19 unique CPD models. Furthermore, the five CPD mass models were varied in their dust-to-gas ratio, maximum dust size, and planetary luminosity by the ranges listed in Table 3.

2.2.3 Photoevaporative mass loss

Molecular hydrogen in the disk can be heated to $T > 10^4$ K by EUV radiation, but only begins to drive mass loss for massive stellar encounters of $d \ll 0.03$ pc (Johnstone et al., 1998). FUV photons penetrate below the ionization front and instead heat the neutral hydrogen layer to $\sim 10^3$ K (Johnstone et al., 1998). Where the gas heating drives the sound speed of the gas $c_{\rm s}$ above the local escape velocity, the gas becomes unbound, launching a supersonic outward flow of disk material. The radius beyond which this occurs is the gravitational radius $r_{\rm g}$,

$$r_{\rm g} = \frac{G M_{\rm p}}{c_{\rm s}^2}, \tag{18}$$

where G is the gravitational constant, assuming the disk mass $M_{\rm disk} \ll M_{\rm p}$, and where the sound speed is defined as

$$c_{\rm s} = \sqrt{\frac{\gamma k_B T}{\mu m_H}}. \tag{19}$$

Here γ is the adiabatic index, T is the gas temperature, $k_{\rm b}$ is the Boltzmann constant, μ is the mean molecular mass, and $m_{\rm H}$ is the mass of hydrogen. Because ProDiMo locally determines the sound speed at all grid points, we conservatively estimated the resulting mass outflow where $c_{\rm s}$ exceeds the local escape velocity of the Jovian CPD. At a semi-major axis of 5 au, a 1 $M_{\rm J}$ planet orbiting a 1 $M_{\odot}$ star has a Hill radius $r_{\rm H} \approx 0.34$ au or 711 $R_{\rm J}$. Gravitational interaction with the disk can act to perturb the CPD gas and truncate the disk at $\sim 0.4\ r_{\rm H}$ (Martin and Lubow, 2011), and the Jovian CPD may therefore not have had a radius larger than ~ 0.14 au or 290 $R_{\rm J}$. For a surface layer of the gas disk with a typical speed of sound $c_{\rm s} \sim 5$ km s^{-1} , the associated gravitational radius is 0.03 au. The CPD is thus said to exist in the supercritical regime. The current semi-major axis of the outermost Galilean satellite, Callisto, lies at 0.0126 au, or 0.42 $r_{\rm g}$. Interestingly, given that gap opening may have occurred as early as when Jupiter grew to $M_{\rm p} = 0.1\ M_{\rm J}$, the associated $r_{\rm g}$ lies between the present-day semi-major axes of Ganymede and Callisto at a distance of 0.01 au from Jupiter.

The mass-loss rate per annulus in the CPD at $r > r_{\rm g}$ can be estimated $\dot{M}_{\rm evap} \approx \rho c_{\rm s} {\rm d}a$, where ρ is the volume density of gas at the base of the heated layer, and da is the surface area of the annulus. The escape velocity is $\sqrt{2GM_{\rm p}/r}$. To determine the mass-loss rate as a function of χ , we ran seven ProDiMo models for each of the five considered CPD masses. Each successive step in the model grid increased the background χ field by a factor ten, covering the range $10^1 - 10^7$. At every radial grid point in the resulting ProDiMo disk models, we determined the lowest height above the midplane z at which the escape criterion was satisfied. The sound speed $c_{\rm s}$ at the coordinate (r, z, χ) and volume density $\rho(r, z)$ were calculated to determine the mass loss per unit area. The surface area of the corresponding annulus was then multiplied by the area mass-loss rate to determine a total evaporation rate per annulus, such that

$$\dot{M}_{\rm evap}(r, \chi(t)) = c_{\rm s}(r, z, \chi(t))\rho(r, z)A(r)\ , \tag{20}$$

where $A(r)$ is the area of the annulus at radius r. The resulting radial evaporation rate profile was log-interpolated between the seven values of χ, such that any value within the range $10^1 - 10^7$ could be considered. This is required because the FUV field to which the cluster stars are exposed varies smoothly as a function of time (see Sect. 2.3.1).

2.2.4 Accretion and viscous evolution of the CPD

In our model, mass accretion and viscous evolution of the CPD will act to replace mass lost by photoevaporation. Following from angular momentum considerations, it is believed that matter would accrete not evenly over the CPD surface, but concentrated near a centrifugal radius of $\sim$20 $R_{\rm J}$ (Machida et al., 2008). In each global iteration of our CPD

photoevaporation model, the accreted material was distributed in steps radially outward from the centrifugal radius until the steady-state surface density profile was achieved or the accreted mass budget was exhausted. How rapidly this material can be transported radially is set by the viscous diffusion timescale $\tau_{\rm visc}$. A viscously evolving α-disk has a global viscous diffusion timescale

$$\tau_{\rm visc} \approx \frac{r_{\rm CPD}^2}{\nu} = \frac{r_{\rm CPD}^2}{\alpha H^2 \Omega_{\rm k}}, \tag{21}$$

where ν is the kinematic viscosity and $\Omega_{\rm k}$ is the Keplerian angular frequency (Shakura and Sunyaev, 1973; Canup and Ward, 2009; Armitage et al., 2019). For $\alpha = 10^{-2} - 10^{-5}$ and $r_{\rm CPD} = 500\ R_{\rm J}$, we find $\tau_{\rm visc} \approx 10^3 - 10^6$ yr. The magnitude of CPD viscosity is highly uncertain. An α on the order $10^{-3} - 10^{-2}$ allows for Ganymede-sized moons to migrate inward under type I migration and establish the Laplace resonance (Peale and Lee, 2002). Simulations of turbulence induced by magnetorotational instability (MRI) in CPDs suggest values of α lower than 10^{-3} (Fujii et al., 2014), but baroclinic instabilities have been suggested as means to transport angular momentum in disks (Lyra and Klahr, 2011).

While very high accretion rates of $\dot{M} \sim 10^{-8} M_\odot$ yr^{-1} have been shown to be possible across a gap for a PPD with $\alpha = 10^{-3}$ and $H/r = 0.05$ (Kley, 1999), we also considered cases more similar to the slow-inflow accretion disk scenario where $\dot{M} \sim 10^{-11} - 10^{-10} M_\odot$ yr^{-1} (Canup and Ward, 2002), which is also consistent with the accretion rate of the PDS 70b CPD candidate $\dot{M} \sim 10^{-10.8} - 10^{-10.3} M_\odot$ yr^{-1} (Christiaens et al., 2019) and the presence of volatiles in the Jovian CPD midplane (Canup and Ward, 2002). Hence we considered the range of accretion rates listed in Table 3.

2.3 Results

We simulated the orbital evolution of 2500 stars in the stellar cluster over 10 Myr. We derived incident intracluster radiation field strengths for all of the cluster stars as a function of time. To determine the penetration of this radiation to the CPD, the optical depth and background temperature within the Jovian gap were determined. The heating of the Jovian CPD by the Sun, Jupiter, and intracluster radiation was determined by means of a dust and gas radiation thermochemical model. The resulting gas properties were used to simulate the photoevaporation and radiative truncation of circumplanetary accretion disks as a function of time.

2.3.1 Interstellar radiation field within the cluster

The 2500 stars within the cluster are found to be exposed to a range of intensities of the intracluster radiation field from $G_0 = 10^0 - 10^7$, with a modal $G_0 = 3150^{+12500}_{-2400}$. In Fig. 2.4 the temporal evolution of the distribution of intracluster FUV fluxes incident on each cluster star over the 10 Myr of the simulation is demonstrated. We find a distribution that largely agrees with the distribution suggested by Adams (2010), with a

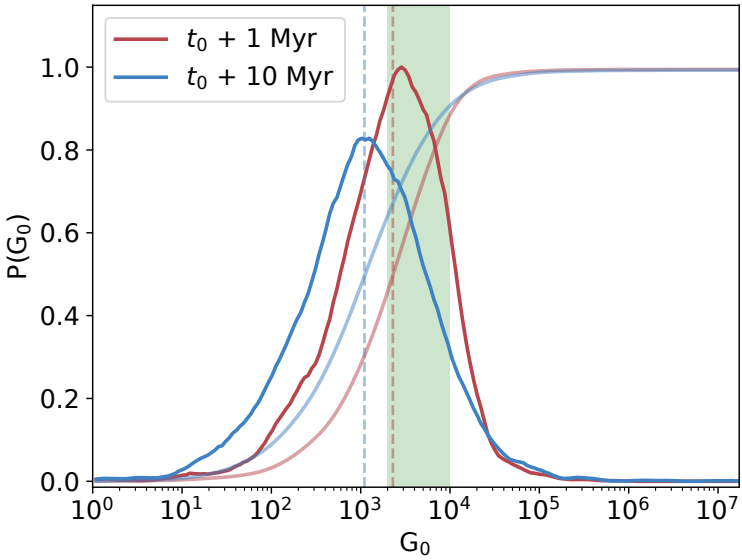

Figure 2.4: Probability distribution of the intracluster radiation field strength G_0 at the position of each cluster star over time, normalized to the maximum likelihood value at $t = t_0 + 1$ Myr. The distribution evolves over 10 Myr from $t = t_0 + 1$ Myr (red) and to $t = t_0 + 10$ Myr (blue). The faded solid lines illustrate the cumulative distributions. The vertical dashed lines indicate the median value of each distribution. The green bar indicates the Solar System constraint of $2000 \leq G_0 \leq 10^4$. Multiple initializations of the cluster have been averaged to minimize the Poisson noise because the number of stars is small ($N_{\rm stars} = 2500$).

typical $G_0 \sim 2800$ and a few systems experiencing prolonged intervals of $G_0 > 10^4$. In a snapshot at $t = 0$ Myr, only 12% of our cluster stars experience $G_0 > 10^4$, while at $t = 10$ Myr this number is reduced to 8%.

Over 10 Myr, dynamical friction segregates the cluster star populations radially by mass and causes it to expand. As lower mass stars are ejected from the cluster center where repeated close (< 0.1 pc) encounters with the high mass ($M > 25 M_\odot$) stars of the cluster occur, we find that the median G_0 field strength experienced by the cluster stars is reduced from an initial 2300 at $t = 0$ Myr (the red line in Fig. 2.4) to 1100 at $t = 10$ Myr (the blue line). The model G_0 declines from an initial 2600 to 1030. The radial intensity of the radiation field at some cluster radius r_c can be described initially by $G_0(r_c) = 0.07 r_c^{-2.04}$ with r_c in parsec for $r_c > 0.05$ pc. The fraction of time that a given star spends irradiated by an FUV field $F(G_0)$ over the simulation time is found to be largely independent of G_0 for values of $10^0 - 10^2$ because these stars are found in

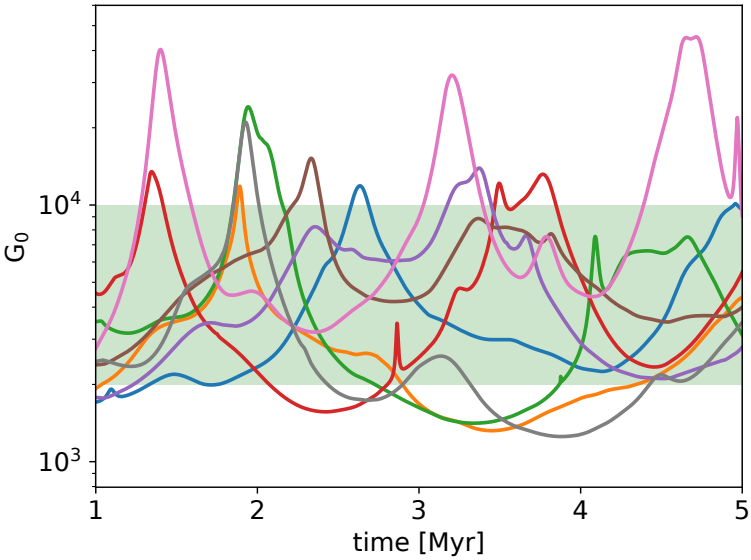

Figure 2.5: Irradiation tracks of eight randomly sampled G-type stars (identified by stellar mass 0.8-1.04 $M_\odot$) where the median background radiation field satisfies the criterion of $2000 \leq G_0 \leq 10^4$. The green bar indicates the boundaries of this constraint. Incident FUV radiation field strength is measured on the ordinate in units of G_0. The time resolution is 1 kyr.

the outer reaches of the cluster and their radial positions evolve slowly. For $G_0 > 10^2$, however, we find that $F(G_0) \propto G_0^{-2}$.

We traced the FUV field strength incident on G-type stars (defined as those with mass $0.84 < M_* < 1.15\ M_\odot$) over 10 Myr to investigate the influence of stellar mass on the irradiation history of a system within the cluster. Adams (2010) described a constraining range of G_0 values necessary to explain the compact architecture of the Solar System while ensuring that the solar nebula can survive over 3-10 Myr (Adams, 2010). A representative sample of these tracks is shown in Fig. 2.5. While only 11% of the G-type stars strictly satisfy the criterion, in practice, brief excursions outside the G_0 range would be consistent with the physical-chemical structure of the Solar System. For a looser constraint that allows very brief (10^4 yr) periods of $G_0 > 10^4$, 17% of the G-type stars satisfy the constraint, while 28% of the median background radiation field of the G-type star falls within the constraint. Periods of heavy irradiation ($G_0 > 10^4$) characteristically last 200-300 kyr as the stars pass rapidly through the inner regions of the cluster. Incidents with higher irradiation ($G_0 > 10^5$, not depicted in Fig. 2.5) occur even more briefly on timescales 50-100 kyr at most. Only $\sim$ 20% of the G-type stars

ever experience radiation fields in excess of 10^6, for which the characteristic duration is $\sim 10-20$ kyr. Half of the G-type stars that undergo the $G_0 > 10^6$ irradiation events are ejected from the cluster before 10 Myr in three-body interactions with massive stars.

2.3.2 Conditions within the Jovian gap

The radiation field intensity within the gap for each surface density profile was extracted and is shown in Fig. 2.6 for a reference $G_0 = 3000$. The ratio between the FUV radiation strength within the gap and the intracluster FUV radiation can be read on the right ordinate. The gap remains optically thick for cases with $t = 1$ Myr and $\alpha = 10^{-3}, 10^{-4}$. In the scenario with $t = 1$ Myr and $\alpha = 10^{-5}$, the gap is marginally optically thin, but the interstellar FUV is still extincted by a factor 6. The gap is highly optically thin for all $t = 5$ Myr models, allowing $> 99\%$ of the vertically incident intracluster FUV to penetrate to the PPD midplane, and hence to the surface of the CPD.

We also analyzed the radiation field inside the gap in the absence of the intracluster radiation field where the gap is illuminated only by the young Sun. We compared the solar radiation penetrating to the PPD midplane in the six surface density profiles of Fig.2.3. After 5 Myr, when Jupiter has grown to its final mass and the gap profiles reach their maximum depth, we find that the G_0 field strength within the three gap profiles is $(L_{\rm UV,*}/0.01L_\odot)\times 10^{3.51}, 10^{3.73}, 10^{3.84}$ respectively. Hence, when $L_{\rm UV} = 0.01L_\odot$ and $a_{\rm p} = 5.2$ au, we find that the young Sun still contributes significantly to the intragap radiation field even in the presence of an optically thick inner disk due to the scattering of photons by the upper layers of the inner disk. For this adopted $L_{\rm UV,*}$ the contribution of the young Sun to the FUV background is greater than that of the intracluster radiation field for 82% of stars in the cluster at 5 Myr. The cluster thus only becomes the dominant source of FUV radiation for stars with this disk-gap configuration if $L_{\rm UV,*} < 2.6\times 10^{-3}L_\odot$.

For a nominal $G_0 = 3000$ at $t = 1$ Myr, we find midplane gas temperatures within the gap of 50-65 K for the $\alpha = 10^{-3}, 10^{-4}$, and 10^{-5} cases. In the $t = 5$ Myr scenarios where the Jovian gap becomes optically thin and volume number densities approach 10^7 cm^{-3}, the intragap gas temperature ranges between $96-320$ K in the midplane due to X-ray Coulomb and photoelectric heating for $G_0 = 3000$. For the maximum $G_0 = 10^6$,we find a midplane gas temperature of 5000 K driven by polycyclic aromatic hydrocarbon (PAH) heating. In all cases, efficient [OI] line cooling leads to a torus of cooler gas of $T < 100$ K suspended above and below the midplane. The cool torus extends vertically and reaches the midplane for the $t = 5$ Myr, $\alpha = 10^{-5}$ case.

The primary source of gap-wall radiation that the CPD is exposed to is thermal emission from the dust. The dust temperature $T_{\rm dust}$ of the gap walls near the midplane at a radial optical depth of 1 is calculated by ProDiMo 2D radiative transfer. This temperature can be considered as the blackbody temperature of the gap walls, and thus the "background temperature" of the CPD. In all cases where the gap is optically thin, we find gap wall temperatures ranging from 60-75 K. The gas and dust temperature structure of the solar PPD for the case of $G_0 = 10^3$, $t = 5$ Myr, and $\alpha = 10^4$ is described in Fig. 2.12 in the appendix of this chapter. The outer gap wall is consistently 10 K

warmer than the inner gap wall. We find that the optically thick surfaces of the gap walls are largely insensitive to increasing G_0 for G_0 up to 10^5, while for $G_0 = 10^6$, we find a general increase of 20 K for the inner and outer gap walls.

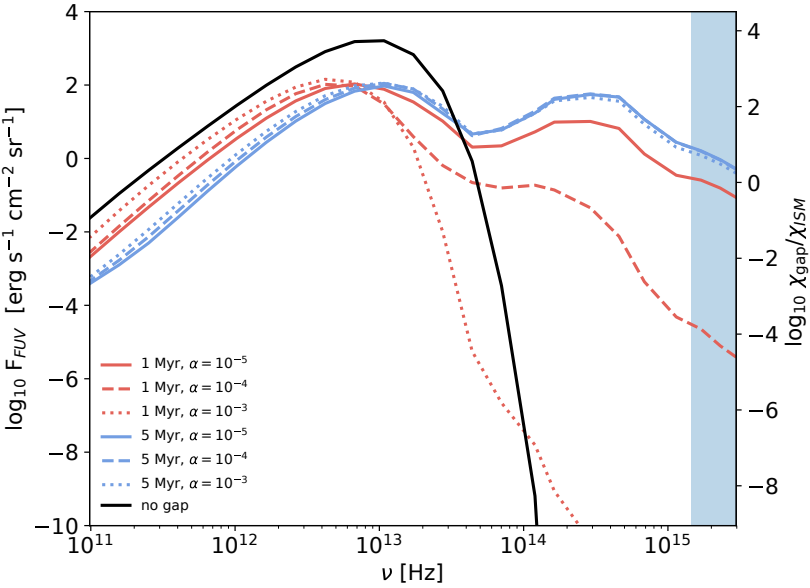

Figure 2.6: Extracted energy distributions of the radiation field in the MMSN midplane at the location of Jupiter for the six gap profiles illustrated in Fig. 2.3, for the case of G_0 = 3000. The shaded light blue region demarcates the FUV region of the spectrum. For comparison, the black line represents the radiation field of the unperturbed solar nebula at the midplane, and hence at the surface of the CPD. The right ordinate indicates the ratio between the external FUV radiation field originating from the cluster and that found within the gap.

2.3.3 Temperature structure and truncation of the CPD

We generated ProDiMo CPD models for intracluster FUV intensities spaced logarithmically in the range $G_0 = 10^1 - 10^7$. We considered five CPD models of different masses (see Table 3). We interpolated over our model grid to derive mass-loss rates for the CPDs exposed to arbitrary values of G_0 in the range $G_0 = 10^1 - 10^7$. For all modeled cluster ISRF cases we find CPD surface layers heated to $T > 10^3$ K and associated regions at which the local sound speed exceeds the escape velocity. The gas and dust temperature structure of the fiducial CPD are shown in Fig. 2.13 in the appendix of this

chapter. In the highly optically thin $M_{\rm CPD} = 10^{-8} - 10^{-9} M_\odot$ cases, we find gas loss that directly occurs from the CPD midplane. We considered a range of steady-state mass accretion rate $\dot{M} = 10^{-12} - 10^{-9} M_\odot$ yr^{-1}, and also the case of an exponential decline and cutoff in the accretion rate.

Circumplanetary disks evolve to a truncated steady state on a 10^3 yr timescale when mass loss through photoevaporation is balanced with the mass accretion rate. As a consequence of the orbital motion of the stars through the cluster, the CPDs in general are maximally truncated on timescales $< 10^5$ yr. For a given mass accretion rate, the instantaneous distribution of CPD truncation radii is then determined by the radial distribution of stars from the cluster center where FUV field strengths are highest.

We find only a weak dependence of CPD mass on steady-state truncation radius, while the accretion rate is found to dominate the resulting steady-state CPD radii. The results are plotted in Fig. 2.7. For each sampled accretion rate, the scatter induced by the CPD mass is bracketed by the shaded regions around the solid line. We find that for low accretion rates ($10^{-12} M_\odot$ yr^{-1}), $\sim 50\%$ of the Jovian CPD analogs in our cluster are truncated to radii within 30 $R_{\rm J}$ with a modal $r_{\rm trunc} = 27\ R_{\rm J}$. For intermediate accretion rates ($10^{-10} M_\odot$ yr^{-1}), 50% of the CPDs are truncated to within 110 $R_{\rm J}$ with a modal $r_{\rm trunc} = 200\ R_{\rm J}$. We find that the truncation radius is proportional to the accretion rate $\dot{M}^{0.4}$. The distribution of the truncation radius for stars that conform to the solar system formation constraint of $2000 < G_0 < 10^4$ is $28.7^{+5.4}_{-2.6} R_{\rm J}$ at $t = 5$ Myr for $\dot{M} = 10^{-12} M_\odot$ yr^{-1}.

The width of the truncation radius distributions in Fig. 2.7 is largely induced by the distribution of G_0 within the cluster, and we find that their relation is fit by

$$r_{\rm trunc} \approx \min\{\, 2 \times 10^7 \left(\frac{\dot{M}^{0.4}}{\log_{10}(\mathrm{G_0})^2} \right), r_{\rm out} \,\}\ R_{\rm J} \tag{22}$$

for accretion rates $10^{-12} \leq \dot{M} \leq 10^{-9} M_\odot$ yr^{-1} and FUV fields $10^1 \leq G_0 \leq 10^7$. We find the relation between the remaining mass of the truncated CPD $M_{\rm CPD,trunc}$ to be a fraction of its initial steady-state mass $M_{\rm CPD,init}$, and the accretion rate $\dot{M}$ is

$$\left(\frac{M_{\rm CPD,trunc}}{M_{\rm CPD,init}} \right) \approx \frac{1 - M_{\rm CPD,min}}{1 + \exp\left[-1.87(\log_{10}(\dot{M}) + 10.42)\right]} + M_{\rm CPD,min}\ , \tag{23}$$

where $M_{\rm CPD,min}$ is the fraction of CPD mass that remains after accretion drops significantly below 10^{-12} $M_\odot$ yr^{-1}. In the case of Jupiter we find the remaining CPD mass to be 8%. For the modal FUV radiation field strength in the cluster, $15^{+6}_{-6}\%$, $34^{+14}_{-12}\%$, $69^{+15}_{-18}\%$, and $99^{+1}_{-8}\%$ of the initial steady-state mass of the CPDs thus remains for mass accretion rates of $\dot{M} = 10^{-12}$, 10^{-11}, 10^{-10}, and $10^{-9} M_\odot$ yr^{-1}, respectively.

2.3.4 Photoevaporation rates with alternative CPD and planet parameters

Pressure bumps can act to filter and segregate dust-grain populations based on grain size (Rice et al., 2006a; Zhu et al., 2012). We also considered the case of a modified grain

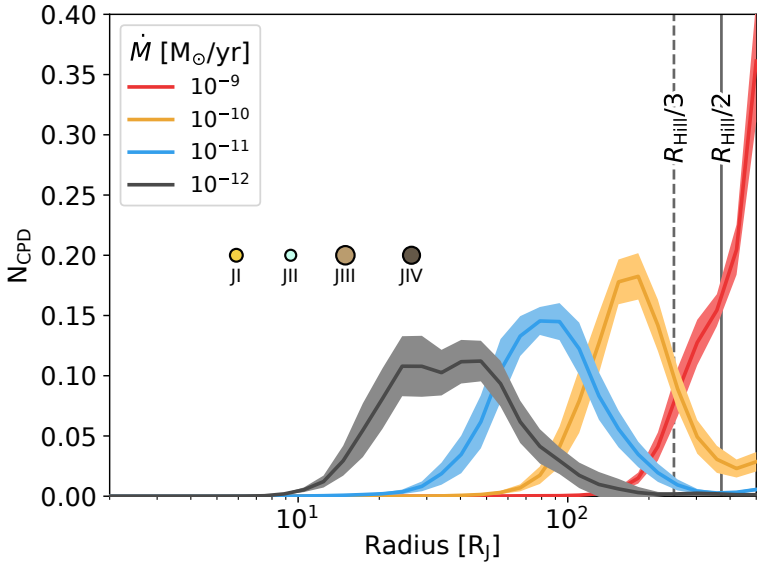

Figure 2.7: Distribution of steady-state truncation radii for the grid of CPD models in the case of intracluster FUV irradiation at 5 Myr. Each colored line represents the instantaneous distribution of the outer radius of 2500 Jovian CPD analogs with a range of external FUV radiation field strengths. The shaded region bracketing each distribution indicates the standard deviation between the different CPD mass models. The four colored circles indicate the radial location of the Galilean satellites JI (Io), JII (Europa), JIII (Ganymede), and JIV (Callisto). The vertical dashed black lines indicate theoretical limits on the CPD outer radius based on gravitational perturbations as fractions of the Hill radius.

size distribution in the CPDs and how it changes the rate of mass loss to photoevaporation. For the grain-filtered scenario, the maximum dust grain size was set to 10 μm rather than 3 mm (Paardekooper, 2007; Zhu et al., 2012; Bitsch et al., 2018). Because the material supplying the CPD may thus be starved of large dust grains, we also varied the dust-to-gas ratio. We considered disks of $d/g = 10^{-2}, 10^{-3}$, and 10^{-4}. The resulting radial mass-loss profiles are shown in Fig. 2.9. The fiducial CPD model we present is the $M_{CPD} = 10^{-7} M_\odot$, with a background radiation field $G_0 = 10^3$ and $d/g = 10^{-2}$. A lower dust-to-gas ratio decreases the disk opacity and pushes the FUV-heated envelope closer to the midplane, where volume density and thus mass-loss rates are higher. The radial mass loss $\dot{M}(r)$ is related to the dust-to-gas ratio d/g as $\dot{M}(r) \propto (d/g)^{0.56}$. The removal of larger (> 10 μm) grains conversely suppresses the photoevaporation as the mass previously stored in the large grains is moved to the small grains where the bulk

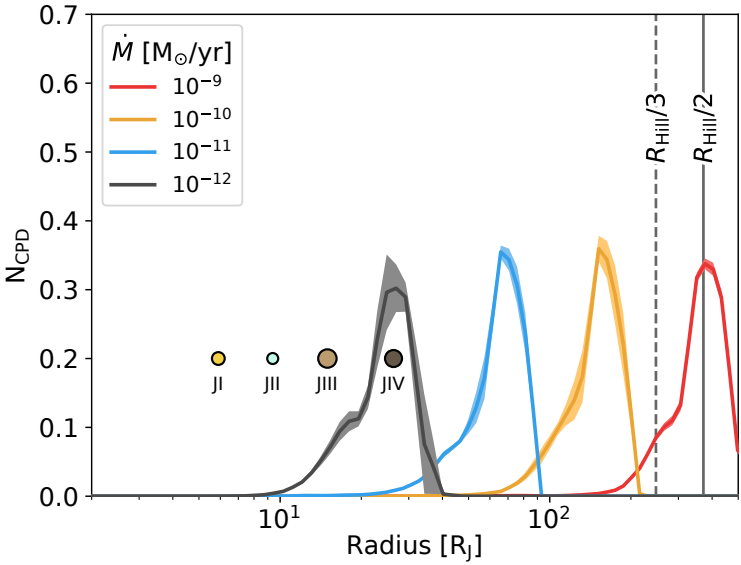

Figure 2.8: Same as in Fig. 2.7, but now also including the effect of the solar radiation.

of the opacity lies. In the combined case of both small grains and a reduced dust-to-gas ratio, the radial mass-loss rate of the fiducial case is closely reproduced, as is shown by the agreement of the blue and purple curve in Fig. 2.9.

We also considered cases of increased planetary UV luminosity driven by the higher rates of mass accretion. For the case of $L_{\rm UV,p} = 10^{-4} L_{\rm p}$, we find that the highly optically thick CPDs of mass $M_{\rm CPD} \geq 10^{-6} M_\odot$ are insensitive to the increased planetary luminosity. The lower mass CPDs experience both an increase in mass loss at radii within 200 $R_{\rm J}$ and mass loss in the innermost radii (see the brown curve in Fig. 2.9). The minimum of the truncation radius distribution is then pushed to lower radii. While an arbitrarily massive CPD exposed to $G_0 > 10^3$ is not truncated inward of 20 $R_{\rm J}$, increasing the planetary luminosity up to 10^{-3} L$_\odot$ can decrease the minimum truncation radius to within 6 $R_{\rm J}$, within the centrifugal radius at which mass is expected to accrete. We do not expect planetary luminosities this high at the late stage of satellite formation, however.

2.3.5 Photoevaporative clearing

We considered how rapidly photoevaporation can act to clear the CPD. Disk-clearing timescales are of particular significance for the fate of satellites undergoing gas-driven migration, with implications for the final system architecture. Jovian planets that are

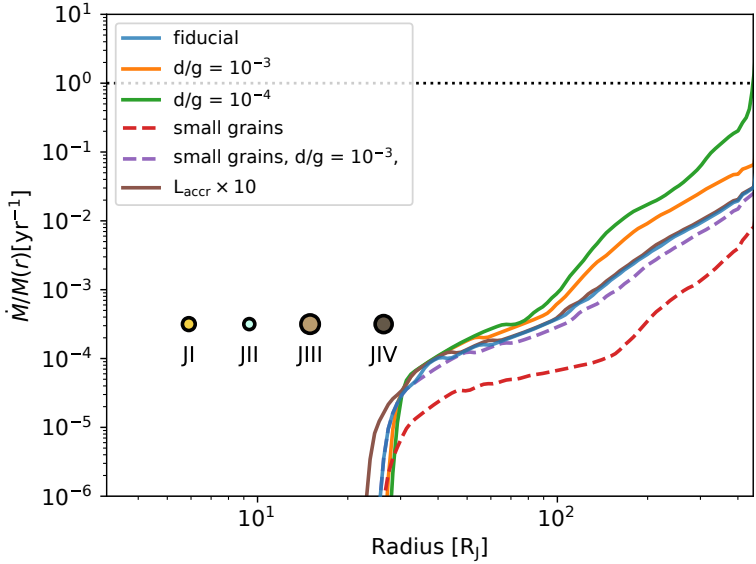

Figure 2.9: Radial photoevaporative mass loss in the CPD as a fraction of the mass available in the respective annulus of the steady-state surface density profile for a variety of modifications to the fiducial CPD model ($M_{\rm CPD} = 10^{-7} M_\odot, G_0 = 10^3$). The red and purple curves labeled "small grains" represent the case where the maximum grain size is 10 μm. The orange, green, and purple curves represent the cases of varying dust-to-gas ratio. The brown curve shows the case of additional planetary UV luminosity originating from accretion, ten times greater than in the fiducial case of planetary UV luminosity. The horizontal dashed black line represents the mass-loss rate at which an annulus would be entirely depleted within one year. The colored circles indicate the current semi-major axes of the Galilean satellites as described in Fig. 2.7.

starved of accretion material, perhaps by the formation of adjacent planets, may lose most of their mass through rapid photoevaporative clearing (Mitchell and Stewart, 2011). A rapid cutoff of the accretion may occur when the gaps of Saturn and Jupiter merge to form a single deeper gap, abruptly starving Jupiter of material originating external to its own orbit (Sasaki et al., 2010). We considered the CPD lifetimes in the context of such a rapid accretion cutoff.

The maximum photoevaporative mass-loss rate occurs for the $10^{-5} M_\odot$ CPD when exposed to the maximum considered radiation field $G_0 = 10^7$. For a static nonaccreting $10^{-5} M_\odot$ CPD, we then find a minimum lifetime against photoevaporation of 5×10^4 yr. In practice, the CPDs are rarely exposed to radiation fields greater than $G_0 = 10^5$ for extended periods of time, with a maximum exposure time of $\sim 10^5$ yr (see Sect. 2.3.1).

For the most likely value of $G_0 \approx 10^3$, we find a static CPD lifetime of $\tau_{\rm disk} = 4 \times 10^5$ yr against intracluster photoevaporation. In the case of the low-mass optically thin $10^{-9} M_\odot$ CPD, we find a disk lifetime against photoevaporation of only 25-300 years. The upper boundary corresponds here to the maximum possible initial CPD outer radius and hence lowest background radiation field strength observed in the cluster of $G_0 \sim 10^1$.

In the absence of photoevaporation, the CPD will dissipate on its viscous diffusion timescale. In Fig. 2.10, we show which regions of the CPD mass and accretion rate parameter space allow for photoevaporation to be the dominant disk-clearing mechanism. Viscous clearing primarily dominates for the high-mass ($\geq 10^{-8} M_\odot$) CPD models with higher mass accretion rates ($\geq 10^{-10.5} M_\odot$ yr^{-1}). Realistically, viscous evolution of the CPD will act in tandem with photoevaporation, transporting material to the more weakly bound regions of the CPD where photoevaporation is far more efficient (Mitchell and Stewart, 2011).

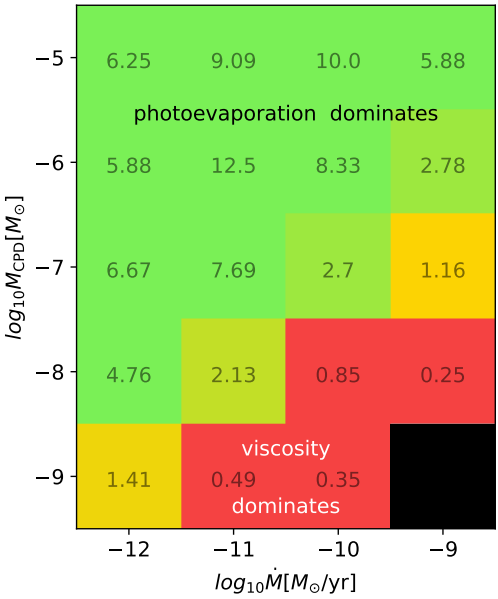

Figure 2.10: Ratio of the viscous diffusion timescale $\tau_{\rm visc}$ over the photoevaporative clearing timescales $\tau_{\rm evap}$ for the grid of CPD mass and accretion rate models. A value greater than 1 indicates that photoevaporation clears the disk more rapidly than viscous evolution. The black region indicates an unphysical corner of the parameter space where $\alpha > 1$.

2.4 Discussion

2.4.1 Relevance of photoevaporation for CPD size and lifetime

We have found that the size of a CPD is directly proportional to the mass accretion rate onto the CPD and FUV radiation field strength by Equation 22. The photoevaporation mass-loss rate of the CPDs has been found to be sufficiently rapid to enable a clearing of the CPD in only $< 10^3$ yr for the low-mass ($< 10^{-7} M_\odot$) CPD cases. A truncated outer radius and a rapid clearing of the CPD at the end of satellite formation has direct implications for the architecture of late-forming satellite systems. Unless the accretion onto the CPD is abruptly reduced to $\dot{M} \ll 10^{-12} M_\odot$ yr^{-1} from a previous steady accretion rate $\dot{M} \geq 10^{-11}$, the Jovian CPD will most likely be truncated to 30 R_J at some stage during or prior to satellite formation.

We find that solar (intrasystem) FUV radiation can still contribute significantly to CPD photoevaporation compared to the cluster FUV field. In the case of the optically thin gap allowing for full exposure of the CPD, we find that solar radiation places a lower limit on disk truncation regardless of the position of the system within the cluster, as illustrated in Fig. 2.8. For the purpose of this figure, each star was assumed to have solar FUV luminosity, therefore it does not represent the distribution of truncation radii arising from the luminosity function of stars within the cluster, but rather the possible positions of the Sun within the cluster.

However, we recommend a more sophisticated radiative transfer model that includes the effects of anisotropic scattering of light by dust grains to determine the effect of the CPD inclination on the efficiency of this solar irradiation. This method would also be able to more accurately probe the radiation contribution of the gap walls, which are heated by the Jovian luminosity.

2.4.2 Comparison with previous work

In their study of the Jovian CPD, Mitchell and Stewart (2011) constructed a 1D model that coupled viscous evolution, photoevaporation, and mass accretion for a range of fixed CPD envelope temperatures. They found a distribution of Jovian CPD truncation radii ranging from 26-330 R_J with a mean value of $\sim 120 R_\mathrm{J}$. To reproduce the same mean truncation radius, our model requires a slightly lower accretion rate of $\sim 10^{-10.4} M_\odot \mathrm{yr}^{-1}$ compared to the $\dot{M} \approx 10^{-9.9} M_\odot$ yr^{-1} considered by Mitchell and Stewart (2011), although this can likely be explained by different choices of CPD surface envelope temperatures. Our truncation radii are found to be tied only to the background radiation field strength and the mass accretion rate, but not significantly to the CPD mass and hence not to the viscosity. This is consistent with the findings of Mitchell and Stewart (2011) that the α-viscosity alone does not significantly alter the truncation radius.

Mitchell and Stewart (2011) also studied photoevaporative CPD clearing timescales, finding evaporation times τ_evap of $10^2 - 10^4$ yr, with the spread arising from the range of envelope temperatures 100-3000 K. For our fiducial $G_0 = 3000$, we find a correspond-

ing CPD surface envelope temperature of 1900 ± 100 K. For CPDs of similar viscosity and mass accretion rate than they considered ($\alpha = 10^{-3}$, $\dot{M} \approx 10^{-9.9} M_{\odot}\mathrm{yr}^{-1}$), we find $\tau_{\mathrm{evap}} = 3 \times 10^2 - 10^3$ yr, with the spread caused by the range of possible initial CPD outer radii. Our results thus appear to be largely consistent for CPDs of similar surface temperatures.

2.4.3 Implications of photoevaporative truncation

In the case $\dot{M} \leq 10^{-12} M_{\odot}$ yr^{-1} , we find that photoevaporative truncation provides a natural explanation for the lack of massive satellites outside the orbit of Callisto. The truncation of the CPD would cause the satellite systems of ∼ 50% Jupiter-mass planets forming in star clusters of N ∼ 2500 to be limited in size to 0.04-0.06 R_{H}. The outermost extent of these Galilean analog systems would follow the truncation distribution of the low-accretion case in Fig. 2.7.

Circumplanetary disk truncation could also act to bias our interpretation of unresolved continuum point-sources suspected to be CPDs. In the optically thin case, fluxes are used to infer CPD mass independent of the physical dimensions of the CPD, while in the optically thick case, the inferred radius of the CPD is proportional to the flux F_{ν} and dust temperature T_{d} by $r_{\mathrm{CPD}}^2 \propto F_{\nu} B_{\nu}(T_{\mathrm{d}})^{-1}$ (Pineda et al., 2019). Our results show that for low accretion rates, CPD outer radii may be as small as 0.04 r_{H} rather than 0.3-0.5 r_{H} (Quillen and Trilling, 1998; Martin and Lubow, 2011; Ayliffe and Bate, 2009; Shabram and Boley, 2013). The dust temperature of a CPD observed at a given flux might then be overestimated by a factor 3-5, with direct implications for the inferred luminosity of the planet.

We also placed limits on the strength of the intracluster radiation field G_0 during the formation time of the Galilean satellites for certain rates of mass accretion. If the Galilean satellites formed late during a period of slow accretion ($\dot{M} \leq 10^{-12} M_{\odot}$ yr^{-1}), we placed upper limits on the FUV field strength $G_0 \leq 10^{3.1}$ that would still allow the satellites to form at their present-day locations due to the correspondingly small CPD truncation radius. The semi-major axis of the Saturn moon Titan would need to be explained in this context as either forming at a later stage in an epoch of lower G_0 or forming much closer in to Saturn initially and migrating outward as a result of tidal dissipation. A close-in formation scenario for Titan has been proposed based on the spreading of tidal disks (Crida and Charnoz, 2012), and high tidal recession has been observed in the Saturnian system, possibly necessitating a close-in formation scenario (Remus et al., 2012; Lainey et al., 2017; Gomez Casajus et al., 2019). With our model applied to a Saturn-mass planet, we find that the inner mean truncation radius corresponding to $\dot{M} = 10^{-12} M_{\odot}$ yr^{-1} shrinks to ∼ 8.3 R_{S}. If Titan formed within this radius, it would necessitate a migration of at least 12.7 R_{S} to approach its current position. With the resonant-locking mechanism, Fuller et al. (2016) suggested a tidal migration timescale defined as $a/\dot{a}$ for Titan of ∼2 Gyr. If we were to naively assume a fixed tidal migration timescale this might suggest a change in semi-major axis of $\delta a_{\mathrm{Titan}} \approx 13.5$ R_{S} over 4.5 Gyr for a final $a_{\mathrm{Titan}} \sim 19.5$ R_{S} for an initial $a_{\mathrm{Titan}} = 6$ R_{S} . This is near

the current semi-major axis of 20.27 R_S. We thus find that the photoevaporative truncation of the Saturn CPD is consistent with a close-in formation scenario for Titan and its subsequent outward migration.

2.4.4 Photoevaporative stranding of Callisto

Rapid clearing of the gas in CPDs could function to prevent the inward migration of satellites already present in the CPD. The inward migration of resonant chains of planets has been suggested as a mechanism to explain compact resonant exoplanet systems such as TRAPPIST-1 (Ormel et al., 2017a; Izidoro et al., 2017; Tamayo et al., 2017). It appears to be a general outcome of planet formation models around low-mass stars that super-Earths migrate inward and form compact systems of resonant chains (Terquem and Papaloizou, 2007; Raymond et al., 2008; McNeil and Nelson, 2010; Liu et al., 2015), although in situ formation is possible (MacDonald and Dawson, 2018).

Callisto is noteworthy in that it does not lie within the Laplace resonance of the inner three Galileans. Previous mechanisms proposed to explain why Callisto is excluded from the resonance have included its insufficiently rapid inward orbital migration (Peale and Lee, 2002; Canup and Ward, 2002), perturbation out of an initial resonance by dynamical encounters between Jupiter and other planets (Deienno et al., 2014), or scattering by close encounters with Ganymede (Shibaike et al., 2019). While the satellites may also have evolved away from their initial positions by secular processes into their current positions (Yoder, 1979; Fuller et al., 2016; Lari et al., 2019), a primordial formation of the current configuration by differential orbital migration and tidal dissipation is also possible (Peale and Lee, 2002).

The observed paucity of intact compact resonant chains in exoplanetary systems suggests that these systems undergo an instability to break the resonant configurations (Goldreich and Schlichting, 2014; Izidoro et al., 2017). The instabilities may be caused by the dissipation of the gas disk in which the planets migrated (Ogihara and Ida, 2009; Cossou et al., 2014). The Galilean Laplace resonance would need to have remained stable during the CPD gas-disk dispersal phase. Resonant chains with the lowest number of planets in the chain and lowest planet masses are the most stable (Izidoro et al., 2019; Matsumoto et al., 2012).

When we assume that the inner Galilean satellites migrated primordially into the 4:2:1 mean motion resonance by gas-driven inward migration and retained the Laplace resonance during dispersal of the gas, the question arises whether a rapid photoevaporative truncation of the CPD might have stranded Callisto by preventing further migration to complete the chain, even for a high-mass CPD. We first investigated the relative timescales of the photoevaporative disk clearing and of the orbital migration. We considered the case of the Laplace resonance being primordial (coeval with the formation of the satellites themselves), and that the resonance survived the dispersal of the gas disk. Additionally, we focused in detail on the case of an abruptly terminated mass inflow rather than a slow tailing-off of the mass accretion rate.

Type I migration is most efficient when the gas disk density is high at small orbital

radii and short orbital periods. In planet formation models, efficient type I migration causes 'fast' migration, which can result in scattering and collisions that leave between four to six planets in mean motion resonances both before and after the gas disk dissipates (Ogihara and Ida, 2009). Superficially, this scenario corresponds to the final configuration of the Galilean satellites. Slower migration results in very efficient resonant capture and the formation of long chains that are broken only when the gas disk dissipates and the effects of eccentricity damping from tidal interaction become negligible (Ogihara and Ida, 2009). We considered that owing to the compact nature of the CPD and the very high ($> 10^5$ g cm^{-2}) surface densities, type I migration may be highly efficient in the Jovian CPD, such that the fast migration scenario is more likely. If MRI-induced turbulence in the disk is limited to the CPD upper layers, the protosatellites may have orbited within a dead-zone dominated by laminar flow. In this case, the type I migration timescale of a satellite is described by the ratio of the orbital angular momentum J_s and the total disk-exerted torque Γ_{tot} of the object. To semi-analytically determine the satellite migration timescales, we adopted the relations of Kley and Nelson (2012), where the migration timescale τ_{mig} is

$$\tau_{mig} = \frac{1}{2}\frac{J_s}{\Gamma_{tot}}, \tag{24}$$

with the orbital angular momentum defined as

$$J_s = m_s \sqrt{G M_* a_s}\,. \tag{25}$$

Here m_s and a_s are the satellite mass and semi-major axis. The total torque is then

$$\Gamma_{tot} = -(1.36 + 0.6\beta_\Sigma + 0.43\beta_T)\Gamma_0\,, \tag{26}$$

where β_T and β_Σ are the power-law exponents of the temperature and surface density profiles, respectively, and the torque normalization is

$$\Gamma_0 = \frac{m_s^2}{M_p}\frac{H}{r_s}^{-2}\Sigma_s r_s^4 \Omega_s^2\,. \tag{27}$$

Here M_p is the planet mass, r_s and Ω_s are the satellite orbital radius and orbital angular frequency, H/r is the ratio between the disk scale height at some radius r and r, and Σ_s is the surface density at the orbital radius of the satellite. We extracted the calculated temperature profile and the parameterized surface density and scale height profiles from our ProDiMo models to calculate migration timescales for all radii and arbitrary satellite masses. We then compared the possible migration paths of Callisto with the disk-clearing timescales determined from our photoevaporation model.

For the initial conditions, we sampled from a range of semi-major axes for Callisto and a CPD outer edge from 26-500 R_J. We then calculated the inward motion of Callisto through the type I migration rate with the Σ and β_T parameters extracted from our ProDiMo photoevaporation CPD model output. β_Σ and $H(r)$ are parameterized inputs. We neglected gravitational interaction between satellites, nongravitational effects

such as aerodynamic drag, and the possibility of type II migration. The rate of photoevaporative shrinking of the CPD was calculated from our truncation model, where we exponentially decayed the mass accretion rate on a short 10^3 yr timescale and allowed photoevaporation to evolve the CPD away from its steady-state surface density profile. We traced both the position of Callisto and the CPD outer radius simultaneously as a function of time. We determined whether the outer edge of the CPD moves inward past Callisto as it migrated (in which case it is stranded), or whether it would be able to migrate into the resonant chain.

It is evident that for a migrating Callisto to be stranded by a rapidly dispersing disk, its migration timescale $\tau_{\rm mig}$ at some radius r must be longer than the disk-clearing timescale $\tau_{\rm evap}$ at that radius. While the type I migration accelerates as Callisto moves into the denser regions of the CPD and increases its orbital frequency, photoevaporation slows as the gas at the shrinking outer radius becomes more gravitationally bound. This means that for each CPD model, a critical radius exists inside of which Callisto can no longer be stranded by photoevaporation. We first considered the mass of proto-Callisto as a free parameter. A CPD of mass $10^{-5} M_\odot$ results in a type I migration timescale so rapid that even a low-mass proto-Callisto ($M_{\rm JIV} = 0.01\ M_{\rm final}$) cannot be caught by disk photoevaporation at its present-day location. In the case of the $10^{-6} M_\odot$ CPD, we find that the proto-Callisto could only have accreted $< 10\%$ of its final mass in order to be caught by photoevaporative disk dispersal, but is highly unlikely to be placed at 26 $R_{\rm J}$ for any considered initial conditions. This scenario would require Callisto to accrete $> 90\%$ of its mass after the dispersal of the gas-disk. We consider this scenario not plausible.

When we instead consider a scenario in which Callisto has acquired a minimum of 90% of its final mass prior to the CPD dissipating, we can constrain the CPD masses that allow for Callisto to be deposed at its current orbital location. The final position of Callisto as a function of its initial position and CPD outer radius for the cases $M_{\rm CPD} = 10^{-6.3} - 10^{-6.6} M_\odot$ is plotted in Fig. 2.11. We find that Callisto can be left stranded at its current position for $M_{\rm CPD} < 10^{-6.2} M_\odot$. Above this mass limit, Callisto migrates inward too rapidly and cannot be stranded. The CPD mass that produces the largest region in the initial condition parameter space to reproduce the exact current position of Callisto is $M_{\rm CPD} = 10^{-6.6} M_\odot$ (Fig. 2.11 lower right panel). In this case, Callisto is required to have achieved 90% of its final mass between 26.5 and 30.8 $R_{\rm J}$ and could have migrated at most ~5 $R_{\rm J}$ inward. For CPDs with mass below $10^{-7} M_\odot$ CPD, the photoevaporation timescale is much shorter than the migration timescale, such that Callisto must have achieved its final mass very near its present-day location.

It is possible to push the initial position of Callisto out to 40 $R_{\rm J}$ for a CPD with mass $10^{-6.2} M_\odot$. However, the resulting combination of the initial position of Callisto and the outer radius of the CPD that places Callisto near 26 $R_{\rm J}$ becomes highly constrained (less than 0.1% of the uniformly sampled initial condition space) and it is far more likely to enter the resonance. Figure 2.11 illustrates that Callisto can be placed at its current position for any possible CPD initial outer radius within the considered range, while the range of initial Callisto positions is more tightly constrained. Thus far, we have only

considered the case of an abrupt exponential decline in mass accretion over $\sim 10^3$ yr. Scenarios wherein the CPD steadily declines in both mass and steady-state truncation radius as accretion slows over several $10^4 - 10^5$ years allow for Callisto to have grown to its final mass at larger separations and still been captured at 26 R_J, but the steady-state truncation radius for 99% of our CPDs with $\dot{M} < 10^{-12} M_\odot$ yr^{-1} is smaller than 215 R_J, and in 50% of cases it is smaller than 35 R_J, placing an upper boundary on the initial position of Callisto. We therefore consider it unlikely that Callisto formed farther out than 40 R_J.

The undifferentiated internal structure of Callisto sets a constraint on its accretion timescale of $> 10^5$ yr (Anderson et al., 1997; Anderson et al., 2001; Mosqueira and Estrada, 2003a,b). We note that the minimum accretion rate we considered is able to supply enough mass to the CPD to build Callisto within 5×10^4 years in the case of perfect accretion efficiency. Depending on the background FUV field strength, we find that a CPD with an accretion rate $\dot{M} = 5 \times 10^{-13} M_\odot$ yr^{-1} (slow enough to form Callisto without melting it) is likely to have a truncation radius within the present-day orbit of Callisto for $G_0 = 3000$. The photoevaporative stranding of Callisto can still be consistent with its internal structure for FUV field strengths of $G_0 \lessapprox 10^{3.1}$.

2.5 Conclusions

We have investigated the radiation field to which the CPD of Jupiter may have been exposed during the formation of the Galilean satellites. Our key findings can be summarized as follows:

1. Jupiter analogs open gaps that are sufficiently deep to expose their CPDs to interstellar FUV radiation for PPD α-viscosities of $10^{-5} - 10^{-3}$. The radiation field of a solar birth cluster analog is sufficient to photoevaporatively truncate a Jovian CPD independent of the steady-state mass of this CPD.

2. For accretion rates $\dot{M} = 10^{-12} M_\odot$ yr^{-1} , a Jovian CPD can become truncated to within the current orbit of Callisto ($\sim 0.04\ r_H$) for 50% of the cluster stars, explaining the lack of regular satellites beyond the orbit of Callisto. The mean truncation radius found in our ensemble of cluster stars is proportional to the CPD accretion rate by $r_{trunc} \propto \dot{M}^{0.4}$.

3. We find that rapid external photoevaporation of the Jovian CPD following the end of accretion can act to stop the inward gas-driven migration of Callisto and prevent it from piling up into the mean-motion resonance of the inner three Galilean satellites. The mass of the CPD in this scenario would be constrained to $\leq 10^{-6.2} M_\odot$, and Callisto must have achieved at least 90% of its final mass at a semi-major axis between 27-40 R_J.

4. We place an upper limit on the strength of the background FUV radiation field $G_0 \leq 10^{3.1}$ during the formation stage of Callisto.

Acknowledgements

The research of N.O., I.K., and Ch.R. is supported by grants from the Netherlands Organization for Scientific Research (NWO, grant number 614.001.552) and the Netherlands Research School for Astronomy (NOVA). This research has made use of NASA's Astrophysics Data System Bibliographic Services. This research made use of Astropy,[3] a community-developed core Python package for Astronomy (Astropy Collaboration et al., 2013; Price-Whelan et al., 2018). The authors would like to thank J. Tjoa, S. Van Mierlo, M. Rovira Navarro, T. Steinke, and J. Szulagyi for their insightful advice and helpful discussion. The authors would also like to thank the anonymous referee for the suggestions and corrections that contributed to improving and clarifying this work.

Appendix

A.1 Disk model temperature and density

[3] http://www.astropy.org

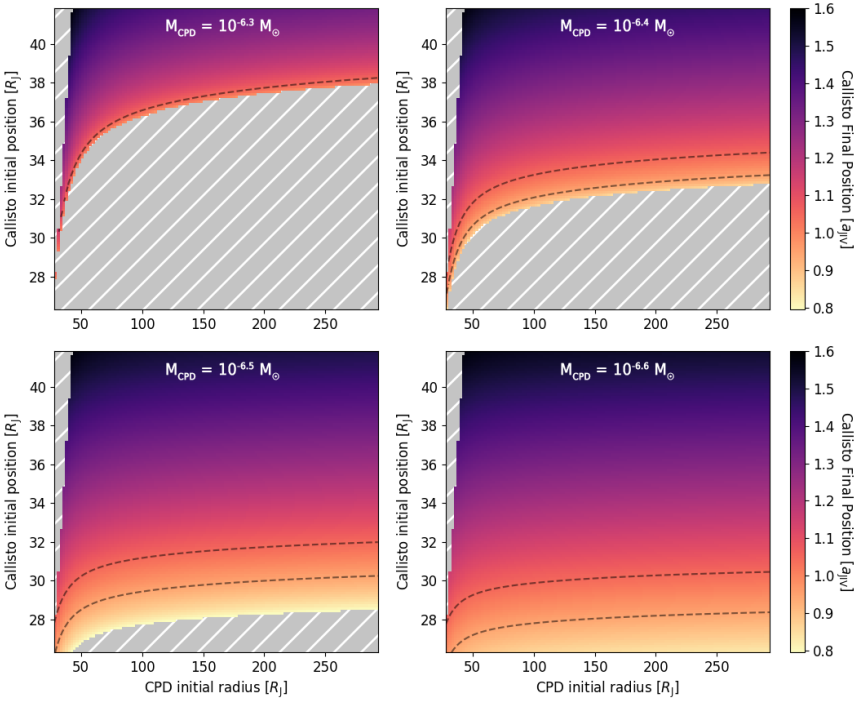

Figure 2.11: Final semi-major axis of Callisto a_{final} in our migration and photoevaporation model for the case of $M_{\text{CPD}} = 10^{-6.3}$ (top left), $10^{-6.4}$ (top right), $10^{-6.5}$ (bottom left), and $10^{-6.6} M_{\odot}$ (bottom right). The initial radius of the CPD is on the ordinate, and initial location of Callisto is on the abscissa. The region of excluded parameter space where Callisto already lies beyond the outer edge of the CPD and where Callisto enters the resonance is filled with gray stripes. The dotted black lines demarcate the interval where the final position of Callisto falls within 5% of its present-day position, $a_{\text{final}} = a_{\text{JIV}}$.

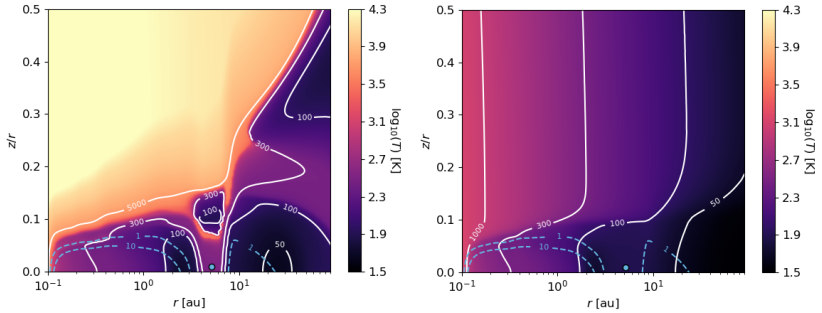

(a) Gas temperature of the solar protoplanetary disk.

(b) Dust temperature of the solar protoplanetary disk.

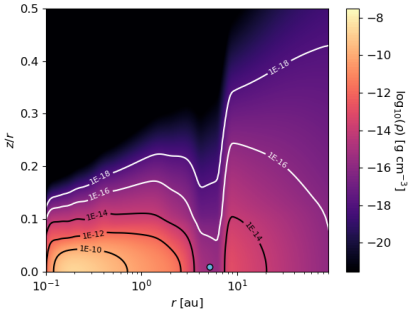

(c) Gas density of the solar protoplanetary disk.

Figure 2.12: Temperature and density structure of the solar PPD ProDiMo model for $t = 5$ Myr, $\alpha = 10^{-4}$. The dashed blue lines trace surfaces with a visual extinction $A_V = 1, 10$, defined by the minimum of either the vertical or radial extinction at a given point. The blue dot indicates the radial location of Jupiter.

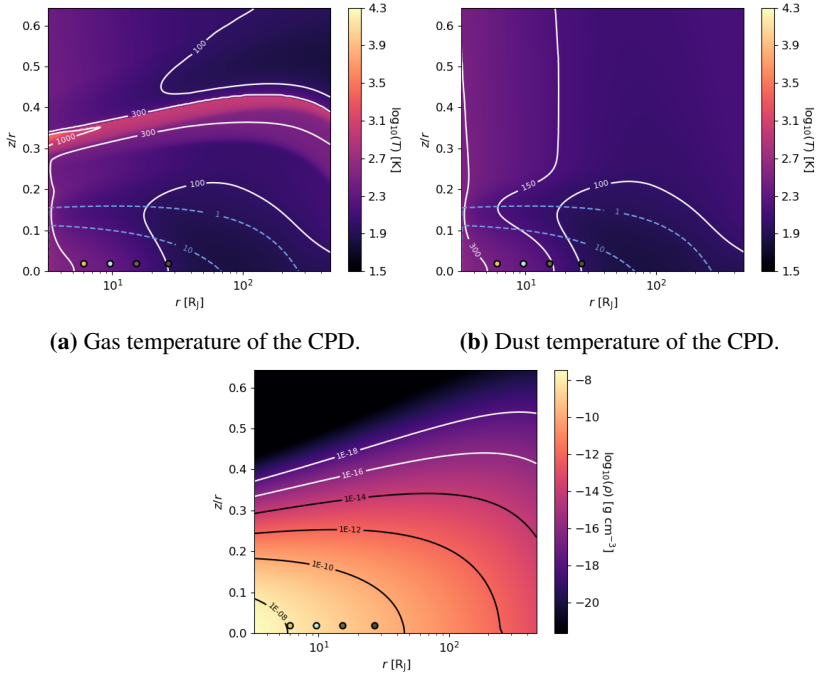

(a) Gas temperature of the CPD.

(b) Dust temperature of the CPD.

(c) Gas density of the CPD.

Figure 2.13: Temperature and density structures of the Jovian CPD ProDiMo model of $M = 10^{-8}\ M_\odot$ and $\dot{M} = 10^{-11}\ M_\odot\ \mathrm{yr}^{-1}$. The dashed blue lines trace surfaces with a visual extinction $A_V = 1$ and 10, defined as the minimum of either the vertical or radial extinction at a given point. The scatter points indicate the radial location of the Galilean satellites (from left to right: Io, Europa, Ganymede, and Callisto).

Chapter 3

Circumplanetary disk ices

I. Ice formation vs. viscous evolution and grain drift

N. Oberg, I. Kamp, S. Cazaux, P. Woitke & W.F. Thi

Abstract

Context: The large icy moons of Jupiter formed in a circumplanetary disk (CPD). CPDs are fed by vertically infalling circumstellar gas and dust which may be shock-heated upon accretion. Accreted material is then either incorporated into moons, falls into the planet, or is lost beyond the disk edge on relatively short timescales. If ices are sublimated during accretion onto the CPD we know there must be sufficient time for them to recondense or moons such as Ganymede or Callisto could not form. The chemical timescale to form sufficiently icy solids places a novel constraint on the dynamical behaviour and properties of CPDs.
Aims: We aim to explore the process of ice formation in CPDs to constrain which disk properties (such as the mass, viscosity, and dust-to-gas ratio) are consistent with the formation of an icy moon system.
Methods: We use the radiation thermochemical code ProDiMo (Protoplanetary Disk Model) to analyze how the radial ice abundance evolves in CPDs. We consider different initial chemical conditions of the disk to explore the consequences of infalling material being inherited from the circumstellar disk or being reset to atomic conditions by shock-heating. We contrast the timescales of ice formation with disk viscous timescales and radial dust drift.
Results: We have derived the radial ice abundance and rate of ice formation in a small grid of model CPDs. Water ice can form very efficiently in the CPD from initially atomic conditions, as a significant fraction is efficiently re-deposited on dust grains within < 1 yr. Radial grain drift timescales are in general longer than those of ice formation on grains. Icy grains of size $a < 3$ mm retain their icy mantles while crossing an optically thin circumstellar disk gap at 5 au for $L_* < 10$ $L_\odot$.
Conclusions: Three-body reactions play an important role in water formation in the dense midplane condition of CPDs. The CPD midplane must be depleted in dust relative to the circumstellar disk by a factor 10-50 to produce solids with the ice to rock ratio of the icy Galilean satellites. The CPD snowline is not erased by radial grain drift, which is consistent with the compositional gradient of the Galilean satellites being primordial.

N.Oberg et al. 2022 *Circumplanetary Disk Ices I. Ice formation vs. viscous evolution and grain drift* , A&A 667, A95

3.1 Introduction

A general feature of regular satellite formation theory is that the circumplanetary disk (CPD) consists of circumstellar material accreted from within the vicinity of the planet (Lubow et al., 1999; Canup and Ward, 2002; Alibert et al., 2005; Shibaike et al., 2019; Ronnet and Johansen, 2020). If the planet is massive enough to open a gap in the circumstellar disk, material continues to flow into the gap (Kley, 1999; Teague et al., 2019) and falls nearly vertically onto the CPD (Tanigawa et al., 2012; Morbidelli et al., 2014). The CPD achieves a steady-state mass when this inflow is balanced by outflow where gas either spirals into the planet or is decreted beyond the Hill sphere (Canup and Ward, 2002; Batygin and Morbidelli, 2020). Independently of disk viscosity, stellar tides induce spiral waves in the CPD which transport angular momentum and promote accretion onto the planet at a rate on the order 10^{-7} M_J yr^{-1} (Rivier et al., 2012), suggesting that for a CPD of mass $\sim$ 10^{-4} M_J (D'Angelo et al., 2002; Gressel et al., 2013; Szulágyi et al., 2014) infalling gas spends only a limited time inside the CPD before being lost (Canup and Ward, 2002).

The timescale of radial dust drift in small disks is also predicted to be short (Pinilla et al., 2013; Shibaike et al., 2017; Rab et al., 2019). A CPD could lose mm-size grains within 10^2-10^3 yr to aerodynamic drag against highly sub-Keplerian gas due to a very steep radial pressure gradient (Zhu et al., 2018). The CPD is thus a very dynamical system, potentially with both inwards and outwards radial transport of both gas and dust on very short timescales.

The amount of time which gas and dust spend within the CPD becomes highly relevant if a chemical "reset" occurs. The infalling circumstellar material may pass through one or more accretion shocks (Lubow et al., 1999; Tanigawa et al., 2012; Zhu, 2015; Szulágyi et al., 2016; Schulik et al., 2020) and can be heated $\geq$ 1000 K during accretion onto the CPD (Szulágyi, 2017; Szulágyi and Mordasini, 2017; Aoyama et al., 2018). For pre-shock velocities in excess of 90 km s^{-1} the shock can be sufficiently hot to leave most of the infalling gas atomic or ionized (Aoyama et al., 2018). The shock may also desorb the icy mantles of grains via sputtering and thermal desorption, which for pre-shock velocities in excess of 8-10 km s^{-1} can effectively strip a grain of H_2O ice (Woitke et al., 1993; Aota et al., 2015; Tielens, 2021). Small icy grains passing through the gap may also lose their volatile contents to photodesorption prior to shock-heating (Turner et al., 2012). We refer to a "reset" scenario if shock-heating or photodesorption effectively destroys molecules in the accretion flow to the CPD. In a reset scenario, the re-formation of ices in the CPD must compete with viscous accretion and decretion of gas and radial drift of dust. Alternatively, if circumstellar disk ices survive incorporation into the CPD, we refer to an "inheritance" scenario.

The Galilean satellites characteristically exhibit a radial compositional gradient of decreasing density with increasing distance from Jupiter. The inner moon Io is ice-free, while Europa has an ice mass fraction of $\sim$ 6-9% (Schubert et al., 2004; Kuskov and Kronrod, 2005) and Ganymede and Callisto have ice mass fractions of 40-55% (McKinnon, 1997; Schubert et al., 2004; Sohl et al., 2002). Theoretically it appears challeng-

ing to reproduce the compositional gradient by tidal heating (Bierson and Steinbrügge, 2021) or impact-driven escape of volatiles (Dwyer et al., 2013). Previously it has been proposed that the gradient was imprinted during the formation of the moons by a radial temperature gradient in the CPD (Lunine and Stevenson, 1982), but the relevant chemical timescales have rarely been taken into account (Mousis and Alibert, 2006). It is an open question whether the gradient can be produced primordially if the chemistry of infalling gas and dust is reset. By analyzing the composition and abundance of ices that are able to form within the relevant timescales we can place a lower bound on how efficiently angular momentum is transported within the CPD.

In this work we investigated the balance of the competing timescales of ice formation, dust grain drift, and gas viscous flow to seek constraints on properties of the CPD such as viscosity, ice mass fraction, and dust-to-gas ratio. We considered the two opposing extreme cases of full chemical inheritance and reset in chemically evolving disk models utilizing a rate-based modeling approach. In Sect. 3.2 we describe our modeling set-up and the assumptions that we make. In Sect. 3.3 we analyze the CPD time-dependent ice abundances for both the reset and inheritance cases, and place novel constraints on the properties of CPDs. In Sect. 3.4 we discuss the implications of the these constraints and place them in the context of solar system formation. We consider also the role that radial grain drift has in competing with ice adsorption and desorption. In Sect. 3.5 we summarize our key findings.

3.2 Methods

We considered two opposing scenarios; one in which the molecular gas-phase and ice chemistry of the circumstellar disk is preserved during accretion onto the CPD (inherit) and one in which it is lost (reset). In the former case the CPD is initially populated with gas and ices extracted from the circumstellar disk. In the latter case the disk is initially populated by a fully atomic gas and dust is free of ice. We followed the build-up of ices in the CPD over time in a thermochemical disk model (see Sect. 3.2.1) and extracted the molecular ice abundance and composition as a function of time.

The net inflow and outflow rate of gas and solids from and to the CPD is assumed to be zero and the disk mass in steady-state. The rate of gas outflow then sets an upper limit on the applicable chemical evolutionary timescales. Hereafter we refer to this as the viscous timescale, defined as

$$t_{\rm visc} = \frac{M_{\rm CPD}}{\dot{M}}, \tag{28}$$

where $M_{\rm CPD}$ is the mass of the CPD and $\dot{M}$ is the infall rate of circumstellar material onto the CPD. The relatively short $t_{\rm visc}$ considered in this work (see Sect. 3.2.2) may cause reactions with high activation energies to be kinetically inhibited, although it has been noted that the relatively high densities characteristic of CPDs may allow these reactions to proceed to equilibrium (de Pater and Lissauer, 2010). Nevertheless we contrast the time-dependent results with the assumption of steady-state chemistry. In

steady-state chemistry the disk is allowed to evolve for an indefinite time period until the rate of formation for every gas and ice species is balanced by the corresponding rate of destruction.

3.2.1 Disk modeling code

We used the radiation thermochemical disk modeling code ProDiMo [4] (**Pro**toplanetary **Di**sk **Mo**del) (Woitke et al., 2009, 2016; Kamp et al., 2010b, 2017; Thi et al., 2011, 2020a,a) to explore the formation rates and resulting abundances of various ices in CPDs. ProDiMo uses a rate equation based approach to compute the gas chemistry using either a time-dependent or steady-state solver. The model represents a 2D slice through an axisymmetric disk, extending radially in distance from the planet r and vertically in distance from the disk midplane z. Our chemical network contains 13 elements and 235 atomic and molecular species. Where not explicitly specified we used the "large DIANA chemical standard" network as described in Kamp et al. (2017). Reaction rates are mainly selected from the UMIST2012 database (McElroy et al., 2013). Important three-body collider reactions are adopted from the UMIST2006 rate file (Woodall et al., 2007). Gas-phase reactions within the CPD produce molecular species which can then freeze-out on grain surfaces. The rate of ice formation is determined by the available grain surface area, dust temperature, and the rates of thermal, photo-, and cosmic-ray desorption (see Sect. 3.2.1 for a detailed description of ice formation).

We made the simplifying assumption that the chemical composition of the infalling material is distributed instantaneously and homogeneously throughout the disk (see appendix A.5 for a discussion of the potential impact of the rate of vertical gas mixing). We assumed that the CPD inherits micrometer to mm-sized dust grains directly from the circumstellar disk. The vertical dust stratification is calculated according to the method of Dubrulle et al. (1995) and kept fixed prior to the calculation of chemical evolution. The timescales of radial dust drift are calculated in a post-processing step described in 3.2.3. The temperature and radiation structure of the CPD is solved in steady-state and then kept fixed during chemical evolution of inherited or reset infalling material.

In Sect. 3.3.2 we considered the implications of including grain-surface chemistry reactions. With surface chemistry ProDiMo models explicitly the formation of H_2 in the CPD for which the inclusion of additional chemical species such as hydrogenated PAH is necessitated (Thi et al., 2020b,a). The selection of the additional species and reactions in the surface chemistry network and their role in the eventual composition of the ices will be discussed in an accompanying work focused on the composition of the ices (Oberg et al. in prep.).

Ice formation

Where conditions in the disk are appropriate, ices can condense onto the grains in

[4] https://www.astro.rug.nl/ prodimo/

successive layers by physical van der Waals bonding (physisorption). The adsorption rate of species i onto a physisorption sites is

$$R_i^{\rm ads} = 4\pi a^2 v_i^{\rm th} n_{\rm d} S_i \ {\rm s}^{-1}, \tag{29}$$

where $4\pi a^2$ is a dust grain surface area, a is the grain radius, $v_i^{\rm th}$ is the thermal speed $(k_{\rm B}T_{\rm g}/2\pi m_i)^{1/2}$, $k_{\rm B}$ is the Boltzmann constant, $T_{\rm g}$ is the gas temperature, m_i is the mass of the gas-phase species, $n_{\rm d}$ is the dust number density, and S_i is the sticking coefficient. The ice adsorption rate coefficients are then

$$\frac{dn_{\#,i}}{dt} = R_i^{\rm ads} n_i \ {\rm cm}^{-3}{\rm s}^{-1}, \tag{30}$$

where n_i is the number density of the gas-phase species.

Physisorbed species can desorb thermally, photodesorb, or desorb after a cosmic ray impact deposits energy in the grain. For physisorption there is no desorption barrier and the desorption energy is equal to the binding energy $E_i^{\rm b}$. The Arrhenius formulation for the rate of thermal desorption is then

$$R_i^{\rm des,th} = \nu_{0,i} e^{-E_i^{\rm b}/k_B T_{\rm d}} \ {\rm in \ s}^{-1}, \tag{31}$$

where the pre-exponential (frequency) factor $\nu_{0,\rm i}$ is

$$\nu_{0,i} = \sqrt{\frac{2N_{\rm surf}E_i^{\rm b}}{\pi^2 m_i}}. \tag{32}$$

$N_{\rm surf}$ is the density of surface binding sites $1.5{\times}10^{15}$ cm^{-2} (Hasegawa et al., 1992), and $T_{\rm d}$ is the dust temperature. Adsorption energies of major volatile species are listed in Appendix A.2.

The photodesorption rate is computed using the UV field strength calculated by the radiative transfer and photodissociation cross-sections. The photodesorption rate for species i is

$$R_i^{\rm des,ph} = \pi a^2 \frac{n_{\rm d}}{n_i^{\rm act}} Y_i \chi F_{\rm Draine} \ {\rm s}^{-1}, \tag{33}$$

where Y_i is the photodesorption yield, $n_i^{\rm act}$ is the concentration of the species in the active layers,

$$\begin{aligned} n_i^{\rm act} &= n_i && \text{if } n_{\#,\,\rm tot} \leqslant 4\pi N_{\rm surf} a^2 n_{\rm d} \\ &= n_i \left(N_{\rm act} / N_{\rm layer} \right) && \text{if } n_{\#,\,\rm tot} > 4\pi N_{\rm surf} a^2 n_{\rm d}. \end{aligned} \tag{34}$$

The number of physisorbed layers $N_{\rm layer} = n_{\#,\,\rm tot}/(4\pi N_{\rm surf} a^2 n_{\rm d})$ and $n_{\#,\,\rm tot} = \sum_i n_{\#,i}$ is the total number of the physisorbed species, $4\pi N_{\rm surf} a^2$ is the number of binding sites per layer, and $N_{\rm act}$ is the number of chemically active layers. $\chi F_{\rm Draine}$ is a measure of the local UV energy density from the 2D continuum radiative transfer (Woitke et al., 2009).

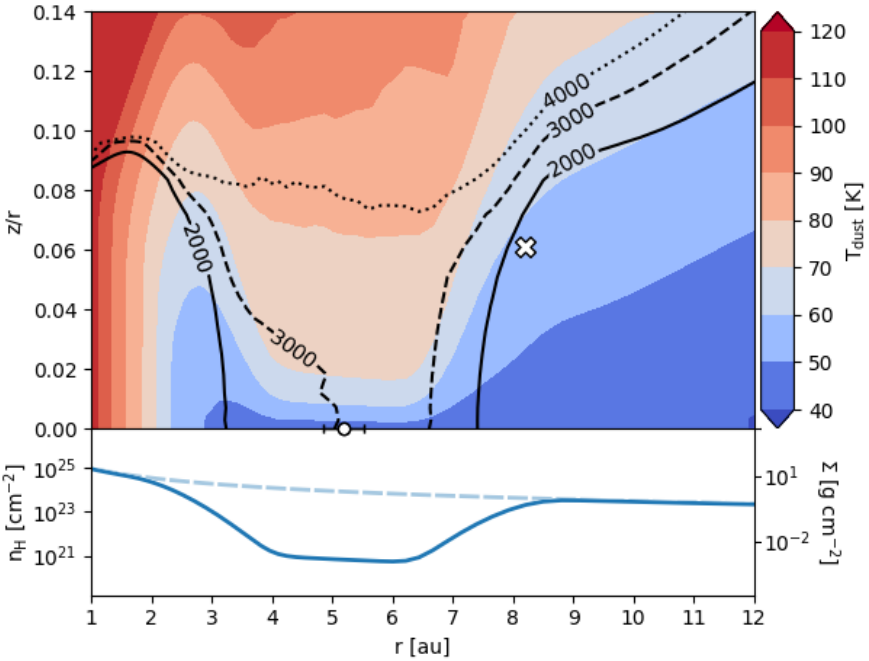

Figure 3.1: 2D dust temperature distribution around the circumstellar disk gap in the range 40-120 K (*top*). Solid, dashed, and dotted black contours indicate the relative UV field strength χ (see Eq.11). The white circle with black border represents the position of Jupiter and the horizontal bar indicates the physical extent of the CPD. The white cross with black border represents the location from which the inherited chemistry is extracted at one scale height $z = H$. Hydrogen nuclei column density (blue line) with unperturbed circumstellar disk density profile for comparison (light blue dashed line) (*bottom*).

The rate of cosmic-ray induced desorption $R_i^{\mathrm{des,CR}}$ is calculated according to the method of Hasegawa and Herbst (1993). The total desorption rate R_i^{des} is the sum of the thermal, photo- and cosmic ray induced desorption rates $R_i^{\mathrm{des,th}}+R_i^{\mathrm{des,ph}}+R_i^{\mathrm{des,CR}}$. The desorption rate of the physisorbed species i is then

$$\frac{dn_i}{dt} = R_i^{\mathrm{des}} n_i^{\mathrm{act}}\ \mathrm{cm^{-3}s^{-1}}, \tag{35}$$

3.2.2 Properties of the Disk Models

The Circumstellar Disk

Table 4: Parameters for the solar circumstellar disk.

Parameter	Symbol	Value	Unit
Stellar Mass	M_*	1.0	$M_\odot$
Stellar Luminosity	L_*	0.84	$L_\odot$
Effective Temperature	$T_{\rm eff}$	4395	K
UV Luminosity	$L_{\rm UV,*}$	0.01	$L_\odot$
X-ray Luminosity	$L_{\rm X}$	10^{30}	erg s^{-1}
Disk Mass	$M_{\rm disk}$	0.001	$M_\odot$
Disk Inner Radius	$R_{\rm in}$	0.1	au
Disk Outer Radius	$R_{\rm out}$	100	au
Column Density Power Ind.	ϵ	1.5	-
Reference Scale Height	$H_{10\rm au}$	1	au
Flaring Index	β	1.15	-
Minimum dust size	$a_{\rm min}$	0.05	µm
Maximum dust size	$a_{\rm max}$	3000	µm
Dust size power law index	$a_{\rm pow}$	3.5	-
Dust-to-Gas ratio	d/g	10^{-2}	-
Dust composition:			
$Mg_{0.7}Fe_{0.3}SiO_3$		60%	
Amorphous carbon		15%	
Vacuum		25%	

Note: Stellar temperature and luminosity are selected from the pre-main sequence stellar evolutionary tracks of Siess et al. (2000) for $t = 4$ Myr. Stellar UV and X-ray luminosities for a representative Class II T Tauri star are adopted from Woitke et al. (2016).

To generate the chemical abundances for our “inheritance" scenario we considered the properties of the surrounding circumstellar disk from which material is accreted onto the CPD. We used a two-step approach to model the chemistry in our circumstellar disk. As a first step, the initial conditions are derived from a zero-dimensional “molecular cloud" model, the parameters of which are listed in Table 9. This stage represents 1.7×10^5 yr (the estimated lifetime of the Taurus Molecular Cloud TMC-1) of chemical evolution in a pre-collapse molecular cloud state (McElroy et al., 2013). The resulting chemical abundances of the majority of the most common species agree within a factor 10 with the observed abundances in TMC-1(see Fig. 3.16). These abundances are then used as initial conditions for the 2D grid of cells in the circumstellar disk model in the second step.

In the second step the circumstellar disk model is evolved for an additional 4 Myr to be consistent with the formation timeline of Jupiter proposed to account for the distinct isotopic population of meteorites found in the solar system wherein Jupiter undergoes runaway accretion >3.46 Myr after the formation of calcium-aluminium rich refractory inclusions (Kruijer et al., 2017; Weiss and Bottke, 2021). The surface density power law and physical extent of the circumstellar disk is based on a modified “Minimum Mass Solar Nebula" (MMSN) (Hayashi, 1981). A parameteric gap has been introduced which reduces the dust and gas density at 5.2 au centered on the location of Jupiter. The gap dimensions are parameterized by an analytical gap scaling relation derived from hydrodynamical simulations and are consistent with a circumstellar disk viscosity of $\alpha \sim 10^{-4}$ and disk age of 4 Myr (Kanagawa et al., 2016). A detailed description of the circumstellar disk model and gap structure methodology can be found in Oberg et al. (2020). The relevant circumstellar disk model parameters can be found in Table 4. The dust temperature, surface density profile, and UV field strength in and around the circumstellar disk gap can be seen in Fig. 3.1.

Finally we extract the chemical abundances from the circumstellar disk model at the outer edge of the gap at a radius of 8.2 au. The gap edge is defined as the radius at which the perturbed surface density profile reaches 50% of the unperturbed profile. As material flows into the gap from above one pressure scale height (Morbidelli et al., 2014), we extract our initial conditions for the CPD model at $z = H$ ($z = 0.5$ au at $r = 8.2$ au). The ambient conditions at this point are listed in Table 5. The extracted abundances are then used as the initial chemical composition for our “inheritance" scenario CPD.

Throughout this work we quantify the iciness of solids with the ice mass fraction,

$$f_{\rm ice} = \frac{m_{\rm ice}}{m_{\rm rock} + m_{\rm ice}}, \tag{36}$$

where $m_{\rm ice}$ is the ice mass and $m_{\rm rock}$ is the total rock (in this case, dust) mass. The $f_{\rm ice}$ of solids in the inherited circumstellar material is 0.48. At a single pressure scale height ($z = H$) there is a factor ~20 reduction of the initial, global dust-to-gas ratio due to settling which is calculated according to the method of Dubrulle et al. (1995) with $\alpha_{\rm settle} = 10^{-2}$ such that the dust-to-gas ratio d/g at one scale height $\mathrm{d/g}_{z=H} = 10^{-3.2}$. Nevertheless we test a range of different d/g values for the CPDs both above and below this value

Table 5: Conditions at the gap edge "inheritance" point of the circumstellar disk at heliocentric distance 8.2 au, altitude 0.5 au (1 pressure scale height) above the midplane.

Parameter	Symbol	Value	Unit
Hydrogen density	$n_{\mathrm{H,in}}$	10^{10}	cm^{-3}
Optical Extinction	$\mathrm{A_{V,in}}$	1.01	-
Dust-to-gas ratio	d/g_{in}	$10^{-3.23}$	-
Dust Temperature	$T_{\mathrm{d,in}}$	57.0	K
Gas Temperature	$T_{\mathrm{g,in}}$	57.3	K
Ice Mass Fraction	$\mathrm{f_{ice,in}}$	0.48	-

(10^{-4}-10^{-2}).

Survival of icy grains passing through the gap

Icy grains must orbit within the optically thin gap for an unknown amount of time prior to being accreted onto the CPD. We considered whether ices on grains can survive against thermal- or photodesorption while crossing through the circumstellar disk gap. The dust and gas temperatures in the gap are not closely coupled as a consequence of the low densities. While the gas temperature extracted from the model at the midplane is ~200 K, the corresponding dust temperature is 48±2 K. Given that pressures in the gap range from 10^{-12}-10^{-10} bar, water ice is stable on the relevant timescales in the absence of irradiation (Lodders, 2003). However, the actual ice abundance at the gap midplane is negligible in steady-state. Despite the presence of a shadowing inner disk, ices within the gap are sublimated as a result of the significant stellar background radiation scattered into the gap.

To assess the longevity of ices crossing through the gap we populated the gap region with the “inheritance" chemical abundances found exterior to the gap and produce snapshots at regular intervals. The resulting decline in ice abundance as a function of time is shown in Fig. 3.2 for various stellar luminosities. The differing luminosities correspond to expected properties of the Sun for a stellar age of 0.1, 0.5, 1 and 4 Myr (Siess et al., 2000). Turner et al. (2012) suggests that grains entering the gap are accreted generally within a single orbital period (~ 10 yr). We find that for a moon formation time > 1 Myr after CAI formation ($\mathrm{L_{*}} \leq 2.34\mathrm{L_{\odot}}$), grains retain > 99% of their volatile content during gap-crossing if they reach the vicinity of the planet within 10 yr. A "full" inheritance scenario is thus not excluded by conditions within the gap, but would instead rely on shock-heating at the CPD surface.

The circumplanetary disks

The CPD is an actively-fed accretion disk with a steady-state mass proportional to its viscosity and mass infall rate. We considered an optically thick CPD of mass 10^{-7}

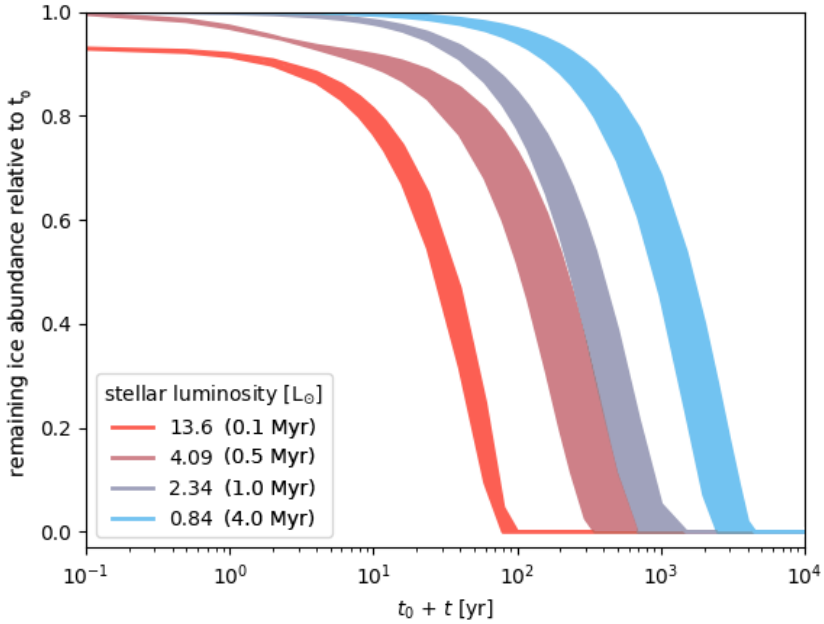

Figure 3.2: Ice abundance in the circumstellar disk gap normalized to the initial abundance of ice for various stellar luminosities as function of time after the onset of UV exposure. The width of each track represents the range of ice sublimation rates corresponding to variable conditions across the gap region ($z = 0 - 0.5$ au, $r = 5.2$ - 8.2 au).

$M_\odot$ as well as a lower mass CPD (10^{-8} $M_\odot$) which is optically thin everywhere outside the orbit of Callisto ($r > 0.03$ R_H where $R_H = 0.34$ au is the Hill radius). For a Jovian-mass planet these represent planet-disk mass ratios of $\sim 10^{-4}$ and 10^{-5} respectively. The CPDs are thus of the "gas-starved" type, and do not instantaneously contain the mass required to form a moon system as massive as the Galilean one.

The outer radius of the CPD is set as the planetary Hill radius R_H, however an exponential decline in the surface density profile is parameterized to begin at $R_H/3$ corresponding to the outermost stable orbit set by tidal interaction and angular momentum considerations (tidal truncation radius) (Quillen and Trilling, 1998; Ayliffe and Bate, 2009; Martin and Lubow, 2011). An empty inner magnetospheric cavity is assumed to exist as the result of magnetic interaction with the planet (Takata and Stevenson, 1996; Shibaike et al., 2019; Batygin, 2018). The parameterized radial surface density profiles of the high- and low-mass CPDs can be found in Fig.3.4 together with the resulting optical extinction profiles derived from the continuum radiative transfer.

The parameter variation grid of models exploring possible CPD mass and viscosity can be found in Table 7 along with the model id's. The format of the id is (*x*-*y*) where

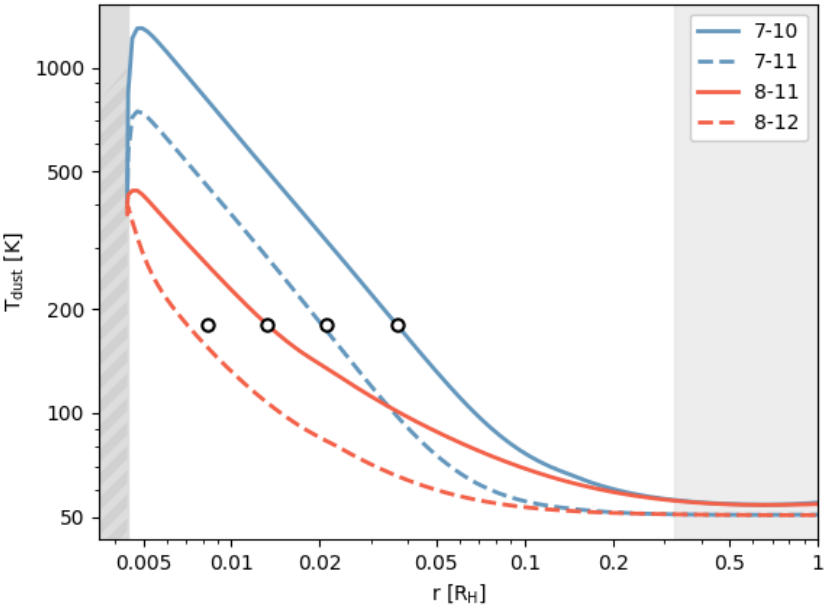

Figure 3.3: Radial midplane dust temperature profiles of the four reference CPDs ($d/g = 10^{-3.3}$), labelled by the model id's in Table 7. The four circles indicate only the present-day radial position of the Galilean satellites. The striped gray area on the left indicates the inner cavity. The light gray area on the right indicates the gravitationally unstable zone outside of $R_H/3$ (where $R_H = 0.35$ au).

x is related to the CPD mass by $M_{CPD} = 10^{-x}$ $M_\odot$ and y to the mass infall rate (and thus viscosity) by $\dot{M}_{CPD} = 10^{-y}$ $M_\odot$ yr^{-1}. The list of parameters which are common between the reference CPDs can be found in Table 6.

CPD viscosity

While the mechanism that produces angular momentum transport in accretion disks is not well understood, it is known that molecular viscosity alone is far too weak to explain observed accretion rates (Shakura and Sunyaev, 1973; Pringle, 1981). The efficiency of angular momentum transport is parameterized by the dimensionless α-viscosity (Shakura and Sunyaev, 1973) which for a circumstellar disk may have a broad distribution ranging from $\sim 10^{-5} - 10^{-1}$ (Rafikov, 2017; Ansdell et al., 2018; Villenave et al., 2022).

Disk gas with a sufficiently high ionization fraction couples to the stellar or planetary magnetic field such that the magnetorotational instability (MRI) induced turbu-

lence may provide the source of the effective viscosity and produce $\alpha \geq 10^{-3}$ (Balbus and Hawley, 1991; Hawley et al., 1995; Balbus, 2003). In the case of a CPD, MRI induced-turbulence may be inhibited by the short orbital periods and presence of magnetic dead-zones, limiting gas transport to a thin surface layer (Fujii et al., 2014). Even if the CPD were effectively inviscid, tidal interaction with the star may promote a minimum rate of angular momentum transport through the excitation of spiral waves (Rivier et al., 2012). In our ProDiMo model the α-viscosity of the disk is not explicitly specified. Instead, a mass accretion rate is specified which controls the heating rate of the disk through viscous dissipation.

The disk mass, accretion rate, and viscosity are highly degenerate properties. 3D hydrodynamical modeling of gas delivery into the vicinity of a Jupiter mass planet at 5 au suggest $\dot{M} = 10^{-9.3}$ $M_\odot$ yr^{-1} of gas (Szulágyi et al., 2022). Stellar tidal perturbation may produce a minimum accretion rate $10^{-9.7}$ $M_\odot$ yr^{-1} (Rivier et al., 2012). In the PDS 70 system, two massive planets are observed to be accreting gas in a large dust cavity (Wagner et al., 2018; Keppler et al., 2018; Haffert et al., 2019). K-band observations of PDS 70 b with the VLT are consistent with $\dot{M} = 10^{-10.8} - 10^{-10.3}$ $M_\odot$ yr^{-1} (Christiaens et al., 2019) with similar values estimated for PDS 70 c (Thanathibodee et al., 2019). HST UV and Hα imaging of the protoplanet PDS 70 b suggest $\dot{M} = 10^{-10.9} - 10^{-10.8}$ $M_\odot$ yr^{-1} (Zhou et al., 2021). Based on these observational and theoretical constraints we adopt $\dot{M} = 10^{-10}$ $M_\odot$ yr^{-1} (with a heating rate corresponding to $\alpha \approx 10^{-2.7}$) and $\dot{M} = 10^{-11}$ $M_\odot$ yr^{-1} ($\alpha \approx 10^{-3.6}$) for the high-mass CPD, representing viscous timescales of 10^3 and 10^4 years, respectively, over which the majority of the CPD mass is replaced by freshly accreted material (see Eq.(28)). For the low-mass CPD we adopt $\dot{M} = 10^{-11}$ $M_\odot$ yr^{-1} and $\dot{M} = 10^{-12}$ $M_\odot$ yr^{-1} to represent the same α-viscosities and $t_{\rm visc}$.

The viscous heating is determined according to the method of D'Alessio et al. (1998). The half-column heating rate is

$$F_{\rm vis}(r) = \frac{3GM_{\rm p}\dot{M}}{8\pi r^3}(1 - \sqrt{R_{\rm p}/r})\ \text{erg cm}^{-2}\text{s}^{-1}, \tag{37}$$

where G is the gravitational constant, $M_{\rm p}$ is the planet mass, r is the distance to the planet, and $R_{\rm p}$ is the planetary radius. We convert the surface-heating to a heating rate per volume as

$$\Gamma_{\rm vis}(r,z) = F_{\rm vis}(r)\frac{\rho_{\rm d}(r,z)}{\int \rho_{\rm d}(r,z')dz'}\text{erg cm}^{-3}\text{s}^{-1}, \tag{38}$$

where $\rho_{\rm d}$ is the mass density of the dust at radius r and height z. The heating is applied directly to the dust. The resulting midplane dust temperature profile of the CPDs can be found in Fig.3.3. The temperature profiles have been calculated using a new diffusion-approximation radiative transfer solver which is described in appendix A.1.

Sources of CPD external irradiation

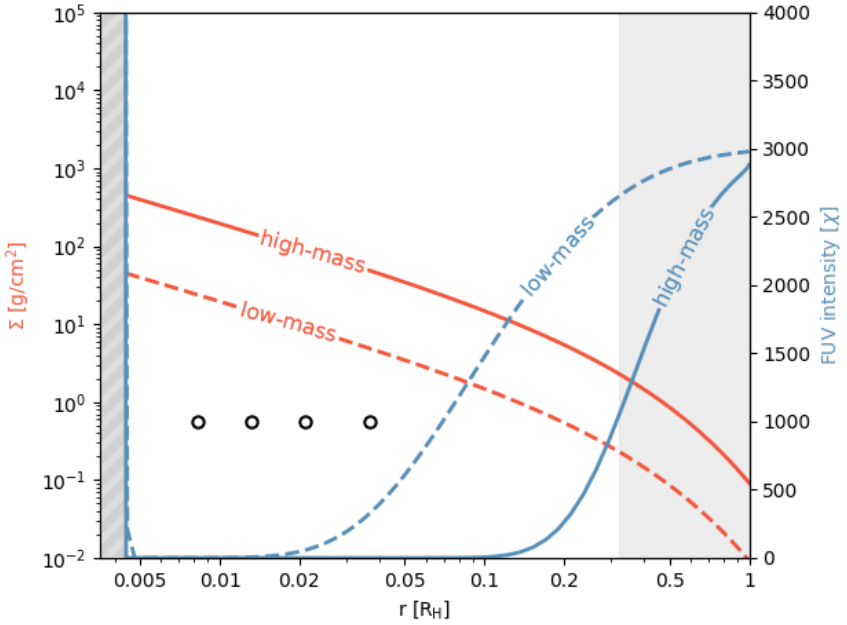

Figure 3.4: Surface density (red) and midplane FUV field strength in units of the Draine field χ (blue) of the high (10^{-7} $M_\odot$) and low (10^{-8} $M_\odot$) mass CPDs. The four circles indicate the present-day radial position of the Galilean satellites and their position on the ordinate is arbitrary. The striped gray region on the left indicates an empty inner magnetic cavity and the light gray region on the right indicates the gravitationally unstable zone outside of $R_H/3$ (where $R_H = 0.35$ au).

The rate of photodesorption plays an important role in determining the ice abundance in the outer optically-thin region of the CPDs. Potential sources of radiation include the planet, the star, and nearby massive cluster stars. For the planet we assume the runaway gas accretion phase has ended and that the luminosity has correspondingly declined to 10^{-5} $L_\odot$ with a surface temperature of 1000 K where it remains relatively constant for 10 Myr (Hubickyj et al., 2005; Marley et al., 2007; Spiegel and Burrows, 2012).

We parameterize the isotropic background radiation intensity with the dimensionless parameter χ. The background intensity is then the sum of a diluted 20000 K blackbody field and the cosmic microwave background,

$$I_\nu^{bg} = \chi \cdot 1.71 \cdot W_{\rm dil} B_\nu(20000K) + B_\nu(2.7K), \tag{39}$$

where the dilution factor $W_{\rm dil} = 9.85357 \times 10^{-17}$ such that a value of $\chi = 1$ corresponds to the quiescent interstellar background, or "unit Draine field" (Draine and Bertoldi,

1996; Röllig et al., 2007; Woitke et al., 2009). Irradiation by the young Sun provides a minimum $\chi \sim 3000$ at 5 au (see Fig.3.1) despite partial shadowing by an inner disk (Oberg et al., 2020). We adopted the same value for the strength of the FUV irradiation in the midplane at Jupiter's location although it is contingent on our assumptions regarding the stellar UV luminosity and geometry of the inner circumstellar disk. Independently of these factors, Oberg et al. (2020) find that interstellar radiation results in a mean χ of O(3) in the gap, as the Sun is believed to have formed in a relatively dense stellar cluster (Adams, 2010; Portegies Zwart, 2019) containing massive OB stars (Pfalzner, 2013). External irradiation heats dust and gas on the surface and in the outer regions of the optically-thin CPD midplane. 3D dust radiative transfer modeling of gap-embedded CPDs suggests scattered stellar radiation can be the dominant heating source in the outer regions of a CPD (Portilla-Revelo et al., 2022). We assumed that the outer edge of the CPD is in thermal equilibrium with the surroundings and set a CPD background temperature lower limit of 50 K equal to that of dust in the circumstellar disk gap (see Fig. 3.1).

CPD dust mass and grain size population

The dust-to-gas ratio is a key parameter that regulates the eventual ratio of ice to rock in the CPD. Planet-induced pressure bumps at the gap edges of the circumstellar disk may filter out dust particles above ~100 μm in size (Rice et al., 2006a; Zhu et al., 2012). For a dust grain size population power law exponent of -3.5, minimum grain size a_{min} 0.05 μm, maximum grain size a_{max} 3000 μm, a filtering of grains larger than 100 μm would reduce the mass of dust entering the gap by a factor ~ 30. As an opposing view Szulágyi et al. (2022) find that a planet within the gap can stir dust at the circumstellar disk midplane and produce a very high rate of dust delivery to the CPD, such that the dust-to-gas ratio can even be enhanced in the CPD to ~ 0.1 for a Jupiter mass planet at 5 au.

The dust population within the CPD may also rapidly evolve. It is possible that mm-sized grains are quickly lost to radial drift in $10^2 - 10^3$ yr (Zhu et al., 2018). Similarly Rab et al. (2019) used the dust evolution code *two-pop-py* (Birnstiel et al., 2012) to show that for an isolated CPD onto which new material does not accrete, an initial dust-to-gas ratio of 10^{-2} can in only 10^4 yr be reduced to $< 10^{-3}$ and in 10^5 yr to $< 10^{-4}$. However, larger dust grains may become trapped in CPDs (Drążkowska and Szulágyi, 2018; Batygin and Morbidelli, 2020). Additionally, we expected that in an embedded, actively-accreting CPD the dust will continually be replenished and that a higher steady-state dust-to-gas ratio will be achieved. Given these considerations we tested various possible dust to gas ratios ranging from $10^{-4} - 10^{-2}$ in Appendix A.8.

3.2.3 Dust grain drift within the CPD

In ProDiMo the chemistry is solved for each grid cell without accounting for radial dust or gas transport. Instead we used properties of the ProDiMo model output to in-

Table 6: Parameters common to the CPD models. Parameters which are not common to the CPD models are listed in Table 7. Where not specified the CPD parameters are identical to the circumstellar disk parameters listed in Table 4.

Parameter	Symbol	Value	Unit
Planet Mass	$M_{\rm p}$	1.0	$M_{\rm J}$
Planetary Luminosity	$L_{\rm p}$	10^{-5}	$L_\odot$
Effective Temperature	$T_{\rm eff,p}$	1000	K
UV Luminosity	$L_{\rm UV,p}$	0.01	$L_{\rm p}$
Background UV Field	χ	3×10^3	-
Background Temperature	$T_{\rm back}$	50	K
Disk Inner Radius	$R_{\rm in,CPD}$	0.0015	au
Taper Radius	$R_{\rm tap,CPD}$	0.12	au
Disk Outer Radius	$R_{\rm out,CPD}$	0.35	au
Column Density Power Ind.	$\epsilon_{\rm CPD}$	1.0	-
Flaring Index	$\beta_{\rm CPD}$	1.15	-
Reference Scale Height	$H_{0.1{\rm au}}$	0.01	au
Maximum dust size	$a_{\rm max,CPD}$	3000	μm
Dust-to-Gas Ratio	d/g	$10^{-3.3}$	-

Table 7: Variation of parameters for the circumplanetary disk model grid. Model id's are of the format (A-B) where the CPD mass is 10^{-A} $M_\odot$ and where the accretion rate onto the CPD is 10^{-B} $M_\odot$ yr^{-1}.

model id	M [$M_\odot$]	$\dot{M}$ [$M_\odot$yr^{-1}]	$t_{\rm visc}$ [yr]	α
(7-10)	$10^{\mathbf{-7}}$	$10^{\mathbf{-10}}$	10^3	$10^{-2.7}$
(7-11)	$10^{\mathbf{-7}}$	$10^{\mathbf{-11}}$	10^4	$10^{-3.6}$
(8-11)	$10^{\mathbf{-8}}$	$10^{\mathbf{-11}}$	10^3	$10^{-2.7}$
(8-12)	$10^{\mathbf{-8}}$	$10^{\mathbf{-12}}$	10^4	$10^{-3.6}$

form the radial dust drift calculations in a post-processing step to compare timescales of chemical evolution vs. dust drift. Disk gas which is pressure-supported orbits at sub-Keplerian velocities such that larger grains feel a headwind and rapidly drift inwards (Weidenschilling, 1977). In a circumstellar disk the degree of sub-Keplerianity can be $< 1\%$ while in a CPD it could be as high as 20-80% due to significant gas pressure support (Armitage, 2007; Drążkowska and Szulágyi, 2018). We considered whether the timescale of grain drift can compete with the processes that shape grain composition In the Epstein regime the radial grain drift velocity $v_{r,d}$ can be approximated as

$$v_{r,d} = \frac{v_{r,g} T_s^{-1} - \eta v_K}{T_s + T_s^{-1}}, \tag{40}$$

where $v_{r,g}$ is the radial velocity of the gas, T_s is the dimensionless stopping time of a grain,

$$T_s = t_s \left(\frac{v_k}{r} \right), \tag{41}$$

where t_s is the stopping time, v_k is the Keplerian orbital velocity, and r is the radius in the CPD. The stopping time is

$$t_s = \left(\frac{\rho_{\text{grain}}}{\rho_{\text{gas}}} \right) \left(\frac{a}{v_{\text{th}}} \right), \tag{42}$$

where a is the grain size, ρ_{gas} is the gas density, ρ_{grain} is the material density of the dust grains, and v_{th} is the thermal velocity of the gas: $c_s \ (8/\pi)^{0.5}$ where c_s is the speed of sound. The parameter η is

$$\eta = n \left(\frac{c_s^2}{v_k^2} \right), \tag{43}$$

and n is the power law exponent of the radial pressure gradient (Armitage, 2010). We extract the gas density ρ_{gas}, sound speed c_s, and pressure gradient from our disk models to consistently determine the grain drift velocities for a grain material density $\rho_{\text{grain}} = 3 \text{ g cm}^{-3}$. The Epstein regime is valid where the dust particle size $a \leq 9\lambda/4$ where λ is the mean free path of the gas particles. In the inner CPD the gas density is sufficiently high that this condition can be violated. For the high-mass CPD this occurs inside of the orbit of Callisto and for the low-mass CPD inside of the orbit of Europa for grains less than 1 cm in size, in which case we transition to the Stokes regime and calculate the drift velocities accordingly (Weidenschilling, 1977).

We adopted several simplifying assumptions regarding the radial velocity structure of the gas. The centrifugal radius r_c of the CPD is the orbital radius at which the specific angular momentum is equal to the average of the infalling material and where solid material is accreted onto the CPD (Canup and Ward, 2002; Sasaki et al., 2010). In the case of a Jupiter-mass planet this lies near the orbit of Callisto. Rather than accreting at precisely this radius infalling matter has some intrinsic spread in angular momentum

(Machida et al., 2008). We adopted the prescription of Mitchell and Stewart (2011) that material will accrete between 16-28 R_J. The gas falling onto the CPD at r_c will viscously spread radially away from where it is accreted (Pringle, 1981). Hence interior to r_c gas flows towards the planet and exterior to r_c it will flow outwards. Recently it has been proposed that to effectively trap dust and allow for planetesimal growth within the CPD, gas may indeed need to flow predominantly away from the planet and thus form a decretion disk (Batygin and Morbidelli, 2020).

In our high viscosity models, a parcel of gas that accretes onto the CPD near r_c and flows outwards must travel $\sim$ 0.3 au within 10^3 yr to be consistent with t_{visc} and thus has a mean outwards radial velocity on the order of 1 m s^{-1}. For our low viscosity case $v_{r,gas} \sim 0.1$ m s^{-1}.

3.3 Results

In our reference model grid (Table 7) we considered the case of a higher mass, optically thick CPD (10^{-7} $M_\odot$), and lower mass, optically thin CPD (10^{-8} $M_\odot$) both with $d/g = 10^{-3.3}$. For each unique mass we considered viscous timescales of 10^3 and 10^4 yr. For each of the four resulting CPDs we tested two initial compositions: of chemical inheritance and reset, for a total of eight models.

3.3.1 Timescales of ice formation

In the following section we discuss by which pathways and at what rate water (ice) formation occurs in a chemically reset CPD. Thereafter we contrast these results with that of the CPDs which inherit an initial chemical composition from the circumstellar disk.

Reset

In our "reset" scenario the species initially present are exclusively atomic (with the exception of PAHs) and singly or doubly ionized. All hydrogen is initially present in the form of H^+. The reset case is characterized by the formation of ice where it is stable against desorption. Ice formation is suppressed in the innermost region of the CPD due to dust temperatures in excess of 160-180 K. In the outer region of the CPD ice formation is suppressed by the low optical depths and correspondingly high intensity of background radiation which causes ices to photodesorb. Between these two boundaries ices begin to form.

The freeze-out occurs step-wise, with two characteristic timescales on which ice formation proceeds. The rate of water ice formation at different disk radii as a function of time is shown in Fig. 3.5. Within 0.01 − 1 yr the first step is completed. This initial, rapid water formation occurs primarily via a path that begins with a three-body recombination reaction important at temperatures below 2800 K (Hidaka et al., 1982; Tsang

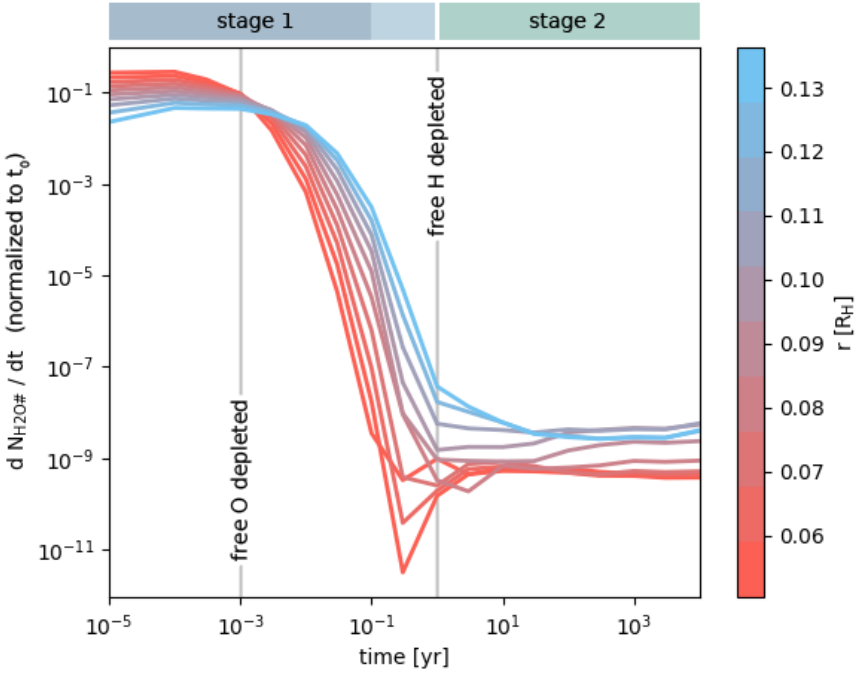

Figure 3.5: Rate of water ice formation as a function of time at different radii beyond the snowline in the high-mass, high-viscosity CPD (7-10), to illustrate the two distinct stages of water ice formation. All values are normalized to the maximum formation rate at 10^{-5} yr, r = 0.08 R_H. The times where the decline in the abundance of free O and free H end are indicated by the gray vertical lines. The starting time t_0 is defined as when the infalling gas is shock-heated to an atomic and ionized state.

and Hampson, 1986),

$$H + O + M \rightarrow OH + M, \tag{44}$$

where the third body M = H, H_2, or He, and to a lesser extent by H + O → OH + photon. The water then forms by radiative association of the OH with free hydrogen;

$$OH + H \rightarrow H_2O + \text{photon}, \tag{45}$$

after which it adsorbs to a grain. Water formation via the reactions 44 and 45 remains proportional to the declining abundance of free H and ends when it is depleted around 10^{-1} yr. Typically half of the maximum possible amount of water ice that could form is produced during this stage.

The first stage of water ice formation proceeds inside-out as a result of the strong density-dependence of the collider reaction. The second stage proceeds outside-in due to the pathway's dependence on intermediate species produced by photo-reactions. This can be seen in Fig. 3.5 where the inner disk formation rate (red lines) is initially higher while later the outer disk rate (blue lines) is relatively higher. At this lower rate of formation the total mass of water ice doubles at the midplane within ~ 1 Myr, approximately half of which forms by

$$NH_2 + NO \rightarrow N_2 + H_2O, \tag{46}$$

near the snowline. The second stage of ice formation also involves the freezing-out of NH_3 and other more volatiles species. We find that the relatively unstable NH_2 exists in abundance at such high densities ($n_H \sim 10^{15}$ cm^{-3}) due to the three-body reaction $N + H_2 + M \rightarrow NH_2 + M$. Although the reaction rate has been experimentally determined $k_0 = 10^{-26}$ cm^6 s^{-1} (Avramenko and Krasnen'kov, 1966), it has been noted as being in need of revisiting due to its importance in water formation via $NH_2 + O \rightarrow NH + OH$ (Kamp et al., 2017). We have adopted a rate more typical of collider reactions (10^{-30} cm^6 s^{-1}), which still produces enough NH_2 for this path to play an important role. The other half of water ice is formed via the more "classical" route

$$H_3O^+ + e^- \rightarrow H_2O + H, \tag{47}$$

and in the outermost part of the disk where water ice is stable via

$$H_3O^+ + H_2CO \rightarrow H_3CO^+ + H_2O, \tag{48}$$

In the high-mass CPDs water ice formation is typically still ongoing by the end of the viscous timescale, and so the midplane ice abundance is not able to converge to the level seen in steady-state within the viscous timescale.

Inheritance

The evolution of the inheritance case is characterized by the desorption of ices in regions where they are not stable against thermal or photo-desorption. Where water ice is stable very little additional water formation occurs within the viscous timescale.

Icy grains interior to the snowline sublimate typically within 10^{-5} yr, and a "snowline" (water iceline) is clearly established. In some cases the snowline can take longer to stabilize, shifting outwards over time, and sometimes continues to evolve radially for up to 10^5 yr. This is notable in the (8-11) CPD where the snowline moves from 0.01 R_H at 10^{-5} yr to 0.03 R_H after 10^4 yr. In practice this implies that there exists a radial span in which the composition of radially drifting icy grains does not immediately begin to reflect the ambient conditions. This is discussed in Sect. 3.4.2.

In the outer optically thin region of the CPDs, ices are also lost to photodesorption although the process is slower than the thermal desorption occurring in the inner disk.

Desorption in this area is typically complete within $10^3 - 10^5$ yr and has not always reached steady-state by the end of the viscous timescale.

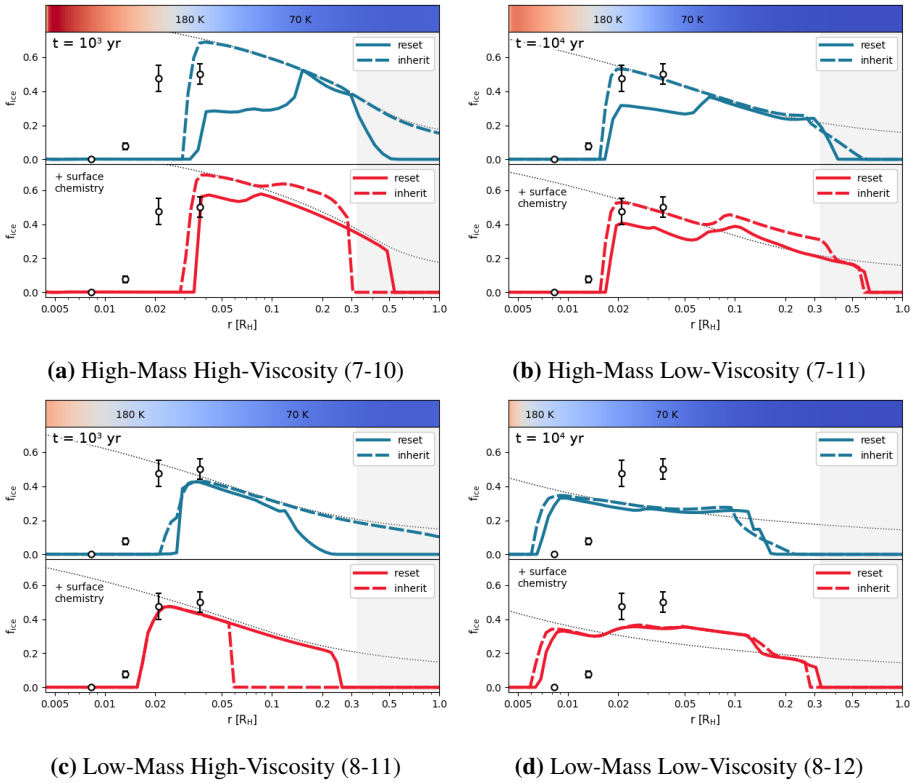

(a) High-Mass High-Viscosity (7-10)

(b) High-Mass Low-Viscosity (7-11)

(c) Low-Mass High-Viscosity (8-11)

(d) Low-Mass Low-Viscosity (8-12)

Figure 3.6: Midplane ice fraction at $t = t_{\rm visc}$ for the CPDs with $d/g = 10^{-3.3}$. The four circles indicate the present day radial location of the Galilean satellites and the uncertainty bars represent their possible range of ice fractions. The thin dotted line indicates the initial radial ice fraction in the inheritance cases. The filled gray region on the right indicates the gravitationally unstable zone outside of $R_H/3$.

3.3.2 The midplane ice mass fraction

While water ice can form efficiently in chemically reset CPDs, the final $f_{\rm ice}$ of the solids depends strongly on the total dust mass in the midplane. We explore the role of the global d/g ratio in the reset and inheritance cases in Appendix A.8, Fig. 3.17. A canonical dust-to-gas ratio of 10^{-2} produces at most grains with an ice mass fraction of < 0.1 and is nowhere consistent with the composition of the icy Galilean satellites. In contrast a dust-to-gas ratio of $10^{-3.3}$ results in solids with $f_{\rm ice}$ both above and below the maxi-

mum Galilean $f_{\rm ice}$ for the high and low-mass CPDs, respectively. Hereafter the global dust-to-gas ratio of $10^{-3.3}$ is considered in discussions of the four reference CPDs.

We show the state of the radial ice mass fraction for the CPDs with $d/g = 10^{-3.3}$ on their respective viscous timescales to allow for direct comparison between the inheritance and reset cases in Fig.3.6. For completeness we include the results where grain-surface chemical reactions are utilized.

The midplane $f_{\rm ice}$ is also dependent on the degree of dust sedimentation (settling). A general feature of the $f_{\rm ice}$ profiles is an inner maximal peak at the snowline followed by a decline towards the outer edge of the disk. As dust settling is more efficient at larger radii, $f_{\rm ice}$ reduces accordingly with increasing radius. Settling of dust to the midplane is counteracted by stochastic advection by turbulent eddies in the gas. We assume that the value of turbulent-α used to determine the degree of settling is equal to the global viscous α used to determine the heating rate by viscous dissipation. In the low viscosity CPDs (7-11) and (8-12) dust settling towards the midplane is thus proportionally enhanced. In the low-viscosity cases the dust density is enhanced in the midplane minimally by a factor $\sim$ 3 over the global d/g, increasing to a factor $\sim$20 at $R_H/3$. As the degree of settling is also dependent on the adopted surface density power law exponent ϵ we explore the impact of deviation from the assumed $\epsilon = 1$ in Appendix A.3. Given that we have no reason to believe this value will depart significantly from the range 1.0-1.3, the resulting $f_{\rm ice}$ in the inner disk should differ from our reference result by no more than 25-30% interior to the ammonia iceline at $\sim$70 K.

In general the high-mass chemically reset CPDs (7-10) and (7-11) are not able to converge entirely towards a steady-state ice abundance in either the "fast" (10^3 yr) or "slow" (10^4 yr) viscous timescales as gas-phase CO is more stable and contains a relatively larger fraction of the total oxygen budget for longer. As a result chemically reset CPDs contain on average less water ice than those which inherit their ices from the circumstellar disk. In contrast, the low-mass chemically reset CPDs (8-11) and (8-12) are able to converge towards the ice abundances seen in the inheritance cases within 100 yr.

The role of surface chemistry

The duration of the initial stage in which water formation is rapid is dependent on the availability of atomic H. When H_2 formation is complete this stage ends. The formation of H_2 is treated differently with the inclusion of grain surface chemistry. When the chemistry is limited to gas-phase reactions and direct adsorption/desorption only, H_2 formation proceeds via the analytic rate determined by Cazaux and Tielens (2002). When surface chemistry is included H_2 formation is instead modeled explicitly via reactions involving hydrogenated PAHs (H-PAH) (Boschman et al., 2012; Thi et al., 2020a).

A chemical reset poses a scenario in which H_2 and H_2O formation occur simultaneously. The analytic rate of Cazaux and Tielens (2002) presupposes that chemisorbed H plays a role in H_2 formation on silicate or carbonaceous surfaces, in which H goes through an intermediate stage of being chemically, rather than physically, bound to the

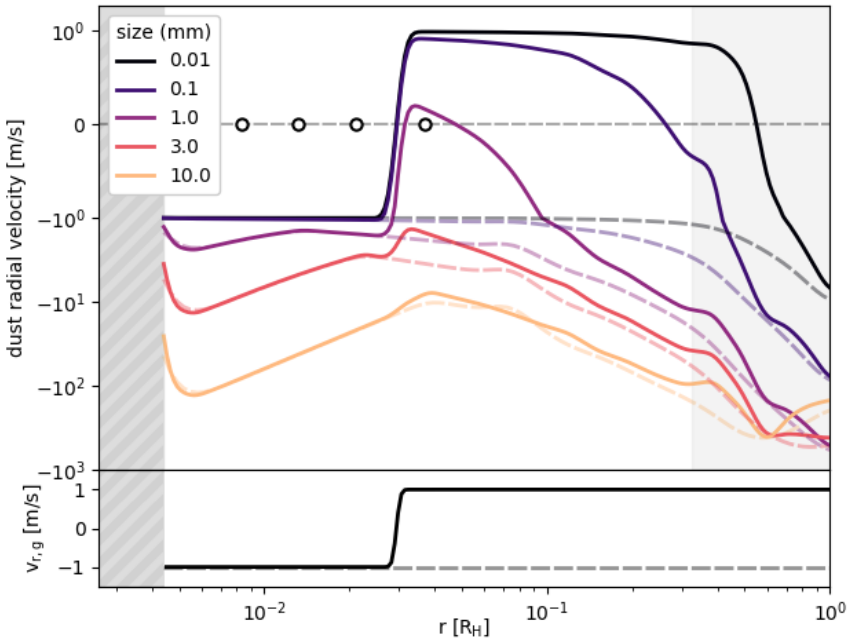

Figure 3.7: Radial drift velocity of particles (*upper panel*) and radial velocity of the gas (*lower panel*) in the high-mass, high-viscosity CPD (7-10). The position of the Galilean satellites on the ordinate is arbitrary. The gray region on the right indicates the tidally unstable region beyond $R_H/3$. The striped region on the left indicates the inner cavity. Solid lines indicate the case of a decretion disk where gas falls onto the CPD at the centrifugal radius (0.03 R_H). Dashed lines indicate the grain drift and gas radial velocity in the case of a pure accretion disk.

grain surface. We find that prior to atomic H depletion several (>3) monolayers of H_2O have formed on the average sized grain. The formation of H_2 via chemisorbed H should thus be suppressed in these regions as the water ice layers prevent H atoms from chemisorbing to the grain surface (Wakelam et al., 2017). In the absence of chemisorbed H, H_2 formation on dust is strongly reduced and H_2 formation proceeds primarily via H-PAH. The H_2 formation rate under these conditions is less efficient than the analytic rate from (Cazaux and Tielens, 2002) near the inner edge of the snowline at 150-170 K. The relatively slower formation of H_2 and the resulting prolonged availability of atomic H results in a $\sim 30-100\%$ increase in water ice abundance interior to the NH_3 iceline prior to t_{visc} and hence narrows the gap between the inheritance and reset cases in this region. Water ice formation in the inner disk is further enhanced by the inclusion of O_2H in the surface chemistry network. Gas-phase three-body reactions with O_2 produce O_2H which in turn lead to early OH formation. The gas-phase O_2 reservoir is thus depleted

and efficiently converted via OH into H_2O via the three-body reaction

$$O_2 + H + M \rightarrow O_2H + M, \tag{49}$$

with rates adopted from UMIST2006 (Atkinson et al., 2004; Woodall et al., 2007), which is highly efficient at the densities in the CPD, and thereafter

$$O_2H + H \rightarrow OH + OH, \tag{50}$$

$$OH + H \rightarrow H_2O + \text{photon}, \tag{51}$$

In the outer disk the ice mass fraction can be enhanced relative to the gas-phase chemical network as the freezing-out of more volatile species is facilitated by grain surface reactions. CO_2 ice is readily formed on the surface via $OH + CO \rightarrow CO_2 + H$ (Oba et al., 2010; Liu and Sander, 2015) for which we adopt an effective barrier of 150 K (Fulle et al., 1996; Ruaud et al., 2016). The formation of carbon bearing ices begins to significantly influence the f_{ice} of the chemically reset CPDs only after 10^3 yr and hence the effect on the high-viscosity CPDs with $t_{visc} = 10^3$ yr is less pronounced. The formation and composition of these ice impurities will be discussed in detail in an accompanying work (Oberg et al. in prep).

3.3.3 Grain drift vs. adsorption and desorption

We calculated the velocity of radially drifting grains in the four reference CPDs and showcase the results for the high-mass high-viscosity CPD (7-10) in Fig. 3.7. We solved for the total time it takes grains of several sizes to reach the inner disk edge. The resulting timescale of grain drift can be seen in Fig. 3.8 which shows the time for a grain deposited at radius r to reach the CPD inner edge. Grains which become trapped are not included in Fig. 3.8, as they do not reach the disk inner edge. The regions where thermal desorption, ice formation, and photodesorption predominantly shape grain mantle composition, as well as their respective timescales, are indicated in the figure. These are the timescales with which grain drift competes.

The regions have been defined as follows: the “thermal desorption region" is found interior to the snowline where inherited, initially icy grains lose their icy mantles within the viscous timescale. The “snow border” is the region where the reset and inheritance cases are not able to converge towards a common snowline within 10^6 yr. Grains here are able to retain their icy mantles but no significant additional ice adsorption occurs. The “ice formation region" is where water begins to adsorb to grains after the CPD has been chemically reset. The “photodesorption region" is the optically thin region exterior to the snowline where inherited grains eventually lose their icy mantles within $\sim 10^6$ yr at most.

We focus on grains of size < 10 mm as the adsorption and desorption timescales derived in Sect. 3.3.1 have only been derived with the thermochemical disk model for grains up to this size. In most cases the grain drift timescale t_{drift} is longer than

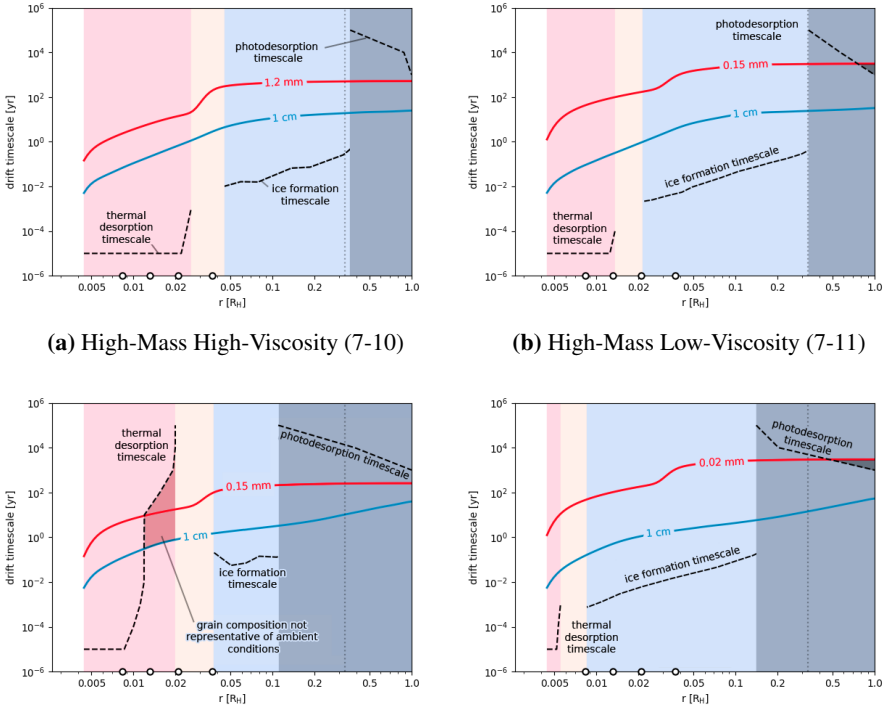

(a) High-Mass High-Viscosity (7-10)

(b) High-Mass Low-Viscosity (7-11)

(c) Low-Mass High-Viscosity (8-11)

(d) Low-Mass Low-Viscosity (8-12)

Figure 3.8: Inwards drift timescale for dust grains (colored lines) relative to the timescales of desorption and ice formation (black dashed lines) in the reference CPDs with $d/g = 10^{-3.3}$. From left to right the colored regions correspond to areas where all ices are eventually thermally desorbed (pink), the iceline (light yellow), where grains become icier (light blue) and where all ices are eventually photodesorbed (dark gray). The red line corresponds to the minimum grain size which is not trapped in the CPD (if there is a sign change in the gas radial velocity) and the blue line to the maximum for which the timescales of desorption and ice formation have been verified. The vertical dotted line indicates the approximate outer region of gravitational stability in the CPD.

the timescales of thermal desorption and the timescale of rapid ice formation. The composition of grains will thus correspond to the f_{ice} profiles derived in Sect. 3.3 except in the case of the low-mass, high-viscosity CPD (8-11). In this CPD icy grains can cross into the "thermal desorption region" but only begin desorbing once they approach the position of Europa.

Dust traps

It is clear from Fig.3.7 that in a decreting CPD dust traps are present. Grains deposited near the centrifugal radius drift outwards with the gas until the force of radial advection is balanced by the loss of orbital energy from drag against gas orbiting at sub-Keplerian velocity. Trapped grains thus become radially segregated by size, with smaller grains drifting to the outer edge of the trap and larger grains remaining near the inner edge. In the high-mass high-viscosity CPD (7-10) grains 0.1-1 mm in size become trapped near 0.1-0.2 R_H. Grains smaller than 0.05 mm advect with the gas and are able to reach the outermost stable orbit at $R_H/3$ where they would be eventually lost to e.g. tidal stripping.

In general the dust traps are spatially coincident with the ice formation region and in the lower-mass CPDs also partially with the photodesorption region. Hence continued ice deposition on trapped grains could facilitate grain growth. This phenomena is discussed further in appendix Sect. A.6.

3.4 Discussion

We set out to explore the process of ice formation in CPDs with relatively short viscous timescales to constrain their physical, chemical, and dynamical properties. We find that even if infalling gas and ice is fully atomized, re-freezing proceeds quickly in the CPD and solids reach an $f_{ice} \sim 0.5$ by t_{visc} for an appropriate midplane dust-to-gas ratio. The midplane ice abundance at t_{visc} is generally insensitive to the initial chemical conditions. Only in the inner disk ($r < 0.05 - 0.1\,R_H$) of the high-mass CPDs is ice formation too slow for the reset and inheritance cases to converge. With our standard chemical network the efficiency of water production in this region is closely tied to the availability of atomic H and thus to the H_2 formation rate, which is not well constrained in these conditions. The three-body reaction H + O + M → OH + M is also critical to the process. For this reaction we have adopted the rate coefficients listed in UMIST2006 (Woodall et al., 2007), the value of which originates from a recommendation of Tsang and Hampson (1986) who noted that literature values represented only rough estimates and suggested a factor 10 uncertainty (Baulch, 1972; Day et al., 1973). More recent estimates of this rate at high temperatures (> 3000 K) suggest this value is accurate to within ~40% (Javoy et al., 2003), but modern low temperature measurements remain desirable. In our expanded grain-surface chemical network, gas-phase O_2H plays an important role in accelerating OH formation in the inner disk, diverting atomic oxygen into water rather than O_2.

3.4.1 Constraints on CPD properties

For reasonable assumptions regarding the properties of the CPD the snowline can fall very near the present-day position of Europa. The CPD with mass 10^{-7} $M_\odot$ (10^{-4} M_J), $\alpha = 10^{-3.6}$ and $d/g = 10^{-3.3}$ matches best the compositional gradient of the Galilean

moons at their present-day orbits. While this seems like a promising outcome, we emphasize that both inwards gas-driven migration (Canup and Ward, 2002; Madeira et al., 2021) and long-term outwards tidally-driven migration (Yoder, 1979; Tittemore, 1990; Showman and Malhotra, 1997; Lari et al., 2020) have potentially played a role in repositioning the satellites both during and post-formation. Other regions of the CPD parameter space are equally capable of producing solids with $0.4 < f_{\mathrm{ice}} < 0.55$, but vary in the position of their snowline. In any case, we believe that it is more meaningful to determine whether a particular CPD can form enough ice on the relevant viscous timescale, rather than at precisely which radii a particular abundance of ice can be found.

To produce solids with a minimum $f_{\mathrm{ice}} \sim 0.5$ the global dust-to-gas ratio of the CPD must be $\leq 10^{-3}$ and does not need to be $< 10^{-3.7}$. We suggest that this does not represent a minimum d/g limit as imperfect accretion (Dwyer et al., 2013), (hydrodynamic) proto-atmospheric escape (Kuramoto and Matsui, 1994; Bierson and Nimmo, 2020), impact-vaporization (Nimmo and Korycansky, 2012), or tidal heating (Canup and Ward, 2009) may all have played a role in reducing the volatile mass of the satellites either during or post-accretion. A minimum d/g is instead implied by the minimum time required to accrete the solid total mass of the Galilean satellites ($\sim 10^{-7}\,\mathrm{M}_{\odot}$) into the CPD. We consider the lifetime of the gaseous circumstellar disk (~ 10 Myr) to be the maximum time over which the CPD can continue to accrete gas. Assuming Jupiter's runaway accretion ended < 3.94 Myr after CAI formation (Weiss and Bottke, 2021) and that moon formation only began at this stage, this leaves ~6 Myr to accrete the refractory material for the moons. We emphasize that this limit is very approximate, as it is possible that circumstellar gas disk lifetimes regularly exceed 10 Myr (Pfalzner et al., 2014). Conversely an even shorter lifetime (< 4.89 Myr after CAI formation) has been proposed for the solar nebula on the basis of paleomagnetic measurements (Weiss and Bottke, 2021).

The midplane dust-to-gas ratio and thus the f_{ice} in the CPD will differ from what has been derived from our models if the grain size distribution is significantly altered in some way. The circumstellar disk gap edge may filter out larger grains from the accretion flow (Rice et al., 2006a; Zhu et al., 2012). Grains larger than 100 μm, which settle efficiently, are those primarily responsible for enhancement of the dust mass at the CPD midplane. Massive planets may however vertically stir circumstellar disk midplane dust outside the gap (Binkert et al., 2021). Szulágyi et al. (2022) found that significant vertical stirring of large grains occurs at the gap outer wall in the presence of planets with mass above that of Saturn, resulting in a substantial delivery of mm-sized grains to the CPD. The high-mass tail of the dust distribution could alternatively be depleted by the more rapid inwards drift of these grains in the CPD. We have shown that grains larger than $\sim$ 1mm no longer advect with the gas in the CPD. The steady-state dust grain size distribution will thus likely be truncated. In the absence of these grains the limits we have derived on the CPD mass are revised upwards by a factor $\sim$ 5.

3.4.2 Does grain drift erase the radial distribution of ices?

We have tested only the "gas-starved" disk paradigm in which a CPD must over time accrete the solids to form large moons. The sequential formation, episodic growth, and potential loss of migrating moons is a characteristic of this theory (Canup and Ward, 2002). In such a dynamical environment the relevancy of the instantaneous radial distribution of icy grains remains to be established. The simplest way in which the chemical properties of dust in the CPD could be imprinted on the final satellite system would be through in-situ formation: the satellites accrete the bulk of their material at fixed radial positions in the CPD (Ronnet et al., 2017). This might occur if the innermost proto-moon were prevented from migrating into Jupiter by the presence of a gas-free magnetically-truncated inner cavity (Takata and Stevenson, 1996; Batygin, 2018; Shibaike et al., 2019). Additional proto-satellites could then pile-up in a resonant chain and be stabilized against further migration by the proto-moon anchored at the disk inner edge (Ogihara and Ida, 2009; Sasaki et al., 2010; Izidoro et al., 2017; Madeira et al., 2021). Drifting grains would still be free to cross the orbit of proto-moons as accretion efficiency remains low when the proto-moons are only a fraction of their final mass (Shibaike et al., 2019). In this paradigm proto-moons orbit at relatively fixed positions, continually accreting grains that drift into their feeding-zone (Ronnet and Johansen, 2020). We find that the ice fraction of small (< 1 cm) drifting grains in the inner disk will almost always reflect ambient conditions (Sect. 3.3.3) independently of whether the gas in the CPD flows radially inwards or outwards (the fate of trapped grains is discussed in Appendix A.6). If the proto-moons (resonantly anchored at fixed radii within the CPD) accrete the majority of their total mass from these drifting grains, their bulk ice fraction would reflect the temperature gradient of the CPD.

3.5 Conclusions

Circumplanetary disks represent a unique chemical environment characterized by high-densities and a relatively short timescale on which gas and dust are viscously or aerodynamically lost. We aimed to explore the process of ice formation in this environment from sharply contrasting initial chemical conditions, knowing that solids with ice/rock ~ 1 must be able to form within the viscous timescale of a Jovian CPD. We tested the paradigm in which solids are delivered directly from the circumstellar disk in the form of small grains (< 1 cm) to a "gas-starved", relatively low-mass CPD. We highlight our key conclusions as follows:

If infalling material is chemically reset:

1. High densities in the CPD facilitate three-body “collider" reactions that lead to rapid water ice formation. Roughly half of the water ice is formed within a single year by the hydrogenation of OH.

2. Solids with the ice fraction of Ganymede or Callisto are produced within $t_{\rm visc}$ for

$\alpha \approx 10^{-3} - 10^{-4}$ if the midplane is depleted in dust by a factor 20-50 relative to the canonical $d/g = 10^{-2}$.

If chemical inheritance occurs:

1. Ices near the planet efficiently sublimate and establish a snowline at a similar location to that of the reset case within $t_{\rm visc}$. Additional ice formation is minimal.

In either case:

1. Icy circumstellar dust grains preserve the majority of their volatile content during gap-crossing if accreted onto the CPD within 100 yr unless the stellar luminosity is $> 10\ L_\odot$.
2. The compositional imprint of the CPD temperature profile is not erased by radial dust drift for grains of size $a < 1$ cm.
3. Only the "high-mass" CPDs ($M_{\rm CPD} = 10^{-4}\ M_J$) are sensitive to the initial chemical conditions: water ice formation in the inner disk is less efficient if a chemical reset occurs as oxygen tends to remain locked in the gas-phase CO.

In the outer regions of our solar system icy moons are common. No matter whether or not ices sublimate upon incorporation into the CPD, we have demonstrated that ices can be efficiently re-deposited onto dust grains and enable the general ubiquity of icy moons.

Acknowledgements

The research of N.O. and I.K. is supported by grants from the Netherlands Organization for Scientific Research (NWO, grant number 614.001.552) and the Netherlands Research School for Astronomy (NOVA). This research has made use of NASA's Astrophysics Data System Bibliographic Services. This research has made extensive use of Numpy (Harris et al., 2020), Matplotlib (Hunter, 2007), scipy (Virtanen et al., 2020), and prodimopy `https://gitlab.astro.rug.nl/prodimo/prodimopy`. The authors would like to thank the anonymous referee for comments that contributed to the accuracy, clarity, and focus of this work.

Appendix

A.1 The RT diffusion solver

ProDiMo solves the radiative transfer equation (see Eq. (12) in Woitke et al., 2009) together with the condition of radiative energy conservation, which in general can be written as

$$\mathrm{div}\vec{F} = \Gamma\,, \tag{52}$$

where $\vec{F} = \int \vec{F}_\nu \, d\nu$ [erg/cm^2/s] is the bolometric radiation flux vector and Γ [erg/cm^3/s] is the non-radiative heating rate per volume. In the viscous case, we use $\Gamma = \Gamma_{\rm vis}$, see Eq. (37) with stellar mass $M_\star$ and stellar radius $R_\star$ instead of $M_{\rm p}$ and $R_{\rm p}$ for circumstellar discs. The additional non-radiative heating leads to a surplus emission of photon energy according to

$$4\pi \int \kappa_\nu^{\rm abs} \Big(B_\nu(T) - J_\nu \Big) d\nu \;=\; \Gamma \,, \tag{53}$$

where $\kappa_\nu^{\rm abs}$ is the dust absorption coefficient at frequency ν, $B_\nu(T)$ the Planck function, and J_ν the mean intensity. For passive discs, we have $\Gamma = 0$, in which case Eq. (53) simplifies to the ordinary condition of radiative equilibrium.

The numerical solution method for the radiative transfer (RT) in ProDiMo involves iterations where formal solutions with isotropic scattering are computed along multiple rays to cover the full 4π solid angle as seen from every point in the disc, see Sect. 4 in Woitke et al. (2009). A formal solution results in new $J_\nu(r,z)$ which are used to update the dust temperatures $T_{\rm dust}(r,z)$ and source functions. The convergence of this Λ-iteration is accelerated by the Ng-method (see Auer, 1984). However, despite this acceleration, the convergence is still slow in the midplane, which is a serious problem for all radiative transfer codes for discs, including the Monte-Carlo codes, see Pinte et al. (2009).

Here we describe a method how to avoid this problem. In the diffusion approximation, the bolometric radiation flux

$$\vec{F}(r,z) = -\frac{4\,\pi}{3\kappa_{\rm R}(r,z)} \, \mathbf{grad}\, J(r,z) \tag{54}$$

is given by the gradient of the bolometric mean intensity $J(r,z)$. The Rosseland-mean and Planck-mean opacities are defined as

$$\frac{1}{\kappa_{\rm R}(r,z)} = \int \frac{1}{\kappa_\nu^{\rm ext}(r,z)} \frac{dB_\nu(T)}{dT} \, d\nu \;\Big/ \int \frac{dB_\nu(T)}{dT} \, d\nu \tag{55}$$

$$\kappa_{\rm P}(r,z) = \int \kappa_\nu^{\rm abs}(r,z) B_\nu(T) \, d\nu \;\Big/ \int B_\nu(T) \, d\nu \,, \tag{56}$$

where $\kappa_\nu^{\rm ext}(r,z)$ is the extinction coefficient and $T = T_{\rm dust}(r,z)$ the dust temperature at position (r,z) in the disk.

At the beginning of a new RT iteration, the Rosseland and Planck opacities are calculated based on the frequency-dependent disk opacity structure and the current $T_{\rm dust}(r,z)$. Next, we compute radial and vertical Rosseland optical depths $\tau_{\rm Ross} = \int \kappa_{\rm R} \, ds$ from every point. When the radial inward, radial outward and vertical upward Rosseland optical depths from that point are all larger than a threshold value (we use a value of 10 here), the point is flagged as being optically thick, and added to the subset of optically thick points

$$\mathcal{M} = \{ (i,j) \mid (r_i, z_{i,j}) \text{ is optically thick} \} \,. \tag{57}$$

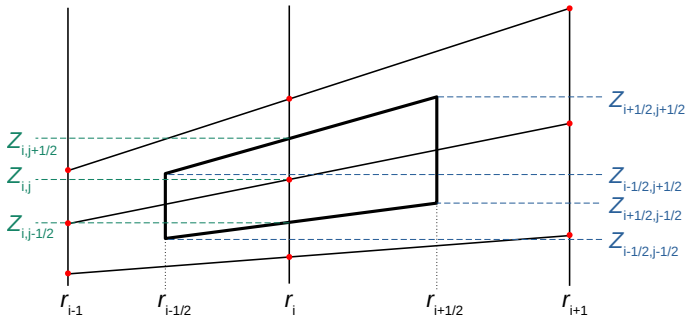

Figure 3.9: Volume and areas for the spatial cell around point (i, j). The mean intensities J and Rosseland opacities κ_R are available on the grid points (i, j) marked with red dots.

where i and j are the 2D-indices of a grid point at radius r_i and height $z_{i,j}$. The following method only updates the mean intensities $J_{i,j}$ and dust temperatures $T_{i,j}$ on the optically thick grid points $(i, j) \in \mathcal{M}$, whereas all other points are regarded as fixed boundary conditions for this problem. To pick up the bolometric mean intensities on the boundary points, we integrate Eq. (53) assuming that J_ν is close to a Planckian, hence

$$J(r,z) = B(T) - \frac{\Gamma(r,z)}{4\pi\,\kappa_P(r,z)}\,. \tag{58}$$

where $B(T) = \sigma\,T_{\rm dust}(r,z)^4/\pi$ is the frequency-integrated Planck function. Integration of Eq. (52) over the volume associated with grid point (i, j) as sketched in Fig. 3.9 results in the following numerical equation

$$\begin{aligned} &A^{\rm ver}_{i-1/2,j} D_{i-1/2,j} \frac{J_{i,j} - J_{i-1,j}}{\Delta r_{i-1/2}} \;+\; A^{\rm ver}_{i+1/2,j} D_{i+1/2,j} \frac{J_{i,j} - J_{i+1,j}}{\Delta r_{i+1/2}} \\ &+\; A^{\rm hor}_{i} D_{i,j-1/2} \frac{J_{i,j} - J_{i,j-1}}{\Delta z_{i,j-1/2}} \;+\; A^{\rm hor}_{i} D_{i,j+1/2} \frac{J_{i,j} - J_{i,j+1}}{\Delta z_{i,j+1/2}} \;=\; V_{i,j}\,\Gamma_{i,j}\,, \end{aligned} \tag{59}$$

where we note that the vertical fluxes through the cell boundaries involve a scalar product with the slanted normal vector of the surface area, hence $A^{\rm hor}_i$ is the cell's horizontal area after projection onto the vertical direction. The following abbreviations are used for the distances, vertical and horizontal areas, and the volume. They are given by the geometry of the ProDiMo grid points, which are aligned on radial rays on which z/r is

constant

$$r_{i-1/2} = \sqrt{r_i r_{i-1}} \tag{60}$$
$$r_{i+1/2} = \sqrt{r_i r_{i+1}} \tag{61}$$
$$\Delta r_{i-1/2} = r_i - r_{i-1} \tag{62}$$
$$\Delta r_{i+1/2} = r_{i+1} - r_i \tag{63}$$
$$z_{i,j-1/2} = \frac{1}{2}(z_{i,j} + z_{i,j-1}) \tag{64}$$
$$z_{i,j+1/2} = \frac{1}{2}(z_{i,j} + z_{i,j+1}) \tag{65}$$
$$z_{i-1/2,j-1/2} = z_{i,j-1/2}\frac{r_{i-1/2}}{r_i} \tag{66}$$
$$z_{i-1/2,j+1/2} = z_{i,j+1/2}\frac{r_{i-1/2}}{r_i} \tag{67}$$
$$z_{i+1/2,j-1/2} = z_{i,j-1/2}\frac{r_{i+1/2}}{r_i} \tag{68}$$
$$z_{i+1/2,j+1/2} = z_{i,j+1/2}\frac{r_{i+1/2}}{r_i} \tag{69}$$
$$A^{\mathrm{ver}}_{i-1/2,j} = 2\pi\, r_{i-1/2}(z_{i-1/2,j+1/2} - z_{i-1/2,j-1/2}) \tag{70}$$
$$A^{\mathrm{ver}}_{i+1/2,j} = 2\pi\, r_{i+1/2}(z_{i+1/2,j+1/2} - z_{i+1/2,j-1/2}) \tag{71}$$
$$A^{\mathrm{hor}}_{i} = \pi(r^2_{i+1/2} - r^2_{i-1/2}) \tag{72}$$
$$V_{i,j} = A^{\mathrm{hor}}_{i}(z_{i,j+1/2} - z_{i,j-1/2}) \tag{73}$$

The radiative diffusion coefficients are defined as

$$D_{i,j} = \frac{4\pi}{3\kappa_{\mathrm{R}}(r_i, z_{i,j})} \tag{74}$$
$$D_{i-1/2,j} = \sqrt{D_{i,j}D_{i-1,j}} \tag{75}$$
$$D_{i+1/2,j} = \sqrt{D_{i,j}D_{i+1,j}} \tag{76}$$
$$D_{i,j-1/2} = \sqrt{D_{i,j}D_{i,j-1}} \tag{77}$$
$$D_{i,j+1/2} = \sqrt{D_{i,j}D_{i,j+1}} \tag{78}$$

Equation (59) states a system of linear equations for the unknown bolometric mean intensities $J_{i,j}$ on the optically thick points $(i, j) \in \mathcal{M}$ of the form

$$\mathcal{A} \cdot \vec{X} = \vec{B}\,, \tag{79}$$

where all quantities in Eqs. (60) to (78) are constants forming the matrix $\mathcal{A}$, and the volumes $V_{i,j}$ and heating rates $\Gamma_{i,j}$ are constants forming the rest vector $\vec{B}$. The unknowns $\{J_{i,j}\}$ at the optically thick points $(i, j) \in \mathcal{M}$ constitute the solution vector $\vec{X}$. All terms in Eq. (59) that involve the other $J_{i,j}$ on the adjacent points are also included into $\vec{B}$.

The matrix equation to solve (Eq. 79) has a typical dimension of a few hundred to a few thousand, depending on disk mass, geometry, and dust parameters.

This way we can solve the 2D radiative diffusion problem for the unknown mean intensities in the optically thick region as a linear boundary value problem in one go, where there is one layer of points surrounding the optically thick regions which sets the boundary values. Our method calculates how the disk transports the photon energy through the optically thick core inside of the boundary layer. It is applicable to both cases, passive discs without viscous heating and active discs with $\Gamma > 0$.

Once the $\{J_{i,j}\}$ on $(i, j) \in \mathcal{M}$ have been determined, we revert the process described by Eq (58)

$$B(T) = J(r, z) + \frac{\Gamma(r, z)}{4\pi\,\kappa_{\rm P}(r, z)} \tag{80}$$

$$T_{\rm dust}(r, z) = \left(\frac{\pi}{\sigma} B(T)\right)^{1/4} \tag{81}$$

and multiply the frequency-dependent mean intensities $J_\nu(r, z)$, as they were determined prior to the application of the diffusion solver, by a constant factor to make Eq. (53) valid again, thereby keeping the previously calculated frequency distribution of $J_\nu(r, z)$.

After having modified $T_{\rm dust}(r, z)$ and $J_\nu(r, z)$ this way on all grid points $(i, j) \in \mathcal{M}$, the normal RT solution method resumes, which begins by calculating the source functions on all grid points and continues by performing a formal solution.

Figure 3.10 shows a benchmark test against the Monte Carlo radiative transfer program MCMax (Min et al., 2011). We consider the disk model that is described in detail by Woitke et al. (2016), see their table 3. The central star is a 2 Myr old T Tauri star with a mass of 0.7 $M_\odot$ and a luminosity of 1 $L_\odot$, the disk has a mass of 0.01 $M_\odot$, with a gas/dust ratio of 100. The dust is composed of 60% silicate, 15% amorphous carbon and 25% porosity. The dust grains have sizes between 0.05 μm and 3 mm, with an unsettled powerlaw size-distribution of index -3.5. The dust is settled according to the prescription of Dubrulle et al. (1995) with $\alpha_{\rm settle} = 0.01$. In contrast to this standard passive T Tauri model, we use here a mass accretion rate of $\dot{M}_{\rm acc} = 10^{-8}$ M$_\odot$/yr to set the viscous heating of the disk according to Eq. (37). We use 140 radial $\times$100 vertical grid points, and 40 wavelength bins. Figure 3.10 shows good agreement.
Figure 3.10 reveals a number of interesting features in the disk temperature structure:

- The dust temperature at the inner rim is not much affected by viscous heating.
- From top to midplane, the temperature first decreases in the disk shadow, but then the trend is reversed and the temperature re-increases towards the midplane as the viscous heat pumped into the disk needs to flow outward, that is mostly upward, which according to the diffusion approximation requires a negative temperature gradient.
- There is little effect of viscous heating on $T_{\rm dust}$ outside of the optically thick region which extends outward to about 10 au and upward to about $z/r \approx 0.1 - 0.15$ in this model.

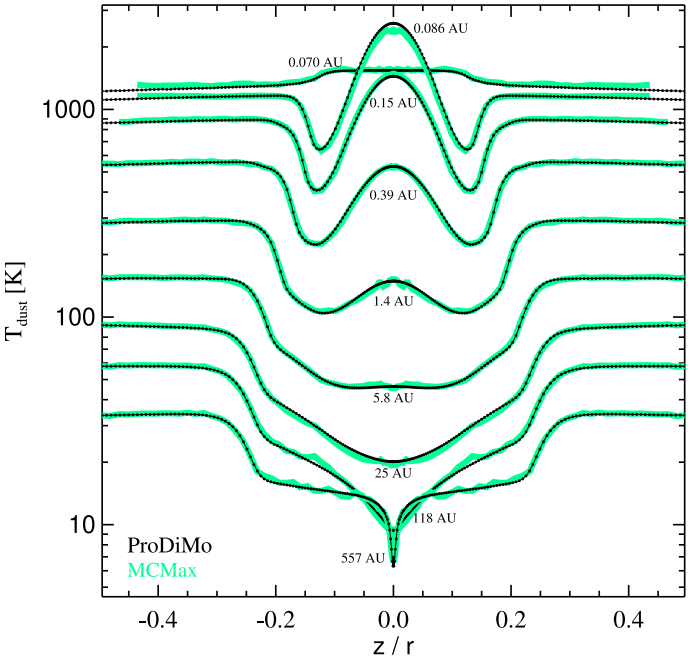

Figure 3.10: Benchmark test for a viscous circumstellar disk with a disk mass of 0.01 $M_\odot$ and a mass accertion rate of $\dot{M}_{\rm acc} = 10^{-8}\,{\rm M}_\odot/{\rm yr}$, see text. The green lines are temperature cuts at selected radii calculated by MCMax, the small wiggles are due to the Monte-Carlo noise. The black dots show the temperatures calculated by ProDiMo.

- The temperature profile across the midplane beyond the tapering radius ($R_{\rm tap}$ = 100 au, see Woitke et al., 2016) shows a deep minimum around the midplane $z = 0$. This is because of the extreme dust settling that occurs in these diluted outer disk regions, creating more optical thickness along the midplane, which brings down the midplane temperature to only 6 K in this model.

Figure 3.11 compares the calculated midplane temperatures between ProDiMo and MCMax, which reveals dust temperatures as high as 2800 K, which is of course questionable because at such temperatures, the dust grains are expected to sublimate.

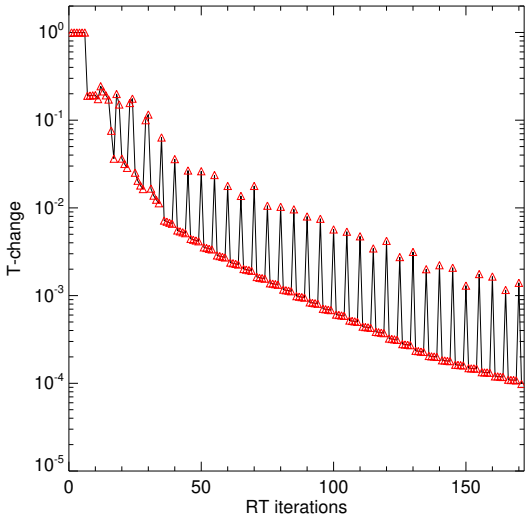

Figure 3.12: Maximum relative temperature change between iterations as function of RT iteration number.

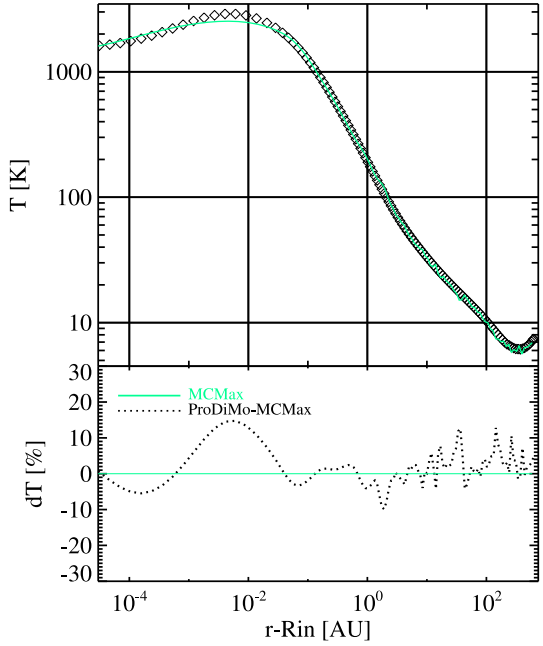

Figure 3.11: Midplane temperature $T_{\mathrm{dust}}(r, 0)$ as function of the log-distance from the inner rim. Again, the green line is the temperature profile calculated by MCMax, and the small black diamonds show the temperature values calculated by ProDiMo.

Figure 3.12 shows the convergence of the RT method, achieving residual relative temperature changes smaller than 10^{-4} after about 150 RT iterations. The maximums occuring each 5th iteration are due to the Ng-acceleration algorithm.

A.2 Adsorption energies

Table 8: Adsorption energies of the most prevalent molecular ices found in our model CPDs.

Ice	E_{ads} [K]	ref.
H_2O	4800	a
NH_3	5534	b
NH_2	3956	b
C_2H_6	2300	c
C_2H_4	3487	b
C_2H_2	2587	d
CO_2	2990	e
CH_3OH	5534	a
OH	2850	b

(a) (Brown and Bolina, 2006)
(b) (Garrod and Herbst, 2006)
(c) (Öberg et al., 2009)
(d) (Collings et al., 2004)
(e) (McElroy et al., 2013)

The adsorption energies of our most common ices and their respective references are listed in Table 8.

A.3 Surface density slope

Our reference CPDs have a surface density powerlaw exponent $\epsilon = 1$. The steady-state solution for a constant-$\dot{M}$ decretion α-disk is $\epsilon \approx 1.25$ (Batygin and Morbidelli, 2020). The midplane ice mass fraction for a variety of possible values of ϵ is shown in Fig. 3.13. For a higher ϵ the NH_3 iceline responsible for the “bump" in the f_{ice} profile at 0.07 R_H moves outwards only negligibly. In the inner disk however the ice mass fraction increases due to a combination of the lower midplane dust-to-gas and more efficient H_2O formation.

A.4 Background temperature

Throughout this work we have assumed that the CPD is embedded in a radiation field in which the equilibrium dust temperature is 50 K. The midplane dust temperature at

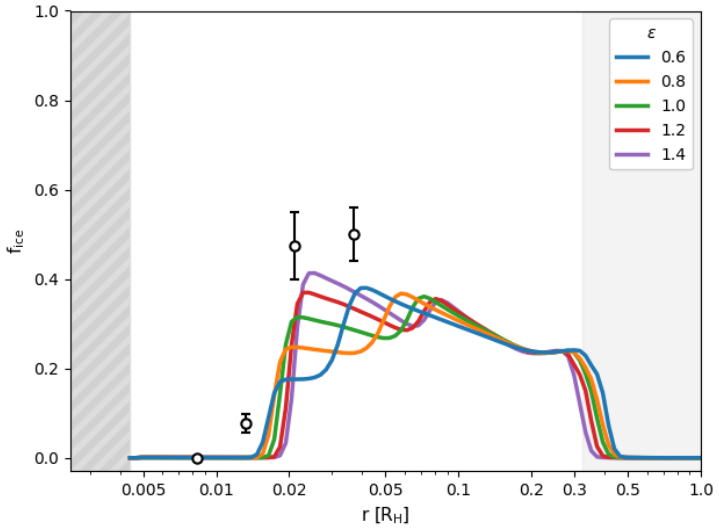

Figure 3.13: Midplane ice mass fraction for a variety of surface density powerlaw exponents ϵ for the (7-11) reset CPD with global $d/g = 10^{-3.3}$.

the gap center within the circumstellar disk is 50±2 K, for a solar luminosity 0.83 $L_\odot$, gap A_V = 0.008, and heliocentric distance 5.2 au. For earlier formation times with correspondingly higher solar luminosities (2.34-13.6 $L_\odot$), we find gap midplane dust temperatures ranging from 70-120 K at 5.2 au.

We have assumed that the final stage of Jupiter's accretion and moon formation occured at a radial distance from the Sun of 5.2 au. Volatile enrichment in Jupiter's atmosphere indicates it may have formed further out at circumstellar disk temperatures < 25 K or at radii > 30 au (Öberg and Wordsworth, 2019). The Nitrogen abundance of Jupiter, approximately 4× solar, may suggest additional N_2 was accreted from the solar nebula near the N_2 iceline (Bosman et al., 2019). In light of this possibility we consider also lower background temperatures down to 20 K. The midplane f_{ice} for the reference (7-11) CPD can be seen in Fig.3.14. Inside the optically thick region of the CPD the influence of the background temperature T_{back} is marginal for temperatures ≤ 70 K. Above 70 K the more volatile NH_3 and CO_2 are unstable as ices and only water ice remains. Below 40 K the outer disk is able to retain ices at radii where A_V < 1 as the photodesorption timescale is in excess of the viscous timescale.

A.5 Vertical mixing

We have made the simplifying assumption that material which accretes onto the CPD is instantaneously distributed vertically throughout the disk. The shock front may be

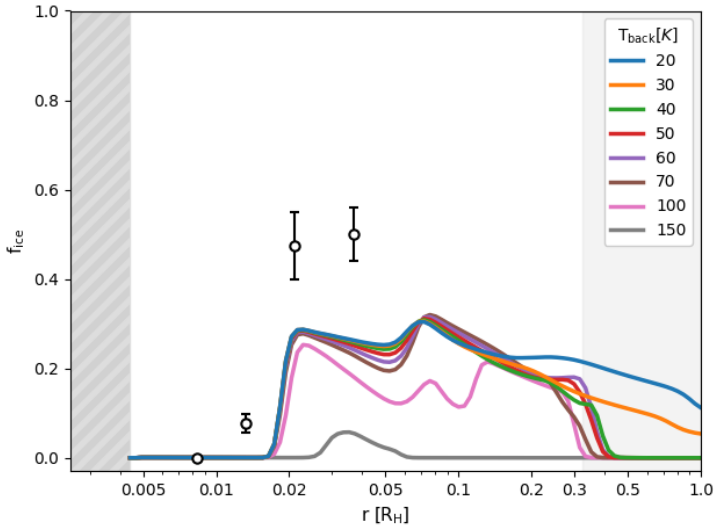

Figure 3.14: Midplane ice mass fraction for a variety of background temperatures $T_{\rm back}$ for the (7-11) reset CPD and global $d/g = 10^{-3.3}$. The four empty circles with error bars represent the Galilean satellites at their present day locations and composition. The gray striped region on the left represents the inner cavity and the light gray shaded region on the right represents the gravitationally unstable zone.

found at a few (~ 5) scale heights above the CPD midplane (Tanigawa et al., 2012). At 5 scale heights above the centrifugal radius the dust temperature $T_{\rm dust} = 123$ K (relative to 89.5 K at the midplane), and optical extinction A_V=0.004 (16.4 at the midplane). The velocity of vertical mixing by turbulent diffusion can be estimated as $v_z = \alpha c_s$ where c_s is the local speed of sound (Heinzeller et al., 2011). We find $v_z \sim 0.5 - 1$ m s^{-1} in this region for the high-viscosity CPDs, assuming that the magnitude of the turbulence is constant from the midplane up to $z = 5H$. The resulting vertical diffusion mixing timescale is 0.01 $t_{\rm visc}$ (10-100 yr). We perform a test in the (7-11) CPD in which a parcel of gas is accreted at $z = 5H$ and iteratively evolve its chemistry in steps as it diffuses towards the midplane over 10 yr to understand the impact of more tenuous and high temperature conditions in the initial stages of ice formation (see Fig. 3.15). By the end of the stage of rapid formation of water (1-2 yr), the ice abundance has equalized to the fiducial case at the midplane.

A.6 Continued ice deposition on trapped grains

In each of the reference CPDs grains of a certain size range remain trapped within the CPD if we assume that gas actively decretes via the outer edge of the disk. A trapped

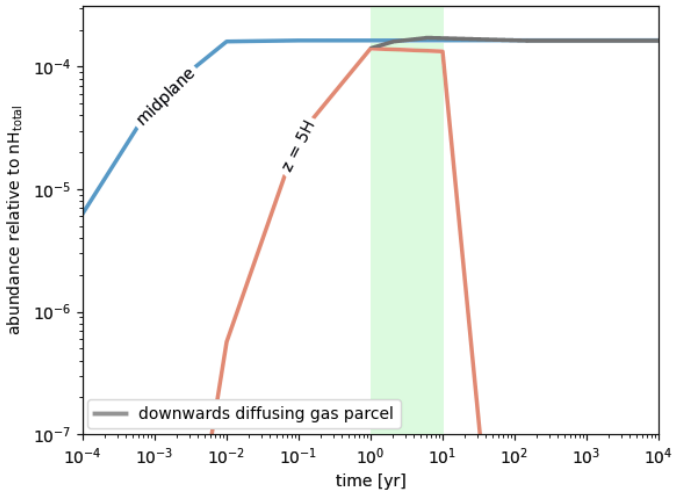

Figure 3.15: Evolution of the water ice abundance relative to the total number of hydrogen nuclei at the midplane (blue) and at 5 scale heights above the CPD midplane (red), and in the case of the gas parcel which drifts from $z = 5H$ downwards to the midplane over a period of 100 yr (grey). The period in which the altitude of the gas parcel was iteratively lowered towards the midplane is highlighted in light green.

grain will increase physically in size as ice adsorbs onto its surface and thus alter its aerodynamic properties. Batygin and Morbidelli (2020) proposes that grain growth and sublimation could play a role in trapping and radial cycling of grains with size 0.1-10 mm. The size range of trapped grains is $\sim 0.01 - 1$ mm in our high-mass CPDs and $\sim 10^{-3} - 0.01$ mm in the low-mass CPDs, representing 2.5% and 0.1% of the infalling dust mass that reaches the midplane, respectively. A modal icy grain is typically coated in no more than 4000 monolayers of water ice. Assuming a monolayer thickness ~ 0.5 nm (Zangi and Mark, 2003) and compact morphology, an icy mantle no more than 1 μm thick will form. A grain of size 0.05 μm can thus increase in size by a factor 20 and have a density corresponding more closely to water ice rather than silicate. For a 1 μm thick mantle the aerodynamic effect of increased cross-section is negated by the corresponding reduction in grain density. If the trapped grain icy mantles continue to grow mantles beyond several 1000 monolayers, the new equilibrium trap radius drifts inwards. Realistically only a fraction (0.01-0.1%) of the total CPD gas mass is accreted per year. Mantle growth for a trapped grain will thus not exceed ~ 2 nm yr^{-1} on average. The time for a grain to grow an icy mantle that allows it to drift to the trap inner edge is then $\sim 10^6$ yr (high-mass CPD) or $\sim 10^5$ yr (low-mass CPD) assuming a compact grain structure. Ice deposition is thus unlikely to allow grains to escape traps. This

estimate does not take into consideration grain growth by coagulation or fragmentation by collision.

A.7 Chemical abundances of the 0D "molecular cloud" model

The input parameters of the 0D molecular cloud model can be found in Table 9. A comparison between the model column densities of several common species with observations of TMC-1 can be found in Fig. 3.16. While most of the common species column density agrees relatively well with observations, the abundance of S-bearing species hinge on the uncertainties regarding the S elemental abundance (Ruffle et al., 1999).

Table 9: Molecular cloud parameters

Parameter	Value	Unit
Hydrogen density	10^4	cm^{-3}
Gas temperature	10.0	K
Dust temperature	10.0	K
Optical extinction	10.0	-
Mean grain radius	0.1	μm
Cloud Lifetime	1.7×10^5	yr

Note: Parameter values of the molecular cloud model and integration time are chosen according to the method of Helling et al. (2014) recommended for TMC-1 (Taurus Molecular Cloud) by McElroy et al. (2013). Initial atomic abundances intended to represent typical diffuse interstellar medium conditions are also adopted from (McElroy et al., 2013).

A.8 CPD dust-to-gas ratio

In Fig. 3.17 we explore the resulting midplane ice mass fraction f_{ice} for possible values of the global dust-to-gas ratio from the canonical 10^{-2} down to 10^{-4}. The maximum grain size and dust population size distribution are kept constant. A global dust-to-gas ratio of $10^{-3.3}$ results in maximum midplane f_{ice} values most consistent with the Galilean satellite bulk compositions and hence is adopted as the reference value throughout this work.

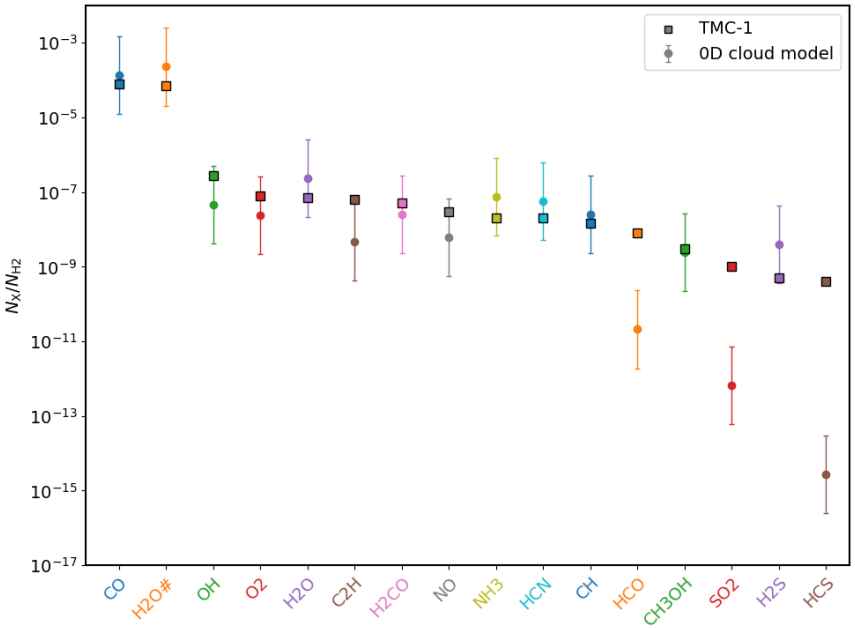

Figure 3.16: Ratio of the column density of several common species relative to H_2 in the 0D molecular cloud model (circles with error bars) to observational values for TMC-1 (squares with black border). Error bars on model values represent a factor 10x uncertainty for illustrative purposes. TMC-1 abundances are taken from (Suutarinen et al., 2011) (OH,CH), (Sakai et al., 2010) (C_2H), (Smith et al., 2004; Walsh et al., 2009) otherwise.

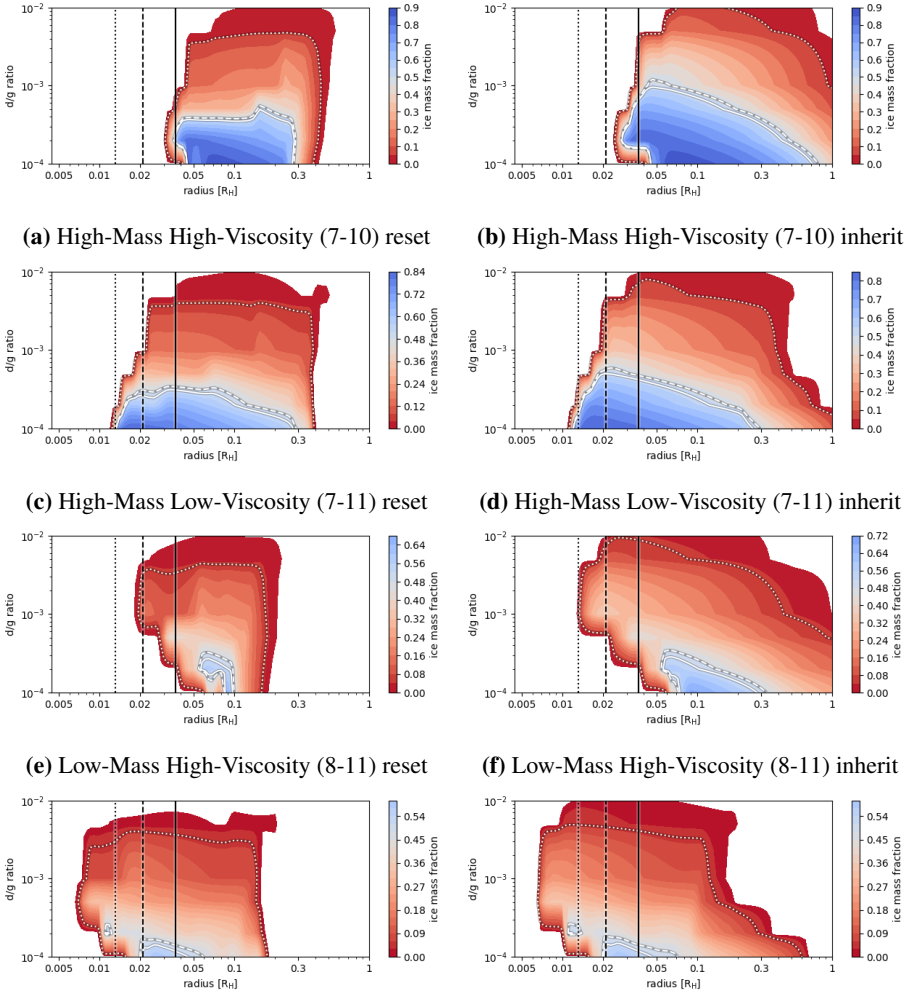

(a) High-Mass High-Viscosity (7-10) reset

(b) High-Mass High-Viscosity (7-10) inherit

(c) High-Mass Low-Viscosity (7-11) reset

(d) High-Mass Low-Viscosity (7-11) inherit

(e) Low-Mass High-Viscosity (8-11) reset

(f) Low-Mass High-Viscosity (8-11) inherit

(g) Low-Mass Low-Viscosity (8-12) reset

(h) Low-Mass Low-Viscosity (8-12) inherit

Figure 3.17: Midplane radial ice mass fraction f_{ice} of the dust-to-gas ratio parameter exploration for the chemically reset (left column) and chemically inherited (right column) reference CPDs. The black dotted, dashed, and solid lines indicate the radial position of Europa, Ganymede, and Callisto. The white dotted, dashed, and solid lines indicate where f_{ice} is equivalent to the estimated ice mass fraction of Europa (0.05), Ganymede (0.48), and Callisto (0.52).

Chapter 4

Circumplanetary Disk Ices

II. Composition

N. Oberg, S. Cazaux, I. Kamp, T.M. Bründl, W.F. Thi & C. Immerzeel

Abstract

Context: The subsurface oceans of icy satellites are among the most compelling potentially habitable environments in the solar system. Whether a liquid subsurface layer can be maintained over geological timescales is influenced by its chemical composition. The composition of icy satellites is linked intimately to that of the circumplanetary disk (CPD) in which they form. The CPD accretes material from the surrounding circumstellar disk in the vicinity of the planet, but the degree of chemical inheritance is unclear.
Aims: We aim to investigate the composition of ices in chemically reset or inherited circumplanetary disks to inform interior modeling and the interpretation of in-situ measurements of icy solar system satellites with an emphasis on the Galilean moon system.
Methods: We use the radiation-thermochemical code ProDiMo to produce circumplanetary disk models from which we extract the ice composition from time-dependent chemistry which incorporates gas-phase and grain-surface reactions.
Results: Initial sublimation of ices during accretion may result in a CO_2-rich ice composition due to efficient OH formation at high gas densities. In the case of a Jovian CPD the sublimation of accreted ices results in a CO_2 iceline between the present day orbits of Ganymede and Callisto. Sublimated ammonia ice is destroyed by background radiation while drifting towards the CPD midplane. Liberated nitrogen becomes locked in N_2 due to efficient self-shielding, leaving ices depleted in ammonia. A significant ammonia ice component remains only when ices are inherited from the circumstellar disk.
Conclusions: The observed composition of the Galilean moons is consistent with the sublimation of ices during accretion onto the CPD. In this scenario the Galilean moon ices are nitrogen-poor, and CO_2 on Callisto is endogenous and primordial. Ice composition is significantly altered after an initial reset of accreted circumstellar ice. The chemical history of the Galilean moons stands in contrast to the Saturnian system, where the composition of the moons corresponds more closely with directly inherited circumstellar disk material.

N.Oberg et al. 2022 submitted to A&A

4.1 Introduction

The search for habitable worlds beyond the solar system has historically focused on planets in the so-called "habitable zone" where surface conditions theoretically support the presence of liquid water (Hart, 1979). In the solar system itself however, icy satellites and minor bodies outside of the classical habitable zone are the most common type of world known to host oceans of liquid water (Hussmann et al., 2006; Nimmo and Pappalardo, 2016). Evidence strongly supports the presence of a subsurface ocean on the Galilean satellites Europa and Ganymede, and to a lesser extent Callisto (Carr et al., 1998; Khurana et al., 1998; Kivelson et al., 2002; Sohl et al., 2002; Saur et al., 2015). The resonant configuration of the satellites prevents damping of orbital eccentricities, producing levels of tidal heating capable of sustaining subsurface oceans over geological timescales (Peale and Lee, 2002; Hussmann and Spohn, 2004; Showman et al., 1997). Whether or not a given level of tidal heating produces subsurface melt depends in part on the composition of the satellite ices. Proposed abundant impurities include NH_3, CH_4, CO, and CO_2, and the salts $MgSO_4$ and NaCl (Kargel, 1992; Mousis and Alibert, 2006). The liquidus temperature of co-deposited ice mixtures can be depressed by the presence of NH_3 (Choukroun and Grasset, 2010; Sohl et al., 2010), or methanol (CH_3OH) (Deschamps et al., 2010; Dougherty et al., 2018), and salts to a lesser extent. Hence, the composition of the volatile reservoir from which icy satellites form is of direct relevance to the presence of a subsurface ocean, their geothermal and physical evolution (Hammond et al., 2018), the interpretation of in-situ geophysical measurements (Vance et al., 2018), and the eventual atmospheric composition by outgassing or impact dissociation (Sekine et al., 2014; Glein, 2015).

Ammonia in particular is important to the interior state and evolution of icy bodies. The presence of NH_3 in the form of dihydrate can drive differentiation of rock and ice (Desch et al., 2009). Ammonia in a pure H_2O-NH_3 eutectic system produces a freezing point depression of ~100 K (Kargel, 1992; Grasset et al., 2000; Leliwa-Kopystyński et al., 2002). Ammonia can also reduce the density of melt with implications for buoyancy and cryovolcanism (Croft et al., 1988) and increase viscosity, reducing the efficiency of convection (Grasset et al., 2000). Ammonia has been detected in the plumes of Enceladus (Waite et al., 2009) but not on the surface of the Galilean moons. Tentative evidence for a subsurface ocean on Callisto would be bolstered by the presence of a 1-5% ammonia component (Kirk and Stevenson, 1987; Showman and Malhotra, 1999; Spohn and Schubert, 2003).

In the "gas-starved" circumplanetary disk (CPD) paradigm, moon formation occurs in a relatively low mass, cool disk which must accumulate the solids to form giant moons over time (Canup and Ward, 2002, 2006; Batygin and Morbidelli, 2020). Infalling material from the surrounding circumstellar disk may be shock-heated during accretion onto the CPD (Szulágyi, 2017; Szulágyi and Mordasini, 2017; Aoyama et al., 2018), with increasing shock temperature for increasing planetary mass. If the shock heating chemically resets infalling gas or ices, new ice formation must occur within the CPD to produce the icy satellites we see today. The resulting composition of the satellite

ices may then depart substantially from those in the planetary feeding zone.

Prior work modeling equilibrium condensation chemistry in a Jovian CPD suggests that in the event of an initial vaporization of ices "mostly inefficient" gas-phase reactions lead to ratios of CO_2:CO:CH_4 and N_2:NH_3 not substantially different than those in the feeding zone of Jupiter (Mousis and Alibert, 2006; Mousis et al., 2006). However it has long been recognized that grain-surface chemistry plays a critical role in the formation of many common molecules under interstellar conditions (Hasegawa et al., 1992; van Dishoeck and Blake, 1998; Cazaux and Tielens, 2002; Caselli et al., 2004; Garrod et al., 2006; Ruaud et al., 2015; Wakelam et al., 2017). The use of a more comprehensive modeling approach including grain-surface and photochemistry to revisit the formation of ices in CPDs is thus motivated. We aim to investigate the composition of ices that form in a chemically reset CPD with viscous timescale $10^3 - 10^4$ yr, where infalling ices are sublimated and gas is atomized by shock-heating. These results will be contrasted with a partial reset in which only ices are sublimated during accretion, and with a full chemical inheritance scenario in which the composition of the circumstellar disk gas and ice is preserved. We intend to link observations of solar system icy satellites with modern chemical disk models to lay the foundation for our understanding of how icy moons are built up from material in the CPD.

4.2 Methods

We use the radiation-thermochemical disk modeling code ProDiMo[5] to model gas and dust chemistry and physics in disks (**Pro**toplanetary **Di**sk **Mo**del) (Woitke et al., 2009, 2016; Kamp et al., 2010b, 2017; Thi et al., 2011, 2020a,a). The gas-grain chemistry is solved self-consistently with the 2D radiative transfer and heating/cooling balance using a rate equation based approach. Most reaction rates are selected from the UMIST2012 database (McElroy et al., 2013) and three-body collider reactions are adopted from the UMIST2006 rate file (Woodall et al., 2007) as they were not included in the 2012 release. In the following sections we review the implementation of the grain surface chemistry (Sect. 4.2.1), extensions to our standard chemical network (Sect. 4.2.1), and properties of the CPD model (Sect. 4.2.2).

4.2.1 Grain surface Chemistry

ProDiMo includes a rate-equation based, statistical two-phase approach to gas and dust grain surface chemistry which is largely based on the work of Hasegawa et al. (1992). Gas-phase atoms and molecules can become weakly adsorbed to grain surface physisorption sites. Physisorbed species diffuse in a random-walk process "hopping" from one physisorption site to another (Barlow and Silk, 1976). Diffusion occurs thermally if there is sufficient energy to overcome a diffusion barrier or can otherwise occur by tunneling. The surface diffusion rate is the sum of the thermal, tunneling, and cosmic-ray induced diffusion rates. The rate of thermal diffusion of species i is

[5] https://prodimo.iwf.oeaw.ac.at/

$$R_i^{\rm diff,th} = \nu_{0,i} Q_i^{\rm diff}(a_i^{\rm diff}, E_i^{\rm diff}) e^{\Delta E_{ij}/k_{\rm B}T_{\rm d}} / n b_{\rm site}\ {\rm s}^{-1} \tag{82}$$

where $k_{\rm B}$ is the Boltzmann constant, $T_{\rm d}$ is the dust temperature, and the frequency term $\nu_{0,\rm i}$ describing characteristic lattice vibration is

$$\nu_{0,i} = \sqrt{\frac{2N_{\rm surf}E_i^{\rm b}}{\pi^2 m_i}}, \tag{83}$$

$N_{\rm surf}$ is the surface density of adsorption sites $1.5{\times}10^{15}$ cm^{-2}. The number of adsorption sites per monolayer on a grain of radius a is $nb_{\rm site} = 4\pi N_{\rm surf} a^2$. $E_{\rm i}^{\rm b}$ is the binding energy and m_i is the mass of the species. We use a tunneling-corrected form of the Arrhenius equation, Bell's formula $Q_i^{\rm diff}$ to determine the surface diffusion tunneling rate (Bell, 1980):

$$Q_i^{\rm diff} = \frac{\beta e^{-\alpha} - \alpha e^{-\beta}}{\beta - \alpha}, \tag{84}$$

where

$$\alpha = E_i^{\rm diff}/k_{\rm B}T_{\rm d} \tag{85}$$

and

$$\beta = \frac{4\pi a_i^{\rm diff}}{h}\sqrt{2m_i E_i^{\rm diff}}. \tag{86}$$

$E_i^{\rm diff}$ is the diffusion activation energy, $a_i^{\rm diff}$ is the diffusion activation barrier width, and h is the Planck constant. ΔE_{ij} is the difference in binding energy between two adsorption sites i and j. $\Delta\ {\rm E}_{ij} = 0$ if $\ {\rm E}_i^b \leq {\rm E}_j^b$, hence for a random hop between two physisorption sites $\Delta E = 0$. The cosmic-ray induced diffusion rate $R_i^{\rm diff,CR}$ is adopted from (Hasegawa and Herbst, 1993; Reboussin et al., 2014)

$$R_i^{\rm diff,CR} = f(70{\rm K}) R_i^{\rm diff,th}(70{\rm K}) \frac{\zeta_{\rm CR}}{5\times10^{-17}}\,{\rm s}^{-1} \tag{87}$$

where $\zeta_{\rm CR}$ is the cosmic ray ionization rate and $f(70{\rm K}) = 3.16\times10^{-19}$ is the duty-cycle of the grain at 70 K. The total diffusion rate $R_i^{\rm diff}$ is then the sum of the thermal and cosmic-ray induced diffusion rates.

Species which are physisorbed to a grain surface can react directly with species coming from the gas-phase (Eley-Rideal) or with other physisorbed species (Langmuir–Hinshelwood). Reaction products can remain on the grain surface or chemically desorb into the gas-phase. Reactions between physisorbed species follow the prescription of Hasegawa et al. (1992). The reaction rate coefficients between two surface-adsorbed species is the probability of a reaction per encounter multiplied by the encounter rate between the two species diffusing across the surface. The encounter rate between two adsorbed species i and j hopping across the surface is then

$$k_{ij} = \kappa_{ij}(R_i^{\rm diff} + R_j^{\rm diff})/n_d\ \ {\rm cm}^3{\rm s}^{-1} \tag{88}$$

where κ_{ij} is the reaction probability, $R_i^{\rm diff}$ and $R_j^{\rm diff}$ are the diffusion rates (s^{-1}) for species i and j, and $n_{\rm d}$ is the dust grain number density (cm^{-3}). The reaction probability κ_{ij} takes into account the competition between association of the species and diffusion (Garrod and Pauly, 2011; Bonfanti and Martinazzo, 2016; Ruaud et al., 2016),

$$\kappa_{ij} = \frac{Q_{\rm Bell}(a_{ij}^r, E_i^{\rm act})}{Q_{\rm Bell}(a_{ij}^r, E_i^{\rm act}) + P_i^{\rm diff} + P_j^{\rm diff}} \tag{89}$$

where a_{ij}^r is the reactive barrier width, $E_i^{\rm act}$ is the activation energy of the reaction barrier, and $P_i^{\rm diff} = R_i^{\rm diff}/\nu_{0,i}$.

We assume the semi-equilibrium theory in which reactions between physisorbed and gas-phase species (Eley-Rideal) is equal to the probability of the gas atom colliding with the physisorbed species multiplied by the probability of the gas-phase species having sufficient energy to overcome the reaction barrier. Impinging gas-phase species are assumed to have an energy relative to the surface species $1/2k_{\rm B}T_{\rm g} + E_i^b$ where $T_{\rm g}$ is the gas temperature and E_i^b is the binding energy.

Photon and cosmic-ray induced dissociation and desorption of grain-surface species are also included. Adsorption and desorption processes are described fully in Thi et al. (2020a).

Extending chemistry beyond the standard network

We develop an extended chemical network based on the "DIANA standard large" network described in Kamp et al. (2017) which contains 235 species and 12 elements + Polycyclic Aromatic Hydrocarbons (PAHs) and is optimized for gas-phase chemistry + direct adsorption/desorption from grains. The use of grain-surface reactions necessitates the inclusion of several additional species to the DIANA standard chemical network to capture the relevant chemistry occurring at the disk midplane. These seven additional gas-phase species and six additional ices are listed in Table 10. Physisorbed atomic hydrogen and H_2 are included for their critical role in many grain-surface reactions. Hydrogenated PAH and O_2H are included for their relevance to the chemical reset scenario in which atomic H is initially very abundant. The rationale for their inclusion is discussed in the following sections. HOCO and HCOOH are more directly involved in the formation of relevant ices and their roles are discussed in Sect. 4.3.1.

Hydrogenated Polyclic Aromatic Hydrocarbons (PAH-H)

In ProDiMo the formation rate of H_2 can be calculated in multiple ways. The standard approach is that H_2 formation proceeds via a pseudo-reaction at a rate calculated according to the analytical approach of Cazaux and Tielens (2002) which presupposes that surface-chemisorbed H atoms play a dominant role at high temperatures ($\geq$100 K). However the formation of H_2 is calculated explicitly when grain-surface reactions are included in the reaction network (Thi et al., 2020a). It was noted in the accompanying

Table 10: Additional species included on top of the DIANA standard large chemical network and their respective adsorption energies and references.

	gas-phase species	
(O-O)	O_2H	
(C-O)	HOCO, HCOOH, $HCOOH^+$, $HCOOH_2^+$	
other	PAH-H,PAH-H^+	
	ices	E_{ads} [K]
	H#	600 (Cazaux and Tielens, 2002)
	H_2#	430 (Garrod and Herbst, 2006)
	O_2H#	3650 (Garrod and Herbst, 2006)
	HOCO#	2000 (Ruaud et al., 2015)
	HCOOH#	5000 (Öberg et al., 2009)
	PAH-H#	5600 (Thrower et al., 2009)

work that H_2 formation occurs in parallel with H_2O ice deposition on grains at the midplane when the CPD is chemically reset (Oberg et al., 2022b). The formation of H_2O ice after the reset is rapid, and a median sized grain is coated in several ($\gg$3) monolayers of water ice prior to the complete conversion of H to H_2. This poses a problem as the formation of H_2 via surface-chemisorbed H is considered implausible where the number of water ice monolayers exceeds a few ($\sim$ 3) (Wakelam et al., 2017). We assume that the diffusion timescale of the atomic hydrogen in a water ice matrix and subsequent difficulty of H_2 escape from the grain silicate surface precludes this formation pathway in our scenario. An alternative path to form H_2 is via hydrogenated polycyclic aromatic hydrocarbons (PAH-H) (Bauschlicher, 1998). Experimental and theoretical work has demonstrated that H_2 can form via Eley-Rideal abstractions on neutral PAH (Bauschlicher, 1998; Rauls and Hornekær, 2008; Mennella et al., 2012; Thrower et al., 2012) and cationic PAH (Hirama et al., 2004; Cazaux et al., 2016; Boschman et al., 2012). We include in the chemical network the singly hydrogenated species PAH-H, PAH-H^+, and the physisorbed ice form PAH-H# (Thrower et al., 2009) to enable this formation path.

As a first step towards H_2 formation, the neutral or ionized PAH is hydrogenated with a small (324 K) activation barrier. The H_2 formation at the CPD midplane then proceeds primarily via

$$\text{PAH-H} + \text{H} \rightarrow \text{H}_2 + \text{PAH} \tag{90}$$

and to a lesser extent ($\sim 1 - 10\%$ of the total H_2 formation rate depending on location in the CPD) directly via the gas-phase neutral-neutral reactions

$$H + HCO \rightarrow H_2 + CO \quad (91)$$
$$H + HNO \rightarrow H_2 + NO. \quad (92)$$

The resulting efficiency of H_2 formation is lower than the analytic rate of Cazaux and Tielens (2002) in part due to the low ambient temperatures (< 200 K, which in combination with the activation barrier impede the process) at the optically thick midplane. The correspondingly longer time over which atomic hydrogen is present has direct consequences for the efficiency of water formation. Gas-phase H_2O can then form via the hydrogenation of OH for an extended period of time (discussed further in Oberg et al. (2022b)).

O_2H

O_2H (hydroperoxyl radical) is a very reactive oxygen species that we have found plays a role in the formation of methanol in the inner region of chemically reset CPDs. We include the gas and ice form of O_2H in the extended chemical network with an adsorption energy of 3650 K (Garrod and Herbst, 2006). The oxygen-bearing gas-phase species abundances are sensitive to the presence of O_2H at high densities. Three-body collider reactions with free atomic hydrogen and O_2 produce O_2H. This reaction has been extensively studied both theoretically (Horowitz, 1985; Sellevag et al., 2008; Morii et al., 2009) and experimentally (Kurylo, 1972; Davidson et al., 1996; Hahn et al., 2004; Mertens et al., 2009) at high and low temperatures. With the inclusion of O_2H in the extended network the gas-phase O_2 reservoir at the midplane (nominally present at an abundance $\sim 10^{-4.4}$ relative to hydrogen in the standard network) is depleted and converted via OH into H_2O through the following reactions

$$O_2 + H + M \rightarrow O_2H + M \quad (93)$$

or

$$O_2 + HCO \rightarrow O_2H + CO \quad (94)$$

followed by

$$O_2H + H \rightarrow OH + OH \quad (95)$$
$$OH + H \rightarrow H_2O + photon \quad (96)$$

These reactions compete for the free H that is required to form methanol via

$$H_2CO + H \rightarrow CH_3O \quad (97)$$
$$CH_3O + H \rightarrow CH_3OH \quad (98)$$

and thus suppress its formation. The inclusion of O_2H in the chemical network reduces the abundance of methanol ice interior to the NH_3 iceline relative to the results of the standard chemical network by 90-99%. However this impacts negligibly the total disk-integrated methanol abundance.

4.2.2 Circumplanetary Disk Model

We adopt the properties of the ProDiMo circumplanetary disk model developed by Oberg et al. (2022b). The CPD is a "gas-starved" actively-fed accretion disk (Canup and Ward, 2002) heated primarily by viscous dissipation at the midplane (Frank et al., 2002; D'Alessio et al., 1998). The parameters of the reference CPD model are listed in Table 6.

The disk structure in terms of radial and vertical dimension, density profile, dust-to-gas ratio, and temperature, are assumed to exist in a steady-state and are kept fixed. Following the gas-starved disk paradigm, the CPD does not contain instantaneously the solid mass required to form the Galilean satellites. The total refractory dust mass is 1.7×10^{-5} $M_\oplus$ and exists in the form of small grains (0.05-3000 μm). The dust grain size distribution is described by a smooth power-law $n \propto a^{-3.5}$. Such a disk is optically thick out to approximately ~1/3rd of the planetary Hill radius R_H, which is coincident with the theoretical limit for stable orbits (Quillen and Trilling, 1998; Ayliffe and Bate, 2009; Martin and Lubow, 2011).

For the ice-to-rock ratio of the solids in the CPD to be consistent with the ice-to-rock ratio of the outer Galilean satellites Oberg et al. (2022b) found that the dust-to-gas ratio of the CPD may be depleted relative to the canonical 10^{-2} by a factor $\gtrsim 10-20$. This depletion in dust corresponds with the rapid inwards drift and loss of grains larger than ~150 μm, which was found to occur naturally for a disk with a mass of 10^{-7} $M_\odot$ and accretion rate $\dot{M} = 10^{-11} M_\odot yr^{-1}$ in Oberg et al. (2022b). For their assumptions regarding the efficiency of settling, surface density power-law, and maximum grain size, the authors found that the global dust-to-gas ratio should not exceed $10^{-3.3}$ for a CPD with mass 10^{-7} $M_\odot$ and accretion rate $\dot{M} = 10^{-11}$ $M_\odot yr^{-1}$. The properties of the disk models are further justified and detailed in Oberg et al. (2022b) in which the authors explored a small grid of plausible CPD parameters.

In this work our analysis is focused on the case of the 10^{-7} $M_\odot$ CPD with accretion rate $\dot{M} = 10^{-11} M_\odot yr^{-1}$, as it was most closely able to reproduce the radial ice-to-rock ratio of the Galilean satellites while being consistent with the circumstellar disk gas component expected lifetime. We contrast our results with those of the "high" viscosity, hotter CPD with $\dot{M} = 10^{-10} M_\odot yr^{-1}$ and correspondingly shorter viscous timescale 10^3 yr given uncertainties in the magnitude of the disk viscosity.

Initial chemical conditions

Three different initial chemical conditions are considered. The first case is a full chemical "reset", in which ices are initially sublimated and the circumstellar gas is re-

verted to a purely atomic, ionized state. A chemical reset may occur if e.g. the circumstellar material is shock-heated during accretion onto the CPD, if the gas and dust are irradiated while crossing the optically thin gap, or if material only flows into the gap from the upper optically thin surface layers of the circumstellar disk. The CPD model is initialized in this fully reset state after which it is allowed to chemically evolve over its viscous timescale t_{visc}. The viscous timescale of the disk is defined as the time over which the majority of the gas mass is lost $t_{visc} = M_{cpd}/\dot{M}$ where $\dot{M}$ is the mass accretion rate. We assume that gas is lost to viscous radial flow either to decretion beyond the disk edge or accretion onto the planet. As the disk mass is assumed to be constant the net inflow-outflow rate of matter is necessarily zero. Our reference CPD model has a viscous timescale of 10^4 yr with a corresponding midplane heating rate equivalent to an α-viscosity of $10^{-3.6}$. We contrast these results with a "partial reset" in which only the ices are placed back in the gas-phase. This is similar to the work of Mousis and Alibert (2006) wherein the authors consider a case in which infalling ices are initially sublimated in a warm disk which subsequently cools, although we consider a disk with a static temperature structure. Finally we consider an "inheritance" case in which the chemical composition at the circumstellar disk outer edge is used as the initial state. The circumstellar disk model and the sampling of the inheritance chemistry are described in the accompanying work Oberg et al. (2022b).

We must also consider the consequences of the gas and dust being shocked at several scale heights above the CPD midplane (Takasao et al., 2021) prior to the gas turbulently diffusing downwards into the optically thick region. The ambient conditions at ~5 pressure scale heights (A_V = 0.01) differ significantly from those at the midplane (A_V=21) given the magnitude of the external stellar irradiation. To take into account this gradual change in ambient conditions we incorporate an additional step necessary to prevent the sublimated ices immediately re-adsorbing to grains. We adapt the model to follow a single parcel of gas and dust that is initialized above the midplane and then settles towards the midplane at the centrifugal radius (~ 0.03 R_H) (Machida et al., 2008). This process is labelled as step 2 in Fig.4.1.

In this step 2 we evolve the chemistry in a 0D grid-cell for a fraction of the diffusion timescale. The resulting composition of the gas and ice is extracted, and used to populate a new grid-cell in which the background conditions are updated to correspond to the downwards motion of the gas parcel. This process is repeated iteratively as ambient conditions (optical depth, density, gas and dust temperature) change. As a simplification owing to significant uncertainties in the origin, magnitude, and spatial distribution of turbulence within the CPD we simply assume that the parcel travels at a constant rate until it reaches the midplane. The timescale of this process is ~ 10 yr (Oberg et al., 2022b) although this value is highly uncertain. Accordingly we consider diffusion timescales of 1, 10, and 100 yr. The final composition of the parcel at the midplane is then used to populate the CPD midplane for the final step (step 3 in Fig.4.1) in which chemical evolution proceeds up until the viscous timescale.

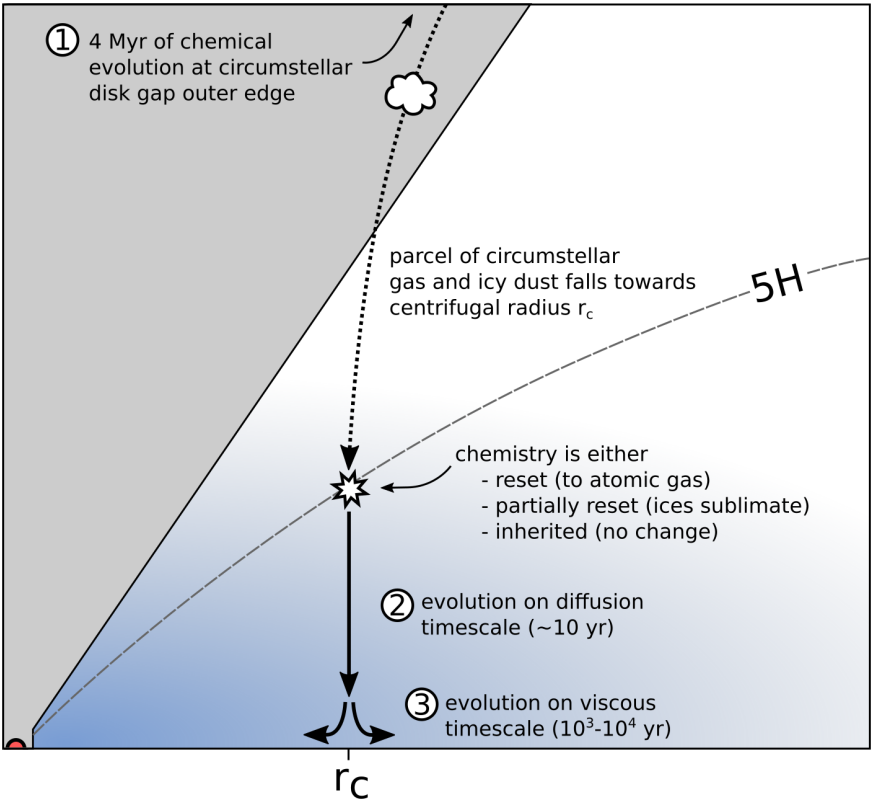

Figure 4.1: Schematic illustration of the modeling process. In step 1 the chemistry in a circumstellar disk model is evolved for 4 Myr. This chemistry is extracted from the gap outer wall region and used as a starting point prior to accretion. To consider various possible accretion scenarios, the composition of the infalling material is either reset to atomic (full reset), the ices are sublimated (partial reset) or the chemistry remains unaltered (inherit). In step 2 the chemistry of a parcel of gas and ice is evolved for 10 yr as it travels towards the CPD midplane. In step 3, the chemistry is evolved at the CPD midplane for the viscous timescale of the disk.

Table 11: Parameters of the reference CPD model.

Parameter	Symbol	Value
Planet Mass	$M_{\rm p}$	1.0 $M_{\rm J}$
Planetary Luminosity	$L_{\rm p}$	10^{-5} $L_{\odot}$
Effective Temperature	$T_{\rm eff,p}$	1000 K
UV Luminosity	$L_{\rm UV,p}$	0.01 $L_{\rm p}$ *
Interstellar UV Field	χ	3×10^3
Background Temperature	$T_{\rm back}$	50 K
Disk Mass	$M_{\rm cpd}$	10^{-7} $M_{\odot}$
Disk Inner Radius	$R_{\rm in,cpd}$	0.0015 au
Exponential Decay Radius	$R_{\rm in,cpd}$	0.11 au
Disk Outer Radius	$R_{\rm out,cpd}$	0.34 au
Column Density Power Ind.	ϵ	1.0
Accretion rate	$\dot{M}$	10^{-11}-10^{-10} $M_{\odot}$ yr^{-1}
Viscosity	α	$10^{-3.6}$-$10^{-2.7}$
Minimum dust size	$a_{\rm min}$	0.05 μm
Maximum dust size	$a_{\rm max}$	3000 μm
Dust-to-Gas Ratio	d/g	$10^{-3.3}$
Flaring Index	β	1.15
Reference Scale Height	$H_{0.1\rm au}$	0.01 au

* Planetary UV luminosity is expressed in multiples of the planetary luminosity $L_{\rm p}$.

4.2.3 Likelihood of chemical reset and magnitude of shock-heating

Icy grains passing through an optically thin gap at 5 au around a sunlike star can retain their icy mantles if swept up by the planet within $\sim 10 - 100$ orbital timescales (Oberg et al., 2022b). If a (partial) chemical reset occurs it must instead be due to either accreted material originating from a higher altitude in the circumstellar disk where ices are unstable, or shock-heating on the CPD surface. We can estimate the shock velocity of infalling matter where it strikes the CPD and consider which of our initial chemical conditions corresponds most appropriately to the formation of the Galilean moon system. Angular momentum of infalling circumstellar gas and dust causes it to accrete onto the CPD near the so-called centrifugal radius $r_{\rm cf}$ (Hayashi et al., 1985; Machida et al., 2008). The infall velocity at $r_{\rm cf}$ must be $\gtrsim 8 - 10$ km s^{-1} for dust grain icy mantles to be lost due to sputtering and thermal desorption (Woitke et al., 1993; Aota et al., 2015; Tielens, 2021). We approximate the infall velocity as a function of planetocentric radius by considering orbits with apoapsis of a single circumstellar disk pressure scale height at the position of Jupiter ($z = 0.5$ au) (Oberg et al., 2022b), with orbital eccentricities corresponding to passage through the planet equatorial plane at some distance r. The

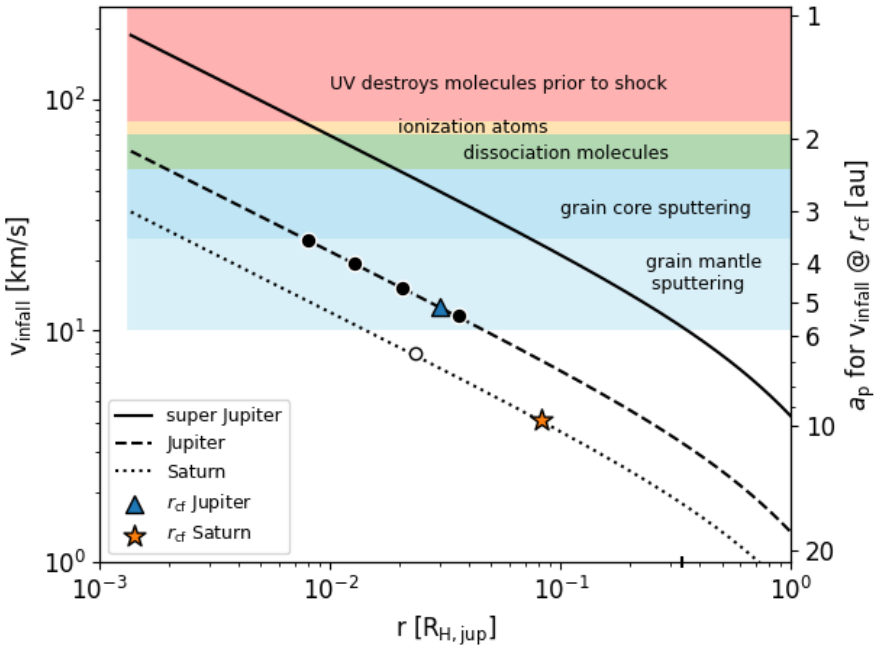

Figure 4.2: Velocity of material falling onto a CPD $v_{\rm infall}$ at radius r for planets of Saturnian (dotted line), Jovian (dashed lines), and super-Jovian (10 M_J) (solid line) mass. The centrifugal radii $r_{\rm cf}$ of Jupiter and Saturn are indicated by the blue triangle and orange star, respectively. The radial position of the Galilean satellites is indicated by the four black circles and the radial position of Titan is indicated by the white circle. The planetary orbital radius $a_{\rm p}$ that corresponds to the infall velocity at the centrifugal radius $v_{\rm infall}(r_{\rm cf})$ is indicated on the right vertical axis. The shaded colored regions indicate different chemical consequences of shock-heating corresponding to a given $v_{\rm infall}$. The units on the abscissa are in multiples of the Jovian Hill radius. All calculations correspond to a solar mass star.

resulting infall velocities $v_{\rm infall}$ can be seen in Fig. 4.2 for planets of Saturnian, Jovian, and super-Jovian (10 M_J) mass. The infall velocity at $r_{\rm cf}$ is independent of the planet mass, but is instead a function of the planetary semi-major axis (for a circular orbit). The shock velocity at the centrifugal radius of Jupiter is in the regime of icy mantle loss to sputtering (Draine and McKee, 1993; Tielens, 2005). Hence if the majority of grains accrete near $r_{\rm cf}$, Jupiter's CPD may be best represented by the "partial reset" scenario. Conversely no ice sublimation is expected to occur due to shock-heating in the case of Saturn. A full chemical reset is more likely to occur for a super-Jupiter at a stellocentric distance of 2-3 au from a solar mass star.

4.2.4 Chemical Network Diagrams

Throughout this work we make use of algorithmically generated chemical network diagrams to describe relations between atomic and molecular species, their relative abundances, formation rates, and the types of reactions that are involved. The diagrams are generated with an implementation of the PyVis software package (itself based on the VisJS library, see Perrone et al. (2020)). A description of how these diagrams are generated and interpreted can be found in Appendix A.1.

4.3 Results and Discussion

Prior to reaching the midplane the accreted gas and dust diffuses downwards from the optically thin surface layer of the CPD at the centrifugal radius r_c. We have iteratively evolved the disk chemistry as the background conditions change during the descent. The relevant properties of the vertical slice through the circumplanetary disk during the descent to the midplane at r_c can be found in Fig. 4.3 panel (a). The post-shock evolution of the water ice abundance during the descent to the midplane can be found in panels (b), (c), and (d) of Fig. 4.3 for the reset, partial reset, and inheritance cases respectively. Solid lines trace the evolution of ice impurity abundances as the gas parcel moves downwards from 5 scale heights (left) to the midplane (right). Dashed lines trace the abundances in the case of a hotter, higher viscosity CPD with $t_{visc} = 10^3$ yr. Initial pre-shock abundances of the impurities are indicated by the colored circles on the ordinate.

In the case of the reference (low viscosity) fully or partially reset CPD, significant quantities of water ice have already formed prior to reaching the midplane. In the fully reset case the ice is predominantly water with $< 0.1\%$ impurities in the form of CH_3OH and HCOOH ice. In the partial reset case, a significant (25%) CO_2 component has formed. In the inheritance case, ices are able to survive the brief exposure to the optically thin upper layers of the disk and the CPD accretes a nitrogen-rich ice composition. In the high-viscosity ($\alpha = 10^{-3}$) CPD model ices are not thermally stable at the centrifugal radius midplane. This can be seen in Fig. 4.3 where ice abundances decline immediately prior to reaching the midplane. Consequently the initial post-shock conditions of 'partial reset' and 'inherit' converge to a similar ice-free molecular gas composition by the time the gas parcel reaches the midplane.

After the step in which accreted gas and dust is followed as it travels towards the midplane (step 4 in Fig. 4.1), the resulting chemical abundances are used to specify the initial conditions for the rest of the CPD as it evolves on the viscous timescale (step 5 in Fig. 4.1). After 10^3-10^4 yr of further evolution we extracted the radial ice composition at the midplane from six distinct CPD models describing three initial chemical conditions (reset, partial reset, and inheritance) and two disk α-viscosities (corresponding to viscous timescales of 10^3 and 10^4 yr). An overview of the radial midplane ice composition, the disk-integrated total molecular ice composition, and the disk-integrated total elemental ice budget of the low-viscosity CPDs can be found in Fig. 4.4. For reference

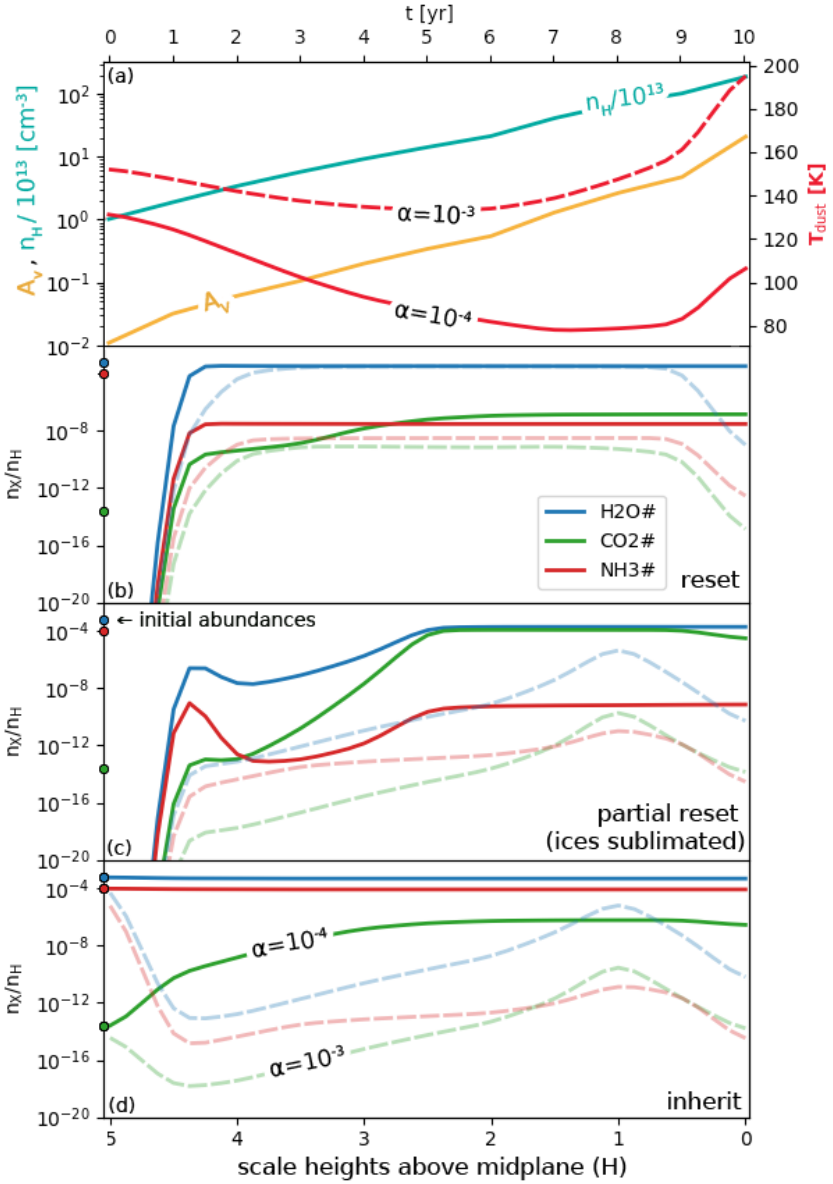

Figure 4.3: (a) Properties of a vertical slice in the circumplanetary disk at the centrifugal radius, from five pressure scale heights (left) to the midplane (right). Evolution of the abundance of H_2O, NH_3 and CO_2 ice as the parcel of gas and dust sinks to the midplane after accretion is shown for the reset case (b), the partial reset case (c), and the inheritance case (d). Solid lines trace the relevant properties and abundances for the low viscosity (t_{visc} = 10^4 yr) case and the dashed line describes the high viscosity (t_{visc} = 10^3 yr) case.

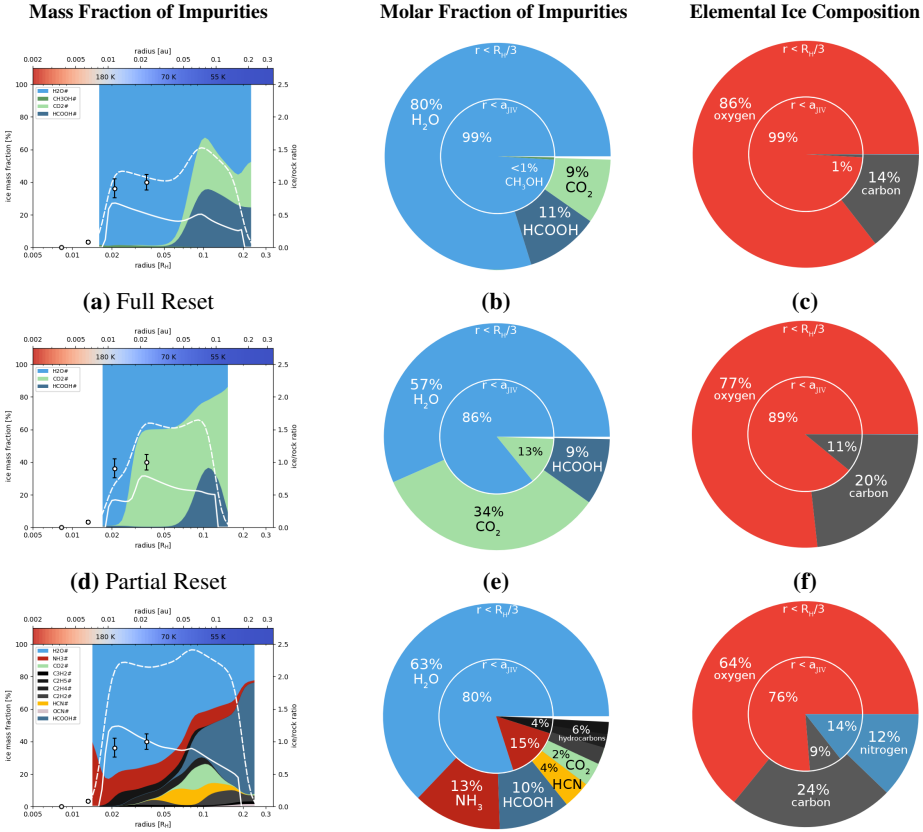

(a) Full Reset **(b)** **(c)**

(d) Partial Reset **(e)** **(f)**

(g) Full Inheritance **(h)** **(i)**

Figure 4.4: Overview of the chemical composition at the CPD midplane for the "full reset" case (*top row*), for the "partial reset" case (*middle row*), and for the "full inheritance" case (*bottom row*). (*Left column*) Radial mass fraction of ices at the CPD midplane (filled colored regions) where $f_{ice} > 0.01$. The white lines indicate the radial ice-to-rock ratio of solids at the midplane (solid line) and integrated up to an altitude above the midplane equal to the Hill radius of Ganymede (dashed line). The estimated ice-to-rock ratio of the Galilean satellites is included (circles with error bars). (*Center column*) Radially-integrated midplane ice composition out to $R_H/3$ (outer ring) and within the orbit of Callisto (inner circle). (*Right column*) Total disk-integrated elemental composition of the ices in the same two radial zones.

the ice-to-rock ratio of the solids at the CPD midplane is also included in Fig.4.4 (left column) as a solid white line. Settling of large grains to the midplane strongly reduces the local ice-to-rock ratio. Realistically, accreting moons may be able to capture solids drifting at higher altitudes above the midplane within their gravitational sphere of influence. Hence we include also the ice-to-rock ratio of solids integrated up to an altitude equal to the Hill radius of a Ganymede-mass object (dashed white line). The radial abundance profiles of NH_3, HCOOH, CO_2, and CH_3OH ice can be found in Fig. 4.5.

Ices at the partially or fully reset CPD midplane are found to contain significant impurities in the form of CO_2 and HCOOH and to a lesser extent CH_3OH. The chemically inherited CPD additionally contains HCN and hydrocarbon ices which were already present at the time of accretion. Trace amounts of OCN, SO, SO_2, NH, NH_2, OH, and HNO ice can also be found, but each at $< 0.1-0.5\%$ of the total ice mass. In the following subsections we discuss the formation and abundance of the impurities NH_3, CO_2, HCOOH and CH_3OH.

4.3.1 Partial reset (initial sublimation of ices)

It is likely that in the case of the Jupiter system the shock velocity of matter accreting at the centrifugal radius did not lead to the full dissociation of molecules. A less extreme C-type shock-heating could simply cause icy grain mantles to desorb by e.g. sputtering. Accordingly we focus our analysis and discussion on this case in which all ices are put back into their respective gas-phase counterpart.

Ammonia (NH_3)

Immediately after accretion onto the CPD and the sublimation of ices, hydrogen is predominantly found in the form of H_2, oxygen in H_2O, and nitrogen in NH_3 and HCN at a ratio 1:0.63. After 10 years of drifting towards the midplane the gas is still H_2-dominated, but nitrogen is found primarily in N_2. After being initially sublimated a minor fraction of the NH_3 immediately re-adsorbs to the grains (see Fig. 4.3 (c)), but it is not stable against photodissociation given the background UV field intensity ($\chi_{RT} > 1000$). Above 2-3 scale heights NH_3 ice is photodissociated on the grain surface to e.g. NH_2# and H# or back into the gas phase as NH. Once the majority of nitrogen is locked into N_2 via NH+NH it is stable against photodissociation due to self-shielding (Li et al., 2013), preventing the accumulation of NH_3. The photodissociation timescale of N_2 is much larger than the disk viscous timescale.

Near the midplane NH_3 ice forms by direct adsorption from the gas phase onto dust grains. The gas-phase NH_3 originates primarily via a sequence of three body collider reactions:

$$H_2 + N + M \rightarrow NH_2 + M \quad (99)$$

$$NH_2 + H + M \rightarrow NH_3 + M \quad (100)$$

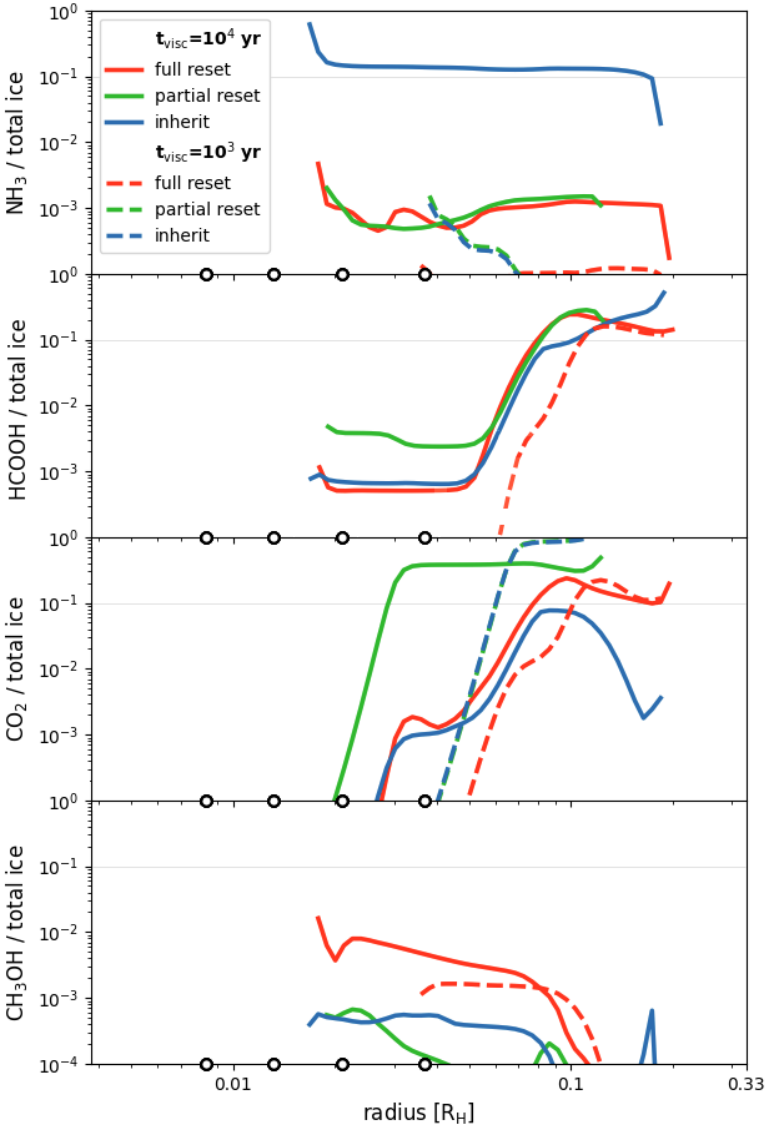

Figure 4.5: Radial abundance of selected non-H_2O ices as a fraction of the total ice abundance for the low viscosity case with $t_{visc} = 10^4$ yr (solid lines) and high viscosity case with $t_{visc} = 10^3$ yr (dashed lines). The position of the Galilean satellites are indicated by the empty circles. A light gray horizontal line indicates a concentration of 1%.

where M = H, H_2, or He. The importance of this pathway is illustrated clearly by the green arrows in the chemical network diagram Fig. 4.6. These collider reactions are very efficient at the typical CPD midplane densities ($n_H \sim 10^{12}$ cm^{-3}). However, the absence of abundant atomic nitrogen prevents the collider pathway from producing significant quantities of NH_3. N_2 is destroyed predominantly by reactions with He ions at a relatively low rate, as He+ is produced only be cosmic-ray ionization. The collider pathway to form NH_3 thus does not result in significant accumulation of NH_3 ice. By the time the gas parcel has reached the midplane, NH_3 ice is present only as a trace species.

The collider-pathway begins with the formation of NH_2 (eq. 99) which is also relevant to the water formation pathway involving $NH_2 + O \rightarrow NH + OH$ (Kamp et al., 2017). While the pre-exponential factor 10^{-26} cm^6 s^{-1} is derived from the work of Avramenko and Krasnen'kov (1966) we have chosen to adopt a significantly lower rate more typical of collider reactions (10^{-30} cm^6 s^{-1}), which still produces enough NH_2 for this path to be the dominant NH_3 formation route in the inner disk. It has been noted that this particular reaction is critical to accurately reproduce observed OH and H_2O gas-phase abundances, but that modern reevaluation of its rate and temperature dependence are needed (Kamp et al., 2017). For the second collider reaction in this path (eq. 100) we adopt the rate coefficients of Gordon et al. (1971) that list a pre-exponential factor 6.07×10^{-30} cm^6 s^{-1}. Other more recent experimental results assuming the reaction to be in the three body pressure regime give values in the range $2.3{\times}10^{-30}$ - $1.42{\times}10^{-29}$ for various 3rd bodies (Altinay and Macdonald, 2012, 2015), hence we consider this a reasonable value.

In the outer disk NH_3 gas is efficiently photodissociated. The NH_3 ice is instead formed primarily by barrier-less successive hydrogenation of atomic nitrogen on icy grain surfaces (Charnley et al., 2001; Fedoseev et al., 2015) which has been experimentally demonstrated to occur (Hiraoka et al., 1995; Hidaka et al., 2011) via the Langmuir-Hinshelwood mechanism. The formation pathway is then

$$NH\# + H\# \rightarrow NH_2\# \quad (101)$$

$$NH_2\# + H\# \rightarrow NH_3\# \quad (102)$$

Both in the inner and outer disk NH_3 ice does not consitute more than 10^{-3} of the total ice by molar fraction.

Carbon Dioxide (CO_2)

While CO_2 ice is initially only a trace species in the accreted circumstellar disk material, it becomes abundant in the CPD prior to the accreted material reaching the midplane. The chemical network diagram of the predominant CO_2 ice formation paths during this stage can be found in Fig. 4.7. This figure illustrates how the production of OH by collider reactions (green arrows) is critical to the efficient formation of CO_2 ice.

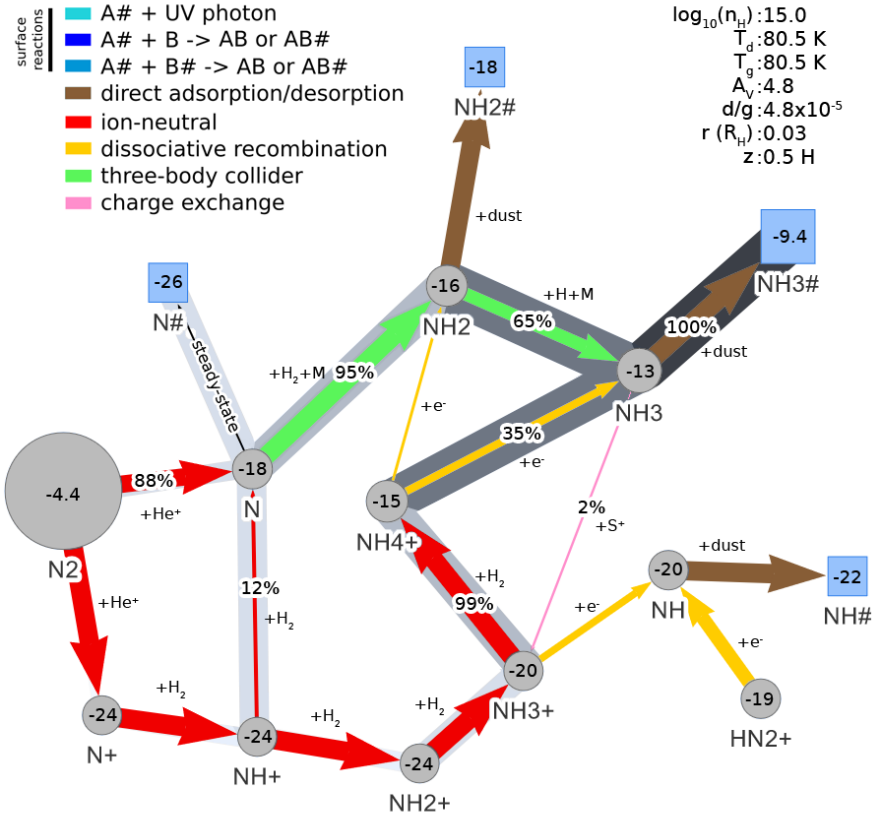

Figure 4.6: Chemical network diagram illustrating the formation of NH_3 ice in the CPD after a partial reset, immediately prior to the accreted gas reaching the midplane. The pathway from N_2 to NH3# is highlighted. Percentages for reaction A→B indicate the fraction of reactions forming B which involve species A. A label “steady-state" indicates that the net rate is zero.

The time that accreted gas and ice spends in the optically thin surface layers of the CPD initially liberates significant quantities of atomic oxygen from gas-phase H_2O, which is hydrogenated via three-body collider reactions. The OH then reacts with abundant gas-phase CO to produce 98% of the CO_2, which then freezes out onto grains. In particular three-body collider reactions account for nearly all (> 99%) OH formation which is critical for the CO+OH gas-phase reaction. It can also be seen in Fig. 4.7 that grain-surface formation of CO_2 ice plays only a minor role prior to the gas parcel reaching the midplane.

After the gas and dust parcel reaches the midplane the chemistry is evolved for an additional 10^3-10^4 yr for the high- and low-viscosity cases, respectively. The resulting composition at $t_{\rm visc}$ is similar to that of the full reset case, with the exception that the inner CPD (near the present day orbit of Callisto) also retains a significant CO_2 ice component. This can be seen in Fig. 4.5 (a) and Fig. 4.5 (d). CO_2 ice formation continues in the outer CPD at the midplane in the absence of abundant atomic O, as OH is produced instead on grain-surfaces by the photodissociation of H_2O#. This is described in the following section and can be seen in Fig. 4.8.

Formic Acid (HCOOH)

HOCO (hydrocarboxyl radical) and HCOOH (formic acid) are of relevance in the cold high density midplane where CO_2 ice can form and hence were included in our extended chemical network. Formic acid is the simplest carboxylic acid and has been identified in star forming regions (Schutte et al., 1999; Ikeda et al., 2001) both in gaseous and solid state, protoplanetary disks (Favre et al., 2018), and in comets (Crovisier et al., 2004). Its abundance typically varies with 1-10% of water ice (Bisschop et al., 2007).

The chemical network diagram of HCOOH formation in the outer CPD can be found in Fig. 4.8. It is clear that grain surface reactions play a completely dominant role in this process. In the outer CPD we find that, although it is not stable as an ice, gas-phase CO freezes out and temporarily occupies a physisorption site on the grain surface. Prior to desorbing the CO# reacts on the grain surface OH# to form CO_2# and H# (Oba et al., 2010; Liu and Sander, 2015) for which we have adopted the effective barrier 150 K (Fulle et al., 1996; Ruaud et al., 2016).

$$\mathrm{CO + dust \rightarrow CO\#} \tag{103}$$
$$\mathrm{CO\# + OH\# \rightarrow CO_2\# + H\#} \tag{104}$$

Alternatively as an intermediate step of the OH# + CO# reaction the van der Waals complex HOCO# is formed which can be hydrogenated to form HCOOH#.

$$\mathrm{CO\# + OH\# \rightarrow HOCO\#} \tag{105}$$
$$\mathrm{HOCO\# + H\# \rightarrow HCOOH\#} \tag{106}$$

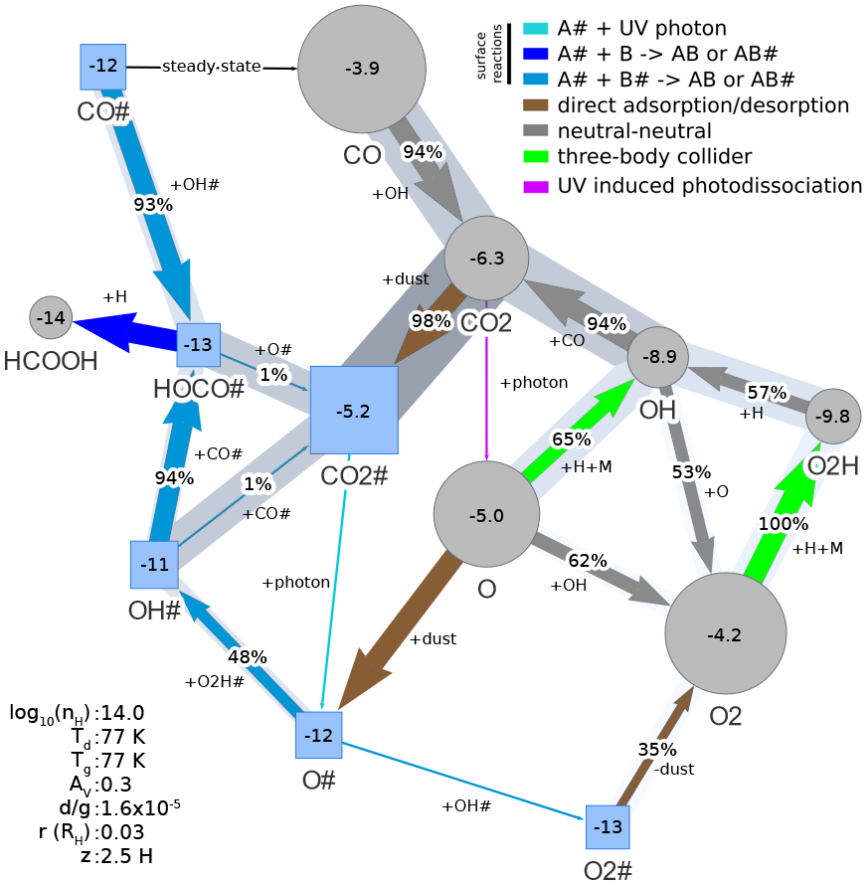

Figure 4.7: Chemical reaction network illustrating the formation of CO_2 ice after a partial reset in which ices accreting onto the CPD are initially sublimated and placed into the gas-phase.

The HOCO# formation route can explain the presence of HCOOH# in cold, dense clouds (Ioppolo et al., 2011; Qasim et al., 2019). The resulting radial abundance of HCOOH# in the reference CPD can be seen in Fig.4.5 (c). In the partial reset case HCOOH ice can locally constitute a significant fraction of the ices in the reference CPD (∼10mol%).

We have found significant abundances (∼ 10% relative to H_2O ice) of HCOOH ice in the outer region of the CPD. This is comparable to the high end of inferred abundances (∼ 1 − 10% level relative to H_2O ice) observed towards young stellar objects (Schutte et al., 1999; Keane et al., 2001; Knez et al., 2005; Boogert et al., 2015). The relatively large abundance of HCOOH ice in the outer CPD relative to its observationally derived abundance in astrophysical ice mixtures in the ISM is noteworthy. However this was not entirely unexpected. The minimum CPD temperature set by equilibrium with the background radiation field ensures that a large region in the outer CPD exhibits a narrow range of temperature from 50-55 K. Given that the majority of the disk surface area is in this zone, the total disk composition is weighted heavily towards these specific conditions. However, background temperatures as low as 30 K or as high as 70 K do not produce abundant alternative impurities, and the outer CPD remains dominated by CO_2 and HCOOH ice.

Additionally, the stability of the HCOOH ice in our model is subject to several uncertainties. The only grain-surface reaction in our network which destroys HCOOH# is the photo-induced dissociation to HCO# and OH#. Alternatively it can be placed directly back into the gas phase by thermal, cosmic-ray, or UV-photon induced desorption. We do not include grain-surface hydrogenation of the HCOOH ice. Bisschop et al. (2007) found that hydrogen bombardment of a pure multilayer HCOOH ice does not result in the production of detectable reaction products, concluding that hydrogenation of HCOOH does not play a role in formation of more complex species and that only minor amounts desorb. In contrast Chaabouni et al. (2020) found that H-bombardment of a $< 1-3$ monolayer coating of HCOOH ice at 10-100 K results in efficient production of CO_2 and H_2O molecules, as well as CH_3OH and H_2CO. The authors suggest that this disagreement stems from the inefficiency of H atom diffusion through the pure HCOOH multilayer used in the experimental setup of Bisschop et al. (2007). Alternatively, the sub-monolayer conditions present in the setup of Chaabouni et al. (2020) potentially cause the substrate itself to become hydrogenated, increasing the sticking coefficient for H atoms and promoting surface reactions. Where HCOOH ice is found in our CPD it is co-deposited with H_2O ice and CO_2 ice (with molar ratio H_2O:CO_2:HCOOH 100:80:80) with an equivalent thickness of several hundred monolayers. Hence we consider it plausible that the majority of the HCOOH embedded within the ice matrix would not be efficiently hydrogenated.

HCOOH ice has not been detected on the surface of any Galilean moon. Experimental results indicate that HCOOH ice has a relatively short 8×10^7 yr half-life against irradiation by galactic cosmic rays, being dissociated into CO or CO_2 (Bergantini et al., 2013). Any HCOOH accreted onto the surface of e.g. Callisto would therefore likely be absent in the present era, having reduced to $< 1\%$ of its initial concentration within

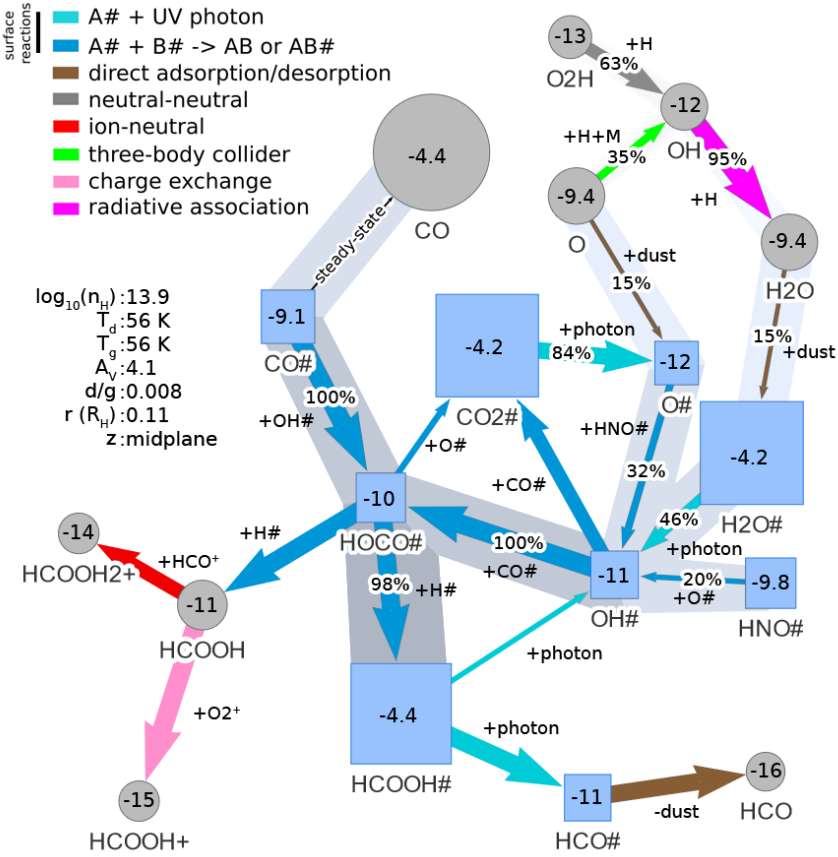

Figure 4.8: Chemical network diagram centered on the formation of HCOOH ice in the outer regions of the CPD at the midplane.

only 0.56 Gyr. There is a paucity of research investigating the role of HCOOH in subsurface melts, although under hydrothermal conditions water can act as a homogeneous catalyst for the decarboxylation pathway of HCOOH decomposition in liquids (Ruelle et al., 1986), where it decomposes to the astrobiologically relevant CO_2 and H_2 (Yu and Savage, 1998).

4.3.2 Full Reset (initially atomic gas)

In the full reset case the gas in the CPD is initially fully atomic and ionized and no ices are present. This state represents e.g. the accretion of a high-mass planet ($M > 1 M_J$) with correspondingly higher infall shock-velocity at the CPD surface, or accretion of material originating from a greater scale height in the circumstellar disk than we have considered. In the fully reset case the abundant free atomic hydrogen enables highly efficient combustion chemistry to produce a water dominated ice composition as was found in Oberg et al. (2022b). Again, ammonia ice is not able to form in abundance as the initially atomic nitrogen is predominantly locked in N_2 within a single year via N + NO $\rightarrow$$N_2$ + O or N + NH $\rightarrow$$N_2$ + H. The radial composition of the ices after 10^4 yr is similar to the partial reset case, although CO_2 ice is found in abundance only in the outer disk beyond $\sim$ 2$\times$ the semi-major axis of Callisto. In contrast to the partial reset case the inner disk region is dominated by water ice with a minor (< 1%) methanol (CH_3OH) component.

Methanol is an important primordial solar system volatile and may act as an anti-freeze in subsurface oceans (Deschamps et al., 2010; Dougherty et al., 2018). It has been found to be abundant in solid form near protostars (Dartois et al., 1999; Boogert et al., 2015), in comets (Bockelee-Morvan et al., 1991; Mumma et al., 1993; Bockelée-Morvan and Biver, 2017; Biver and Bockelée-Morvan, 2019), and in the gas-phase in planet-forming disks (Walsh et al., 2016; Booth et al., 2021) where it may be formed via grain-surface reactions involving hydrogenation of CO# (Hiraoka et al., 1994; Watanabe and Kouchi, 2002). At typical pressures in our reference CPD the freeze-out temperature of methanol is greater than that of NH_3 and CO_2 (Mousis et al., 2009; Johnson et al., 2012). Thus, if the CO_2 ice observed on Callisto's surface was formed primordially in the CPD we could expect that temperatures in the CPD could have allowed for stable methanol ice to be present as well. Indeed we find that in the inner disk this occurs for $t_{visc} > 10^3$ yr where methanol ice is present at the 1% level at temperatures above 65 K with a peak abundance at 95-100 K. At these densities it originates almost exclusively from reactions in the gas-phase via sequential hydrogenation of CO in two- and three-body reactions. Approximately 70% is formed by

$$CO + H + M \rightarrow HCO + M \quad (107)$$
$$HCO + H + M \rightarrow H_2CO + M \quad (108)$$
$$H_2CO + H \rightarrow CH_3O \quad (109)$$
$$CH_3O + H \rightarrow CH_3OH \quad (110)$$

and the remainder by

$$H_2CO + H \rightarrow CH_2OH \quad (111)$$
$$CH_2OH + H \rightarrow CH_3OH. \quad (112)$$

For the reaction $H_2CO \rightarrow CH_3OH$ we have adopted the rate coefficients from Huynh and Violi (2008) with a barrier of 865 K. In the absence of this reaction we find that methanol is produced in similar quantities via the CH_2OH pathway. The rate of formation is thus highly contingent on the availability of free atomic hydrogen in the gas-phase. The absence of abundant atomic hydrogen prevents the accumulation of methanol in the partial reset or inheritance cases. An additional "bottleneck" in the reaction network is H_2CO. This can be seen in Fig. 4.9. H_2CO is formed almost exclusively (> 99%) by gas-phase three-body collider reactions.

In the ISM methanol ice abundances can significantly exceed those which we find in the CPD. The grain-surface hydrogenation of H_2CO to form CH_3O (Eq. 109) has been observed at low temperatures experimentally (Hidaka et al., 2004; Fuchs et al., 2009; Chuang et al., 2016) suggesting that successive hydrogenations of CO can explain the observed abundance of interstellar methanol at low temperatures (< 15 K). Above this temperature the desorption of H atoms and lower sticking efficiency of H due to the absence of H_2 causes a considerable drop in this reaction rate. While these reactions are included in our chemical network, the gas temperature in the CPD does not fall below 50 K and hence this path is inefficient.

4.3.3 Full inheritance case

In the event of a full chemical inheritance from the circumstellar disk gap edge, the ice accreting onto the CPD consists predominantly of water, with ratios H_2O:NH_3:HCN of 100:15:10 and a significant ~ 10% component of hydrocarbon ices (e.g. C_2H_2, C_3H_2). This result is generally consistent with modeling of the outer regions of the circumstellar disk where $NH_3/H_2O = 0.14$ with as much as 80% of the nitrogen locked into NH_3 and to a lesser extent HCN (Dodson-Robinson et al., 2009).

The final composition of the ices in the inheritance scenario is highly contingent on their initial composition. Given the difficulties in correctly capturing the relevant physical conditions at the outer gap edge and the uncertainty from which altitude the gas originates, we consider it more informative to discuss how the ices are altered post-accretion, rather than focusing on their final composition.

Some minor processing of the ices occurs once they are incorporated into the CPD. The more volatile HCN and hydrocarbon ices are lost in the inner region of the disk where only NH_3# and a minor component of hydrocarbon ices remain as impurities. In the outer region of the CPD, some conversion of H_2O and HCN to HCOOH occurs, and to a minor extent CO_2.

At temperature below 70 K HCOOH is co-deposited with the NH_3 ice. In the presence of the proton acceptor NH_3, HCOOH will convert to the formate anion $HCOO^-$ and $NH4^+$ (Hudson and Moore, 1999; Schutte et al., 1999; Gálvez et al., 2010), however

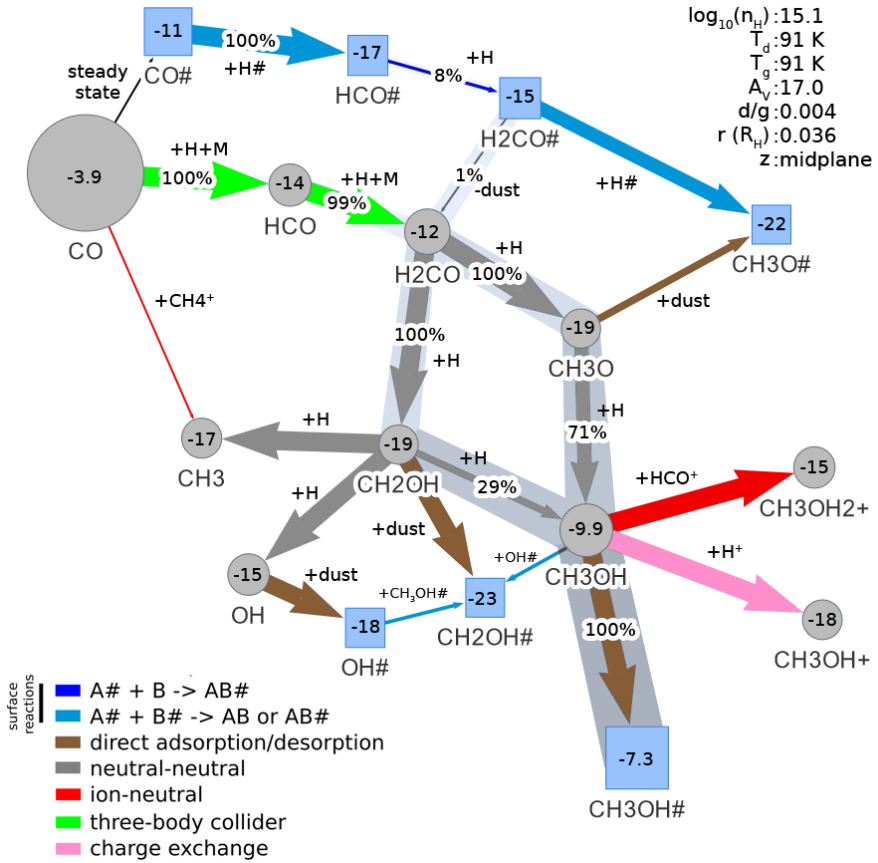

Figure 4.9: Chemical network diagram centered on the formation of CH_3OH at the CPD midplane in the reset case.

formate is not included in our chemical network. Likewise the salt formation reaction is not included in the network. We consider what impact the inclusion of this process could have on our final derived abundances. While the activation barrier of the reaction is negligible, the barrier against diffusion prevents it from occurring at 50-70 K (Schutte et al., 1999). However some of the HCOOH will react immediately upon deposition due to the acid and base being in direct contact at adjacent binding sites. 10% of the HCOOH ice is observed to react promptly at 10 K in H_2O-NH_3-HCOOH mixtures with equal parts NH_3-HCOOH (Schutte et al., 1999). Hence we might expect that as much as $\sim$ 20% of the HCOOH present in the outer disk could be converted upon adsorption to HCOO-NH_4+.

4.3.4 Differing diffusion timescales

Owing to the uncertainity in the diffusion timescale on which the gas parcel drifts towards the CPD midplane we considered also the case of 10× shorter and longer $t_{\rm diff}$. For $t_{\rm diff}$ = 100 yr all three initial conditions converge towards a similar final composition which is CO_2-dominated (> 95% by weight) across the entire disk. This is clearly inconsistent with observations of the Galilean moons. The shorter $t_{\rm diff}$ = 1 yr leaves the chemistry less affected by the time spent at the disk surface. In the partial reset case, a minor fraction (3%) of the accreted circumstellar NH_3 ice survives and can still be found at the CPD midplane after 10^4 yr. In the full reset case, the CH_3OH component in the inner disk region becomes more substantial, increasing to a peak of 4% of the total ice mass. This additional CH_3OH forms because more of the initially atomic hydrogen survives until ices become stable against photodissociation, and are available to hydrogenate H_2CO and CH_3O.

4.4 Implications

Absence of ammonia as an indicator of chemical reset

We have found that a partial or complete chemical reset of the CPD tends to suppress NH_3 formation as efficient N_2 self-shielding locks up nitrogen in N_2. Even if a substantial component ($\sim 20-30\%$) of NH_3 ice were present in Jupiter's feeding zone, a partial or complete reset would prevent its accumulation in the building blocks of the moons. Without a substantial NH_3 component the liquidus temperature of the Galilean subsurface oceans may not differ substantially from that of a pure water ice. Europa appears to be the only Galilean moon where tectonic or cryovolcanic processes have recently exchanged material between the surface and subsurface where it could provide clues to composition of an ocean (Kargel et al., 2000; Zolotov and Shock, 2001). NH_3 brought to the surface in the form of an NH_3-H_2O matrix could be lost on geologically brief timescales to external radiation (Moore et al., 2007; Bergantini et al., 2014). Longevity of surface ammonia might be extended if it would appear in a more stable form such as a hydrate or salt (Cook et al., 2018) but no positive detection has thus far

been made (Clark et al., 2014). The non-detection of ammonium compounds on Europa's surface is compatible with a lack of ammonia in a subsurface ocean, although is certainly not conclusive evidence of its absence.

In contrast to the Galilean system, several lines of evidence indicate the presence of NH_3 ice during the accretion of the Saturnian moons. The inferred interior composition of the Saturnian moon Enceladus appears to resemble more closely well-mixed outer solar system material and is generally consistent with a composition inherited from solar nebular (cometary) material (Waite et al., 2009). Enceladus contains a liquid water ocean (Thomas et al., 2016) from which interior material is ejected through plumes (Spahn et al., 2006; Porco et al., 2006; Waite et al., 2006). The presence of NH_3 in the plumes of Enceladus has been established by measurements from several instruments onboard the Cassini spacecraft (Waite et al., 2009) at $> 0.1\%$ relative to H_2O, besides CO_2, CH_4 and H_2 (Magee and Waite, 2017). Likewise NH_3 ice is considered to be a likely source of Titan's nitrogen (McKay et al., 1988; Sekine et al., 2011; Mandt et al., 2014).

We suggest that the CPDs of sufficiently massive planets lose accreted NH_3 ice to mild accretion shocks and subsequent chemical evolution, and that the absence of NH_3 ice may indicate a (partial) chemical reset has occurred. As NH_3 represents one of the most potent and potentially abundant anti-freezes, subsurface ocean occurrence rates and longevity may then be relatively enhanced in the icy moons that accompany lower-mass giant planets which inherit circumstellar material.

Carbon Dioxide at the origin of Ganymede and Callisto

Several lines of evidence suggest the surface of Callisto is among the most primordial of the regular satellites, potentially providing a direct link to the formation environment of the Galilean moons (Moore et al., 2004; Zahnle et al., 2003). CO_2 ice has been detected on the surface of both Ganymede and Callisto (Carlson et al., 1996; McCord et al., 1997) but is only inferred to be below the surface on Callisto (Hibbitts et al., 2002; Hibbitts et al., 2003), where it appears to be exhumed by impact cratering. In contrast, CO_2 on the surface of Ganymede appears to be of exogeneous or radiolitic origin (Hibbitts et al., 2003). Hence if we consider Callisto's reservoir of CO_2 ice to be primordial we can consider which of our assumptions are consistent with its presence.

In the partial reset case, which we considered *a priori* to be the most likely initial condition of accreted material, CO_2 ice is present in significant quantities at the present-day position of Callisto but less so near Ganymede. Superficially this appears to be consistent with the proposed distinct origins of Ganymede and Callisto's CO_2. However, the local ice mass fraction of CO_2 in the CPD is high ($\geq$60%). This appears to be in conflict with the inferred surface abundance of CO_2 ice on Callisto, where it constitutes no more than 0.01-0.16% of the host material mass (Hibbitts et al., 2002). It is however unclear whether the observationally inferred surface abundance of CO_2 on Callisto is truly representative of the subsurface composition. Pure CO_2 ice is not stable at the surface of the Galilean moons and CO_2 may instead be present in the form

of clathrates (Chaban et al., 2007). Hence, an initially large CO_2 component exposed to the surface could have been lost to sublimation and dissociation. A substantial subsurface CO_2 reservoir is nevertheless implied by continuous replenishment of Callisto's CO_2 exosphere (Carlson, 1999). In contrast to the partially reset case, we find CO_2 ice at a concentration of $\sim 0.2\%$ near Callisto's location in the fully reset CPD. While this appears to be more representative of what is known of the Galilean moon surface composition, the primordial CO_2 concentration of Callisto's building blocks cannot simply be derived from the present state of the surface.

Our findings are consistent with a primordial origin for Callisto's CO_2, and point to the possibility that Ganymede and Callisto's icy building blocks had distinct chemical compositions. While it has been suggested that Ganymede may have formed with a primordial CO_2 component which was lost during an episodic period of surface melting, our results suggest icy grains in its vicinity were CO_2-poor. A CPD midplane temperature profile which is dominated by viscous heating and in which the water iceline falls between Europa and Ganymede naturally produces a CO_2 iceline between Ganymede and Callisto.

4.5 Summary and Conclusions

If CPD ice composition is (partially or fully) reset, NH_3 ice formation is inefficient due to N_2 self-shielding. The resulting $\ll 1\%$ concentration of NH_3 ice is unlikely to significantly alter the thermophysical/chemical properties of subsurface melt. The most significant impurities are the carbon-bearing CO_2 and HCOOH ices and each make up at most $\sim$ 10% of the molar ice fraction. If the growth of the moons occurred near their present-day positions they are largely free of impurities, being composed of 98% water ice, $\sim$ 2% CH_3OH, and trace amounts of CO_2. If instead the CPD ice composition is inherited from the circumstellar nebula, NH_3 ice can survive conditions at the CPD midplane and becomes the most abundant impurity. Observations indicating the presence of NH_3 in the Saturnian satellite system but not in the Galilean one are consistent with a reset-inheritance dichotomy. NH_3 in the planetary feeding zone of Jupiter, if present, may have been destroyed during accretion onto the CPD and then could not form again in time. Our key findings are summarized as follows:

1. The ice composition of the Galilean moons corresponds to a partial or full chemical reset, as opposed to the ices of the Saturnian moons which may have been more directly inherited from the circumstellar disk.

2. A partial reset prevents efficient formation of ammonia ice. The building blocks of the Galilean moons (and of exomoons forming in similar CPDs) would have been nitrogen-poor (NH_3 ice abundances w.r.t. H_2O ice of $\sim 0.1\%$).

3. Our results are consistent with a primordial origin for CO_2 ice on Callisto and an ice composition which is chemically distinct from Ganymede.

Acknowledgements

The research of N.O. and I.K. is supported by grants from the Netherlands Organization for Scientific Research (NWO, grant number 614.001.552) and the Netherlands Research School for Astronomy (NOVA). This research has made use of NASA's Astrophysics Data System Bibliographic Services. This research has also extensively used Numpy (Harris et al., 2020), Matplotlib (Hunter, 2007), Scipy (Virtanen et al., 2020), and Prodimopy https://gitlab.astro.rug.nl/prodimo/prodimopy. N.O would like to thank S. Ceulemans for her suggestion that greatly improved the visualizations in this work, as well as J. Tjoa and S. van Mierlo for helpful discussions and support.

Appendix

A.1 Chemical network diagrams annotated

The chemical network diagrams are generated algorithmically according to the following rules depicted in Fig. 4.10 :

1. A single species is selected as the seed from which the diagram will be generated.
2. In the first iteration, all species which are involved in the formation or destruction of the seed above a certain rate threshold are added as nodes to the network (one degree of separation).
3. The reaction with the highest rate relating two species is represented as a connection (arrow) between the two nodes.
4. This process is iterated starting from (2) for n degrees of separation.

While one species may be involved in the formation of another through multiple distinct reactions (i.e. H+OH→H_2O and OH+OH→H_2O+O), we color code the reaction connecting the nodes with the type (i.e. ion-neutral) of the reaction with the highest rate v. The arrow width is proportional to the net formation rate (v(A→B) - v(B→A)) between the two species. The node size is proportional to the abundance of the species. For some reactions the fraction of the reactions forming species B involving species A is included as a percentage (i.e. for A→B 20% of all the reactions that form B involves A). Networks are generated for a single grid point in the CPD model (ambient conditions are listed in the respective diagram) and at a specific time only, and are thus to be considered as "snapshots". H and H_2 are not displayed as nodes. Arrows are not displayed if they contribute less than 1% to the total formation rate of a species.

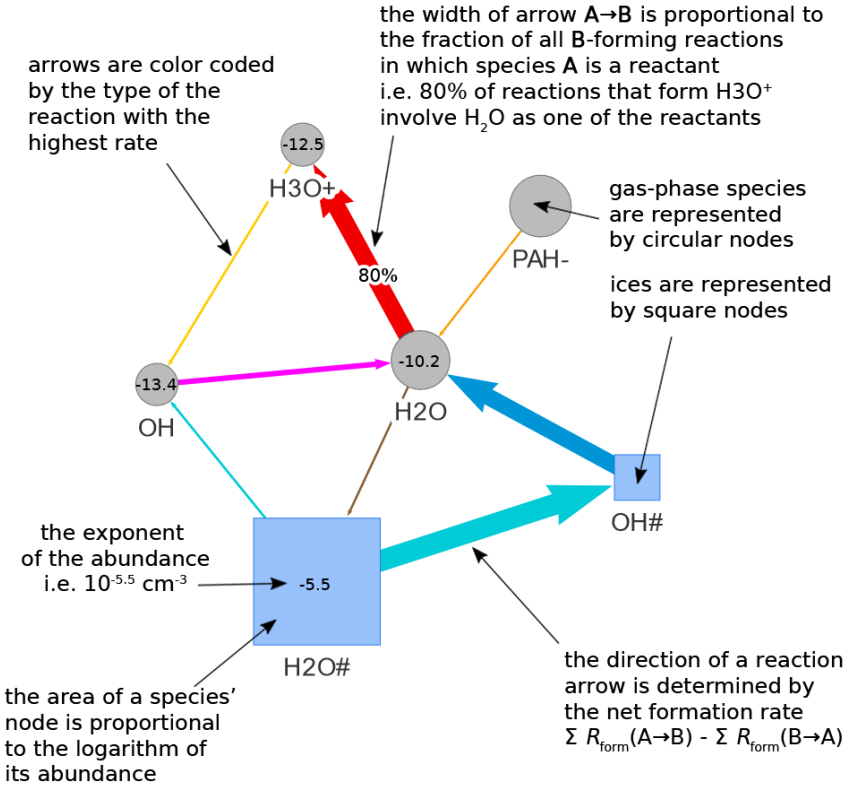

Figure 4.10: Example chemical network diagram with annotations describing how the diagram can be interpreted. The primary formation pathway of a species may also be highlighted for reference (not depicted).

Chapter 5

Modeling Circumplanetary Dust Emission in the Mid-Infrared

Abstract

Context: Mid-infrared (mid-IR) imaging traces the sub-micron and micron-sized dust grains in protoplanetary disks and it offers constraints on the geometrical properties of the disks and potential companions, particularly if those companions have circumplanetary disks.
Aims: We aim to put new constraints on the sizes of the emitting regions of the protoplanetary disks and the presence of possible companion objects associated with dusty subdisks. We use the VISIR instrument and its upgrade NEAR on the VLT to take new mid-IR images of five (pre-)transition disks and one circumstellar disk with proposed planets and obtain the deepest resolved mid-IR observations.
Methods: Where available, we compare the data to ProDiMo (**Pro**toplanetary **Di**sk **Mo**del) radiation thermo-chemical models to place upper limits on the flux of continuum point sources associated with putative substellar companions. We focus on the well-studied HD 100546 system for which we acquired the deepest observations.
Results: We refined the existing ProDiMo HD 100546 model spectral energy distribution (SED) fit in the mid-IR by increasing the PAH abundance relative to the ISM, adopting coronene as the representative PAH, and increasing the outer cavity radius to 22.3 AU. We produced flux estimates for putative planetary-mass companions and circumplanetary disks, ruling out the presence of planetary-mass companions with $L > 0.0028\,L_\odot$ for $a > 180$ AU in the HD 100546 system. Upper limits of 0.5 mJy-30 mJy are obtained at $8\,\mu$m-$12\,\mu$m for potential companions in the different disks. We rule out companions with $L > 10^{-2}\,L_\odot$ for $a > 60$ AU in TW Hydra, $a > 110$ AU in HD 169142, $a > 150$ AU in HD 163296, and $a > 160$ AU in HD 36112.
Conclusions: The mid-IR emission comes from the central regions and traces the inner areas of the disks, including inner disks and inner rims of outer disks. Planets with mid-IR luminosities corresponding to a runaway accretion phase can be excluded from the HD 100546, HD 169142, TW Hydra, and HD 36112 systems at separations $>1''$. We calculated an upper limit to the occurrence rate of wide-orbit massive planets with circumplanetary disks of 6.2% (68% confidence). Future observations with METIS on the ELT will be able to achieve a factor of 10 better sensitivity with a factor of 5 better spatial resolution. MIRI on *JWST* will be able to achieve 250 times better sensitivity. Both will possibly detect the known companions to all six targets.

This chapter is based on the work published as Petit dit de la Roche et al. 2021 *New Mid-Infrared Imaging Constraints on Companions and Protoplanetary Disks around six Young Stars* A&A 648, A92
D. J. M. Petit dit de la Roche, N. Oberg, M. E. van den Ancker, I. Kamp, R. van Boekel, D. Fedele, V. D.Ivanov, M. Kasper, H. U. Käufl, M. Kissler-Patig, P. A. Miles-Páez, E. Pantin, S. P. Quanz, Ch. Rab, R.Siebenmorgen & L. B. F. M. Waters

Table 12: Stellar and disk properties of the target stars. Stellar masses, luminosities, and temperatures, where possible, have been taken from the DIANA models of the targets, which are fit to multiple data sets. *(a)* Gaia Collaboration et al. (2020). *(b)* Wichittanakom et al. (2020); Miley et al. (2019); Casassus and Pérez (2019); Jamialahmadi et al. (2018); Mendigutía et al. (2017); Pineda et al. (2014); Avenhaus et al. (2014); Walsh et al. (2014); Leinert et al. (2004). *(c)* Garufi et al. (2014); Wichittanakom et al. (2020). *(d)* Pérez et al. (2019); Panić et al. (2008); Raman et al. (2006); van Boekel et al. (2005). *(e)* Nayakshin et al. (2020); Sokal et al. (2018). *(f)* Wichittanakom et al. (2020); Rosotti et al. (2020); Yu et al. (2019); Long et al. (2017); Benisty et al. (2017); Wagner et al. (2015). *(g)* Isella et al. (2010); Meeus et al. (2012).

Target	Age (Myr)	M_* ($M_\odot$)	T (K)	L_* ($L_\odot$)	d (pc)[a]	PA (°)	i (°)	Structures	Companions detected
HD 100546[b]	5	2.5	10600	30	108.1	140	46	gap, spiral arms	3
HD 163296[c]	6	2.5	9000	34.7	101.0	137	43	rings	3
HD 169142[d]	4-16	1.8	7800	9.8	114.9	5	13	rings	3
TW Hydra[e]	3-15	0.8	4000	0.2	60.1	150	7	rings	1
HD 100453[f]	11	1.5	-	6	103.8	145	35	gap, spiral arms	M dwarf
HD 36112[g]	4	2.0	8200	22	155.9	62	21	cavity, rings, clumps, spirals	2

5.1 Introduction

Transition disks are believed to represent an intermediate stage of planet formation between the protoplanetary disk and a gasless, fully formed planetary system. Scattered light imaging in the near-infrared (near-IR) and thermal sub-millimetre observations with ALMA have revealed detailed structures in many transition disks, including rings, spirals, and warps (e.g. Francis and van der Marel, 2020). These features can be a result of the accretion of gas and dust onto a planet, although they can also be explained by other processes in the disk such as shadowing from the inner rim, snowlines, or hydrodynamic effects (e.g. Siebenmorgen and Heymann, 2012; van der Marel et al., 2018). Studying transition disks is an important step in understanding planet formation. Mid-infrared (mid-IR) direct imaging traces dust of ~150 K in the disk. Additionally, the disk is expected to re-emit a large fraction of the stellar flux in the infrared (e.g. Dullemond and Monnier, 2010). Mid-IR imaging can thus further constrain disk properties, especially when combined with observations at other wavelengths. It also allows us to search for thermal emission from (planetary) companions, especially if these companions still have dusty circumplanetary disks (CPDs).

We used the radiation thermo-chemical disk modeling code ProDiMo (**Pro**to- planetary **Di**sk **Mo**del; see Sect. 5.3) to contextualise observations of our primary target HD 100546 and secondary targets. Our HD 100546 disk model is the result of a multi-wavelength spectral energy distribution (SED) fit, which will allow us to compare the predicted and observed total flux within the observed bands (Woitke et al., 2019). Our synthetic images of the HD 100546 circumstellar disk enabled us to search for a non-axisymmetric disk structure. The radiative transfer modeling allows us to determine the

mid-IR extinction along line-of-sights to the disk midplanes and the resulting extinction of any putative embedded companions. The disk modeling code can be applied further to produce SEDs for planetary companions and circumplanetary disks to compare theoretical fluxes with detection limits (Rab et al., 2019).

We compared our modelled circumplanetary dust emission signature with new observations of six young star systems. We used the VLT Imager and Spectrograph for the mid-InfraRed (VISIR; Lagage et al., 2004) and its upgraded version Near Earths in the AlphaCen Region (NEAR; Kasper et al., 2017) to obtain the deepest resolved mid-IR images of five Herbig Ae/Be (pre-)transition disks and one other circumstellar disk to date. The instruments that we used are more sensitive and the observation time is longer than in any previous studies (Liu et al., 2003; van Boekel et al., 2004; Leinert et al., 2004; Verhoeff, 2009; Panić et al., 2014; Mariñas et al., 2011; Doucet et al., 2006; Honda et al., 2012; Okamoto et al., 2017; Maaskant et al., 2013; Ratzka et al., 2007; Arnold et al., 2012; Khalafinejad et al., 2016). Additionally, the use of adaptive optics (AO) on NEAR provides us with better angular resolution and PSF stability. These new data allowed us to put new constraints on the disk and the presence of possible companions of each of the six targets.

The ProDiMo model is discussed in Sect. 5.3 and compared to the data in Sect. 5.5. Section 5.2 describes the targets and in Sect. 5.4 we show the observations and the data analysis. Limits on possible companions are discussed in Sect. 5.6 and for three of the targets planetary models with circumplanetary disks are analysed. Finally, our discussion and conclusions are presented in Sect. 5.7.

5.2 Targets

The following targets were observed: HD 100546, HD 163296, HD 169142, TW Hydra, HD 100453, and HD 36112/MWC 758 (see Table 12). These stars were selected to study the influence of features such as spiral arms, circular gaps, and inner cavities, seen in near-IR scattered light images on the mid-IR morphology of the disk which is dominated by thermal emission.

All six targets are young disks with ages of 3-16 Myr and, with the exception of HD 163296, are classified as (pre-)transition disks with a central cavity (or large inner gap). While HD 163296 does not have the traditional (pre-)transition disk SED, it nonetheless has other structures in the disk and proposed companions, similar to the remaining targets in the sample and was therefore included here (Espaillat et al., 2014; Isella et al., 2016). In addition to central cavities, sub-millimetre dust emission and near-IR scattered light imaging have revealed features such as rings, clumps, and spirals in all the disks. At distances of 60-160 pc, the extended disks of the targets are expected to be large enough to be resolved with the Very Large Telescope (VLT) at Paranal in the 8-12 μm wavelength range.

Below, we provide an overview of the HD 100546 system and possible companions, specifically those inferred through direct imaging. A description of the secondary targets can be found in Appendix A.1.

5.2.1 HD 100546

This disk is divided into an inner disk and an outer disk, separated by a single gap from ~1-21 AU (e.g. Bouwman et al., 2003; Grady et al., 2005; Menu et al., 2015; Jamialahmadi et al., 2018; Pineda et al., 2019). It is possible that the inner and outer disks are misaligned (Pineda et al., 2019; Kluska et al., 2020). The outer disk has spiral structures that have so far only been detected in the near-IR (Follette et al., 2017; Quillen, 2006) and there is a tentative detection of a bar-like structure across the gap which could indicate small-scale inflow or be the base of a jet (Mendigutía et al., 2017; Schneider et al., 2020). There have been some suggestions of warping in the inner and outer disk, but this has so far remained inconclusive (e.g. Quillen, 2006; Panić et al., 2014; Pineda et al., 2014; Walsh et al., 2017; Sissa et al., 2018; Kluska et al., 2020).

There has been much discussion about possible companions. One companion, HD 100546 b, was identified at a separation of 55 AU at a position angle of 9° (Quanz et al., 2013a; Currie et al., 2014; Quanz et al., 2015). However, this has been called into question by Rameau et al. (2017), who failed to detect any accretion at the planet location in Hα and posit the L′ band (3.8 μm) detection might be related to the chosen method of data reduction. The lack of detection in Hα is supported by Cugno et al. (2019). A different companion, HD 100546 c, may have been detected just inside the central cavity at ~13 AU (Brittain et al., 2014; Currie et al., 2015), although this too has been contested (Fedele et al., 2015; Follette et al., 2017; Sissa et al., 2018). ALMA observations at 1.3 mm have revealed a 6σ point source of 92 ± 9 μJy at a position angle of 37° and a projected separation of 7.8 AU, which could represent an additional planetary candidate (herafter HD 100546 d; Pérez et al., 2020). A final planet candidate has also been suggested by the presence of a Doppler flip observed in the disk ^{12}CO kinematics. Such a planet would be embedded within the disk continuum emission region exterior to the gap, corresponding to a projected radial distance of 20.5 ± 5 AU (Casassus and Pérez, 2019).

5.3 Protoplanetary disk modeling with ProDiMo

We used the radiation thermo-chemical disk model ProDiMo[6] (Woitke et al., 2009; Kamp et al., 2010a; Thi et al., 2011) to simulate observations of the HD100546 system. ProDiMo self-consistently and iteratively determines the physical and chemical state anywhere within the disk with a frequency dependent 2D dust continuum radiative transfer, including gas-phase and photo-chemistry, ice formation, and non-LTE heating and cooling mechanisms. ProDiMo performs a 2D continuum radiative transfer with a ray-based, long-characteristic, accelerated Λ-iteration method at every disk grid point to calculate the local radiation field $J_\nu(r, z)$ (Woitke et al., 2009). The full radiative transfer methodology is described in Woitke et al. (2009). We adopt the standard DIANA[7] dust opacities as described in Woitke et al. (2016) and Min et al. (2016b).

[6] https://www.astro.rug.nl/~prodimo/

[7] https://dianaproject.wp.st-andrews.ac.uk/data-results-downloads/fortran-package/

Table 13: Overview of the observations used in this paper. HD 100546 was observed as part of different programmes than the other observations, leading to the difference in filters and observation times.

Target	Instrument	Date	Filter	$\lambda_0(\mu m)$	$\Delta\lambda(\mu m)$	Integration time (s)
HD 100546	VISIR	28-04-2018	J8.9	8.70	0.74	3600
	NEAR	11-12-2019	PAH1	8.58	0.41	540
			ARIII	8.98	0.14	540
			PAH2	11.24	0.54	540
		12-12 2019	PAH2_2	11.68	0.37	540
HD 163296	NEAR	14-09-2019	PAH1	8.58	0.41	600
		13-09-2019	NEAR	11.25	2.5	600
HD 169142	NEAR	13-09-2019	PAH1	8.58	0.41	600
			NEAR	11.25	2.5	600
TW Hya	NEAR	13-12-2019	PAH1	8.58	0.41	600
		16-12-2019	NEAR	11.25	2.5	600
HD 100453	NEAR	12-12-2019	PAH1	8.58	0.41	600
			NEAR	11.25	2.5	600
HD 36112/MWC 758	NEAR	18-12-2019	NEAR	11.25	2.5	600

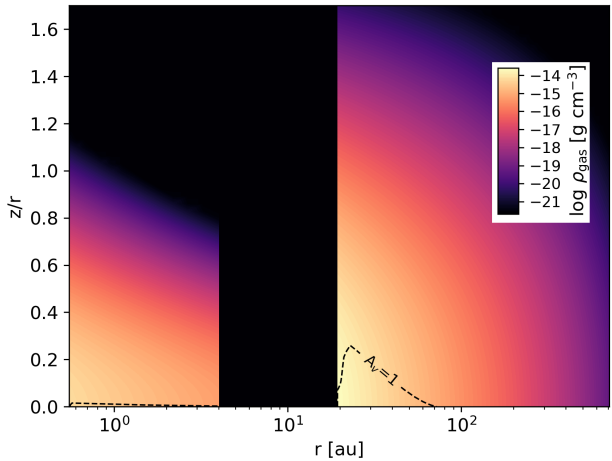

Figure 5.1: Gas density profile of the ProDiMo HD 10056 disk model. The dashed contour line traces the surface where the minimum optical extinction A_V in the combination of the vertical or radial direction is 1.

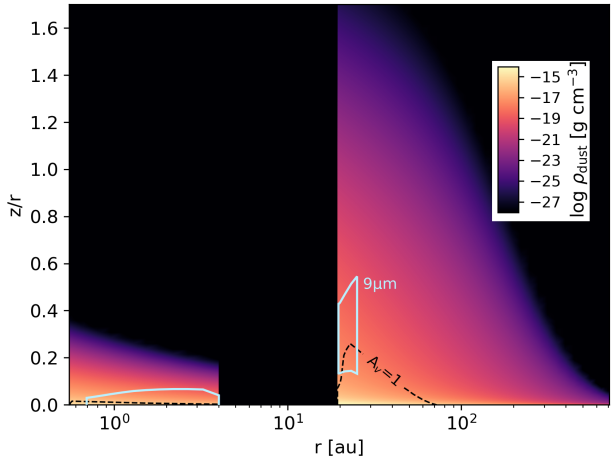

Figure 5.2: Dust density profile of the ProDiMo HD 100546 disk model. The light blue contour outlines the region where half of the total 9 μm emission originates. The dashed contour line traces the surface where the minimum optical extinction A_V in the combination of the vertical or radial direction is 1.

Table 14: DIANA SED-fit parameters for the HD 100546 system used in the ProDiMo disk model. Parameters that were modified to improve the mid-IR fit are included in parenthesis.

Parameter	Symbol	Value
Stellar Mass	M_*	2.5 $M_\odot$
Stellar Luminosity	L_*	30.46 $L_\odot$
Effective Temperature	$T_{\rm eff}$	10470 K
Interstellar Extinction	A_V	0.22 mag
Dust composition:		
$Mg_{0.7}Fe_{0.3}SiO_3$		58.17 %
Amorphous carbon		16.83%
Vacuum		25%
Dust size power law	p	3.34
Disk Inner Zone		
Mass	$M_{\rm d}$	8.81×10^{-8} $M_\odot$
Inner Radius	$R_{\rm in}$	0.55 AU
Outer Radius	$R_{\rm out}$	4.00 AU
Col. Density Power Index	ϵ	0.35
Minimum dust size	$a_{\rm min}$	0.042μm
Maximum dust size	$a_{\rm max}$	2.9 μm
PAH abundance	$f_{\rm PAH}$	0.0028
Disk Outer Zone		
Mass	$M_{\rm d}$	7.15×10^{-3} $M_\odot$
Inner Radius	$R_{\rm in}$	19.34 (22.3) AU
Outer Radius	$R_{\rm out}$	600 AU
Tapering Radius	$R_{\rm tap}$	100 AU
Col. Density Power Index	ϵ	1.12
Minimum dust size	$a_{\rm min}$	0.042μm
Maximum dust size	$a_{\rm max}$	2983 μm
PAH abundance	$f_{\rm PAH}$	0.0028 (0.0034)
Inclination	i	42°
Dust to Gas Ratio	d/g	0.01

The parameters for the HD 100546 disk model were derived from the SED fitting work done as part of the European FP7 project DIANA[8] (Woitke et al., 2019). Parameters of the HD 100546 disk and stellar model can be found in Table 14 and the 2D gas density profile can be found in Fig. 5.1. The fitting was performed for a pre-Gaia

[8]More information about the fitted stellar and disk parameters, the 2D modeling results, and the predicted observables can be found at http://www-star.st-and.ac.uk/~pw31/DIANA/DIANAstandard

distance of 103 pc (van den Ancker et al., 1997). Further details regarding the disk modeling and SED fitting process can be found in Section 5.3.1.

As ProDiMo finds formal solutions to the continuum radiative transfer during the calculation of the SED, the resulting modelled intensity can be visualised as an image. ProDiMo includes only the effect of isotropic scattering, and hence the preferential forward-scattering of light by larger dust grains is not represented realistically. As a result, the ProDiMo model appears brighter on the far side than on the near side and it cannot reproduce the observed asymmetry in brightness of actual disks. While this effect is cancelled out in the disk SED model and radial intensity profile, it must be taken into consideration when comparing the model image to data on a per-pixel basis. The resulting ProDiMo data cube was attenuated by multiplying each synthetic disk image with the VISIR and NEAR relative filter transmission curves created with the VISIR imaging detector and VISIR calibration unit, and then by the sky transmission[9] at each wavelength. Subsequently the data cube was flattened into a single image for each filter. The images were then convolved with a reference PSF to simulate our observations. This was HD 93813 for the J8.9 filter, HD 27639 for the ARIII filter, and the HD 163296 data for the PAH1 and NEAR filters. For the PAH2 and PAH2_2 filters, reference PSFs were not available and the PSF from the ARIII filter was scaled to the new central wavelength and used instead.

5.3.1 Standard disk models and SED fitting methodology

To perform the SED fit of the HD 100546 system, a comprehensive set of publicly available observational data, consisting of photometric fluxes, interferometric data, low and high resolution spectra, emission line fluxes, line velocity profiles, and maps were used from which the physical and chemical parameters of the disk could be derived (references for which can be found in Dionatos et al. (2019)). The fits were performed by iteration of parameter sampling in MCFOST radiative transfer models by means of a genetic algorithm described in Woitke et al. (2019). HD 100546 was fit with 120 data points, two disk zones, PAHs, and 16 free parameters total after 632 generations and 7584 models. Further details of the standard disk models, SED fitting procedures, and the limitations of SED fitting can be found in Woitke et al. (2016), Kamp et al. (2017), Woitke et al. (2019), and Dionatos et al. (2019).

Limitations

The DIANA SED fitting procedure was performed with dust opacities corresponding to a mixture of amorphous pyroxene silicates and amorphous carbon (see Table 14; Dorschner et al., 1995; Zubko et al., 1996). Due to the use of standard dust opacities and a fixed PAH morphology, only the power-law of the dust size distribution and volume fraction of amorphous carbon was varied for the fit, so detailed matching of the spectral

[9] https://www.eso.org/observing/etc/bin/gen/form?INS.MODE=swspectr+INS.NAME=SKYCALC

features is not expected. The 8.6 μm PAH complex feature, associated with in-plane C-H bending modes, is not fit in detail relative to the *ISO-SWS* spectrum. The presence of an unidentified broad feature at 7.9-8 μm is not explained by the model, but it has been suggested by Joblin et al. (2009) to originate from a PAH population known as PAH^x consisting of compact but large ionised PAHs with ~100 or more carbon atoms not included in our radiative transfer modeling.

We opted not to explore the parameter space of possible dust compositions to perform a detailed opacity fitting across the mid-IR given that properties, such as the amorphous carbon volume fraction, can have a large impact on the SED at all wavelengths, e.g. by changing the millimetre and centimetre slopes (Woitke et al., 2016). While the mid-IR traces the disk surface, any observed features may not be indicative of e.g. the midplane dust properties. The observed features could instead represent surface effects originating from high-altitude PAHs which are generated locally. In this case, altering the model global dust properties may not be the correct approach.

We did not re-perform the global SED fitting procedure to account for the increased GAIA EDR3 distance for HD 100546, but we did consider the implications of an increased stellar luminosity to match the observed luminosity and new distance. To test the sensitivity of the SED to this adjustment, we considered a modest increase in our stellar effective luminosity to 34.74 $L_\odot$. If we were then to scale the physical dimensions of the disk and its gap accordingly, the resulting SED would exhibit a net decrease in mid-IR emission; across the J8.9 band, we find a deficit in emission over the fiducial model of 2.9%. As this falls within our own observational uncertainty, we do not consider the implications of the new distance estimate further.

5.4 Observations and data analysis

Observations of HD 100546 were obtained during April 2018, with the VLT Imager and Spectrometer for the mid-IR (VISIR, Lagage et al. 2004), and of all six disks during the science verification of its upgrade, with NEAR (Kasper et al. 2017) in September and December of 2019. The benefit of NEAR is its use of AO, which results in improved angular resolution, PSF stability, and sensitivities (a factor of ~4) across the N-band. An overview of the observations used in this paper is presented in Table 13.

For all targets, all observations were taken in the pupil tracking mode, where the derotator is turned off to allow for field rotation during the observation sequence. For the NEAR observations, AO was enabled and the targets themselves were used as the reference star for wavefront sensing. The chopping and nodding sequence was enabled to subtract the sky background. In the VISIR data, the chop throw is 8″ in the direction perpendicular to the nodding direction; whereas, in the NEAR data, the chop throw is 4.5″ in the parallel direction. Since the throw determines the useful field of view, the VISIR and NEAR data have an effective field of view of 16″x16″ and 9″x9″, respectively. The VISIR data have a chopping frequency of 4 Hz and a detector integration time (DIT) of 0.012 s. The NEAR data have a chopping frequency of 8 Hz and a DIT of 0.006 s. Both NEAR and VISIR have platescales of 0.0453″.

The standard VISIR data reduction pipeline[10] is not suited to reduce data taken in the pupil tracking mode, so special purpose python scripts were employed to reduce and analyse the data. VISIR and NEAR data are delivered in chop difference images with integration times of 20-50 s each. Data from the different nod positions are subtracted from each other and the resulting images are derotated. The beams from the chopping and nodding from all images are then median combined with 3σ sigma clipping into a single master image. Only the VISIR observations of HD 100546 have a reliable reference star (HD 93813) with which to calibrate the result, leading to an observed flux of 27 ± 3 Jy. For HD 100546 observations in other bands and in the cases of HD 163296, HD 169142, and TW Hya, we used the flux predicted by the ProDiMo models (described in Section 5.3) to calibrate the data. Since the model is fitted to SED data from a collection of previous observations of the targets taken with other instruments, including data around 8-12 μm, it is the most accurate way available to determine the brightness in the images and this allowed us to calculate the flux in the specific wavelength ranges of the different filters (Dionatos et al., 2019; Woitke et al., 2019). The calibration is done by multiplying the model fluxes with the filter and sky transmissions and averaging the total flux over the required wavelength range. This is then set as the total flux of the data. As there are no models available for HD 100453 and HD 36112, the averages of previous flux measurements in similar filters had to be used (van Boekel et al., 2005; Carmona et al., 2008; Verhoeff, 2009; Mariñas et al., 2011; Khalafinejad et al., 2016; Li et al., 2018).

The final master images of the disks are shown in Figures 5.3 and 5.4. The star is not visible in any of the images as it does not contribute significantly to the flux in the mid-IR (<10% of the total flux in the ProDiMo models). Most of the central emission at these wavelengths is from unresolved inner disks or inner rims of outer disks.

5.4.1 HD 100546

The master images of HD 100546 in the different filters are shown in Figure 5.3, along with the corresponding model images after convolution with an appropriate PSF. For the J8.9 filter, this is the PSF of reference star HD 93813. While there were no appropriate flux calibration observations for the other filters, point sources were observed in the PAH1 and ARIII filters, which were used as PSF references. For the PAH1 filter and the ARIII filter, we used our own observations of HD 163296 and HD 27639, respectively. As there were no reference PSFs available in either the PAH2 or PAH2_2 filters, we used scaled versions of the ARIII reference instead. Since the different filters on the NEAR instrument result in similar sensitivities over time, and the observations in the different filters have similar exposure times, all master images are expected to have similar sensitivities. The exception are the observations with the J8.9 filter which were taken with VISIR and where the increased observation time compensates for the lack of AO, meaning the final sensitivity of the master image is still expected to be similar to those in the other filters. While the disk is resolved in all filters, the VISIR data are

[10] https://www.eso.org/sci/software/pipelines/visir/visir-pipe-recipes.html

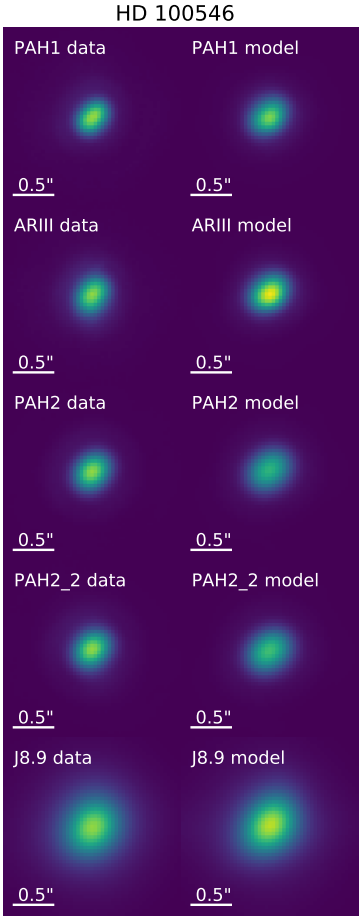

Figure 5.3: Master images (left) and model images (right) of HD 100546 in various filters. North is up and east is left in all images. The observations were scaled to have the same flux as the model images. The PAH1, ARIII, PAH2, and PAH2_2 filter master images were taken with NEAR and show a resolved, inclined disk. The J8.9 data were taken with VISIR and are more extended compared to the NEAR data due to image elongation from the telescope resulting in a distorted and enlarged PSF. The model images provide a good match for the master images in each filter.

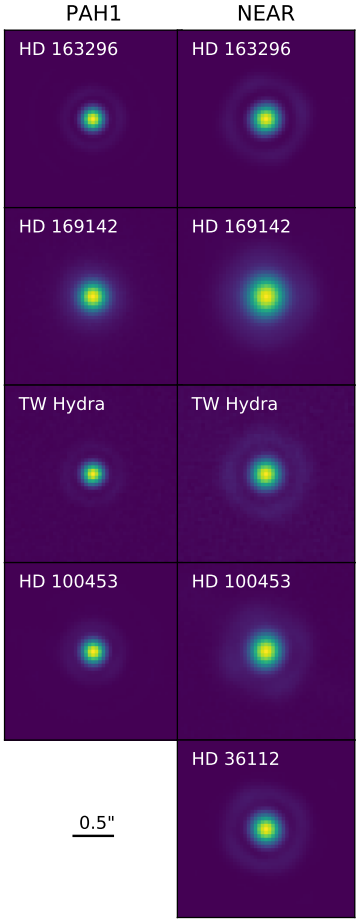

Figure 5.4: Normalised master images of the disks observed with NEAR. North is up and east is left in all images and the scale bar in the bottom left indicates 0.5″. The left column shows the disks in the PAH1 filter and the right column in the NEAR filter. HD 163296 and TW Hydra are unresolved in both filters. HD 36112 was not imaged in the PAH1 filter, but it is unresolved in the NEAR filter. Compared to these images, it can be seen that HD 169142 and HD 100453 are more extended in both filters.

clearly more extended than the NEAR data. The J8.9 band contains both the PAH1 and ARIII bands and so the VISIR image would be expected to have a similar extent as the NEAR images in these bands. Some of the difference is because the AO on NEAR means the images are more compact, but mostly due to the telescope operations during the VISIR observations. During this night, there was a decrease in the precision of the altitude axis of the telescope, resulting in elongation of the image along the paralactic angle (de Wit, 2020). As this was at an angle of 40 degrees with the semi-major axis of the disk, the image is smeared along both axes and the smearing is not immediately obvious without a comparison. This is accounted for by using a reference PSF of the standard star HD 93813. Since this data set was taken immediately preceding the science observations in the same filter, it has a similar smearing effect.

The central bright emission in each image is from the unresolved inner disk, as the star is expected to be an order of magnitude fainter than the disk at mid-IR wavelengths based on the model data. Beyond that, emission is expected to be dominated by the inner rim of the outer disk, which is irradiated by the star and puffed up as a result. The rest of the outer disk is not warm enough to be detected in the image.

Using a Levenberg-Marquardt algorithm and least squares statistic to fit a simple two dimensional Gaussian to the surface brightness of the disk in each filter results in an average position angle of $141 \pm 2°$. Since we are fitting a two-dimensional function to a three-dimensional disk, we are sensitive to projection effects. This is especially the case because the inner wall of the outer disk is only visible on the far side of the disk and not on the close side. This means what we are calculating is actually the position angle of the two-dimensional projection of the disk, which we call the projected position angle. We also applied this method to model images of HD 100546 at the same wavelengths and found that the projected position angle is $\sim 130°$, compared to the input of 140°, so we expect a difference between the projected position angle and the real position angle of roughly 10 degrees. This would still be in agreement with previous position angle values of 135-150° (Miley et al., 2019; Casassus and Pérez, 2019; Jamialahmadi et al., 2018; Mendigutía et al., 2017; Pineda et al., 2014; Avenhaus et al., 2014; Walsh et al., 2014; Leinert et al., 2004). A more precise determination of the disk orientation requires extensive modeling and is outside the scope of this paper.

The deprojected disk has a full-width-half-maximum (FWHM) of 0.82″ in the J8.9 filter and 0.35″-0.41″ in the other filters. The larger size of the J8.9 image is due to the above-mentioned PSF smearing from uncertainty in the altitude axis of the telescope. The FWHM values for all the disks and filters are listed in Table 15. From the disk FWHM and the PSF FWHM (the diffraction limit is 0.22″ – 0.30″ depending on the filter), we can calculate the true size of the emitting region, assuming that both the data and the PSF are well described by Gaussian functions (e.g. Mariñas et al., 2011; van Boekel et al., 2004), as follows:

$$\mathrm{FWHM_{disk}} = \sqrt{\mathrm{FWHM_{data}}^2 - \mathrm{FWHM_{PSF}}^2}. \tag{113}$$

Due to the PSF smearing in the J8.9 image, we used the reference PSF FWHM rather than the theoretical diffraction limit for this filter. Since the other data were observed

with the NEAR instrument, which thanks to its adaptive optics is expected to have a Strehl ratio of close to one (Kasper et al., 2017), the FWHM of a point source PSF corresponds to the diffraction limit. This can be seen in the data of HD 163296, TW Hydra, and HD 36112, as is discussed in Sect. 5.4.2. The deconvolved FWHM of all resolved sources and the corresponding 5σ upper limits for unresolved sources are also listed in Table 15. While spectroscopic data show that the disk is more extended in PAH emission bands (van Boekel et al., 2004; Verhoeff, 2009), the PAH1 and PAH2 filter images are no more extended than their continuum counterparts. This is because the extent of the emission is averaged over the filter wavelength range and the PAH emission is estimated to be around 22% of the total flux in the PAH1 filter and 13% in the PAH2 filter (van Boekel et al., 2004). As a result, both PAH filter images are dominated by the continuum emission and have similarly sized emission regions as the images in the continuum filters. The 2σ discrepancy between the J8.9 and the PAH1 and ARIII deconvolved FWHM means the errorbars on the J8.9 image are probably underestimated, possibly due to a worsening of the smearing effect as the night went on.

Removing the PSF component along both axes also gives a more accurate inclination, since the semi minor axis of the disk is relatively more extended by the PSF than the semi-major axis. The calculated inclination is $47 \pm 3°$. The projection effect is not expected to be as strong here, since even on the model data the resulting inclination was well within 1σ of the input value. The projected inclination is in agreement with literature inclination values of 42-50° (Miley et al., 2019; Casassus and Pérez, 2019; Jamialahmadi et al., 2018; Mendigutía et al., 2017; Pineda et al., 2014; Avenhaus et al., 2014; Walsh et al., 2014). This value is the combined inclination across all the available filters, except for J8.9 due to the deformed PSF in this image.

5.4.2 Other sources

HD 163296 is unresolved in both filters and has FWHMs around the diffraction limit of the telescope which is 0.22″ in the PAH1 filter and 0.30″ in the NEAR filter. This results in 5σ upper limits of 7 AU and 6 AU, respectively. Previous mid-IR observations between 8 μm and 13 μm have not resolved the disk, but set an upper limit on the FWHM of the emission region of 21 AU at 11.7 μm (Jayawardhana et al., 2001; van Boekel et al., 2005; Mariñas et al., 2011; Li et al., 2018). Our images of HD 163296 improve on the emission size upper limits by a factor of three.

HD 169142 is the most resolved disk in the sample after HD 100546. The measured and deconvolved FWHM are listed in Table 15. Additionally, the measured projected inclination of the deconvolved disk is $13 \pm 2°$, which is in agreement with previously measured inclinations of $13 \pm 1°$ (Pérez et al., 2019; Panić et al., 2008; Raman et al., 2006).

TW Hydra is unresolved in our observations with upper limits of 3 AU in the PAH1 band and 49 AU in the NEAR band. The high limit in the NEAR band is due to the data being taken with the coronograph. While this allows for increased sensitivity for finding planets, it also means that the extent has to be calculated with the off-axis chop and

Table 15: FWHM of the disks in each filter is given in arcseconds. HD 100546 is clearly resolved in all bands. HD 169142 and HD 100453 are resolved in both the PAH and NEAR bands, while HD 163296, TW Hydra, and HD 36112 are unresolved point sources. For resolved images, the FWHM after deconvolution is listed in AU. For unresolved images, the 5σ upper limits are listed instead.

Object	Filter	$FWHM_{data}$ ($''$)	$FWHM_{disk}$ (AU)
HD 100546	J8.9	0.82 ± 0.10	61 ± 11
	PAH1	0.349 ± 0.003	28.9 ± 0.5
	ARIII	0.356 ± 0.002	29.0 ± 0.3
	PAH2	0.392 ± 0.002	28.2 ± 0.4
	PAH2_2	0.414 ± 0.002	30.5 ± 0.3
HD 163296	PAH1	0.216 ± 0.002	<7
	NEAR	0.282 ± 0.001	<6
HD 169142	PAH1	0.336 ± 0.003	28.6 ± 0.5
	NEAR	0.465 ± 0.003	41.1 ± 0.5
TW Hydra	PAH1	0.219 ± 0.001	<3
.	NEAR	0.297 ± 0.029	<49
HD 100453	PAH1	0.234 ± 0.002	9.3 ± 0.6
	NEAR	0.352 ± 0.035	20.7 ± 6.6
HD 36112	NEAR	0.315 ± 0.002	<13

nod beams. Based on the PAH1 data taken the same night, the beams are expected to be smeared by ∼ 10%. These limits are consistent with previous interferometry measurements which found the size of the emitting region of the disk to be 1-2 AU around 8-12 μm (Ratzka et al., 2007; Arnold et al., 2012).

HD 100453 is resolved in both bands. Similar to TW Hydra, the NEAR band images of HD 100453 were taken with the coronograph, resulting in a 10% error in the extent of the emission region. The difference between the deconvolved PAH1 and NEAR band sizes suggests this might still be an underestimate. The disk has a calculated projected inclination of 35 ± 5°, which is in agreement with literature values of the inclination of 30-38° (Rosotti et al., 2020; Long et al., 2017; Benisty et al., 2017; Wagner et al., 2015).

Finally, HD 36112 is unresolved, with a NEAR band upper limit of the size of the emission region of 13 AU. This is an improvement by almost a factor of 10 over previous observations which set an upper limit of 120 AU on the 11.7 μm emission size (Mariñas et al., 2011).

5.5 Comparison to ProDiMo disk models

5.5.1 Spectral energy distribution of HD 100546

Figure 5.6 illustrates the resulting SED for variants of the fiducial ProDiMo HD 100546 model between 7.5 and 10 μm, along with the averaged flux of the J8.9 band observation. The VISIR observations are included in black, as are the flux measured by AKARI and the spectrum from ISO (Malfait et al., 1998; Ishihara et al., 2010). Near 8.7 μm, the observational data to which the SED was fit includes the *ISO-SWS* spectrum and a photometric data point from *AKARI* with the S9W filter (Malfait et al., 1998; Ishihara et al., 2010). While our data are in agreement with previous observational data, the expected flux of the basic ProDiMo model falls outside the uncertainty interval. We consider both disk parameter modifications included and not included in the previously performed SED fitting process that may improve upon the local fit in the mid-IR without reducing the quality of the global fit.

In our disk model, the continuum flux at 8.7 μm is emitted largely from the surface of the inner disk between 1-4 AU, while in the outer disk the 8.7 μm flux originates largely from the gap wall which is directly illuminated by the star and heated to ~300 K (see Fig. 5.2). Modifying the location of the cavity's outer rim ($r_{\in}$ of the disk outer zone) allowed us to reduce the temperature of the gap wall and reduce the continuum emission in the mid-IR. We find the optimal balance between moving the gap outer wall further outwards and maintaining the quality of the global fit occurs where the gap wall is moved outwards from 19 to 22.3 AU. As demonstrated in Fig. 5.6 by the line r_{in} = 22.3 AU, this brings the SED within formal agreement to our observed mid-IR flux. Of the observed excess flux over the continuum around 10 μm, ~60% has been explained by the presence of amorphous olivine and crystalline forsterite emission features with the remainder explained by PAHs (Malfait et al., 1998). We thus also consider further refinements to the mid-IR fit by exploring the properties of the disk PAH population. These considerations can be found in Section 5.5.1.

Across the wavelength coverage of the *ISO-SWS* spectrum, we reduced the sum of the squares of the ratio between the old fit $F_\nu^{\rm old}$ and the new fit $F_\nu^{\rm new}$, that is $\Sigma(F_\nu^{\rm new}/F_\nu^{\rm old})^2$, from 12.6 to 4.2. It should be noted that while dust settling allows for a variety of average grain sizes across the vertical extent of the disk model, dust grains are not radially segregated by size in ProDiMo, such that within our model's disk zones, every grid column contains the same underlying dust grain size distribution. Hence we can solve for only one gap outer radius, rather than a radius for each corresponding grain size.

HD 100546 disk model PAH properties exploration

Several PAH features contribute to the disk opacity near 9 μm. The broadband filter used in these observations covers an area around 8.6 μm where PAH C-H in-plane bending modes can contribute to the continuum emission. ProDiMo uses synthetic PAH opacities for neutral and charged PAHs as calculated according to Li and Draine (2001). Exploring the properties of PAHs in the model offers the possibility of modifying the

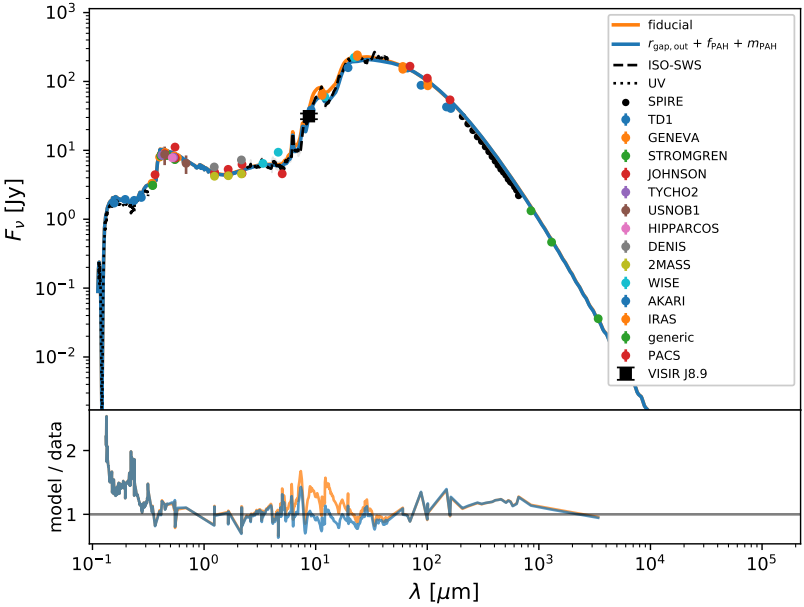

Figure 5.5: Global SED of the HD100546 disk models and comparison to the observational data folded into the fit. The fiducial model SED is the orange curve and our adjusted disk gap geometry model is the blue curve. The relative residual as defined by dividing the model by the data is shown at the bottom.

disk flux across the J8.9 filter without globally modifying the disk dust properties and breaking the quality of the global SED fit.

The contribution of PAHs was estimated by van Boekel et al. (2004) to be around 22% of the total flux near 9 μm. They found the PAH emission to be more extended than the continuum along the spatial dimension of their longslit spectra, with a FWHM of ≈150 AU. Using the low resolution spectroscopic mode of VISIR, Verhoeff (2009) found a statistically significant increase in the spatial extent of the disk emission at 8.6 μm over the resolved continuum emission at a 27 σ level. While they found the ratio between the continuum subtracted peak flux at the 8.6 μm PAH feature over the peak flux was only 2.4%, the deconvolved FWHM size of the continuum subtracted feature was $1.64^{+0.37}_{-0.38}$ ″. At a distance of 108 pc, this corresponds to a disk radius of 178^{+40}_{-41} AU. Furthermore, the variability of the 8.6 μm features between *ISO* and TIMMI2 spectra and their respective slit sizes implies that the PAH emitting region is at least 100 AU in size (Verhoeff, 2009). Additionally, Panić et al. (2014) found the 8.6 μm PAH emission to be emitted primarily from angular scales corresponding to ∼100 AU from the star.

While the HD 100546 disk model PAH abundance and charge fraction was fit for, these parameters were not varied between the inner and outer disk zones. We thus considered modifications to the PAH population in the outer disk, outside of $r = 22$ AU, specifically. The DIANA models use a single representative PAH, circumcoronene ($C_{54}H_{18}$), and a constant mixture of charged and neutral opacities throughout the disk (Woitke et al., 2016). For HD 100546, the abundance of PAH relative to the ISM $f_{\rm PAH}$ (defined such that in the ISM $f_{\rm PAH} = 1$) is 0.0028. The mean PAH charged fraction is 0.9. We considered both differing PAH types and abundances in the inner and outer disk zones to refine our fit.

We have explored a grid of a PAH abundance and morphologies in an attempt to minimise the residuals with our mid-IR observational data. Simultaneously allowing for the outer wall of the gap, the abundance of the PAHs, and the type of the PAHs to vary has allowed us to improve upon the standard SED fit without reducing the quality of the fit globally (see Fig.5.5). The result of this multi-parameter exploration can be seen in the green line in Fig. 5.6. We find that a smaller PAH, coronene ($C_{24}H_{12}$), and a 22% increase in $f_{\rm PAH}$ outside of the gap wall produce the best agreement with an observation across the J8.9 filter.

5.5.2 Radial intensity profile

Radial intensity profiles of all the disks in the sample in the different filters were constructed by azimuthally averaging over the deprojected disks for both the observations and the convolved models and this is shown in Figs. 5.7 and 5.8. In all cases the radial profile is dominated by the telescope PSF. The unresolved sources show clear Airy rings in the images (see Fig. 5.4). The Airy rings are less obvious in the resolved sources and the central disk of the Airy pattern is larger, but they are still visible in the radial profiles. None of the profiles show signs of spirals, rings, or other features in the extended disk. Although the models do not include these previously observed features, this result is still consistent with the models, which show that the mid-IR emission is dominated by the central regions and the outer regions where features have been detected at other wavelengths contribute less than 5% of the flux at 8.7 μm.

For most models used in this comparison, the distance was measured before the Gaia data release. With the release of the Gaia data, it appears that these distances were off by around 10% in most cases (HD 100546, HD 163296, TW Hydra). For these disks, it was not necessary to rerun the model, as the differences between the old and new distances are small. Simply rescaling the model to the new distance is sufficient to compare the extent of the disks. However, for HD 169142, the difference between the distance assumed in the model and the distance measured by Gaia is more significant: The assumed distance is almost 30% too large. Because of this, the model was rerun with an adapted luminosity for the new distance.

HD 100546

The normalised radial flux distribution of both the real, deprojected data in each filter

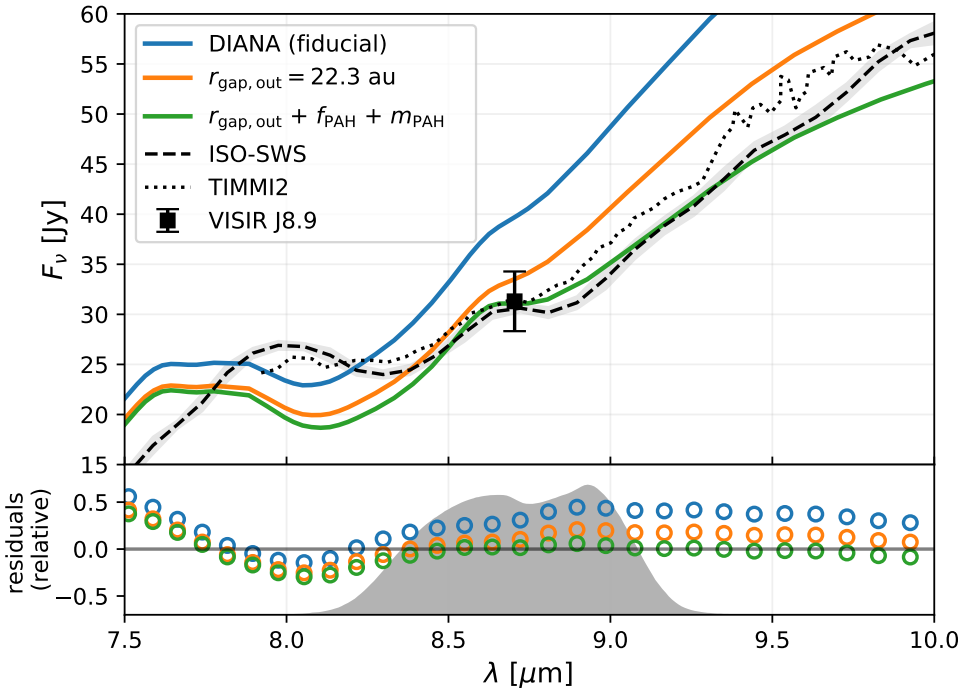

Figure 5.6: Comparison between the fiducial ProDiMo HD 100546 disk model (Woitke et al., 2019) and multi-parameter variants of the model. We include the observational VISIR data corrected for sky transmission and additional observational data (Malfait et al., 1998; van Boekel et al., 2004; Ishihara et al., 2010). The grey filled area illustrates the J8.9 filter response curve (arbitrary vertical scaling). Residuals between the various disk models and the *ISO-SWS* spectrum are shown in the lower panel as the ratio between the model SED and the observed spectrum.

and the corresponding simulated data are shown in Fig. 5.7. The model and the data are in good agreement out to ~160 AU, where the noise starts to dominate the signal. The peak in the noise in the data is caused by the source subtraction in the chopping and nodding. The subtraction shadows are located at ~500 AU (4.5″) in the four NEAR filters and at ~900 AU (8″) in the J8.9 filter. In Fig. 5.8 we can compare the different filters to each other for the observed and synthetic data. In both cases the shorter wavelength filters PAH1 and ARIII result in narrower profiles with a smaller FWHM than the longer wavelength filters PAH2 and PAH2_2. Due to the smearing of the PSF, the J8.9 filter profile is much wider in both cases. The residuals from subtracting the

model curves from the data are shown in Fig. 5.9. The errorbars in the image represent the 1σ error. The residuals show that the synthetic data is a good representation of the real data. The residuals at larger separations are 0 because the chopping and nodding process removes the background emission from the data and the model does not include sky or instrument background emission.

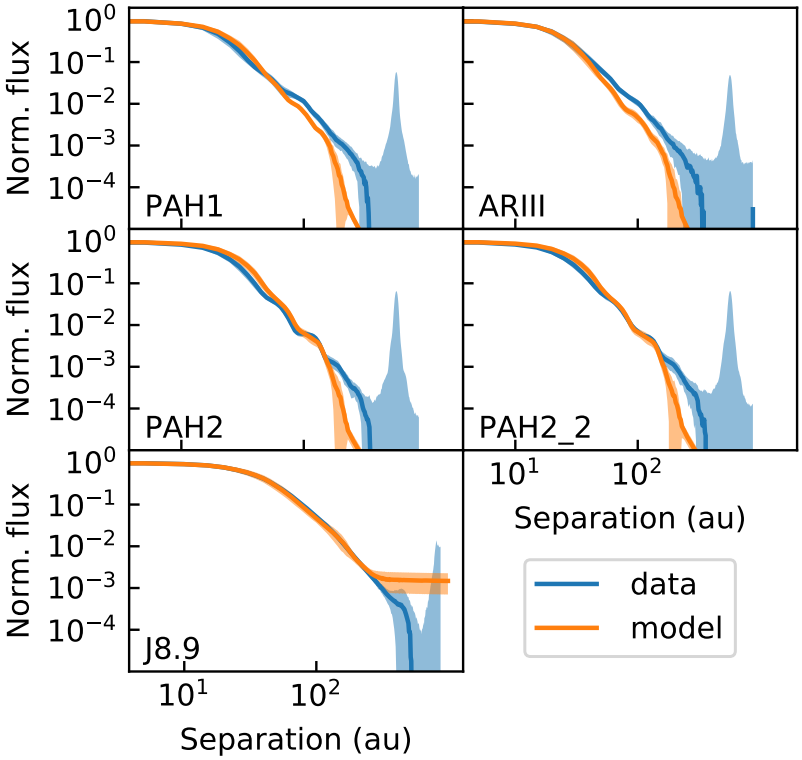

Figure 5.7: Radial profile of the HD 100546 protoplanetary disk in the PAH1, ARIII, PAH2, PAH2_2, and J8.9 filters. The profile from the data is shown in blue with the 1σ range in light blue. The profile from synthetic observations based on the ProDiMo model is shown in orange with the 1σ range indicated in lighter orange.

HD 163296

Previous observations in near-IR and sub-millimetre wavelengths show that HD 163296 has multiple bright rings (e.g. Garufi et al., 2014; Isella et al., 2016; Isella et al., 2018). The ProDiMo model does not include rings, but instead assumes a flared, optically thick inner region up to 0.02″ and a shadowed outer region beyond that. As a result, it predicts

that 95% of the flux is contained within a radius of 0.01″ in the PAH1 band and within 0.04″ in the NEAR band. This makes the emitting region much smaller than in the case of HD 100546, where there is a cavity and the inner rim of the outer disk also contributes to the flux. It is also entirely consistent with an unresolved image.

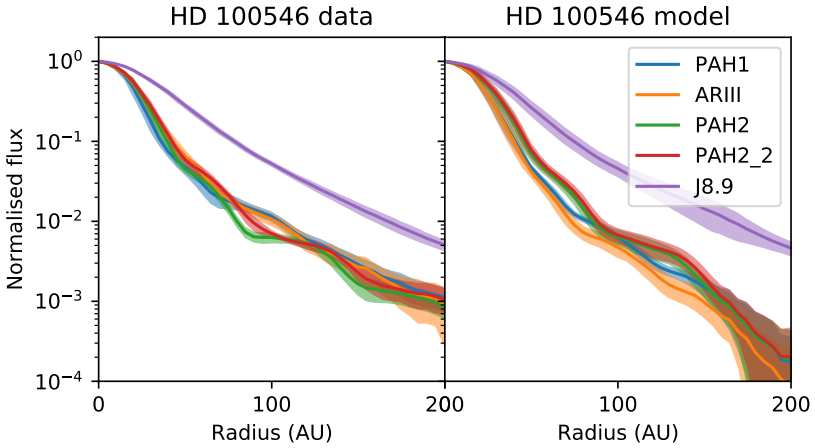

Figure 5.8: Radial flux profile of the HD 100546 protoplanetary disk in the PAH1, ARIII, PAH2, PAH2_2, and J8.9 filters, with the real data profiles on the left and the synthetic data profiles on the right. The shaded areas indicate 1σ errors for the data and confidence intervals for the models. For the model profiles, these intervals come from the PSF convolution and the azimuthal averaging and deprojection. In both the data and the model, it can be seen that the radial extent at $1/10^{th}$ the maximum flux is smaller for the shorter wavelength filters (PAH1, ARIII) than for the larger wavelength filters (PAH2, PAH2_2). This is expected as the PSF is larger for larger wavelengths. The J8.9 data, both real and synthetic, remain far more extended due to the smeared PSF.

HD 169142

ALMA observations have detected three bright rings between 0.2″ and 0.6″ (45−80 AU) in the disk around HD 169142 (Pérez et al., 2019). Again, the model does not include the rings, but instead divides the disk into an inner and an outer zone with a gap at 0.1″ (22 AU), which is consistent with the inner gap seen at other wavelengths. Assuming the observed disk is described by a Gaussian function, the apparent size as defined by ProDiMo (the radius containing 95% of the flux) corresponds to the 2σ radius of the Gaussian, which is larger than the FWHM, which only contains half the flux. After deconvolution, the apparent size of HD 169142 is 24 ± 1 AU in the PAH1 band and 35 ± 1 AU in the NEAR band. This means that the inner gap is unresolved and part of the flux in both bands is from the inside of the inner ring, but the outer two rings are too faint to be observed.

The HD 169142 model has an apparent size of 43 and 45 AU in the PAH1 and NEAR bands. While this is approximately consistent with the observed apparent size in the NEAR band, there is a discrepancy with the smaller PAH band observation. This is consistent with observations by Okamoto et al. (2017), who find that the size of the emitting region is much smaller at 8.6 and 8.8 μm than it is at 12.6 μm. They conclude that at wavelengths smaller than 9 μm, the inner disk and halo dominate; whereas, at wavelengths larger than 9 μm, the inner wall of the disk dominates which results in a larger observed size. Modeling performed by Maaskant et al. (2014) suggests that gas flowing through disk gaps can contribute significantly to the observed ionised PAH emission. This could manifest as an increase in emission at ~8 μm relative to ~12 μm, corresponding to the angular size of a gap. If the neutral PAH emission primarily originates from the gap wall, we would expect a correspondingly smaller emitting region for the predominantly ~8 μm PAH flux. This difference is not reproduced by the model, leading to a mismatch with the data in the PAH band. This can be due to the complete lack of gas and dust in the model gap and hence lack of associated emission.

The previously derived inclination of 13 ± 2° is consistent with the model value of 13°. It is also consistent with previous literature (Pérez et al., 2019; Panić et al., 2008; Raman et al., 2006).

TW Hydra

Studies in near-IR and sub-millimetre have found six gaps located between 0.11″ and 0.84″ (6 – 44 AU) (Tsukagoshi et al., 2016; Andrews et al., 2016; van Boekel et al., 2017). The model assumes an optically thin inner region corresponding to the inner gap and a dense outer region for the rest of the disk. All the emission in both bands is predicted to be from this thin inner region and the inner wall of the outer disk. The other gaps are not expected to be visible as they are further out in the disk, where there is no more emission. This means that there is an apparent size of 3-4 AU in both filter bands and this is consistent with the observations being unresolved. More recent observations also suggest the central optically thin region may be much smaller than in the model, which would shrink the expected apparent size (e.g. van Boekel et al., 2017; Andrews et al., 2016).

HD 100453

Deconvolving the data results in apparent sizes of 7 ± 1 and 18 ± 1 AU in the PAH1 and NEAR filter bands, respectively. The contribution of PAHs to the flux in the PAH1 band is expected to be weak, as Meeus et al. (2001) did not detect any PAH features at 8.6 μm in *ISO* data. We therefore expect the flux in the PAH1 band to be dominated by the continuum emission. The emission in both bands is well inside the radius where spiral arms have been found and this suggests that HD 100453 follows the other targets in the sample in which the mid-IR emission is dominated by the central regions. Since the outer disk starts at 17 AU, the PAH emission seems to come from inside the gap and the NEAR band emission includes the inner wall of the disk which is heated by the star, similar to what is seen in HD 169142.

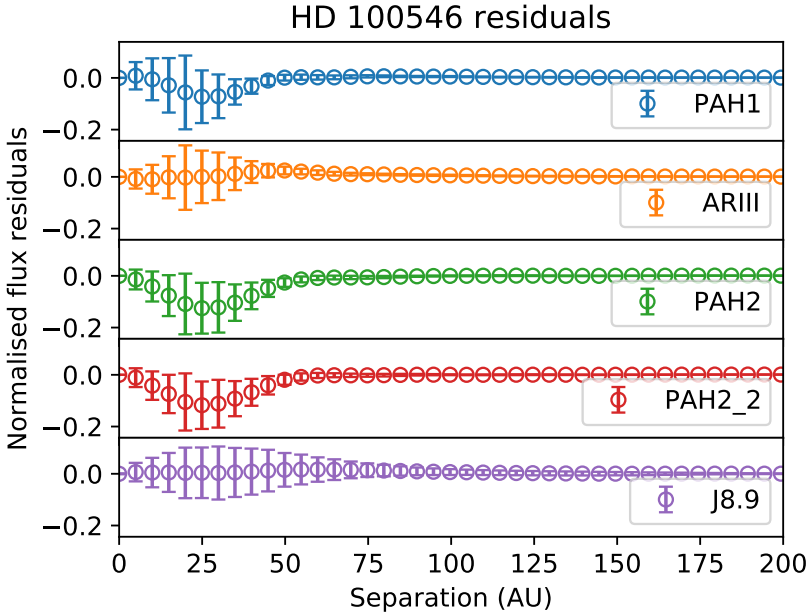

Figure 5.9: Residuals from subtracting the radial profile of the synthetic data from that of the observed data in each of the observed filters. The errorbars indicate 1σ uncertainties. The residuals all being within 1σ of 0 show that the model represents the data well.

HD 36112

HD 36112 has a large cavity, with an outer disk that has rings, clumps, and spiral arms (e.g. Dong et al., 2018; Wagner et al., 2019). However, in our observations, the cavity is unresolved. Since the cavity has a radius of 0.2″ and the upper limit for the 95% flux radius is 0.07″, this means that most of the emission comes from inside the cavity and not from the inner rim of the outer disk, unlike the NEAR filter emission of the other sources.

5.6 Companions

The proposed companions of the disks in this sample are potential hosts to circumplanetary disks, which thus far have only been tentatively identified in the PDS 70 system (Keppler et al., 2019; Christiaens et al., 2019; Haffert et al., 2019; Isella et al., 2019). To search for planetary companions and associated dust concentrations in the disk, the circularised PSF subtraction described in Petit dit de la Roche et al. (2020) was applied to the data. This method creates an individual reference PSF from the data for every

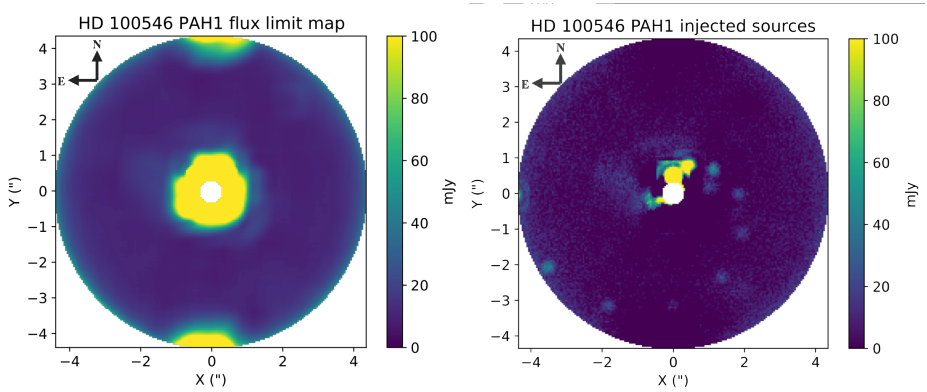

Figure 5.10: *Left:* Mapped 5σ flux limits of the HD 100546 PAH1 data, where the disk image is the most elliptical. The shape of the emitting region does not significantly influence the flux limits, especially beyond 1″ where the data are background limited. *Right:* HD 100546 PAH1 data with sources injected at different separations and position angles at 5 sigma. Most of the sources are clearly visible.

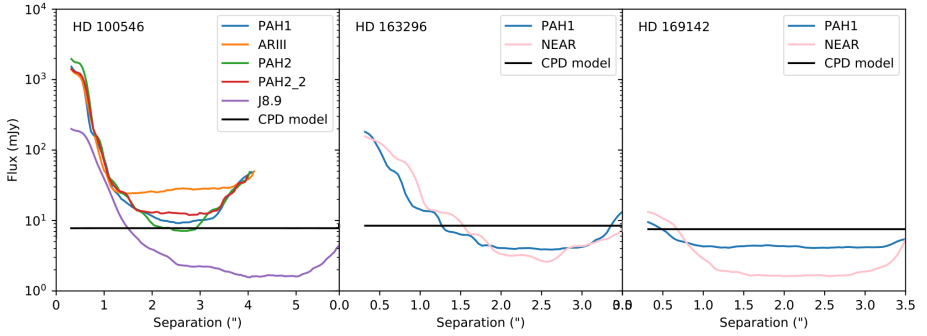

Figure 5.11: 5σ flux limits of potential companions to three targets compared to the CPD model described in Table 16 inserted in the circumstellar disk. *Left:* limits for the different observations of HD 100546 in PAH1 (blue), ARIII (orange), PAH2 (green), PAH2_2 (red), and J8.9 (purple) filters. The black line indicates the estimated flux as a function of radial separation for our fiducial CPD model as described in column 2 of Table 16. Only one line is included as the model values are similar across the different filters. The increase at 7″ in the J8.9 filter and at 4″ in the other filter are the results of chopping and nodding shadows. *Middle:* Limits for the observations of HD 163296 in the PAH1 (blue) and NEAR (pink) filters, along with the expected flux of the same CPD in the HD 163296 disk. *Right:* The same as the middle figure, but for HD 169142.

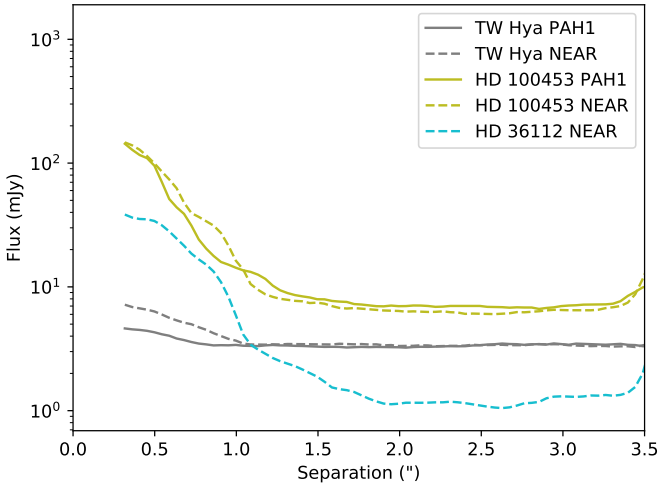

Figure 5.12: Observational limits on potential companions to TW Hya (grey), HD 100453 (yellow-green), and HD 36112 (turquoise) in the PAH1 (solid lines) and NEAR (dashed lines) filters. The increase at 4″ is the result of shadows from the chopping and nodding in the observations.

nod-subtracted image by azimuthally averaging it. The resulting rotationally symmetric PSF was then subtracted from the original data to remove the radially dependent stellar flux. This was decided upon because there is not sufficient rotation in the images to do angular differential imaging and most of the data do not have reference stars available for standard PSF subtraction. Standard PSF subtraction would also not subtract any spatially extended disk emission. Subtracting a circularly symmetric PSF from an elliptical disk image does leave residuals, but the bulk of the disk emission (>80%) is subtracted. Additionally, the sizes of the emitting regions in our data are small and the flux limits are not influenced by their shapes beyond the very inner pixels, where the disk is visible. This is the case even within roughly 1″, beyond which the background dominates and the shape of the emitting region becomes irrelevant. An example of this can be seen in the left panel of Fig 5.10, where the limits are mapped for HD 100546 in the PAH1 filter, which has the most elliptical image of our entire dataset. While none of the proposed companions are detected in any of the disks, it is possible to set 5σ upper limits on the fluxes of any possible companions, based on the residual noise at each possible location. A limit of 5σ was chosen, since injected 5σ sources were clearly recovered in the reduced data, as can be seen in the right panel of Figure 5.10. The only exception is the source directly to the south of the star, which, although still present, is less clear due to its proximity to one of the shadows induced by the nodding. However, the affected areas around these shadows are small.

Fig. 5.11 and 5.12 show the resulting flux limits, with Fig. 5.11 including the flux

of a model planet with a circumplanetary disk, which is discussed in the next section. The obtained limits are of the order of a few millijanskys between 1″ and 3.5″ separation up to a few tens of millijanskys at 0.5″. This is more sensitive than any previous mid-IR imaging observations by a factor of 10-100. Beyond 3.5″, the limits are dominated by the shadows induced by the chopping and nodding procedure in the observations. The differing sensitivities between objects with the same integration times are the result of different observing conditions influencing the data quality of the different targets.

5.6.1 Companion models

The presence of planetary accretion and a CPD or circumplanetary dust envelope can act to significantly increase the mid-IR luminosity of a putative companion (e.g. Zhu, 2015). To determine our own mid-IR observational limits for the planet candidates with accompanying CPDs, we explored a grid of CPD models using ProDiMo. Our model grid consists of a range of possible planet CPD masses, CPD dimensions, dust grain size distributions, and planet luminosities.

Properties of the planet and CPD models

We consider planetary masses of 1 to 10 M_J, with correspondingly sized CPDs defined by the planet's Hill radii. As CPDs could be tidally truncated to ~1/3 of this radius (Quillen and Trilling, 1998; Martin and Lubow, 2011), or even photoevaporatively truncated to 0.1-0.16 R_{Hill} (Mitchell and Stewart, 2011; Oberg et al., 2020), we set our CPD surface density tapering radius to the point at which the surface density begins to decline exponentially at $R_{Hill}/3$ and the outer radius at R_{Hill}.

We considered a range of CPD masses relative to the planet masses $M_{CPD} = 10^{-4} - 10^{-2} M_p$, and a range of planetary luminosities corresponding to various stages of accretion such that $L_p = 10^{-6} - 10^{-2}\,L_\odot$ (Mordasini et al., 2012). Marley et al. (2007) found that a 10 M_J planet in a 'hot start' evolution scenario can decline monotonically in luminosity from an initial $\sim 4 \times 10^{-3}\,L_\odot$ to $\sim 4 \times 10^{-4}\,L_\odot$ within 5 Myr. In the core accretion case, they found a peak luminosity during runaway accretion of $> 10^{-2}\,L_\odot$ which lasts $\sim 3 \times 10^5$ yr, rapidly declining to $\sim 2 \times 10^{-6}\,L_\odot$ by 3 Myr. Given that the planetary luminosity is expected to peak only briefly at or above $L_p \sim 10^{-2}\,L_\odot$, we consider the case of $L_p = 10^{-2}\,L_\odot$ to be the most optimistic detection scenario.

Pressure bumps at gap edges are suspected to act as filters for dust grain size, preventing the accretion of grains significantly larger than 10 μm onto planets within the gap (Rice et al., 2006b). We thus also considered CPDs where the dust grain size population is limited to maximum sizes of 100 and 10 μm.

A companion orbiting within an optically thin region of the circumstellar disk can be exposed to significant UV radiation from its host star (Oberg et al., 2020). Photons of energy 6-13.6 eV are known as FUV and can efficiently heat disk surfaces. The significant FUV luminosity of the host star can act to heat the surface of the CPD and increase its IR luminosity. We parameterised the FUV flux with the Draine field

$G_0 = 1.6 \times 10^{-3}$ erg cm^{-2} s^{-1}, which was integrated from 6-13.6 eV (Habing, 1968). We extracted the G_0 field intensity using ProDiMo from the results of the 2D radiative transfer within the DIANA circumstellar disk models and applied this as a UV background field to our own CPD models. Given that dust is the dominant source of opacity in the UV, it should be noted that the gaps in the DIANA disk models (see Fig.5.2 for the HD100546 dust structure) are free of dust and do not contribute to the UV opacity.

Companion flux estimates

We extracted the planet and CPD flux from the SEDs produced by the ProDiMo continuum radiative transfer and weighed it across the filter response curves. This flux represents the idealised total flux emitted by the unresolved companion, unconvolved with the observational PSF. We find that for high planetary luminosities ($> 10^{-4}\,L_\odot$), the mid-IR flux is dominated by the planet itself, whereas the CPD only contributes $3-6\%$ of the combined emission largely independent of CPD properties.

For our disk models, the size of the CPD as estimated by its Hill stability and the strength of the background FUV field both vary in predictable ways. For a given CPD model, our parameter grid exploration thus allowed us to fit for the resulting planet and CPD flux given an arbitrary radial separation from the star. As the vertical dust opacity at arbitrary wavelengths was also calculated as part of our model radiative transfer for various circumstellar disks, we were able to determine the radial dependence of the extinction to the midplane as well. We solved for the dust column density as a function of the viewing inclination for each radial position in the disks, and from this we derived the resulting 9 μm optical depth. The black line in Fig. 5.11 represents the resulting expected flux of the planet and CPD model in the J8.9 filter for a 10 M_J planet with a CPD of mass $10^{-2} M_p$ as described in Table 16. The line was derived from a fit performed to the J8.9 flux of our model grid of CPDs in which the background FUV radiation field, the disk size, and extinction to the midplane were simultaneously varied as a function of radial separation, although the predicted flux is relatively flat for planets found outside of the optically thick regions of the circumstellar disks. For low radial separations, the background FUV field heats the CPD surface and results in increased mid-IR emission. The CPD size grows with increasing distance from the star as the companion's Hill sphere increases correspondingly; however, as the majority of the CPD mid-IR emission originates from the innermost regions of the CPD, this contribution becomes negligible at large separation. The flux of our CPD models in the other filters is similar, varying for non-pathological model cases by at most ~10%, and they are thus roughly comparable, as illustrated in Fig. 5.13.

Results for HD 100546

While previous estimates of the age of HD 100546 indicate an older (~ 10 Myr) system (van den Ancker et al., 1997), Fairlamb et al. (2015) derived an age of 7.02 ± 1.49 Myr and an accretion rate of $\dot{M} \approx 10^{-7}\,M_\odot\,yr^{-1}$. The mass of the HD 100546

inner disk was fit to be 8.72×10^{-8} $M_\odot$ (Woitke et al., 2019), thus requiring continuous replenishment from the outer zone across the gap. The plausibility of an actively fed circumplanetary accretion disk is thus supported by the ongoing presence of radially evolving dust within the circumstellar disk (Marley et al., 2007; Mordasini et al., 2012).

We considered companions placed in the midplane at multiple radial separations from the star to study the influence of the background radiation field and circumstellar dust extinction on the predicted flux. We considered the properties of the planet candidate HD 100546b described by Quanz et al. (2015), which was found at a radial separation of 53±2 AU. When the planet was treated as a single-temperature blackbody, Quanz et al. (2015) found the best fit solution to be an emitting region of $R = 6.9^{+2.7}_{-2.9} R_J$ with $T = 932^{+193}_{-202}$ for a luminosity $L = 2.3^{+0.6}_{-0.4} \times 10^{-4} L_\odot$. As the addition of a CPD may produce an emission signature diverging significantly from a single-temperature blackbody, we loosened the constraints on the temperature and emitting area. For a 2.5 $M_\odot$ star, a planet of 1, 5, or 10 M_J at 55 AU has a Hill radius of 2.77, 4.73, or 5.96 AU, respectively. We considered three cases in detail: a planet immediately interior to the outer gap wall at 18 AU, a planet embedded within the outer gas and dust disk at 55 AU, and a wide-separation planet in the optically thin region of the PPD at 100 AU, with correspondingly sized CPD outer radii, maximum dust grain sizes, FUV backgrounds, and optical depths to the midplane (see Table 16). While the CPD size, as set by the Hill radius, only varies by a factor of 100 across the disk surface from 5-500 AU, the background UV radiation field varies more dramatically by a factor $> 10^6$.

At the radial location of the 55 AU planet candidate, we extracted an FUV flux of $G_0 = 10^{3.65}$ in the midplane from the results of our circumstellar disk model radiative transfer. At 5 AU in the shadow of the inner disk, we find $G_0 = 10^{5.4}$ and at 18 AU $G_0 = 10^{6.5}$. The maximum G_0 within the gap is found to be 3×10^6. The gas component of a CPD experiencing such irradiation acquires an optically thin heated envelope with a temperature of around 5000 K at $z/r \sim 0.4$. The ~70 K optically thick surface below this envelope gives rise to significant re-radiated emission peaking at 30-50 μm. The short-wavelength tail of this component contributes non-negligibly to the J8.9 flux across the entire CPD surface for $G_0 > 10^5$.

From the HD 100546 disk model dust density distribution and dust opacities, we determined the optical depth to the midplane along the line-of-sight to the observer across the J8.9 band to determine extinction at arbitrary radii. While emission arising from planets inside the gap would be largely unextincted, immediately outside of the gap we find a maximum optical depth $\tau_{J8.9}$ of 5.6. The disk becomes optically thin at 8.7 μm only outside of 82 AU. We find that at the large separations where our sensitivity is maximal at $a > 160$ AU, $\tau_{9\mu m}$ is at most 0.18 and $\tau \propto a^{-2.4}$.

The model planet with a mass of 10 M_{Jup} and a luminosity of 10^{-2} $L_\odot$ would have been detected in the J8.9 data beyond this radius and in PAH2 between 2″ and 3″. Hence, our new mid-IR imaging data prove that no such massive, luminous planets exist in the HD 100546 system at radii larger than 160 AU from the central star. A companion with a luminosity of 10^{-3} $L_\odot$ would be marginally detectable at angular separations of 4-5″ only.

Results for other systems

We used a single best-case representative planet and CPD to derive detection limits for the other observed systems as a function of separation. The model CPD mid-IR flux levels are constant at large radii, because at large separations the UV radiation emitted by the star no longer significantly contributes to the heating and re-radiation of the CPD. The fact that the CPD is free to physically increase in size as the planet's Hill radius increases also no longer acts to increase the flux, as for the optically thick CPDs we consider, the planet acts only to heat the innermost regions of the CPD, from which the majority of the 9 μm emission originates.

For HD 163296, we excluded a 10 M_{Jup}, 10^{-2} $L_{\odot}$ companion between 1.5″ and 3.5″, as it would have been observed in both filters. For HD 169142, TW Hydra, and HD 36112, we excluded it beyond 1″. HD 100453 is the only system in which it would remain undetected.

5.6.2 Reconciling prior observational constraints

In previous work, the planet candidate HD 100546 b at 55 AU separation is the only companion that has had its putative CPD constrained in mass to 1.44 $M_{\oplus}$ (or 2.7×10^{-3} M_p for a planet mass 1.65 M_{Jup}) in the optically thin case, and a size of 0.44 AU in radius for the optically thick case, although this rests on assumptions regarding the grain size population of the CPD and the ratio between planetary and CPD mass (Pineda et al., 2019). ALMA observations of HD 100546 at 870 μm set a 3σ limit of 198 μJy for any planet candidate (Pineda et al., 2019) with which we can further constrain any CPD's longwave emission.

We find that for our fiducial CPD surrounding a 10 M_{Jup} planet of 10^{-2} $L_{\odot}$, we overpredicted the upper limit set by ALMA observations at 870 μm by a factor of 13. When the fiducial CPD is modified with a maximum grain size of 10 μm, this overprediction is reduced by a factor of ∼2. Our planet and CPD models can be brought into agreement with the ALMA flux limits by reducing the mass of the CPD relative to the planet or by reducing the dust-to-gas ratio. We find that while the 9 μm flux of the CPDs is largely insensitive to their mass, the continuum flux in ALMA band 10 is primarily dependent on our CPD mass, radius, and dust-to-gas ratio owing to the emission region corresponding to cooler dust at larger separation from the planet (Rab et al., 2019). For a fixed radius, dust-to-gas ratio, maximum and minimum dust grain size, and grain size power law, the 870 μm flux is proportional to the CPD mass as $F_{870\mu m} \propto M_{CPD}^{0.81}$ for the range $M_{CPD} = 10^{-6} - 10^{-2}$ M_p. We find that the maximum CPD mass allowed by the constraint is 3.2×10^{-7} $M_{\odot}$. A smaller, optically thick CPD of a higher mass still satisfies the constraint. We find that a modification to our fiducial CPD of a mass $> 9.5 \times 10^{-6}$ $M_{\odot}$ with a tapering radius of 0.2 AU and an outer radius of 0.6 AU has a 870 μm flux of 190 μJy and would thus satisfy the constraint set with ALMA. This places no additional constraints on our 9 μJy flux prediction, as the mid-IR flux is instead primarily dependant on the planet's luminosity and the CPD's inner radius.

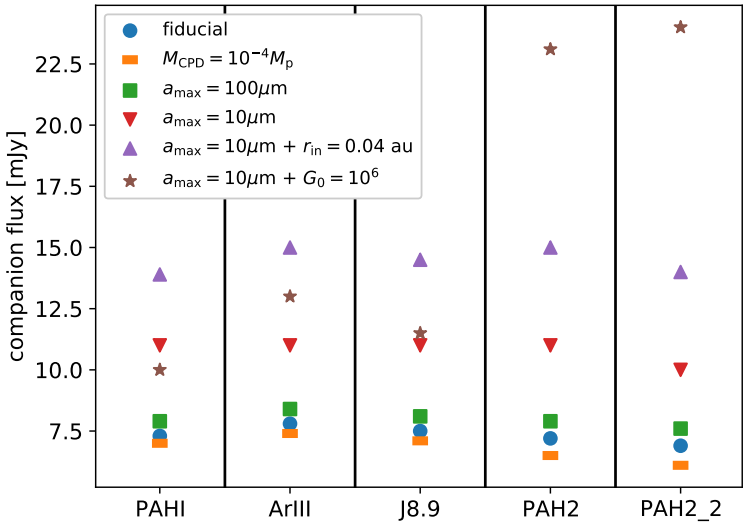

Figure 5.13: Model companion (planet and CPD) unextincted flux estimates. The 'fiducial' case is described by the planet and CPD parameters found in column 2 of Table 16 at 55 AU for the HD 100546 system. We also consider a variety of maximum dust grain sizes a_{max}, CPD mass M_{CPD}, CPD inner radius r_{in}, and background FUV radiation field strength G_0.

5.7 Discussion and conclusions

We analysed images of HD 100546 in five different mid-IR filters and a further five young stellar objects in the PAH1 and NEAR infrared filters with the VISIR instrument and its upgrade NEAR. The resolved disks had their FWHMs and inclinations determined. HD 100546 has a FWHM of 28-61 AU across five different filters, a projected inclination of 44±4°, and a projected position angle of 130°. HD 169142 has FWHMs of 29 AU and 41 AU in the PAH1 and NEAR filter bands, respectively, and a projected inclination of 13±2°. HD 100453 has a FWHM of 9 AU in the PAH1 band and 21 AU in the NEAR band and an inclination of 35±2°. The observed values are consistent with the DIANA circumstellar disk models and previous observations of the sources. We set upper limits of 6 AU and 7 AU on the size of the emission region of HD 163296 in the PAH1 and NEAR filter bands, respectively, thus improving previous limits by a factor of three. We set upper limits of 3 AU and 7 AU on TW Hydra in the same filters, which is consistent with previous observations. Finally, we set an upper limit of 13 AU on the size of the NEAR filter emission of HD 36112, which is an improvement over previous

Table 16: HD100546 candidate planets and CPD model parameters for our optimistic detection scenario (parameters listed above the first horizontal divider) for a variety of radial separations (parameters below the first horizontal divider) and associated J8.9 band predicted fluxes. Dust composition is identical to that listed in Table 14.

Parameter	Symbol	18 AU	55 AU	100 AU
Planet mass [M_J]	M_p	10	10	10
Planet luminosity [L_*]	L_p	10^{-2}	10^{-2}	10^{-2}
CPD mass [M_p]	M_{CPD}	10^{-2}	10^{-2}	10^{-2}
CPD inner radius [AU]	$R_{CPD,in}$	0.01	0.01	0.01
Minimum dust size [μm]	a_{min}	0.05	0.05	0.05
Col. density power index	ϵ	1	1	1
Dust to gas ratio	d/g	0.01	0.01	0.01
Reference scale height	$H_{0.1au}$	0.01	0.01	0.01
Planet semi-major axis [AU]	a_p	18	55	100
CPD tapering radius [AU]	$R_{tap,CPD}$	0.40	1.99	3.61
CPD outer radius [AU]	$R_{out,CPD}$	1.19	5.96	10.84
Maximum dust size [μm]	a_{max}	10	3000	3000
FUV background	G_0	$10^{6.7}$	$10^{4.1}$	3500
Optical depth at 8.7 μm	τ	~ 0	1.27	0.43
Predicted 8.7 μm flux (extincted) [mJy]	$F_{P,1}$	11.5	2.1	4.88
Predicted 8.7 μm flux (unextincted) [mJy]	$F_{P,0}$	11.5	7.6	7.5

values of a factor of 10. The fact that we did not resolve these targets is also consistent with the DIANA ProDiMo models (Woitke et al., 2019). Because of the method by which the variety of observational data were weighted during the original fitting procedure performed by Woitke et al. (2019), and because of the non-complete set of disk model parameters for which the fits were performed, localised improvements to the SED were still possible. After a minimal adjustment of the HD 100546 disk model gap geometry, an examination of the disk radial profile showed that our ProDiMo model was a good match for the data and that it reproduces the radial profile of the disk to within 1σ without the need to include a companion object. In all cases, the mid-IR emission originates from the central area of the disk from the most highly irradiated areas: unresolved inner disks and/or the inner rims of the outer disks.

Given our new flux estimate for the HD 100546 system, we have improved upon the global SED fit from 2-18 μm by simultaneously increasing the gap outer edge from 19.3 AU to 22.3 AU, increasing the abundance of PAHs in the outer disk relative to the ISM from 2.8×10^{-3} to 3.4×10^{-3}, and replacing the representative PAH circumcoronene with coronene. The details of the PAH properties fitting can be found in Section 5.5.1. Given that the spectral properties of alternative dust compositions have not been thoroughly explored nor the marginal improvement of the detailed PAH fit, we tend to favour

the simple modification of only the disk gap geometry. The χ^2 statistic between the model SED and the *ISO-SWS* spectrum for 2-18 μm reduces from 588 to 278 when the inner radius is increased to 22.3 AU. It should be noted that increasing the model gap outer radius would act to increase the tension with the location of the dust continuum gap edge observed with ALMA at 16-21 AU (Pérez et al., 2020), although as ALMA traces millimetre-sized grains, this may not be inconsistent. Additionally, the model gap outer radius is the one parameter that we adjusted which was previously fit by means of a genetic algorithm (Woitke et al., 2016; Kamp et al., 2017; Woitke et al., 2019; Dionatos et al., 2019).

We produced planet and CPD flux estimates using the thermochemical disk modeling code ProDiMo for the VISIR filters with a variety of CPD parameters, finding that in the absence of extreme external FUV radiation fields, the maximum unextincted flux in the J8.9 band is expected to be ~15 mJy for a CPD with an inner radius of 0.04 AU and a maximum dust grain size of 10 μm. We find that this flux is largely dependent on the planet properties and not on those of the circumplanetary disk. The CPD is found to contribute 3 − 6%, at most, of the companion flux at 9 μm. The CPD contribution at 9 μm is greatest when the maximum grain size is reduced to 10 μm and the CPD is irradiated by a significant FUV field of $G_0 \geq 10^6$.

Such conditions are found within the gap of the HD 100546 disk, where we determined that the G_0 field strengths up to 3×10^6, despite the presence of the inner disk. A planet and CPD within the gap at 18 AU, while more gravitationally truncated than our test cases at 55 and 100 AU, is unobscured by dust and we expect $F_{J8.9} = 11.5$ mJy. We note that while the 9 μm emission of the CPD is largely unaffected for $G_0 \leq 10^6$, it rises precipitously above this, and for a $G_0 = 10^7$ we find $F_{J8.9} = 0.6$ Jy. While a CPD within the gap would be found at angular separations of less than 0.2″ and thus be unresolved in our observation, the contribution to the flux of the star and circumstellar disk (31 ± 3 Jy) would thus be non-negligible. It should be noted however that a significantly FUV irradiated CPD can become photoeveporatively truncated such that the effective emission region is greatly reduced (Oberg et al., 2020).

For our $a = 55$ AU HD 100546 companion test case, we find $F_{J8.9} = 2.1$ mJy owing to significant dust extinction. In the event that the planet is able to clear obscuring dust from its immediate neighbourhood in a localised cavity, the observed flux may increase to 7.5 mJy. Even in this 'best case' scenario of high planetary luminosity, it can be seen in Fig. 5.11 that the flux limiting sensitivity at 55 AU is 200 mJy. For our $a = 100$ AU companion case, we find $F_{J8.9} = 4.9$ mJy, 7.9 mJy unobscured, and the accompanying limiting sensitivity is 30 mJy. Only outside of 180 AU would such a planet and CPD be detectable. Outside of 180 AU, we find a limit on planetary luminosity of 0.0028 $L_\odot$, above which we would have detected any companion.

In the HD 100546 system, we rule out the presence of planetary mass companions with $L > 0.0028 L_\odot$ for $a > 180$ AU. We find that the contribution of a planet and CPD would still be of the order of the uncertainties inherent in the model, as relatively minor modifications to the HD 100546 gap dimensions (an increase of 2-3 AU in the outer radius) produce changes in expected continuum flux of 7-10 Jy at 9 μm. We place no

stringent constraints on the planetary mass, CPD radius, or CPD grain size distribution. In the HD 169142, TW Hydra, and HD 100453 systems, we can exclude companions with $L > 10^{-2}\,L_{\odot}$ beyond 1″.

We consider whether the lack of detection of wide-separation (a>50 AU) planetary mass companions (PMCs) of mass $< 20\,M_{\rm J}$ in the five studied systems is remarkable. While the presence of a dusty CPD may act to enhance the observability of a companion, it has been found that rapid dust evolution in CPDs of isolated wide-separation PMCs could act to suppress the dust-to-gas ratio of CPDs on short timescales ($d/g \leq 10^{-4}$ after 1 Myr), rendering a continuum detection more challenging (Pinilla et al., 2013; Zhu et al., 2018; Rab et al., 2019). Sub-stellar companions have been detected in wide orbits around young stars (Neuhäuser et al., 2005; Ireland et al., 2011; Bryan et al., 2016; Naud et al., 2017; Bohn et al., 2019). It has been suggested that such objects may form in situ by the fragmentation of massive, self-gravitating disks (Boss, 1997, 2011; Vorobyov, 2013) by the direct collapse of molecular cloud material (Boss, 2001), or by core- or pebble accretion (Lambrechts and Johansen, 2014) and subsequent outwards scattering by an interaction with other massive planets (Pollack et al., 1996; Carrera et al., 2019). In the latter case, a detection of a wide-separation PMC may thus directly imply the presence of additional massive planets in the inner system.

Bowler (2016) suggests that around single, young (5-300 Myr) stars, 5–13 $M_{\rm J}$ companions at separations of 30-300 AU occur $0.6^{+0.7}_{-0.5}$% of the time. With VLT/NaCo, Vigan et al. (2017) found that 0.5-75 $M_{\rm J}$ companions at separations of 20-300 AU are found around 0.75 − 5.7% of stars, and with the Gemini Planet Imager Exoplanet Survey, Nielsen et al. (2019) found that 5-13 $M_{\rm J}$ companions with separations of 10-100 AU occur around 9^{+5}_{-4}% of stars. Our sensitivity at the limiting angular resolution restricted our search to relatively wide separation companions ($a > 160$ AU). Given the PMC occurrence rate of Bowler (2016), we expect an absolute upper bound of $\sim 3.4^{+3.9}_{-3.3}$% probability of a single detection in our sample, assuming a perfect detection efficiency from 30-300 AU. In this context, it is difficult to make new conclusions regarding the prevalence of wide-separation PMCs in our observed systems given the relatively low a priori likelihood of detection and the relatively large companion luminosity ($10^{-3} - 10^{-2}\,L_{\odot}$) necessitated. We were able to set an upper limit to the occurrence rate for wide-separation PMCs with a luminosity $\geq 10^{-2}$ of ≤ 6.2% at 68% confidence.

Future observations with METIS (Brandl et al., 2018) on the ELT are expected to achieve ten times better sensitivities than NEAR and 40 times better sensitivities than VISIR at the same wavelengths, as well as improving the spatial resolution by a factor of 5, allowing for one to image more close in companions. MIRI[11] on *JWST* is expected to achieve 250 times better sensitivities than NEAR and 1000 times better sensitivities than VISIR. Both will be able detect the known companions to all six targets.

[11] https://www.stsci.edu/jwst/science-planning/proposal-planning-toolbox/sensitivity-and-saturation-limits

Acknowledgements

This project was made possible through contributions from the Breakthrough Foundation and Breakthrough Watch program, as well as through contributions from the European Southern Observatory.

Appendix

A.1 Targets

Information regarding the secondary target systems is listed in this section.

HD 163296

Near-IR and sub-millimeter wavelength observations show that HD 163296 has four gaps. They are centred on 10 AU, 50 AU, 81 AU, and 142 AU with bright rings in between (e.g. Garufi et al., 2014; Isella et al., 2016; Isella et al., 2018).

Companions have been suggested based on their possible role in forming the ring structures in the disk. For example, Liu et al. (2018) fitted three half-Jovian-mass planets and Teague et al. (2018) found the radial pressure gradients can be explained by two Jupiter-mass planet at 83 and 137 AU (see also Teague et al. 2019). Additionally, Pinte et al. (2018) found a Jupiter-mass companion at 223 AU based on deviations from Keplerian velocity in the gas of the disk. So far, observations have not been able to confirm or rule out such companions due to a lack of sensitivity. Guidi et al. (2018) claim to have found a 5-6 M_{Jup} companion at a separation of 50 AU from the star in the L′ band with Keck/NIRC2, but neither this object nor the one proposed by Pinte et al. (2018) was found by Mesa et al. (2019), who set upper limits of 3-5 M_{Jup} on possible companions in the gaps of the disk with SPHERE H band (1.6 μm) and K band (2.2 μm) data. Due to extinction from the disk setting, these kinds of mass limits remain challenging, especially outside the gaps, as only a fraction of the intrinsic, modelled flux of the companion may be observable.

HD 169142

The disk around HD 169142 has been imaged at near-IR and at sub-millimetre wavelengths. Various teams have imaged two (Fedele et al., 2017; Quanz et al., 2013a; Momose et al., 2015; Pohl et al., 2017), three (Macías et al., 2017; Osorio et al., 2014), or four (Macías et al., 2017; Pérez et al., 2019) rings around the star. The inner ring is located at 20 AU and is more than twice as bright as the outer rings. As a result, it was found in all the previously mentioned works. The three outer rings (located between 45 AU and 80 AU) are faint and close together, leading to blending in some observations and resulting in the different numbers of rings found in different studies.

Four disk features that could be associated with forming planets have been found. The first was found between the 20 AU and 50 AU dust rings by Osorio et al. (2014) at 7 mm, the second was found in the L′ band just within the edge of the inner gap by

Reggiani et al. (2014) and Biller et al. (2014). However, the L′ band source was not recovered by either team in the J (1.3 μm), H, or K bands and it is concluded by Biller et al. (2014) that the feature cannot be due to planet photospheric emission and must be a disk feature heated by an unknown source, although Reggiani et al. (2014) argue that the accretion of material in the gap enhances the L′ band flux, resulting in a lower mass planet, which is not as easily observed in other bands. The presence of circumstellar material with entrained dust grains spreading across the gap or being accreted onto a planet could also subject the planet to further extinction in the J band. Biller et al. (2014) detected the third source in the H band, with no L′ band counterpart, but Ligi et al. (2018) show that this is actually part of the inner ring. They did find another H band structure close to the star that is consistent with the detections by Biller et al. (2014) and Reggiani et al. (2014), but it appears to be extended and they cannot rule out that it is not part of a marginally detected ring at the same separation. Finally, Gratton et al. (2019) combined different SPHERE datasets and suggest that this source could actually be a combination of two extended blobs observed in the disk. They find a different, fourth, feature located between the inner and outer rings that does not correspond to any of the previous detections and could indicate the presence of a $2.2 \pm 1.4\,M_{Jup}$ planet.

TW Hydra

TW Hydra is a 3-15 Myr old T Tauri star (Vacca and Sandell, 2011; Weinberger et al., 2013; Herczeg and Hillenbrand, 2014). At a distance of 60.14 ± 0.06 pc (Gaia Collaboration et al., 2020), it is one of the nearest known hosts of a protoplanetary disk. Studies in the near-IR and sub-millimetre wavelength regimes have found between three and six different gaps in eight different locations between 0.6 AU and 90 AU (Nomura et al., 2016; Tsukagoshi et al., 2016; Andrews et al., 2016; van Boekel et al., 2017; Huang et al., 2018).

Tsukagoshi et al. (2016) suggest the presence of a $\lesssim 26\,M_{\oplus}$ planet interacting gravitationally with the gap at 22 AU. Tsukagoshi et al. (2019) found an azimuthally elongated 1.3 mm continuum source in the south-west of the disk at a radial separation of 54 AU that could be either dust that has accumulated into a clump in a vortex or a circumplanetary disk associated with an accreting Neptune mass planet. Nayakshin et al. (2020) argue the feature can be explained by a Neptune-mass planet disrupted in the process of accretion and expelling dust into the circumstellar disk. Observations with SPHERE suggest from the gap profiles that if planets are responsible for forming the gaps in the circumstellar disk, they are at most several $10\,M_{\oplus}$ (van Boekel et al., 2017).

HD 100453

HD 100453 has been found to possess a misaligned inner disk, a gap between 1 AU and 21 AU, and an outer disk with two shadows, two spiral arms around 30 AU, and a faint feature in the south-west of the disk (Benisty et al., 2017; Kluska et al., 2020). It also has an M dwarf companion at a separation of 125 AU whose orbit is not aligned with the disk plane (van der Plas et al., 2019).

Dynamical modeling has shown that tidal interactions with the M dwarf companion are responsible for at least some of the disk features, such as the spirals and the truncation of the outer disk (Wagner et al., 2018; van der Plas et al., 2019; Gonzalez et al., 2020). However, they have also suggested that the presence of a planet is required to fully explain the origin of the features in the disk, particularly the misalignment between the inner and the outer disks (e.g. Nealon et al., 2020). There have been no direct detections of planet candidates to date.

HD 36112

HD 36112 (MWC 758) has a large cavity with a radius of 32 AU. Its broad outer disk has rings, clumps, and spiral arms (e.g. Dong et al., 2018; Wagner et al., 2019).

For the spiral structures in the disk of HD 36112 to be caused by a perturber, it is estimated that it must have a mass of ~5-10 M_{Jup} (Grady et al., 2013; Dong et al., 2015b). However, upper limits on companion fluxes obtained in the same works and by Reggiani et al. (2018) rule out the presence of >5 M_{Jup} planets beyond 0.6″, or 94 AU. Reggiani et al. (2018) found an L band (3.5 μm) point source at 18 AU that they interpret as a planet with a circumplanetary disk that is embedded in the disk. Wagner et al. (2019) did not find this object in the L′ and M′ bands, even though they achieved better sensitivities. Instead, they found a point source at the outer end of one of the spiral arms that could be a planet with a CPD and could be responsible for driving the spirals.

Chapter 6

Observing Circumplanetary Disks with METIS

N. Oberg, I. Kamp, S. Cazaux, Ch. Rab & O. Czoske

Abstract

Context: Gaining a full understanding of the planet and moon formation process calls for observations that probe the circumplanetary environment of accreting giant planets. The mid-infrared ELT imager and spectrograph (METIS) will provide a unique capability to detect warm-gas emission lines from circumplanetary disks.
Aims: We aim to demonstrate the capability of the METIS instrument on the Extremely Large Telescope (ELT) to detect circumplanetary disks (CPDs) with fundamental v=1-0 transitions of ^{12}CO from 4.5-5 μm.
Methods: We considered the case of the well-studied HD 100546 pre-transitional disk to inform our disk modeling approach. We used the radiation-thermochemical disk modeling code ProDiMo to produce synthetic spectral channel maps. The observational simulator SimMETIS was employed to produce realistic data products with the integral field spectroscopic (IFU) mode.
Results: The detectability of the CPD depends strongly on the level of external irradiation and the physical extent of the disk, favoring massive ($\sim$ 10 M_J) planets and spatially extended disks, with radii approaching the planetary Hill radius. The majority of ^{12}CO line emission originates from the outer disk surface and, thus, the CO line profiles are centrally peaked. The planetary luminosity does not contribute significantly to exciting disk gas line emission. If CPDs are dust-depleted, the ^{12}CO line emission is enhanced as external radiation can penetrate deeper into the line emitting region.
Conclusions: UV-bright star systems with pre-transitional disks are ideal candidates to search for CO-emitting CPDs with ELT/METIS. METIS will be able to detect a variety of circumplanetary disks via their fundamental ^{12}CO ro-vibrational line emission in only 60 s of total detector integration time.

Oberg et al. 2022 *Observing Circumplanetary Disks with METIS* accepted A&A

6.1 Introduction

Observations of circumstellar dust have revealed a plethora of intriguing substructures in planet-forming disks (Andrews, 2020), such as arms (e.g., Pérez et al. (2016); Muto et al. (2012); Huang et al. (2018)), arcs (e.g., Casassus et al. (2013); van der Marel et al. (2013); Isella et al. (2013)), rings, gaps, and cavities (e.g., Calvet et al. (2002); Piétu et al. (2006); Quanz et al. (2013b); ALMA Partnership et al. (2015); Andrews et al. (2018); Long et al. (2018)). A number of these features have been interpreted to be the result of planet-disk interactions (Kley and Nelson, 2012; van der Marel et al., 2016; Zhang et al., 2018; Andrews, 2020). Disks with large inner cavities or gaps are known as (pre-)transition disks (Espaillat et al., 2014) and serve as promising targets in the search for giant planets embedded within them (Strom et al., 1989; Dodson-Robinson and Salyk, 2011; Zhu et al., 2011). Massive planets in gaps are expected to continually accrete gas and dust from the surrounding circumstellar disk (Kley, 1999; Lubow and D'Angelo, 2006; Morbidelli et al., 2014; Teague et al., 2019) into a moon-forming circumplanetary disk (CPD) (Canup and Ward, 2002; Mosqueira and Estrada, 2003a; Szulágyi et al., 2016).

As of July 2022, the direct detection of extrasolar circumplanetary dust associated with an accreting planet has only been confirmed in the PDS 70 system. The PDS 70 circumstellar disk features a gap with a radial width of 70 au (Hashimoto et al., 2012) containing two planets. The first planet PDS 70 b was detected in the NIR (Keppler et al., 2018; Müller et al., 2018) and in H-α (Wagner et al., 2018; Haffert et al., 2019). A second planet PDS 70 c was discovered also in H-α (Haffert et al., 2019). Unresolved sub-mm dust thermal emission is co-located with this planet, interpreted as originating from a dusty CPD (Isella et al., 2019; Benisty et al., 2021). Self-consistent radiative transfer modeling of the system suggests the CPD is optically thick with an upper limit on the dust mass of 0.7 $M_\oplus$ (Portilla-Revelo et al., 2022), but it has been noted that high spatial and spectral resolution observations of the gas component are needed to break degeneracies between the planet and disk properties.

No other (pre-)transitional disk gap has been found to contain circumplanetary dust. Francis and van der Marel (2020) suggested that PDS 70 is anomalous in that the gap may only recently have been opened, with correspondingly high rates of accretion onto the planets within the gap. Alternatively, episodic accretion may limit the visibility of planets to brief periods, with the relatively inviscid CPD acting as an accretion "bottleneck" (Lubow and Martin, 2012; Brittain et al., 2020). The rapid depletion of dust due to fast, inwardly directed aerodynamic drift in CPDs may also hinder attempts to detect them in continuum emission (Zhu et al., 2018; Rab et al., 2019).

An additional candidate CPD has been detected in the AS 209 disk by ^{13}CO J=2-1 gas line emission (Bae et al., 2022). The CPD candidate is embedded within an annular gap seen in the ^{12}CO emission at a radial distance of 200 au. The gap region is still optically thick in ^{12}CO and, hence, there is no corresponding detection in ^{12}CO. However, a perturbation in the velocity field of the ^{12}CO gas and evidence of localized heating further supports the interpretation of a planet+CPD. Assuming a standard ^{13}CO

abundance, the gas mass of the CPD is estimated to be 30 $M_\oplus$. Given the nondetection of associated continuum emission the dust mass of the CPD must be < 0.027 $M_\oplus$, suggesting a dust-to-gas ratio of $< 9 \times 10^{-4}$, in line with prediction of rapid dust depletion of wide-separation CPDs (Zhu et al., 2018; Rab et al., 2019). Gas line observations thus provide a way of detecting CPDs, even if they are strongly dust depleted.

One of the best studied pre-transitional disks surrounds the Herbig star HD 100546 (van den Ancker et al., 1997; Vioque et al., 2018). The system lies at a distance 108.1 ± 0.5 pc, right ascension 11h 33m 25.3s, declination -70° 11' 41.2″ (Gaia Collaboration et al., 2021). The age is estimated to be 7.02 ± 1.49 Myr (Fairlamb et al., 2015) or $5.5^{+1.4}_{-0.8}$ Myr (Vioque et al., 2018). The system is comprised of a clearly divided inner and outer disk, with a gap depleted in gas and dust radially spanning ~1-20 au (Bouwman et al., 2003; Grady et al., 2005; Brittain et al., 2009; Avenhaus et al., 2014; Fedele et al., 2015; Jamialahmadi et al., 2018; Pineda et al., 2019).

The HD 100546 system hosts several potential planet candidates, either claimed via a direct detection or indirectly via their influence on the circumstellar disk structure and dynamics. The first candidate companion "b" was identified by direct imaging at 3.8 μm at a separation 0.48″±0.04 (projected separation ~70 au) (Quanz et al., 2013a; Currie et al., 2014; Quanz et al., 2015). However, the existence of this object has been called into question as a potential artifact of data reduction (Rameau et al., 2017; Cugno et al., 2019).

A second closer-in companion "c" has been tentatively detected inside the cavity during multi-epoch monitoring of spatially unresolved CO (v=1-0) line profile asymmetries potentially originating from the gas component of a CPD inside the cavity (Brittain et al., 2013, 2014). This claim has also been disputed, with the line asymmetry being attributed, for instance, to a slit misalignment (Fedele et al., 2015). However Brittain et al. (2019) has rebutted this claim, arguing that a slit misalignment is not plausible given that the CO (v=1-0) and hot band lines were observed simultaneously – displaying, however, different spectro-astrometric signals and profiles from 2006 to 2013. Furthermore, the signal attributed to the CPD appears to vanish when the predicted position of the planet moves behind the cavity inner edge (Brittain et al., 2019). Evidence for the "c" companion within the gap at 10-15 au has been further strengthened by modeling efforts that reproduce the observed mm-dust disk substructure with planet-disk interaction (Pinilla et al., 2015; Pyerin et al., 2021; Fedele et al., 2021). In this work, we focus on the direct detection of the CPD of this potential planet candidate "c" via the ^{12}CO (v=1-0) line emission.

The Extremely Large Telescope (ELT) is a next-generation observatory under construction at the peak of Cerro Armazones in the Atacama desert of Chile. With a segmented primary mirror diameter of 39.3 meters, the sensitivity and angular resolution of the ELT promise to significantly bolster the capabilities of ground-based IR astronomy (Ramsay et al., 2018). The Mid-infrared ELT Imager and Spectrograph (METIS) is a planned instrument designed for the observation of exoplanets and protoplanetary disks (Brandl et al., 2021). The single-conjugate adaptive optics system allows METIS to perform high-contrast, diffraction-limited integral field unit (IFU) spectroscopy at a

spectral resolution of $R \sim 10^5$ in the L and M bands. This offers the capability to observe the fundamental transitions of ^{12}CO (v=1-0) from 4.5-5 μm. This CO emission primarily traces warm gas, such as that of the inner rim of the disk gap above the midplane, and has been used to deduce the presence of cavities or gaps (Brittain et al., 2009; Banzatti and Pontoppidan, 2015; Hein Bertelsen et al., 2016; Antonellini et al., 2020). A CPD inside a disk gap may be exposed to significant scattered stellar radiation (Turner et al., 2012; Oberg et al., 2020), heating the gas in the CO line emitting region of the CPD and increasing emission.

An analysis of the emission allows for the kinematic derivation of a planet's mass (Rab et al., 2019). Limits on the CPD gas temperature, composition, physical extent, and total mass may also be determined. High spectral-resolution observations in the MIR and NIR can thus provide clues useful for determining the properties of the planet, the process of gas giant accretion, and the formation of regular satellite systems around massive planets. If CPDs are strongly dust-depleted and accretion onto the planet is only episodic, gas line observations may offer the most promising avenue to probe the circumplanetary environment.

We performed simulations to demonstrate how the METIS instrument capabilities will enable the detection of a planet+CPD located in the gap of (pre-)transitional disks, as well as how high spectral-resolution IFU spectroscopy of CO ro-vibrational emission will make it possible to gain unprecedented insights into the nature of these objects. The outline of this work is as follows. In Sect. 6.2, we describe the capabilities of the disk modeling code, the properties of the disk model, and capabilities of the telescope observing simulation tools. In Sect. 6.3, we describe our results and we discuss the implications and conclusions in Sections 6.4 and 6.5, respectively.

6.2 Methods

To model the disk physics and chemistry, as well as to produce synthetic line emission data cubes of the HD 100546 circumstellar disk (CSD) and candidate CPD, we used the radiation thermochemical disk modeling ProDiMo[12] code (Woitke et al., 2016; Kamp et al., 2017; Woitke et al., 2019; Thi et al., 2020a). The CO abundance in the disks is self-consistently calculated with a rate-based approach using the "large" chemical network, including 235 species and 13 elements described in Kamp et al. (2017). The adopted elemental abundances of C and O are 1.38×10^{-4} and 3.02×10^{-4} relative to H, respectively (Savage and Sembach, 1996). ProDiMo has previously been used to model observations of CO line emission from CPDs around wide-orbit companions in the sub-mm (Rab et al., 2019). To model CO emission from Herbig disks, ProDiMo utilizes a CO molecule model that includes up to 50 rotational levels and 9 vibrational levels for the electronic ground state, $X^1\Sigma^+$, and the first excited electronic state, $A^1\Pi$. Collisions between CO molecules and hydrogen molecules (H_2), hydrogen atoms (H), helium (He), and electrons are taken into account (Thi et al., 2013; Song et al., 2015). Order-of-magnitude uncertainties in rate coefficients result in model CO line flux variations of up

[12] https://prodimo.iwf.oeaw.ac.at/

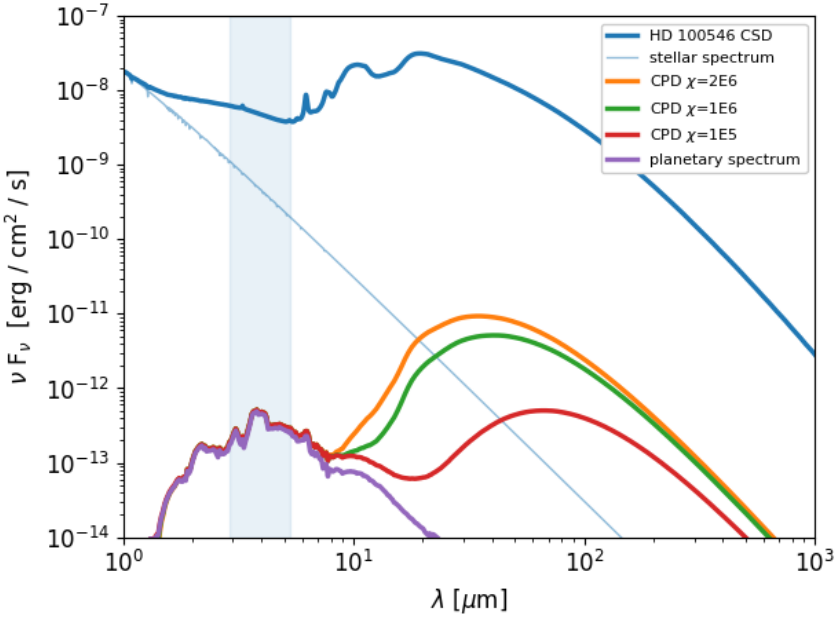

Figure 6.1: Continuum SED of the HD 100546 circumstellar disk (blue line) and of the CPD for three cases of differing background radiation (orange, green, and red lines) and in the case of no CPD (purple line) for a planet with $T_{\rm eff}$ = 1000 K. The HD 100546 stellar spectrum is also included (thin blue line). The METIS LMS wavelength range is indicated by the light-blue filled region.

to 20%.

6.2.1 System model properties

In this section, we describe the properties of the circumstellar and circumplanetary disk models. We assumed the following: the CSD and CPD are coplanar ($i_{\rm CSD} = i_{\rm CPD}$), the CPD lies within the midplane of the CSD on a zero-inclination orbit, and the CPD and CSD are co-rotating (rotating in the same direction). The CPD is assumed to lie on a circular orbit ($e_{\rm CPD} = 0$) at a distance of 15 au from the star. For the production of combined CPD+CSD data cubes the position angle of the CPD is varied from 0-180° in steps of 45° relative to the total system position angle of ~ 140°. The continuum SED of the CSD and CPD for several of the models can be found in Fig. 6.1.

Properties of the HD 100546 Circumstellar Disk

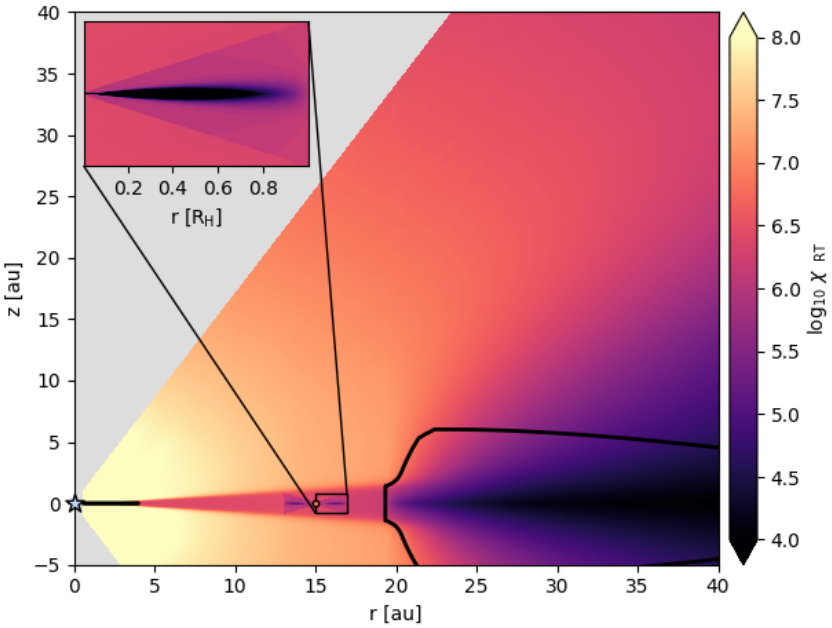

Figure 6.2: Geometry and intensity of the UV field strength χ_{RT} at each position in the CSD and CPD derived from the results of the 2D radiative transfer. The CPD model UV field map is overlaid for illustrative purposes. The black contours trace the surface of minimum optical extinction A_V=1 in the vertical or radial direction.

The properties of the HD 100546 disk have previously been derived by spectral energy distribution (SED) fitting by means of a genetic algorithm (Woitke et al., 2019). A multi-wavelength set of publicly available photometric fluxes, low- and high-resolution spectra, and interferometric data have been collated to produce a global SED (Dionatos et al., 2019). Sixteen free parameters describing the disk physical and chemical parameters have been fit to the SED by iteratively performing MCFOST radiative transfer simulations. Details of the disk modeling procedure, SED fitting, and limitations of the SED fitting process can be found in Woitke et al. (2016), Kamp et al. (2017),Woitke et al. (2019) and Dionatos et al. (2019). The disk gap is parameterized to span 4-19.3 au. A detailed description of the model parameters can be found in Petit dit de la Roche et al. (2021) [13]. Inside the gap the vertical gas column density does not exceed $N_{\langle H \rangle} = 10^{17}$ cm^{-2}. However, in the following section, we also consider the implications of additional gas and dust being present in the gap.

[13]The model parameters and output can also be accessed directly at http://www-star.st-and.ac.uk/~pw31/DIANA/SEDfit/HD100546_model_index.html

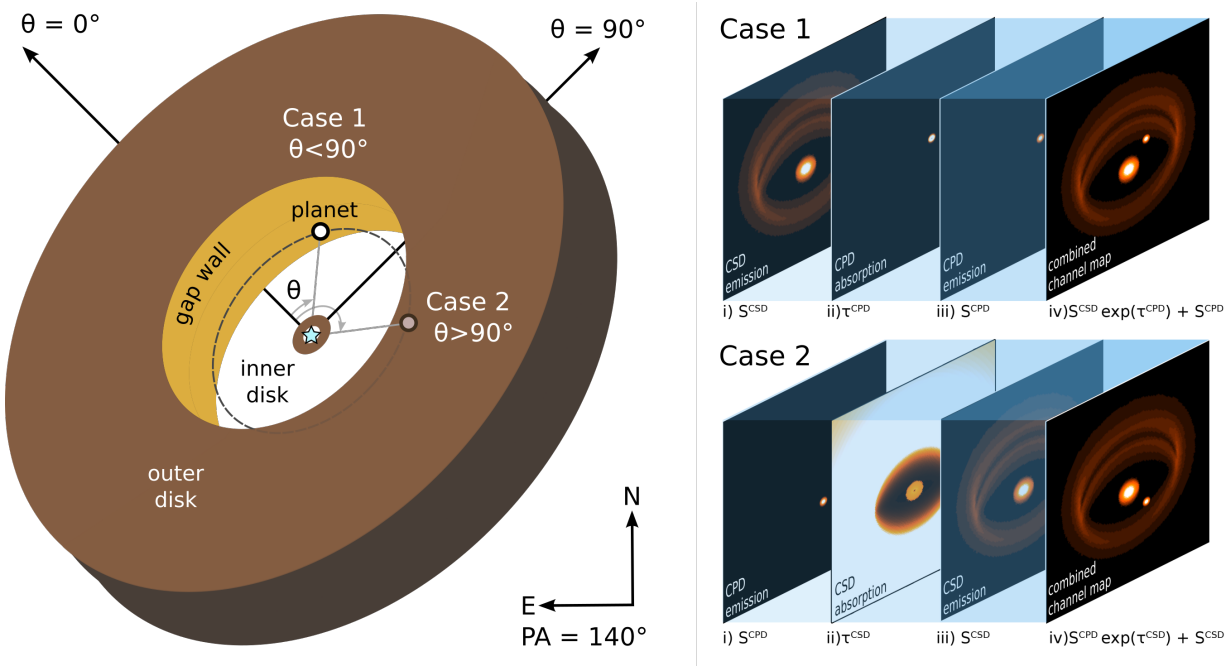

Figure 6.3: Illustration of the circumstellar disk geometry and the components contributing to the channel maps. In case 1 the CPD phase angle θ is $< 90°$ (CPD as foreground object relative to the CSD). The CPD absorption map (ii) is used to extinct the CSD emission map (i). The CPD emission (iii) is then added to produce the final image (iv). When $\theta > 90°$ the CSD gap edge becomes the foreground object, and the process follows case 2. At $\theta = 90°$ the extinction caused by either object on the other is negligible and the two channel maps are simply co-added.

Properties of the planet and CPD

We considered two cases for the physical size of the CPD. The first reference case is one in which the outer radius $R_{\rm out}$ of the CPD is equal to the planetary Hill radius R_H. In the second case we assume that the CPD is truncated to one third of the Hill radius due to tidal interaction or photoevaporative effects ($R_{\rm out}$ = 1/3 R_H) (Martin and Lubow, 2011; Mitchell and Stewart, 2011; Oberg et al., 2020). For the reference model, we assumed a planetary mass of 10 M_J, but we also considered the case of a 5, 3, and 1 M_J planet, with correspondingly smaller Hill radii. An exponential decline in the surface density profile of the CPD is parameterized to begin at one third of the outer radius in either case. The planetary luminosity is set to be 10^{-5} $L_\odot$ to be consistent with the predicted post-runaway accretion phase of giant planet evolution (Mordasini et al., 2017). The planetary spectrum is adopted from the DRIFT-PHOENIX library for an object with $T_{\rm eff}$ = 1000 K (Helling et al., 2008).

Given the short timescales of dust depletion in the CPD (Zhu et al., 2018; Rab et al., 2019) and the possibility that pressure bumps at the gap edge prevent significant transport of dust towards the CPD (Rice et al., 2006b; Zhu et al., 2012), we adopted a relatively dust-depleted CPD with a dust-to-gas ratio $d/g = 10^{-3}$; however, we find that adopting a canonical value of 10^{-2} has a negligible impact on the ro-vibrational CO line emission characteristics of the CPD. We consider also more extreme cases of dust depletion with $d/g = 10^{-4}$, 10^{-5} and 10^{-6}. A summary of the various CPD variations of parameters can be found in Table 17. The parameters which remain fixed and are shared between all models are found in Table 18.

The CPD is externally irradiated by the star located at the center of the circumstellar disk. The strength of the attenuated UV field $\chi_{\rm RT}$ was calculated throughout the circumstellar disk as part of the full 2D radiative transfer. The value of $\chi_{\rm RT}$ represents the strength of the local UV radiation field with respect to the standard interstellar radiation field (Röllig et al., 2007). We extracted the intensity of this attenuated stellar radiation at the position of the CPD. This extracted radiation field was then applied as a background to the CPD. In practice, the external radiation field is represented in the radiative transfer by a diluted 20000 K blackbody component which is isotropically incident on the CPD.

The geometry of the UV radiation field intensity derived from the 2D radiative transfer in the CSD is depicted in Fig. 6.2. For the purposes of illustration, the corresponding radiation field in and around the reference CPD has been scaled and positioned at the stellocentric radius corresponding to its physical separation and extent. The shadowing effect of the inner disk is apparent, and the CPD sits entirely within this shadow. In the midplane the $\chi_{\rm RT}$ field strength at 15 au is $1.8{\times}10^6$. When applied as a background UV field to the CPD model, the irradiation is assumed to be isotropically incident. Given the geometry and alignment of the CPD relative to the star and corresponding potential for self-shadowing, we also tested significantly reduced external UV field strengths of $\chi = 10^4$, 10^5, and 10^6. We did not consider the possibility of a warped or inclined inner disk, which might periodically vary the magnitude of the inner disk's

shadowing.

We assessed the contribution of back-scattered light by performing a separate radiative transfer simulation where the outer disk component of the HD 100546 CSD model is removed to prevent back-scattering from the gap wall at 19.3 au. If the outer disk is removed entirely, the $\chi_{\rm RT}$ value at the position of the CPD reduces by a factor 20 to 10^5 – hence, 95% of the incident emission is scattered radiation originating from the outer gap wall. The question of how much external radiation is effectively incident on the CPD is discussed further in Sect. A.3.

The distribution of gaseous CO in the reference CPD is shown in Fig.6.11a. The 2D gas temperature and density structure of the CPD are shown in Fig. 6.11c and Fig. 6.11b, respectively. For the calculation of the line Doppler shift, for the stellar rest frame we adopted a radial velocity of 9.25 km s^{-1} (Gaia Collaboration et al., 2021). The planetary radial velocity at maximum elongation is 8.15 km s^{-1} for $a = 15$ au, $i = 42°$.

6.2.2 Radiative transfer post-processing

The ProDiMo line radiative transfer implementation precludes a full 3D treatment of the combined CPD and CSD system. Instead, two independent disk models are combined in a post-processing step. First a 2D axisymmetric radiative transfer is performed independently in the CSD model (see Section 6.2.1). We extracted the properties of the radiation field in the gap midplane of the CSD model. These properties were used to inform the plausible magnitude of external UV irradiation of the CPD. The CPD disk model was then initialized with these background conditions.

A line radiative transfer was performed independently for the CSD and CPD, producing data cubes for selected CO ro-vibrational lines in the METIS LMS-mode wavelength range. In both cases, a map of the line-of-sight optical depth (τ map) through the disks was also produced at each wavelength. The line data cubes of the CSD and CPD were then combined. The details of the combination process are dependent on the phase angle θ of the CPD along its orbit (where $\theta = 0°$ corresponds to the northern minor axis of the disk). For a given value of θ, the line-of-sight velocity of the CPD is calculated to determine the wavelength shift $\delta\lambda$ of the line center. At values of $\theta < 90°$ (where 90° corresponds to maximum elongation), the CPD partially occludes the CSD emission originating from the near-side cavity wall. The τ map was used to calculate the extinction of the background CSD emission due to the CPD dust and gas. At each pixel i, j in the CSD cube, the flux S is extincted at the wavelength λ according to:

$$S_{i,j}(\lambda) = S^{\rm CSD}_{i,j}(\lambda)\, e^{-\tau^{CPD}_{i,j}(\lambda+\delta\lambda)} + S^{\rm CPD}_{i,j}(\lambda + \delta\lambda). \tag{114}$$

The CPD channel map is then co-added with the partially extincted CSD channel map. The data products that contribute to this overall process are illustrated as case 1 in Fig. 6.3. In the event that the CPD phase angle θ is $> 90°$, the roles are reversed and the CPD is then partially extincted by foreground dust and gas in the CSD cavity wall (case 2 in Fig. 6.3) . In this case, the τ map of the CSD is used to extinct the CPD.

Table 17: CPD model variations. Variations on the reference model are highlighted in bold.

model id	$\chi_{\rm gap}$	$R_{\rm out}$ [au]	$M_{\rm p}$ [$M_{\rm J}$]	$M_{\rm CPD}$ [$M_{\rm P}$]	d/g
reference	2×10^6	1.62	10	10^{-2}	10^{-3}
chi1E6	$\mathbf{1\times10^6}$	1.62	10	10^{-2}	10^{-3}
chi5E5	$\mathbf{5\times10^5}$	1.62	10	10^{-2}	10^{-3}
chi1E5	$\mathbf{1\times10^5}$	1.62	10	10^{-2}	10^{-3}
chi2E6-s	$\mathbf{2\times10^6}$	**0.54**	10	10^{-2}	10^{-3}
chi1E6-s	$\mathbf{1\times10^6}$	**0.54**	10	10^{-2}	10^{-3}
chi5E5-s	$\mathbf{5\times10^5}$	**0.54**	10	10^{-2}	10^{-3}
chi1E5-s	$\mathbf{1\times10^5}$	**0.54**	10	10^{-2}	10^{-3}
chi2E6-5mj	2×10^6	**1.29**	**5**	10^{-2}	10^{-3}
chi2E6-3mj	2×10^6	**1.08**	**3**	10^{-2}	10^{-3}
chi2E6-1mj	2×10^6	**0.75**	**1**	10^{-2}	10^{-3}
mcpd3	2×10^6	1.62	10	$\mathbf{10^{-3}}$	10^{-3}
mcpd4	2×10^6	1.62	10	$\mathbf{10^{-4}}$	10^{-3}
mcpd5	2×10^6	1.62	10	$\mathbf{10^{-5}}$	10^{-3}
chi2E6-dg4	2×10^6	1.62	10	10^{-2}	$\mathbf{10^{-4}}$
chi2E6-dg5	2×10^6	1.62	10	10^{-2}	$\mathbf{10^{-5}}$
chi2E6-dg6	2×10^6	1.62	10	10^{-2}	$\mathbf{10^{-6}}$

6.2.3 SimMETIS

To simulate the capabilities of the METIS instrument, we used the SimMetis software package [14] based on SimCADO. The telescope altitude is set to 3060 m at a latitude of -24.59° and longitude of -70.19°. The telescope temperature is 282.15 K. The detector pixel scale is 8.2 mas[15], corresponding to ~ 1.1 au at 108 pc (Gaia Collaboration et al., 2021). The exposure time and number of exposures have been varied. We consider a detector integration time (DIT) of 10 s and a number of DITs (NDIT) for total exposure times of 10 s, 60s, 1h, and 4h. A longer DIT was not adopted so as to prevent any saturation of the detector. From the maximum possible elevation of HD 100546 and altitude of the ELT, we adopted an airmass of 1.5 for observing parameters. The atmospheric conditions are "median."

[14] https://github.com/astronomyk/SimMETIS release v0.2 (retrieved 19 Feb 2019)

[15] In reality the LMS mode FOV is 0.58 × 0.93" cut into 28 slices of 0.021 x 0.93". The slices are projected onto a detector with plate scale 0.0082" per pixel. Hence as the PSF is undersampled in the across-slice direction an observation will require a series of exposures with dithers/offsets or rotations, from which a spatially fully sampled data cube will be reconstructed. The SimMetis pixel scale thus represents an ideal data reduction scenario.

Table 18: Common parameters shared between all CPD models listed in Table 17.

Parameter	Symbol	Value	Unit
Planetary Luminosity	$L_{\rm p}$	10^{-4}	$L_\odot$
Effective Temperature	$T_{\rm eff,p}$	1000	K
UV Luminosity	$L_{\rm UV,p}$	0.01	$L_{\rm p}$
Disk Inner Radius	$R_{\rm in}$	0.01	au
Column Density Power Ind.	ϵ	1.0	-
Flaring Index	β	1.15	-
Reference Scale Height	$H_{0.1{\rm au}}$	0.01	au
Minimum dust size	$a_{\rm max}$	0.05	μm
Maximum dust size	$a_{\rm max}$	3000	μm
Dust size power law index	$a_{\rm pow}$	3.5	-
Dust composition:			
$Mg_{0.7}Fe_{0.3}SiO_3$		60%	
Amorphous carbon		15%	
Vacuum		25%	

6.3 Results

At the CO line centers, we find the CPD flux is 10^2-10^4 greater than the planet+CPD continuum emission at 4.6-4.9 μm, depending on the magnitude of external irradiation. Over this wavelength range, the CPD dust contributes at most 10% of the combined planet+CPD emission. For the reference case, we find the peak CO line flux near 4.83 μm is of the same order as the entire CSD disk-integrated continuum flux. This is evident in Fig. 6.8.

The flux of the CPD is extracted by placing a circular aperture at the position of its centroid and summing across all pixels in the aperture. The aperture has a radius of 3 pixels and is sized to include > 99.5% of the emission originating from the CPD. Expressing the statistical significance of the CPD emission is complicated by contamination (blending) of CSD emission within the aperture. Despite the Doppler shifting of the CPD line emission, we find that some contamination from circumstellar disk emission occurs in every case for a CPD radial separation of 15 au. The fluxes are extracted from the spectral channel with the maximum contrast with the CSD. A value of 100% would indicate a doubling of the emission within the aperture relative to a no-CPD model. With real data, a similar analysis would require the subtraction of modeled CSD emission.

A lower dust-to-gas ratio allows UV radiation to penetrate more deeply into the CPD and heat the gas, increasing the CO line emission by up to a factor ~ 2.5. A CPD for a planet mass as low as 1 M_J is still present as a localized excess emission of 10-60%. If the CPD gas mass is reduced by a factor 1000 (to 10^{-4} M_J), the UV background

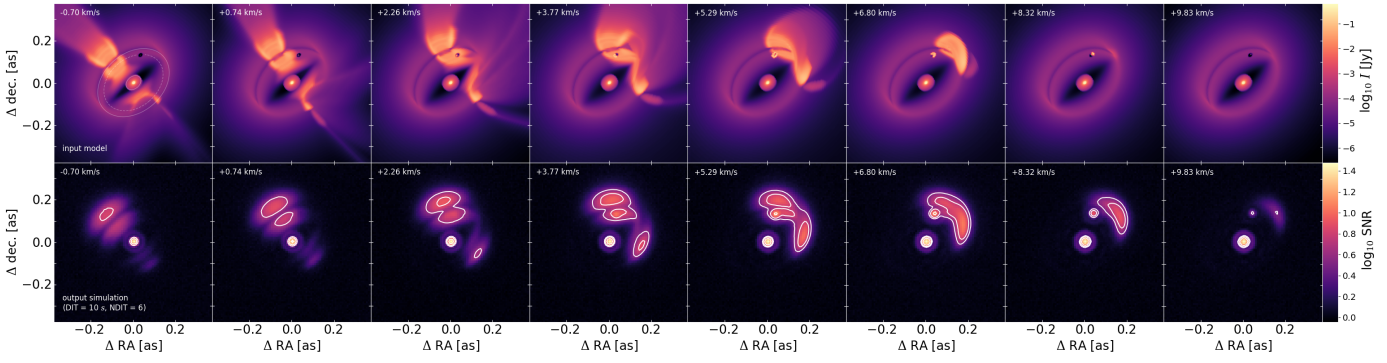

(a) $\chi_{\mathrm{RT}} = 2 \times 10^6$, $\theta = 45°$, $R_{\mathrm{out}} = \mathrm{R_{Hill}}$

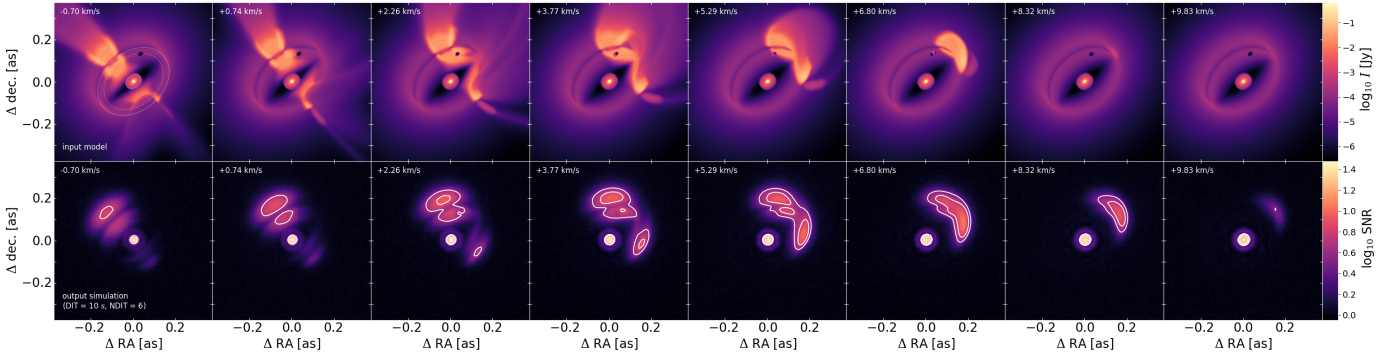

(b) $\chi_{\mathrm{RT}} = 10^5$, $\theta = 45°$, $R_{\mathrm{out}} = \mathrm{R_{Hill}}$

Figure 6.4: Synthetic channel maps of the v(1-0)P08 line (4.73587 μm) of the HD 100546 CSD + CPD model for the high external irradiation case (a) and for the low external irradiation case (b). In both cases, the CPD outer radius $R_{\mathrm{out}} = \mathrm{R_{Hill}}$ (1.62 au). The ProDiMo model used as input for SimMetis is in the top row of each subfigure. The ellipses in the upper-leftmost panel indicate the inner and outer edges of the gap at 4 and 19 au, and the companion orbit at 15 au (dotted line). The corresponding simulated METIS observation panels represent six detector integrations of 10 s each in the bottom row of every subfigure. The white contour lines represent the signal-to-noise ratio values (S/N) of 3, 5, and 10. The velocity offset is relative to the stellar reference frame.

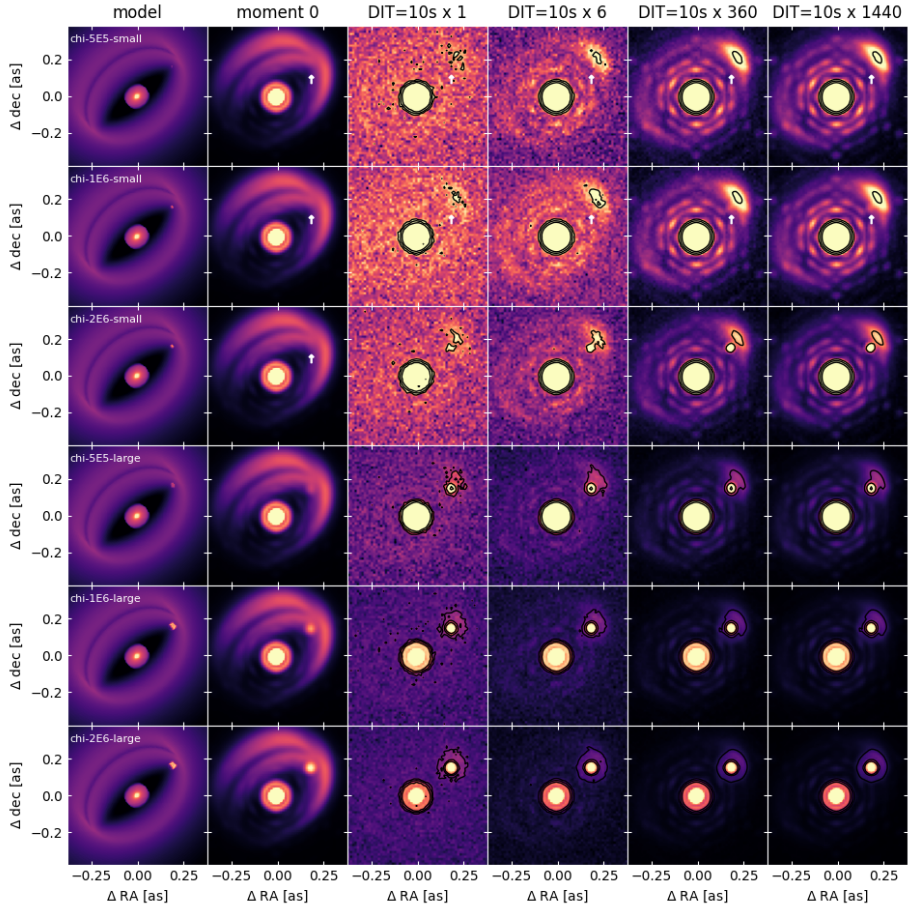

Figure 6.5: Synthetic channel maps of v(1-0)P08 line (4.73587 μm) from the CPDs of varying physical extent and background irradiation. The CPD is placed at maximum elongation ($\theta = 90°$) The leftmost column contains the input model at the extracted velocity (+6.8 km s^{-1} relative to the stellar reference frame). The asymmetry in the moment 0 map in column 2 is due to telluric contamination. The third to sixth columns include the synthetic channel maps for an increasing series of total detector integration times indicated at the top of each column. The black contours indicate a count value excess relative to the background of 25%, 50%, and 100%. The color range of each image has been logarithmically scaled with boundaries corresponding to the minimum and maximum values found outside of the central half of the stellar PSF. Where it is not apparent by eye the position of the CPD is indicated with a white vertical arrow. The six-fold symmetry apparent in longer integration times is a result of the ELT point spread function acting on the central star. The colormap normalization has been configured to maximize the visibility of the CPD.

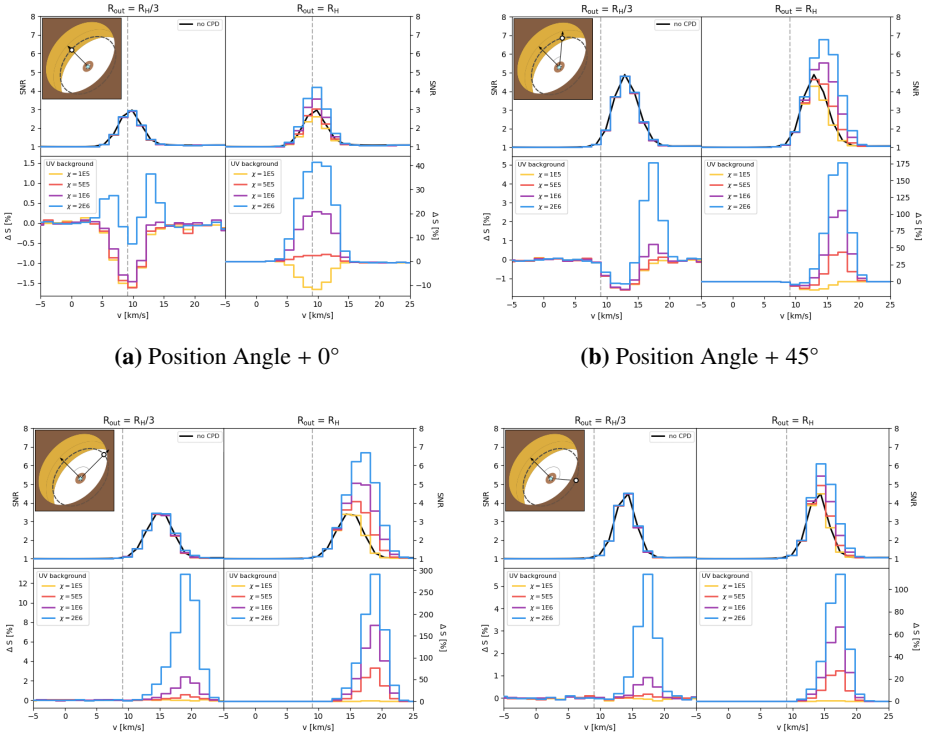

(a) Position Angle + 0°

(b) Position Angle + 45°

(c) Position Angle + 90°

(d) Position Angle + 135°

Figure 6.6: ^{12}CO line profiles represented as the signal-to-noise ratio (S/N) of the aperture centered on the CPD (top row of each subfigure) compared to the case of no CPD (black line) for the CPDs with varying levels of background UV irradiation χ. Excess or deficit in flux ΔS in the aperture relative to a no-CPD model (bottom row of each subfigure). Results are shown for a companion position angle relative to the disk semiminor axes of (a) 0°, (b) 45°, (c) 90°, and (d) 135°. The signal present in the case of no CPD is indicated by the black lines, and arises purely from circumstellar disk emission. The rest frame of the star is indicated by the vertical dashed gray lines. A negative ΔS indicates that the CPD is seen in absorption. Note: the vertical axis scaling can differ significantly between the left and right sides of each subfigure.

is reduced by a factor 20, or if the CPD gas component radius is reduced to $R_H/3$, the signal of the CPD is not present as an excess of more than 10% and thus it becomes more challenging to detect. A phase angle of 90° (maximum elongation) increases the contrast with circumstellar disk emission by a factor of 2 relative to $\theta = 45°$. Conversely, the CPD is not detectable at $\theta = 180°$, where the CPD is spatially coincident with the optically thick line-emitting region of the CSD ($\tau > 1300$).

The CPD ^{12}CO line strength is found to be coupled only weakly to the planetary

luminosity. Although the inner rim of the CPD is heated by the planet, the corresponding effective emitting area is negligible. The majority of the line emission originates instead from the disk surface. Background UV irradiation of the CPD efficiently increases gas temperatures in a thin surface layer up to 4000 K. This can be seen in Fig. 6.11c. The resulting emission region is comparable to the total disk surface area. The main emission region is highlighted in Fig. 6.11a. The line luminosity is thus closely proportional to the physical extent of the circumplanetary gas and the intensity of the UV background. In the "best case" scenario for detection, a Hill sphere-filling CPD with background $\chi = 2 \times 10^6$ produces spatially resolved emission with peak signal-to-noise ratio of S/N = 5 in 60 s of total exposure. If the external irradiation is reduced by a factor 20 the CPD becomes difficult to distinguish from background circumstellar disk emission. Likewise, if the CPD outer radius is truncated to $R_{Hill}/3$, detection of the CPD gas requires the most extreme case of background irradiation to ensure the CPD emission can be distinguished from the background CSD gap wall at a level greater than 10% localized excess.

We produced a series of synthetic channel maps for each combined CSD+CPD model, representing plausible observational parameters. Synthetic channel maps of the combined CSD+CPD for the high- and low-levels of background radiation can be found in Fig. 6.4a and 6.4b, respectively. The CPD is both spatially and spectrally resolved in Fig. 6.4a, owing to the line-of-sight velocity offset with the gap wall emission surface. Interestingly, the presence of the CPD can be inferred in Fig. 6.4b even in the absence of detectable line emission. The CPD dust continuum absorption produces a silhouette on the background of the CSD gap-wall line-emitting region if the external irradiation is sufficiently low. This effect is clearly demonstrated in Fig. 6.4b at +2.26 km s^{-1} and +3.77 km s^{-1}, where the position of the CPD is apparent in absorption.

The greatest contrast between the CPD and CSD is found at maximum elongation ($\theta = 90°$) when the relative Doppler shifting between the planet and star is at maximum. Synthetic channel maps for the high- and low-levels of background radiation for both small ($R_{out} = R_H/3$) and large ($R_{out} = R_H$) CPD models at maximum elongation can be found in Fig. 6.5. In all cases where $R_{out} = R_H$, the CPD emission can be easily distinguished from the circumstellar disk by eye.

The detectability of the CPD represented both in terms of the aperture S/N and as an excess or deficit in emission relative to a no-CPD model for different phase angles can be found in in Fig. 6.6. The CPD continuum absorption silhouette effect is also clear in Fig. 6.6 (a) and (b) for $\theta = 0°$ and 45°, respectively, with a localized reduction in flux relative to a smooth axisymmetric of $\sim$ 10%. We summarize our parameter exploration in terms of the significance of the CPD emission as an excess or deficit in the flux relative to a no-CPD model in Fig. 6.7 for all model configurations.

Given the instantaneous spectral coverage of the METIS instrument, as many as eight ^{12}CO v=1-0 lines may be present in a single observation. Depending on the magnitude of telluric contamination, the eventual S/N of a CPD detection may thus be increased by a factor $\sim 2.5 - 3$ over what we demonstrate here, for instance, in Fig. 6.6.

As the C/O ratio of material accreting from the outer circumstellar disk onto the

CPD may differ substantially from abundances corresponding to the ISM (e.g., Ansdell et al. 2016; Zhang et al. 2019), we also considered the case of a carbon depletion by a factor 10. Given that the ^{12}CO v=1-0 lines are highly optically thick, we find that a 10× depletion of C results in peak line fluxes being reduced by $\sim$ 20% relative to the value corresponding to standard ISM abundances.

6.4 Discussion

We have found that a sufficiently large and externally irradiated CPD can produce a signal that can be detected even if the entire gap region of the CSD were to be spatially unresolved. Although without a priori knowledge of the line-of-sight velocity offset of the CPD signal with regard to the circumstellar disk emission, multi-epoch observations would be required to deduce the Keplerian motion of the signal originating from the CPD. In the most extreme case, we find the CPD peak line luminosity approaches $\sim$ 40% of the disk-integrated circumstellar emission at the same wavelength (see Fig. 6.8). This is comparable with the magnitude of the candidate CPD signal observed in ^{12}CO P26 line emission discussed in Brittain et al. (2013). The centrally peaked CO line morphology arises as a result of the emission originating from across the entire disk surface at relatively low Keplerian velocities.

Dust depletion of CPDs due to grain drift is predicted to occur on relatively short timescales (Zhu et al., 2018; Rab et al., 2019), which impedes attempts to detect CPDs by continuum emission. This is consistent with the non-detection of CPD-like dust emission in several pre-transitional disk cavities. However, we find that a CPD with severely depleted dust ($d/g \sim 10^{-6}$) can still be readily detected in CO emission, while being simultaneously impossible to detect in continuum emission with, for instance, ALMA. Other pre-transitional disks around UV-bright Herbig Ae/Be stars, for instance: UX Tau A , HD34282, HD97048 ,CQ Tau, MWC 758 (Andrews et al., 2011; van der Plas et al., 2017a,b; Ubeira Gabellini et al., 2019; Calcino et al., 2020) offer similar opportunities to search for CO emission from externally irradiated CPDs.

The possibility to detect the CPD in absorption against the CSD gap wall represents a unique observational scenario, allowing for the dust properties of the CPD to be revealed. In this sense, the CPD is comparable to an externally irradiated proplyd such as Orion 121-1925 (McCaughrean and O'dell, 1996). In the event that the magnitude of the external radiation is as low or lower than the minimum we have considered, this possibility will allow for the physical extent, dust properties, and minimum dust mass of the CPD to be estimated. However, even in the most optimistic case the spatially localized reduction in flux relative to a no-CPD model ($\sim$ 10%) is minor, and any spatial inhomogeneity of background circumstellar disk CO emission could easily obscure such a signal. Thus, in practice, it may be very difficult to achieve lest the position of the planet and CPD were known a priori.

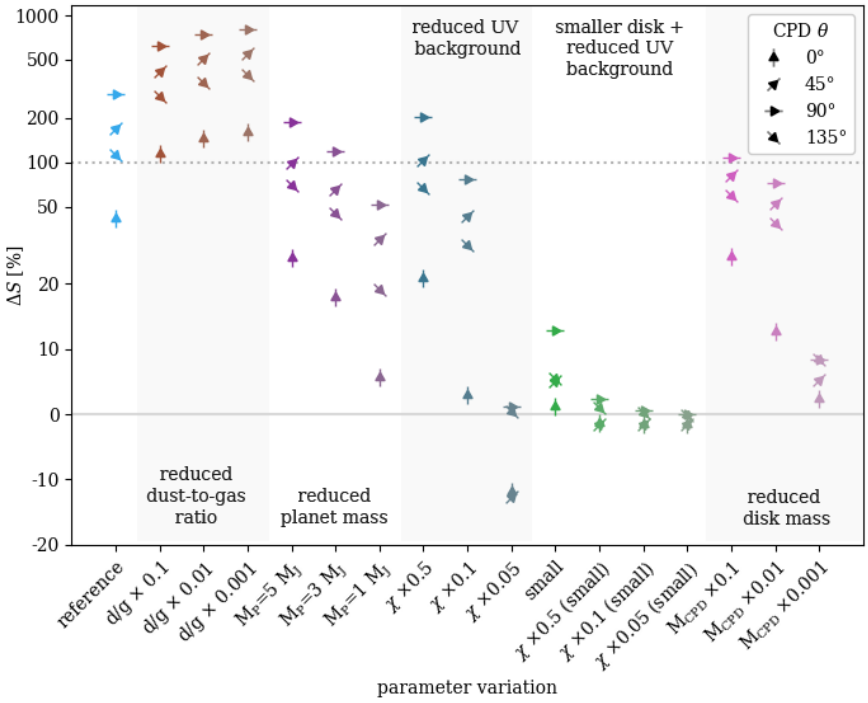

Figure 6.7: CPD induced excess or deficit flux in aperture for all CPD model configurations and phase angles θ. Fluxes are extracted from the spectral channel with the maximum contrast with circumstellar disk emission. A value below 0 indicates the CPD is seen in absorption. A value larger than 100 indicates that the aperture flux is more than double that of a no-CPD model. The variation of parameters are relative to the reference CPD with planet mass $M_{\rm P} = 10{\rm M_J}$, $\rm M_{CPD} = 0.01 M_P$, $\chi_{\rm RT} = 2 \times 10^6$, and $d/g = 10^{-3}$. A label "small" indicates that the CPD outer radius has been truncated to one third of the planet Hill radius. The angle of the triangle markers indicates the phase angle of the CPD relative to the circumstellar disk northern minor axes.

6.5 Conclusions

In this work, we used thermochemical disk models to produce synthetic channel maps that represent ^{12}CO line observations of the HD 100546 system in an effort to determine the plausibility of detecting CPDs in transition disk gaps with METIS. We list our key findings:

1. Fundamental ^{12}CO ro-vibrational line emission from the gas component of a circumplanetary disk can potentially be detected in only 60 s of detector integration time with ELT/METIS

2. Visibility of the CPD depends strongly on the level of external irradiation and the physical extent of the disk, favoring massive ($\sim$ 10 M_J) planets and spatially extended disks with radii approaching the planetary Hill radius.

3. The majority of ^{12}CO line emission originates from across the entire disk surface and, thus, the CO line profiles are centrally peaked. The planetary luminosity does not play a significant role in exciting the ^{12}CO line emission.

4. Massive, UV-bright star systems with pre-transitional disks are ideal candidates in the search for CO-emitting CPDs with ELT/METIS.

The capabilities of METIS represent a critical component of the multi-pronged effort to unveil the processes of giant planet and moon formation. If CPDs prove to be strongly dust-depleted, gas line observations will play a critical role in this endeavour.

Acknowledgements

The research of N.O. and I.K. is supported by grants from the Netherlands Organization for Scientific Research (NWO, grant number 614.001.552) and the Netherlands Research School for Astronomy (NOVA). CHR acknowledges the support of the Deutsche Forschungsgemeinschaft (DFG, German Research Foundation) Research Unit "Transition discs" - 325594231. Ch.R is grateful for support from the Max Planck Society. N.O. would like to thank B.R. Brandl and R. van Boekel for helpful discussions. This research has made use of NASA's Astrophysics Data System Bibliographic Services. This research made use of Astropy 3 a community-developed core Python package for Astronomy (Astropy Collaboration et al., 2013; Price-Whelan et al., 2018)) This research has also used Numpy (Harris et al., 2020), Matplotlib (Hunter, 2007), Scipy (Virtanen et al., 2020), and Prodimopy `https://gitlab.astro.rug.nl/prodimo/prodimopy`.

Appendix

A.1 CPD line emission strength relative to the continuum

The estimated peak emission strength of each of the modeled ^{12}CO lines is shown in Fig. 6.8 for the circumstellar disk, three cases of varying background radiation incident on the CPD, and the case of a planet without CPD.

A.2 Spatially unresolved CPD emission

We find that the CPD CO line emission can in certain cases be sufficient to be detectable even when spatially unresolved. In Fig. 6.9 we demonstrate a synthetic P26 line profile in the event that the disk would be spatially unresolved. The spectral resolution and noise level of the combined CSD (blue line) + CPD (red line) line profile has been degraded to correspond to the excess CO emission observed with CRIRES and discussed

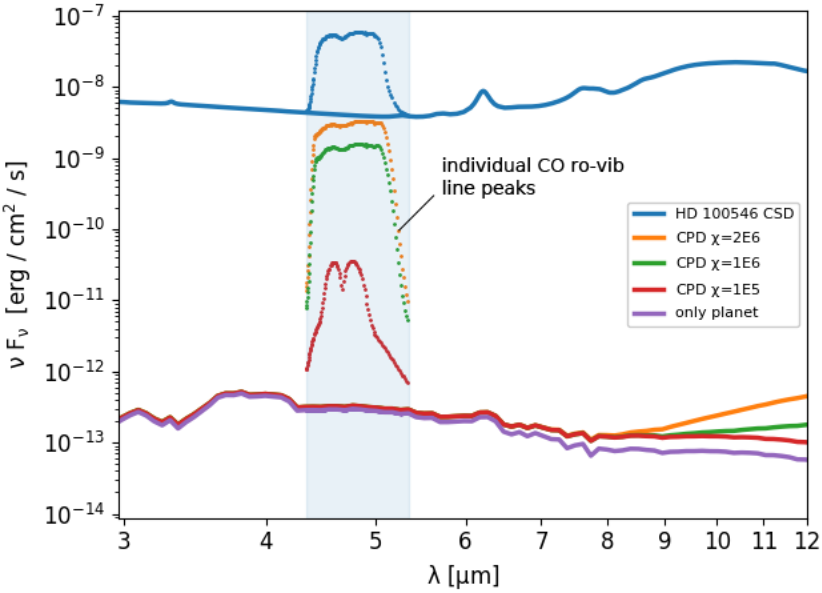

Figure 6.8: Comparison of the estimated CPD and CSD ^{12}CO line fluxes (dots) for varying intensities of background UV radiation with the continuum SED of the CSD and CPDs (solid lines). Only the ^{12}CO lines are plotted.

in Brittain et al. (2014, 2019) (black line). The corresponding line profile in the absence of a CPD is indicated by the gray line. While the CPD-induced excess is notable, without a priori knowledge of the properties and orbital phase of the CPD, spectral decomposition would be implausible without long-term monitoring of the signal.

A.3 Considering how much stellar radiation may reach the CPD

In our reference model, we have assumed the gap to be effectively empty with a correspondingly negligible optical depth. As a verification step, we performed a series of radiative transfer simulations in which we populate the gap with additional dust and gas to explore the potential for extinction of stellar UV towards the CPD and of CPD emission towards the observer. Several cases of increased gap dust mass are displayed in Fig. 6.10. Non-neglible extinction of the stellar UV begins to occur if the gap is populated by 10 times the dust mass inferred to be present in the inner disk. With a gap dust mass of $10 \times m_{\mathrm{dust,inner}}$, the midplane FUV intensity χ_{RT} falls to 30% of the reference value at the position of the CPD. The SED of the CSD in this case is still consistent with observations, increasing the flux at 4 μm by no more than ~ 4%. If the gap dust mass is increased to 100× the inner disk dust mass, the SED begins to diverge

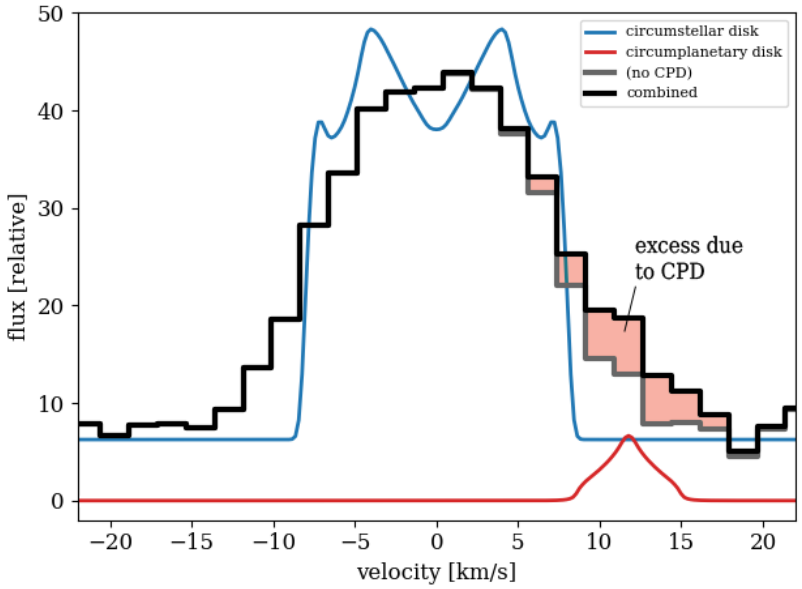

Figure 6.9: Synthetic ^{12}CO v(1-0)P26 (4.9204 μm) line profiles of the circumstellar disk (blue) and circumplanetary disk (red) from the ProDiMo radiative transfer. The combined and degraded signal corresponds to the spectral resolution of the CRIRES observations performed by Brittain et al. (2014, 2019) during multi-epoch monitoring of the HD 100546 system. The light shaded red region indicates the contribution of the CPD.

significantly from WISE, ISO-SWS, and VISIR observations at 2-11 μm and is ruled out by observations. Hence, we consider it plausible that additional dust in the gap may reduce the CPD-incident FUV flux by at least ∼ 70% without becoming inconsistent with the observations.

As we show in Sect. 6.2.1, we find that upwards of 95% of the UV radiation incident on the CPD originates from back-scattering off of dust in the gap outer wall. While radiative transfer in ProDiMo is calculated only using isotropic scattering of photons, at wavelengths of ∼ 0.1 μm, molecular gas can act as an effective Rayleigh-scatterer. Furthermore, stellar Ly-α photons may be resonantly scattered downwards into a gap by atomic hydrogen in the upper layers of the circumstellar disk, although this phenomenon is also not included in the 2D radiative transfer (Bethell and Bergin, 2011). This leads us to believe that isotropic incidence of external UV is a reasonable approximation in this case. Nevertheless, we consider the case where the external radiation has been decreased by a factor 20 under the assumption that scattering of UV photons would be particularly inefficient or that significant quantities of undetected dust is filling

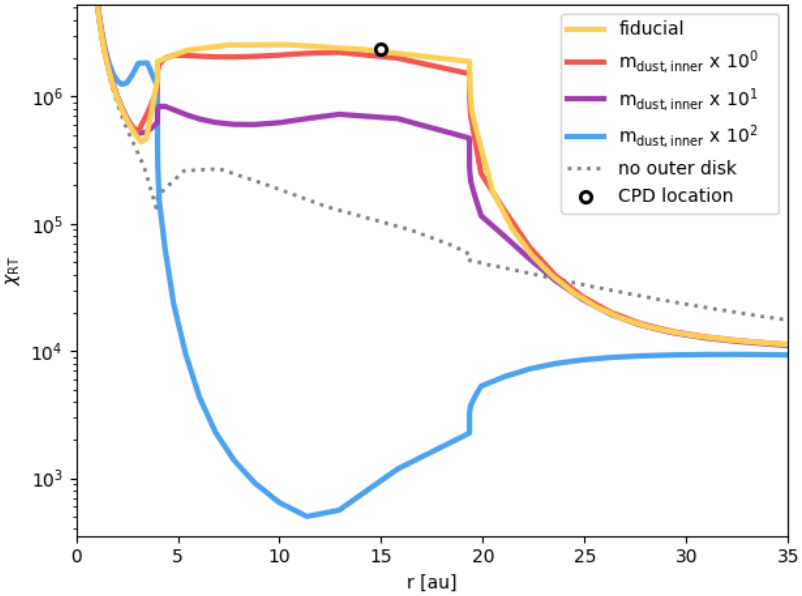

Figure 6.10: Midplane χ_{RT} extracted from the 2D radiative transfer of the ProDiMo HD 100546 disk model for the reference case, and in the case of the dust mass in the gap being equal to 1, 10, and 100 times the amount of dust in the inner disk. The case of no outer disk is included as the gray dashed line to highlight the role of back-scattering off the gap outer wall.

the gap.

A.4 Properties of the reference CPD model

The ^{12}CO abundance and v=1-0 line emitting region of the reference CPD can be found in Fig. 6.11a. The gas temperature and density structure can be found in Fig. 6.11c and 6.11b. Small dust grains in the upper layers of the CPD absorb external UV photons but cool efficiently to radiative equilibrium. This heats the surrounding gas which in turn cools predominantly by the relatively inefficient H_2O and CO rotational and vibrational emission. Hence, the gas and dust temperature are not closely coupled in this hot surface layer. The parameters of the CPD models which are common to all models described in Table 17 are listed in Table 3.

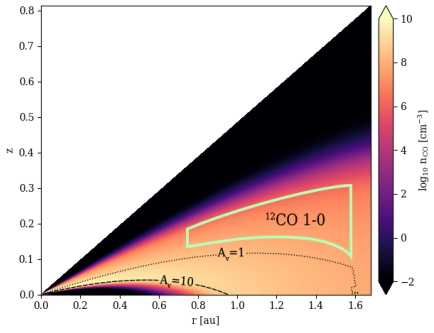

(a) CPD CO abundance.

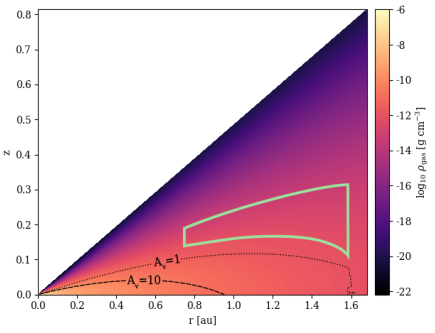

(b) CPD gas density.

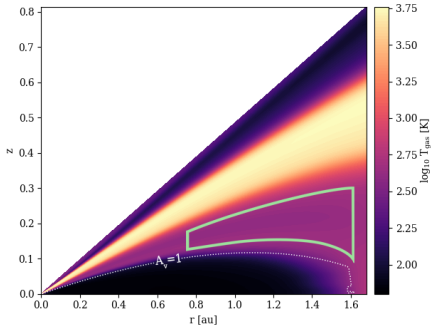

(c) CPD gas temperature.

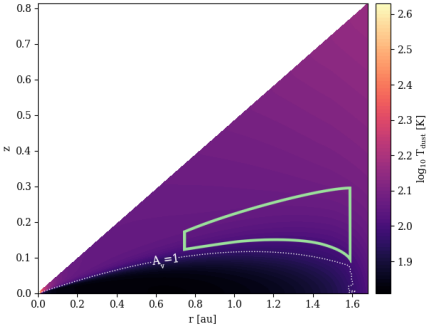

(d) CPD dust temperature.

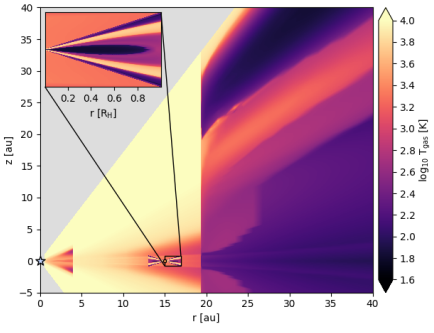

(e) CPD and CSD gas temperature.

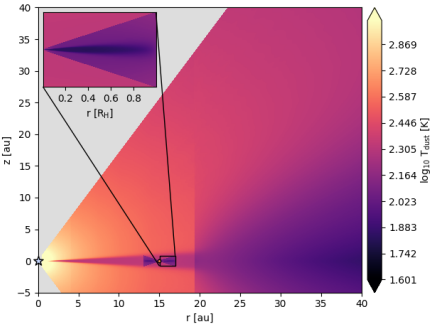

(f) CPD and CSD dust temperature.

Figure 6.11: Properties of the reference CPD with $\chi = 2\times10^6$ and $R_{\rm out} = R_{\rm Hill}$ (a,b,c,d). The majority of the ^{12}CO v=1-0 line emission originates from within the green "box" region in panels a-d. The dotted contour lines in panels (a,b,c,d) represent minimum optical extinction A_V surfaces of 1 (dotted line), 10 (dashed line) in the radial or vertical direction. The gas and dust temperature structure of the CPD is contrasted for illustrative purposes with that of the circumstellar disk in panels (e) and (f).

7 Conclusion

For then why may not every one of these
Stars or Suns have as great a Retinue as
our Sun, of Planets, with their Moons,
to wait upon them?

- Christiaan Huygens, *The Cosmotheoros, Book II*

Are Jupiter's moons unique? In the Introduction we enumerated several properties of the Galilean moon system that warranted further investigation. We can now consolidate several of these characteristics and recapitulate.

7.1 System architecture

The Galilean system's peculiar architecture is unlike that of the solar system. The Jovian 'planets', although being regular satellites, are arranged compactly and orbit close-in to their primary. The orbits are 'packed' in the sense that no additional major satellites could be fit between them while remaining dynamically stable. The inner three moons are linked in a mean-motion resonance that regulates the secular evolution of their orbital inclination and eccentricities. This arrangement has not escaped the notice of the exoplanet community. The Galilean system has slowly drifted into focus for its notable similarity to a subset of low-mass exoplanet systems (Kane et al., 2013). Namely, compact close-in systems in which multiple similarly sized worlds orbit in proximity to their primary (Lissauer et al., 2011; Fressin et al., 2013; Petigura et al., 2013). The jewel of the known compact multiplanet systems is, arguably, the TRAPPIST-1 system (Gillon et al., 2017). In the TRAPPIST-1 system, seven planets with masses ranging from 0.3885-1.377 $M_\oplus$ orbit a 0.0898 $M_\odot$ star in orbits ranging from 0.01154-0.06189 au (Agol et al., 2021). The entire Galilean system would fit very nearly within the orbit of the innermost planet TRAPPIST-1 b. Remarkably, the entire TRAPPIST system is also linked by a mean-motion resonant chain relating the orbital period of the planets (24:15:9:6:4:3:2 vs. 4:2:1 in the Galilean system).

Initially this configuration was considered difficult to explain, as both in-situ and migration scenarios were unable to easily reproduce the system architecture in simulations. The pebble accretion scenario is able to explain how the TRAPPIST-1 system formed. Planet formation began with the accumulation of pebbles near the water iceline (Ormel et al., 2017b; Drążkowska and Alibert, 2017; Müller et al., 2021). A locally sufficient density of solids allowed for planetesimal formation to be triggered via the streaming instability. Once large enough, proto-planets migrate inwards via Type I migration until they are stopped at the gas-free magnetospheric cavity surrounding the planet (Ormel et al., 2017b). Critically, planet formation occurs sequentially in the manner proposed by Canup and Ward (2002), for the formation of moons in a CPD. Resonant trapping of migrating planets occurs as additional proto-planets form and move inwards. Planet growth is limited by the pebble isolation mass, above which dynamical

feedback on the disk prevents pebbles from reaching the planet. The entire formation process occurs in a gaseous disk. The pebble flux originates from the icy outer disk region. In many respects this scenario is similar to the comprehensive framework for Galilean moon formation proposed by Shibaike et al. (2019).

The TRAPPIST-1 system architecture is however far from common (Fabrycky et al., 2014). Despite thousands of known exoplanet systems, only a handful are known to exhibit resonant chains of four planets or more, with notable examples Kepler-223 (Mills et al., 2015), K2-138 (Christiansen et al., 2018), and TOI-178 (Leleu et al., 2021). Why do the majority of low mass planetary systems not exhibit such a resonant chain? When the gas-disk is still present, orbital eccentricity and inclination of planets are damped (Tanaka and Ward, 2004). A resonant chain system is kept stable by the eccentricity-damping of the gas disk (Matsumoto et al., 2012). As the gas disk clears, up to 90-95% of the resonant chains may destabilize (Cossou et al., 2014; Izidoro et al., 2017). It is unclear why some resonant chains are able to survive the gas disk dispersal. Simulations suggest that MRI-inactive disks with low total solid mass tend to preserve a chain, as do systems in which the solid mass is initially concentrated in a narrow ring (Ogihara et al., 2018). Chains may destabilize if they initially contain too many planets and the frequency of close encounters is too high after gas disk dispersal (Matsumoto et al., 2012). Finally, whether or not the chain is destabilized may depend on the rate at which the gas disk disperses or by what process it disperses. If the gas disk clears inside out by e.g. photoevaporation, the innermost planet may briefly not experience the eccentricity-damping forces while the other planets still do, triggering an instability (Liu et al., 2022; Sánchez et al., 2022).

In this context how is a CPD gas disk expected to evolve and dissipate? This was the problem we approached in Chapter 2. When attempting to determine whether the Galilean system is unique, a natural starting point was to focus on peculiarities characteristic to the solar system itself. The orbital architecture of the solar system may have been influenced by photoevaporation, and its thermal evolution and chemical composition influenced by the death of nearby massive stars (Pfalzner, 2013). This might occur if the Sun formed in a high-mass stellar cluster, unlike the Taurus molecular cloud star formation region. Given that the Jovian CPD could have been exposed to similar levels of external irradiation, it was clear that the architecture of the Galilean moon system may also have been shaped by the loss of CPD gas.

We modeled a high-mass stellar cluster to derive a time-dependant background far-ultraviolet (FUV) radiation field for our model solar system. At the position of Jupiter, the expectation value for the intracluster radiation was found to be on the same order as the contribution of the Sun itself. Although uncertainties in the geometry of the inner protosolar disk meant that the CPD could be shielded from the solar radiation, the cluster radiation could not be as easily blocked. The photoevaporation in the CPD increased the total rate of mass outflow significantly. For accretion rates onto the CPD below 10^{-10} $M_\odot$ yr^{-1} the CPD was found to be truncated more so than it would be by tidal interaction with the star alone. The new steady-state size of the CPD was found in the majority of cases to correspond roughly to the present-day orbit of Callisto for an

accretion rate corresponding to the tail end of planet growth of 10^{-12} $M_\odot$ yr^{-1}. Hence, there simply may have been no circumplanetary gas exterior to Callisto's orbit at the time of moon formation. This presents a straight-forward answer to the question as to why no additional major satellites are found to orbit exterior to Callisto. In a gas-free environment the further concentration of pebbles and spontaneous formation of planetesimals would be impossible. The gas disk may not even need to be truncated to Callisto's present-day position to terminate additional moon formation. If planetesimal formation in the CPD only occurs at the location of a dust trap, moon formation may end at an earlier time. The radial position of a dust trap in the CPD may be as far out as 100 Jupiter radii (Drążkowska and Szulágyi, 2018), or nearly four times further out than Callisto orbits[16]. If gas in the dust trap region was disrupted by photoevaporation, sequential satellite formation would terminate when the accretion rate falls to 10^{-11} $M_\odot$ yr^{-1}. In Chapter 3, we found that this particular accretion rate is able to best reproduce an ice-to-rock ratio in the CPD that corresponds to the compositional gradient of the Galilean moons. Hence, the tailing off of accretion in a highly irradiated environment may naturally limit the build-up of moons in wide orbits around gas giants, leaving the majority of the planetary Hill sphere empty.

The circumplanetary gas clears almost instantaneously once accretion ends (Mitchell and Stewart, 2011; Oberg et al., 2020). Although, as the circumstellar disk outer gap wall photoevaporates, so too would the CPD (Batygin, 2018) owing to their comparable gravitational binding energies. One possible consequence of this fast dispersal is that a migrating moon or planet could in effect be stranded during its migration, and hence not enter the resonant chain (Oberg et al., 2020). This proffers a scenario to explain the exclusion of Callisto from the Laplace resonance even in a very gas-rich disk. However, the timing of abrupt gas disk dispersal requires significant fine-tuning for this to occur in practice, rather than e.g. a secular reduction in the Type I migration rate by a thinning of the circumplanetary gas disk. Additionally, rapid CPD gas clearing may prevent the destabilization of the resonance. If the evaporation of the CPD occurs outside-in rather than inside-out, it would be Callisto rather than Io that might face the sudden loss of eccentricity-damping forces. If external, rather than internal, photoevaporation is the fate of most CPDs, multi-satellite resonant chains may be more stable against destabilization than planetary systems that photoevaporate inside-out. In that context, the Galilean moons may be only the first of many resonant satellite systems to be discovered.

7.2 Compositional Gradient

The Galilean moon compositional gradient is unique among the regular satellites of the solar system. The outer two Galilean satellites are significantly more massive and ice-rich than the inner two. Notably, the outer two differ only negligibly in bulk density and size from each other. The reader may be led to the conclusion that all four moons were

[16]Note that such a dust trap could represent the initial narrow ring of solids found to promote stable resonant chain formation by Ogihara et al. (2018)

primordially of similar dimension and composition, and that in some post-facto process the inner two lost either all or the majority of their icy mantles. Such a process could not have occurred in the Saturnian satellite system given the ice-rich composition of the inner satellites. Tidal heating appears to be incapable of delivering enough energy to an initially ice-rich proto-Io and proto-Europa to devolatilize them to their current state (Bierson and Steinbrügge, 2021) while hydrodynamic escape offers one plausible route by which they might lose the majority of their volatiles (Bierson and Nimmo, 2020). However, this process may not be necessary in the pebble accretion scenario. It is clear in Fig.7.1 that Europa and Io are unique in that their bulk density is significantly higher than all other gravitationally rounded satellites of the solar system gas giants. If we construct a simple metric by which to estimate the relative insolation at the position of each satellite according to the protoplanet mass-luminosity relation of Mordasini et al. (2017), we see that Io and Europa again stand out from all gas giant satellites with respect to their current density and primordial insolation. Were the moons simply devolatilized post-formation by proximity to their luminous primary as icy mantles melted, vaporized, and thermally escaped? If instead the compositional gradient was produced during the accretion of the moons in the CPD, we would need to demonstrate that the composition of drifting pebbles reflected the final composition of the satellites. But we found that heating in the midplane of an optically thick CPD is dominated by viscous dissipation, and not the planetary luminosity. As viscous heating is coupled to the magnitude of the effective viscosity in the CPD, we need to be able to constrain the magnitude of this property.

We set out to constrain the CPD viscosity in a novel way. We know that massive planets can clear gaps in their circumstellar disk, and we know that circumstellar matter continues to flow across such gaps and is swept up by the planet (Kley, 1999). This matter falls from several circumstellar disk scale heights, and is nearly vertically incident on the CPD (Morbidelli et al., 2014; Szulágyi et al., 2022). The more massive the planet is, the greater the gravitational acceleration of infalling material. Once the infall velocity is in excess 8-10 km/s, a shock-front may begin to form on the surface of the CPD (Draine and McKee, 1993; Tielens, 2005). If the shock is sufficiently strong it can sublimate the icy mantles on dust grains. In the most extreme case, even molecules can be destroyed and atoms ionized by the accretion shock. Given that we know that the outer two Galilean satellites are ice-rich, ices must have been present at the time of their accretion. As Jupiter is massive enough to have accelerated infalling material to a shock-velocity that sublimates ices, it allowed us to place a new constraint on the behaviour of the CPD. Namely, ices must be able to form on timescales less than the viscous timescale of the disk.

However, the timescale of ice formation was found to be far shorter than the shortest plausible disk viscous timescale, and hence the CPD viscosity could not be constrained in this way. Several interesting features of ice evolution in the CPD were nevertheless revealed. For one, we found that the dust mass in the disk must be depleted relative to the canonical dust-to-gas ratio in the ISM by a factor of twenty to reproduce the ice-to-rock ratio of the Galilean satellites. This depletion factor happens to coincide

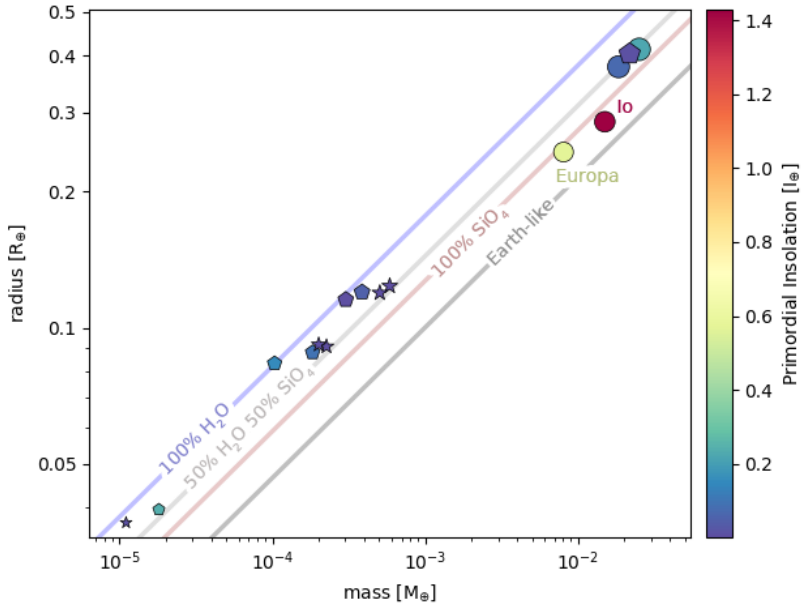

Figure 7.1: Mass-radius relation of the major, regular satellites of the solar system. Circles represent moons of Jupiter, pentagons represent moons of Saturn, and stars represent moons of Uranus. Solid lines indicate densities corresponding to pure water, a 50:50 ice-to-rock ratio, a pure silicate composition, and an Earth-like density (5.5 g / cm^3). Marker sizes correspond to the surface escape velocity. The color of the symbols indicates the insolation in units of the Earth insolation $I_\oplus$ they would receive at their present-day orbits for a primordial planet luminosity corresponding to the planet mass-luminosity relation of Mordasini et al. (2017). This value is meant to illustrate plausible relative levels of radiative heating due to the planet after the CPD has cleared.

very nearly with the expected loss of the largest dust grains to rapid inwards aerodynamic drift (Zhu et al., 2018; Rab et al., 2019). Grains smaller than a minimum cut-off size would instead remain trapped within the CPD (Oberg et al., 2022b).

Secondly, the iceline in the Jovian CPD was found to fall quite naturally between the present-day positions of Europa and Ganymede for an accretion rate of 10^{-11} $M_\odot$ yr^{-1} (corresponding to an α-viscosity of $10^{-3.6}$). But this result would be meaningless if the inwardly drifting grains were able to transport ice as they moved across the iceline. In that case, the iceline might be "smeared out", and we could expect a smooth continuum of increasing iciness rather than the relatively abrupt jump that is observed in the Galilean system. We found that these drifting pebbles would effectively lose their icy mantles virtually instantaneously upon crossing inwards of the iceline as long as their size was below 10 μm. Previous work found that larger grains, effectively meter-sized

boulders, would however be able to bring at least some volatiles interior to the iceline with them and supply the relatively thin veneer of ice to Europa (Ronnet et al., 2017). Europa's intermediate iciness is otherwise difficult to reproduce in a thermochemical disk model with a very discrete iceline. Hence, our result supports the pebble accretion scenario in which moon embryos initially migrate inwards, are stopped at a cavity, and lock into a resonance after which they continue to slowly accrete inwardly drifting pebbles from the outer CPD.

While the TRAPPIST-1 system exhibits many similarities to the Galilean moons, the most recent estimates of the planet properties indicate that they are all of similar bulk density (Agol et al., 2021). This stands in striking contrast to the Galilean moons, despite the similar formation scenarios discussed in the previous section. Was the TRAPPIST-1 circumstellar disk surface density insufficient for viscous heating to devolatilize inwardly drifting pebbles? Perhaps the absence of MRI-driven turbulence in the CPD and corresponding low α-viscosity allows for the build up of relatively massive disks with correspondingly high midplane heating rates.

7.3 Chemical Composition and Impurities

Another property by which the Galilean system further distinguishes itself from the Saturnian is that none of the Galilean moons host a substantial atmosphere in the way that Titan does. Titan hosts a thick N_2-dominated atmosphere that obscures the surface at optical wavelengths. The origin of Titan's atmosphere has long been debated. Either Titan accreted N_2 directly from the circumsolar or circumSaturnian disk, or accreted a nitrogen-rich ice which was later converted to N_2. The prevailing theory is now that Titan's atmosphere is secondary, being outgassed from nitrogen-bearing ices in its interior (Mandt et al., 2014). The most promising candidate for the source of nitrogen is ammonia (NH_3) ice. Analysis of the nitrogen isotopic ratios in Titan's atmosphere support the hypothesis that it directly inherited circumstellar ice described as "cometary" (Owen, 2000). Similarly, the Saturnian moon Enceladus appears to exhibit an interior chemical composition corresponding to comets as revealed through its spectacular plume emissions (Waite et al., 2009).

Why do the Galilean moons not host secondary atmospheres like Titan? Tenuous exospheres on Callisto and Ganymede are continually replenished largely by H_2O and CO_2 (Carlson et al., 1999; McGrath et al., 2004; Roth et al., 2021) but clearly the current atmospheric loss rate does not allow for the accumulation of a substantial atmosphere. Interestingly, there appears to be no evidence of N_2 outgassing on Callisto or Ganymede. Our own thermochemical modeling of the circumstellar disk shows that NH_3 was the dominant carrier of nitrogen in ices at the midplane from 5-10 au. If Saturnian moons were inheriting NH_3 ice directly from the circumstellar nebula, we might expect that the Galilean satellites could have accreted it as well. A critical difference between these two systems is the mass of the primary. Matter accreting from the circumstellar disk onto the Jovian CPD is accelerated to greater velocities by Jupiter's mass. A significant fraction of the infalling material accretes near the so-called centrifugal radius (Machida et al.,

2008). In the Jovian system, the infall velocity at the centrifugal radius is in excess of 10 km/s. In this regime we can expect a weak shock to form above the surface of the CPD. This transient shock heating leads to the sublimation of icy grain mantles. The sublimated volatile molecules are returned to the gas-phase and hence may be chemically processed within the CPD. In this case we speak of a chemical 'reset', rather than inheritance. Uncovering the chemical history of the Galilean moon ices is critical to understanding their potential interior composition.

We found that NH_3 is destroyed if ices are initially sublimated during accretion onto the Jovian CPD. Once the NH_3 is returned to the gas-phase it is photodissociated in the optically thin surface layers of the disk. By the time the accreted gas has reached the midplane, nitrogen is primarily found in the form of N_2 and remains in the gas phase. Moons with the mass of Ganymede cannot easily accrete this gas directly for the surface temperatures expected from accretional heating. In this initial sublimation reset scenario the ices in the CPD evolve to be nitrogen-poor. Instead, the composition is dominated by H_2O and CO_2 ice, with an additional component of HCOOH ice in the outer CPD. If the shock-heating above the CPD is even more extreme and the ice molecules are destroyed during accretion, CO_2 ice formation is further inhibited in the inner CPD and the ice is instead H_2O dominated. The infall velocities corresponding to such an atomic reset might occur for a planet more massive than Jupiter.

In this paradigm icy moon system composition will be determined by the primary mass (and to a lesser extent primary-star mass ratio and orbital separation as these regulate the location of the centrifugal radius). The distinct chemical initial conditions of inheritance or reset produce distinct icy grain compositions within a CPD of Jovian mass. We can expect that the most massive planets with correspondingly strong CPD-surface shock-heating will produce disks containing predominantly water ice, with traces of methanol. Planets of Jovian mass will host disks with carbon-enriched ices where CO_2 and HCOOH form major components even relatively close-in to the planet. Primaries of lower mass (Saturnian) will instead host CPDs with icy solids that have been relatively unprocessed. Although some processing of circumstellar ices does occur in the CPD for the inherited chemistry (in particular the conversion of HCN to CO_2), in general the majority of any accreted ammonia ice survives and could be incorporated into moons. Hence the mass of the primary may play a very important role in determining the final chemical state of the moons not only via its luminosity but simply by virtue of its mass.

7.4 Moons around planets around other stars

7.4.1 At wide separation

In the end the answer to our question will be settled only through rigorous and systematic observation of reality. In the present epoch we are limited in terms of the direct detection of planets to those that are still excessively luminous due to their accretion and subsequent contraction. Typically owing to instrumental limitations in terms of contrast and spatial resolution we are limited to the detection of wide-separation objects

that orbit at 10's or even 100's of au from their star. While the population of directly imaged planets is overwhelmingly to be found in systems where the gas disk has already dispersed, the first directly detected CPD was found inside a transition disk cavity (Christiaens et al., 2019).

Multiple theoretical studies suggest that dust will be removed extremely quickly from CPDs which are not continually fed fresh material from the surrounding nebula or disk (Zhu et al., 2018; Rab et al., 2019). In this case perhaps it is not surprising that detection of continuum emission from cool circumplanetary dust is not commonly associated with these wide-separation objects. Nevertheless, this idea was put to the test by our observation campaign in Chapter 5. In search of companion objects to a collection of disks in (pre-)transitionary states, we used VISIR and its upgrade NEAR on the VLT to search for continuum emission from planets and circumplanetary dust. Although no companion objects were identified as part of this campaign, we were able to place some limits on wide-separation companion luminosities for this set of systems. The deepest integrations were performed for the HD 100546 system.

Analysis of continuum sub-mm emission at 870 μm from the HD 100546 circumstellar disk has revealed an annular gap at 40-150 au. Smoothed particle hydrodynamics simulations can reproduce the observed structure if one 3 M_J planet is placed inside the innermost gap at 15 au and another 8.5 M_J planet at 110 au (Fedele et al., 2021). A similar study performed by Pyerin et al. (2021) suggests a similar arrangement of companions with the masses reversed (8 M_J at 13 au and 3 M_J at 143 au). We found no mid-infrared emission associated with the outermost theoretical planet. The luminosity would thus be constrained to $\lessapprox 0.003$ $L_\odot$ for a > 160 au, suggesting that any companion would likely be planetary, rather than stellar in nature. Interior to this orbit the limiting sensitivity was severely degraded by disk thermal emission.

7.4.2 Embedded within disk gaps

Planets have been consistently implicated in the formation of gaps and cavities in (pre-)transition disks. The detection of planets orbiting within cavities or gaps poses several observational challenges relative to the wide-separation companions, namely the extreme contrast and angular resolution requirements for systems observed at a typical distance of 100-120 pc in Taurus. The HD 100546 system is host to a plethora of planet candidates as can be seen in Fig. 7.2.

In the HD 100546 system multi-epoch monitoring of spatially unresolved ^{12}CO rovibrational emission has revealed an unexplained excess emission source with a time-variable line-of-sight velocity (Brittain et al., 2013, 2019). This excess may represent a gaseous circumplanetary disk around a planet orbiting very near the inner gap outer wall.

As described in the above section it has recently been speculated that CPDs might be dust depleted. Aerodynamic drag of large grains against sub-Keplerian gas may suppress the dust-to-gas ratio by a factor 10-100 within only 10^3 yr unless a continuous supply of fresh grains can be delivered to the CPD. Even with a fresh supply of dust,

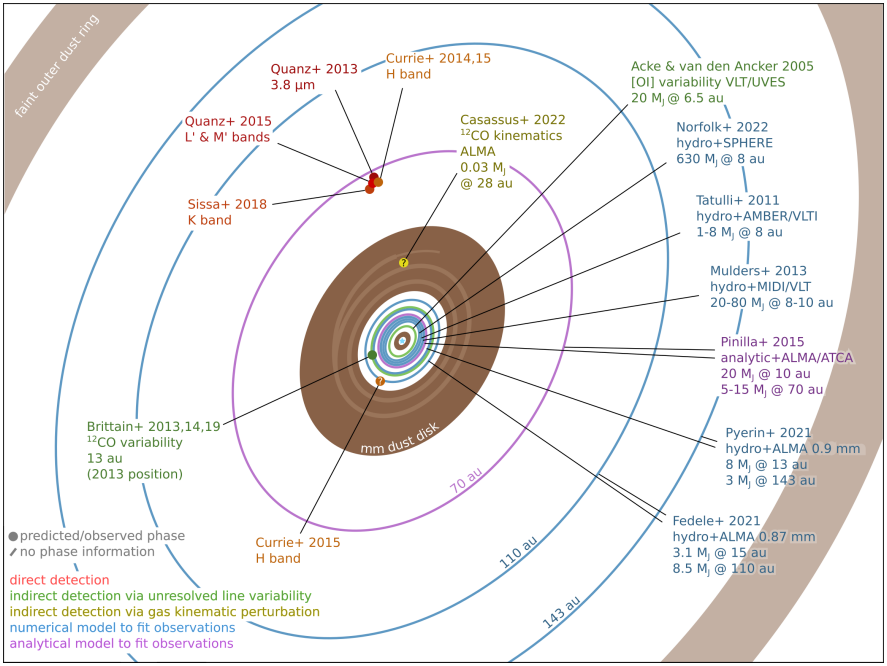

Figure 7.2: Summary of all planet candidates either observed or inferred to exist in the HD 100546 system. A question mark on a planet candidate indicates the authors making the claim emphasized that the existence of the companion is questionable. Candidates represented by a small circle indicate that the planet phase angle was supplied. Candidates represented by a circular zero-inclination orbit indicate no phase information was supplied. Light structures/spirals on the inner mm-dust disk represent non-axisymmetric structure observed in continuum mm-emission. (Quanz et al., 2013a; Quanz et al., 2015; Currie et al., 2014, 2015; Sissa et al., 2018; Brittain et al., 2013, 2014, 2019; Casassus et al., 2022; Acke et al., 2005; Norfolk et al., 2022; Tatulli et al., 2011; Mulders et al., 2013; Pinilla et al., 2015; Pyerin et al., 2021; Fedele et al., 2021)

grains may become trapped in a relatively narrow annulus with a minimal effective emitting surface area further frustrating detection attempts. The PDS 70 system, in which dust associated with one of the planet candidates has been positively identified and spatially resolved, potentially represents a special case (Francis and van der Marel, 2020). Possibly the system may have only recently opened its gap or a transient event in which a significant amount of dust has been transported into the cavity has recently occurred (Brittain et al., 2020). If this is so, the general outcomes of rapid dust depletion or confinement could complicate continuum detection of CPDs. The CPD gas component may instead provide a more direct avenue to detect these objects. If the CO excess observed by Brittain et al. (2013) does indeed arise from a CPD and not from a transient spiral

feature it would represent an unambiguous CPD detection if spatially resolved.

The upcoming Mid-Infrared E-ELT Imager and Spectrograph (METIS) instrument on the Extremely Large Telescope (ELT) will couple the spatial and spectral resolution of the instrument with the collecting area and advanced adaptive-optics systems of the ELT (Brandl et al., 2018). METIS is suited to observe the full ro-vibrational emission spectrum of ^{12}CO. In chapter 6 we found that METIS will be able to detect a CPD in the gap of the HD 100546 system if two conditions are satisfied. The first condition stems from the issue that the planet luminosity is expected to be insufficient to locally heat the CPD such that it excites significant CO ro-vibrational emission. Instead, an external source of radiation is required. As the HD 100546 star is an A0 stellar type (Gray et al., 2017) with ~30 $L_\odot$ there is a significant source of FUV in the system. Our 2D radiative transfer found that the HD 100546 inner gap region may be permeated by an FUV field over 10^6 times as powerful as the quiescent ISM. This irradiation is able to heat a surface layer in the CPD which is then the origin of the majority of its ^{12}CO ro-vibrational emission. The second condition is that the detection limiting sensitivity depends strongly on the physical parameters of the CPD, namely its size. As the CO emission is externally excited it originates from across nearly the entire CPD surface. The total flux is thus strongly proportional to its projected surface area.

If the CPD is truncated by tidal interaction with the star or by external photoevaporation, the detection will be made more challenging. We found in Chapter 2 that external FUV flux only 10^{-3} as intense as the level expected in the HD 100546 system could truncate the gas component of a CPD, although this was tested only for a Jupiter mass primary. As a planet in the HD 100546 inner dust gap has been so repeatedly implicated by observed gas and dust dynamical perturbations, a non-detection of circumplanetary gas with METIS would imply that its CPD may be stripped down to less than a third of the planetary Hill radius. If the CPD gas component is prevented from settling into a disk around the planet the process of moon formation could be inhibited. This might lend evidence to the idea that companions around massive UV-bright stars like HD 100546 may not be able to easily form large moons. In the absence of a thick circumplanetary gas disk there would be no damping force to sediment dust grains to the midplane and planetesimal formation might never be able to initiate. METIS may thus help us uncover a stellar upper mass limit to the formation of giant planet regular moon formation.

7.5 Outlook

During the execution of this dissertation the total number of unambiguously identified circumplanetary disks has increased from zero to one [17] (Christiaens et al., 2019). Although, in the strictest sense, the point-source continuum emission co-located with the protoplanet PDS 70 c has not yet been definitively identified as a disk, rather than e.g. a spherical envelope. In any case, what *is* unambiguous is that we have glimpsed the

[17] With the latest candidate in the AS 209 system potentially and dramatically doubling the total (Bae et al., 2022).

founding a new field of observation wherein we witness the birth of distant satellites. Detecting CPDs clearly demands the extreme spatial resolution of facilities like ALMA, but if a larger population of dust-depleted CPDs continues to evade detection, the development of enormous ~30-40 meter class ground-based observatories will reveal the rich molecular gas disks surrounding growing planets in this decade (Neichel et al., 2018; Oberg et al., 2022a).

Closer to home, the JUpiter Icy Moons Explorer (JUICE) has launch from Kourou in 2023 and will drift through interplanetary space for ~8 years before entering the Jupiter system in 2031 (Grasset et al., 2013; Witasse, 2022). It will be the first spacecraft to enter orbit around a Galilean satellite. Critically, JUICE will allow us to build a more detailed understanding as to how the moons, and in particular Ganymede, evolved since their formation. High-resolution topographical mapping with the 'Ganymede Laser Altimeter' (GALA) (Hussmann et al., 2022) will enable the detailed study of e.g. mass-wasting. Analysis of the physical-mechanical properties of the surface can provide insights into the immediate subsurface composition, as previously the presence of CO_2 has been inferred on Callisto by its influence on the degradation rate of topographical features (Hibbitts et al., 2003). Direct compositional mapping of the surface with the 'Moon and Jupiter Imaging Spectrograph' (MAJIS) (Piccioni et al., 2014) in the visible and near-infrared may reveal or exclude the presence of ammonia-bearing compounds, which could be tied directly back to the late-stage formation conditions of the moons and the chemical history of their icy building-blocks. The thin exospheres of the icy moons will also be studied with the 'ultraviolet spectrograph' (UVS) (Gladstone et al., 2013) and the 'sub-millimeter wave instrument' (SWI) (Hartogh et al., 2013). The presence of subsurface ices can be detected by their out-gassing, and may provide another avenus to detect nitrogen hidden under the surface of the icy moons. Gravity measurements that probe the interior structure of the moons and their radial mass distributions and differentiation-state may provide the strongest constraint on their accretion history (Parisi et al., 2012).

It is likely that the findings of JUICE will, while undermining many of the assumptions we make today, reveal new questions we had not yet considered. At the end of its mission, JUICE will come to impact the surface of Ganymede and will be the first, but certainly not the last, human work to mark the moons of Jupiter.

To human beings, the major satellites of Jupiter played a pivotal role in coming to understand our place in the solar system and by extension the entire cosmos - namely by knocking us firmly from its center. The next steps in the "great demotions" outlined by Carl Sagan may be the first to situate ourselves relative to the other living, thinking beings of the cosmos (Sagan, 1994). But the discovery of even a modest microbe beneath the icy crust of e.g. Europa would, according to some, serve as a warning: if two unconnected origins of life are found to have occurred within a single star system under vastly different initial conditions, then life may be commonplace. If life is commonplace, the lack of evidence for the longevity of technological civilization only emphasizes the fragility of our own (Gray, 2015; Haqq-Misra et al., 2020) in the face of catastrophic anthropogenic forcing of the climate (Slade, 2018; Hoegh-Guldberg et al.,

Figure 7.3: Artist's impression of a newly formed icy moon orbiting a still dimly glowing gas giant planet, waiting to be found.

2018). If instead the other potentially habitable environments of the solar system are found to be lifeless, the irreplaceable nature of our biosphere and the climate on which it relies may be demonstrated even more profoundly.

By venturing out to explore (and touch!) the outer icy moons within our reach we might settle the issue. And on the way who is to say what else we might discover? When Galileo first serendipitously noticed his "curious little lights", he hadn't justified the search through rigorous building of a science case. Would a dedicated campaign to observe Jupiter for speculative anomalous phenomena (using the world's most precious astronomical instrument, no less) be approved today?

References

Acke, B., van den Ancker, M.E. and Dullemond, C.P. A&A, 436:209–230, 2005.
Adams, F.C. Annual Review of Astronomy and Astrophysics, 48:47–85, 2010.
Adams, F.C., Hollenbach, D., Laughlin, G. and Gorti, U. ApJ, 611:360–379, 2004.
Agol, E., Dorn, C., Grimm, S.L., Turbet, M., Ducrot, E. et al. The Planetary Science Journal, 2(1):1, 2021.
Aitken, R.G. PASP, 18:111, 1906.
Alibert, Y., Mousis, O. and Benz, W. A&A, 439(3):1205–1213, 2005.
ALMA Partnership, Brogan, C.L., Pérez, L.M., Hunter, T.R., Dent, W.R.F. et al. The Astrophysical Journal Letters, 808:L3, 2015.
Altinay, G. and Macdonald, R.G. The Journal of Physical Chemistry A, 116(9):2161–2176, 2012.
Altinay, G. and Macdonald, R.G. The Journal of Physical Chemistry A, 119(28):7593–7610, 2015.
Anderson, J., Jacobson, R., McElrath, T., Moore, W., Schubert, G. et al. Icarus, 153(1):157 – 161, 2001.
Anderson, J.D., Sjogren, W.L. and Schubert, G. Science, 272(5262):709–712, 1996.
Anderson, J.D., Lau, E.L., Sjogren, W.L., Schubert, G. and Moore, W.B. Nature, 387(6630):264–266, 1997.
Anderson, J.D., Schubert, G., Jacobson, R.A., Lau, E.L., Moore, W.B. et al. Science, 281:2019, 1998.
Anderson, J.D., Johnson, T.V., Schubert, G., Asmar, S., Jacobson, R.A. et al. Science, 308:1291–1293, 2005.
Andrews, S.M. ARA&A, 58:483–528, 2020.
Andrews, S.M., Wilner, D.J., Espaillat, C., Hughes, A.M., Dullemond, C.P. et al. ApJ, 732(1):42, 2011.
Andrews, S.M., Wilner, D.J., Zhu, Z., Birnstiel, T., Carpenter, J.M. et al. ApJ, 820(2):L40, 2016.
Andrews, S.M., Huang, J., Pérez, L.M., Isella, A., Dullemond, C.P. et al. ApJ, 869(2):L41, 2018.
Ansdell, M., Williams, J.P., van der Marel, N., Carpenter, J.M., Guidi, G. et al. ApJ, 828(1):46, 2016.
Ansdell, M., Williams, J.P., Trapman, L., van Terwisga, S.E., Facchini, S. et al. ApJ, 859(1):21, 2018.
Antonellini, S., Banzatti, A., Kamp, I., Thi, W.F. and Woitke, P. A&A, 637:A29, 2020.
Antoniadi, E.M. Journal of the British Astronomical Association, 9:66–66, 1898.
Aota, T., Inoue, T. and Aikawa, Y. ApJ, 799(2):141, 2015.
Aoyama, Y., Ikoma, M. and Tanigawa, T. ApJ, 866(2):84, 2018.
Armitage, P., Kley, W., Audard, M., Meyer, M. and Alibert, Y. From Protoplanetary Disks to Planet Formation: Saas-Fee Advanced Course 45. Swiss Society for Astrophysics and Astronomy. Saas-Fee Advanced Course. Springer Berlin Heidelberg, 2019. ISBN 9783662586877.
Armitage, P.J. arXiv e-prints, art. astro-ph/0701485, 2007.
Armitage, P.J. Astrophysics of Planet Formation. 2010.
Arnold, T.J., Eisner, J.A., Monnier, J.D. and Tuthill, P. ApJ, 750(2):119, 2012.
Astropy Collaboration, Robitaille, T.P., Tollerud, E.J., Greenfield, P., Droettboom, M. et al. A&A, 558:A33, 2013.
Atkinson, R., Baulch, D.L., Cox, R.A., Crowley, J.N., Hampson, R.F. et al. Atmospheric Chemistry and Physics, 4(6):1461–1738, 2004.
Auer, L. In Numerical Radiative Transfer, page 101. Cambridge Univ. Press, Cambridge, 1984.
Avenhaus, H., Quanz, S.P., Meyer, M.R., Brittain, S.D., Carr, J.S. et al. ApJ, 790(1):56, 2014.
Avramenko, L.I. and Krasnen'kov, V.M. Bulletin of the Academy of Sciences of the USSR, Division of chemical science, 15(3):394–397, 1966.
Ayliffe, B.A. and Bate, M.R. MNRAS, 397(2):657–665, 2009.
Bae, J., Teague, R., Andrews, S.M., Benisty, M., Facchini, S. et al. ApJ, 934(2):L20, 2022.
Bai, X.N. ApJ, 739(1):50, 2011.
Bai, X.N. ApJ, 845(1):75, 2017.
Bai, X.N. and Stone, J.M. ApJ, 722(2):1437–1459, 2010.
Balbus, S.A. ARA&A, 41:555–597, 2003.
Balbus, S.A. and Hawley, J.F. ApJ, 376:214, 1991.
Banzatti, A. and Pontoppidan, K.M. ApJ, 809(2):167, 2015.
Barlow, M.J. and Silk, J. ApJ, 207:131–140, 1976.
Barnard, E.E. MNRAS, 55:382, 1895.
Barr, A.C. and Canup, R.M. Icarus, 198(1):163–177, 2008.
Batygin, K. AJ, 155(4):178, 2018.
Batygin, K. and Morbidelli, A. ApJ, 894(2):143, 2020.

Baulch, D.L. Evaluated kinetic data for high temperature reactions. 1972.
Bauschlicher, Charles W., J. ApJ, 509(2):L125–L127, 1998.
Bell, R. The Tunnel Effect in Chemistry. Springer US, 1980. ISBN 9781489928917.
Benisty, M., Stolker, T., Pohl, A., de Boer, J., Lesur, G. et al. A&A, 597:A42, 2017.
Benisty, M., Bae, J., Facchini, S., Keppler, M., Teague, R. et al. ApJ, 916(1):L2, 2021.
Bergantini, A., Pilling, S., Rothard, H., Boduch, P. and Andrade, D.P.P. MNRAS, 437(3):2720–2727, 2013.
Bergantini, A., Pilling, S., Nair, B.G., Mason, N.J. and Fraser, H.J. A&A, 570:A120, 2014.
Bethell, T.J. and Bergin, E.A. ApJ, 739(2):78, 2011.
Beuther, H., Churchwell, E.B., McKee, C.F. and Tan, J.C. In Reipurth, B., Jewitt, D. and Keil, K., editors, Protostars and Planets V, page 165, 2007.
Bierson, C.J. and Nimmo, F. ApJ, 897(2):L43, 2020.
Bierson, C.J. and Steinbrügge, G. The Planetary Science Journal, 2(3):89, 2021.
Biller, B.A., Males, J., Rodigas, T., Morzinski, K., Close, L.M. et al. ApJ, 792(1):L22, 2014.
Binkert, F., Szulágyi, J. and Birnstiel, T. arXiv e-prints, art. arXiv:2103.10177, 2021.
Birnstiel, T., Klahr, H. and Ercolano, B. A&A, 539:A148, 2012.
Bisschop, S.E., Fuchs, G.W., Boogert, A.C.A., van Dishoeck, E.F. and Linnartz, H. A&A, 470(2):749–759, 2007.
Bitsch, B., Morbidelli, A., Johansen, A., Lega, E., Lambrechts, M. et al. A&A, 612:A30, 2018.
Biver, N. and Bockelée-Morvan, D. ACS Earth and Space Chemistry, 3(8):1550–1555, 2019.
Bockelée-Morvan, D. and Biver, N. Philosophical Transactions of the Royal Society of London Series A, 375 (2097):20160252, 2017.
Bockelee-Morvan, D., Colom, P., Crovisier, J., Despois, D. and Paubert, G. Nature, 350(6316):318–320, 1991.
Bohn, A.J., Kenworthy, M.A., Ginski, C., Manara, C.F., Pecaut, M.J. et al. MNRAS, 492(1):431–443, 2019.
Bonfanti, M. and Martinazzo, R. International Journal of Quantum Chemistry, 116(21):1575–1602, 2016.
Boogert, A.C.A., Gerakines, P.A. and Whittet, D.C.B. ARA&A, 53:541–581, 2015.
Booth, A.S., Walsh, C., Terwisscha van Scheltinga, J., van Dishoeck, E.F., Ilee, J.D. et al. Nature Astronomy, 5:684–690, 2021.
Booth, R.A., Clarke, C.J., Madhusudhan, N. and Ilee, J.D. MNRAS, 469(4):3994–4011, 2017.
Boschman, L., Reitsma, G., Cazaux, S., Schlathölter, T., Hoekstra, R. et al. ApJ, 761(2):L33, 2012.
Bosman, A.D., Cridland, A.J. and Miguel, Y. A&A, 632:L11, 2019.
Boss, A.P. Science, 276:1836–1839, 1997.
Boss, A.P. ApJ, 551(2):L167–L170, 2001.
Boss, A.P. ApJ, 731(1):74, 2011.
Bouwman, J., de Koter, A., Dominik, C. and Waters, L.B.F.M. A&A, 401:577–592, 2003.
Bowler, B.P. PASP, 128(968):102001, 2016.
Bowler, B.P., Andrews, S.M., Kraus, A.L., Ireland, M.J., Herczeg, G. et al. ApJ, 805:L17, 2015.
Boynton, J. In Bulletin of the American Astronomical Society, volume 14 of BAAS, page 718, 1982.
Boynton, J.E. In Bulletin of the American Astronomical Society, volume 15 of BAAS, page 857, 1983.
Brandl, B., Bettonvil, F., van Boekel, R., Glauser, A., Quanz, S. et al. The Messenger, 182:22–26, 2021.
Brandl, B.R., Absil, O., Agócs, T., Baccichet, N., Bertram, T. et al. In Ground-based and Airborne Instrumentation for Astronomy VII, volume 10702 of Society of Photo-Optical Instrumentation Engineers (SPIE) Conference Series, page 107021U, 2018.
Brennecka, G.A., Borg, L.E. and Wadhwa, M. Proceedings of the National Academy of Sciences, 110(43): 17241–17246, 2013.
Brittain, S.D., Najita, J.R. and Carr, J.S. ApJ, 702(1):85–99, 2009.
Brittain, S.D., Najita, J.R., Carr, J.S., Liskowsky, J., Troutman, M.R. et al. ApJ, 767(2):159, 2013.
Brittain, S.D., Carr, J.S., Najita, J.R., Quanz, S.P. and Meyer, M.R. ApJ, 791(2):136, 2014.
Brittain, S.D., Najita, J.R. and Carr, J.S. ApJ, 883(1):37, 2019.
Brittain, S.D., Najita, J.R., Dong, R. and Zhu, Z. ApJ, 895(1):48, 2020.
Brott, I. and Hauschildt, P.H. In Turon, C., O'Flaherty, K.S. and Perryman, M.A.C., editors, The Three-Dimensional Universe with Gaia, volume 576 of ESA Special Publication, page 565, 2005.
Brown, W.A. and Bolina, A.S. MNRAS, 374(3):1006–1014, 2006.
Bryan, M.L., Bowler, B.P., Knutson, H.A., Kraus, A.L., Hinkley, S. et al. ApJ, 827(2):100, 2016.

Bryden, G., Chen, X., Lin, D.N.C., Nelson, R.P. and Papaloizou, J.C.B. ApJ, 514(1):344–367, 1999.
Butler, R.P., Marcy, G.W., Williams, E., Hauser, H. and Shirts, P. ApJ, 474:L115–L118, 1997.
Calcino, J., Christiaens, V., Price, D.J., Pinte, C., Davis, T.M. et al. MNRAS, 498(1):639–650, 2020.
Calvet, N., D'Alessio, P., Hartmann, L., Wilner, D., Walsh, A. et al. ApJ, 568:1008–1016, 2002.
Calvet, N., D'Alessio, P., Watson, D.M., Franco-Hernández, R., Furlan, E. et al. ApJ, 630:L185–L188, 2005.
Calvin, W.M., Clark, R.N., Brown, R.H. and Spencer, J.R. Journal of Geophysical Research: Planets, 100 (E9):19041–19048, 1995.
Canup, R.M. and Ward, W.R. AJ, 124:3404–3423, 2002.
Canup, R.M. and Ward, W.R. Nature, 441:834–839, 2006.
Canup, R.M. and Ward, W.R. Origin of Europa and the Galilean Satellites, page 59. 2009.
Carlson, R., Smythe, W., Baines, K., Barbinis, E., Becker, K. et al. Science, 274(5286):385–388, 1996.
Carlson, R.W. Science, 283:820, 1999.
Carlson, R.W., Anderson, M.S., Johnson, R.E., Smythe, W.D., Hendrix, A.R. et al. Science, 283:2062, 1999.
Carmona, A., van den Ancker, M.E., Henning, T., Pavlyuchenkov, Y., Dullemond, C.P. et al. A&A, 477(3): 839–852, 2008.
Carr, M.H., Belton, M.J.S., Chapman, C.R., Davies, M.E., Geissler, P. et al. Nature, 391(6665):363–365, 1998.
Carrera, D., Raymond, S.N. and Davies, M.B. A&A, 629:L7, 2019.
Casassus, S. and Pérez, S. ApJ, 883(2):L41, 2019.
Casassus, S., van der Plas, G.M., Perez, S., Dent, W.R.F., Fomalont, E. et al. Nature, 493(7431):191–194, 2013.
Casassus, S., Cárcamo, M., Hales, A., Weber, P. and Dent, B. ApJ, 933(1):L4, 2022.
Caselli, P., Stantcheva, T. and Herbst, E. In Pfalzner, S., Kramer, C., Straubmeier, C. and Heithausen, A., editors, The Dense Interstellar Medium in Galaxies, pages 479–486, Berlin, Heidelberg, 2004. Springer Berlin Heidelberg.
Cassen, P., Reynolds, R.T. and Peale, S.J. In Bulletin of the American Astronomical Society, volume 11 of BAAS, page 601, 1979.
Cazaux, S. and Tielens, A.G.G.M. ApJ, 575:L29–L32, 2002.
Cazaux, S., Boschman, L., Rougeau, N., Reitsma, G., Hoekstra, R. et al. Scientific Reports, 6:19835, 2016.
Chaabouni, H., Baouche, S., Diana, S. and Minissale, M. A&A, 636:A4, 2020.
Chaban, G.M., Bernstein, M. and Cruikshank, D.P. Icarus, 187(2):592–599, 2007.
Charnley, S.B., Rodgers, S.D. and Ehrenfreund, P. A&A, 378:1024–1036, 2001.
Charnoz, S., Crida, A., Castillo-Rogez, J.C., Lainey, V., Dones, L. et al. Icarus, 216:535–550, 2011.
Chevalier, R.A. ApJ, 538:L151–L154, 2000.
Choukroun, M. and Grasset, O. J. Chem. Phys., 133(14):144502–144502, 2010.
Christiaens, V., Cantalloube, F., Casassus, S., Price, D.J., Absil, O. et al. ApJ, 877(2):L33, 2019.
Christiansen, J.L., Crossfield, I.J.M., Barentsen, G., Lintott, C.J., Barclay, T. et al. AJ, 155(2):57, 2018.
Chuang, K.J., Fedoseev, G., Ioppolo, S., van Dishoeck, E.F. and Linnartz, H. MNRAS, 455(2):1702–1712, 2016.
Cilibrasi, M., Szulágyi, J., Mayer, L., Drążkowska, J., Miguel, Y. et al. MNRAS, 480:4355–4368, 2018.
Clark, R.N., Swayze, G.A., Carlson, R., Grundy, W. and Noll, K. Reviews in Mineralogy and Geochemistry, 78(1):399–446, 2014.
Clarke, C.J. MNRAS, 376:1350–1356, 2007.
Collings, M.P., Anderson, M.A., Chen, R., Dever, J.W., Viti, S. et al. MNRAS, 354(4):1133–1140, 2004.
Cook, J.C., Ore, C.M.D., Protopapa, S., Binzel, R.P., Cartwright, R. et al. Icarus, 315:30–45, 2018.
Cossou, C., Raymond, S.N., Hersant, F. and Pierens, A. A&A, 569:A56, 2014.
Crida, A. and Charnoz, S. Science, 338(6111):1196, 2012.
Crida, A., Morbidelli, A. and Masset, F. Icarus, 181:587–604, 2006.
Croft, S.K., Lunine, J.I. and Kargel, J. Icarus, 73(2):279–293, 1988.
Crovisier, J., Bockelée-Morvan, D., Colom, P., Biver, N., Despois, D. et al. A&A, 418:1141–1157, 2004.
Cugno, G., Quanz, S. P., Hunziker, S., Stolker, T., Schmid, H. M. et al. A&A, 622:A156, 2019.
Currie, T., Muto, T., Kudo, T., Honda, M., Brandt, T.D. et al. ApJ, 796(2):L30, 2014.
Currie, T., Cloutier, R., Brittain, S., Grady, C., Burrows, A. et al. ApJ, 814(2):L27, 2015.

D Anderson, J., Schubert, G., Jacobson, R., Lau, E., B Moore, W. et al. Science (New York, N.Y.), 281: 2019–22, 1998.
D'Alessio, P., Canto, J., Calvet, N. and Lizano, S. ApJ, 500:411, 1998.
Dalton III, J.B., Shirley, J.H. and Kamp, L.W. Journal of Geophysical Research: Planets, 117(E3), 2012.
D'Angelo, G. Exoplanets. 2010.
D'Angelo, G. and Podolak, M. ApJ, 806(2):203, 2015.
D'Angelo, G., Henning, T. and Kley, W. A&A, 385:647–670, 2002.
Dartois, E., Schutte, W., Geballe, T.R., Demyk, K., Ehrenfreund, P. et al. A&A, 342:L32–L35, 1999.
Davidson, D., Petersen, E., Rohrig, M., Hanson, R. and Bowman, C. Symposium (International) on Combustion, 26(1):481–488, 1996.
Day, M., Thompson, K. and Dixon-Lewis, G. Symposium (International) on Combustion, 14(1):47–59, 1973.
de Pater, I. and Lissauer, J.J. Planetary Sciences. 2010.
de Sitter, W. MNRAS, 91:706–738, 1931.
de Wit, W.J. personal communication, 2020.
Deienno, R., Nesvorný, D., Vokrouhlický, D. and Yokoyama, T. AJ, 148(2):25, 2014.
Desch, S.J., Cook, J.C., Doggett, T.C. and Porter, S.B. Icarus, 202(2):694–714, 2009.
Deschamps, F., Mousis, O., Sanchez-Valle, C. and Lunine, J.I. ApJ, 724(2):887–894, 2010.
Dionatos, O., Woitke, P., Güdel, M., Degroote, P., Liebhart, A. et al. A&A, 625:A66, 2019.
Dobos, V., Charnoz, S., Pál, A., Roque-Bernard, A. and Szabó, G.M. PASP, 133(1027):094401, 2021.
Dodson-Robinson, S.E. and Salyk, C. ApJ, 738(2):131, 2011.
Dodson-Robinson, S.E., Willacy, K., Bodenheimer, P., Turner, N.J. and Beichman, C.A. Icarus, 200(2): 672–693, 2009.
Dong, R. and Fung, J. ApJ, 835(2):146, 2017.
Dong, R., Zhu, Z., Fung, J., Rafikov, R., Chiang, E. et al. ApJ, 816(1):L12, 2015a.
Dong, R., Zhu, Z., Rafikov, R.R. and Stone, J.M. ApJ, 809(1):L5, 2015b.
Dong, R., Liu, S.y., Eisner, J., Andrews, S., Fung, J. et al. ApJ, 860(2):124, 2018.
Dorschner, J., Begemann, B., Henning, T., Jaeger, C. and Mutschke, H. A&A, 300:503, 1995.
Doucet, C., Pantin, E., Lagage, P. O. and Dullemond, C. P. A&A, 460(1):117–124, 2006.
Dougherty, A.J., Bartholet, Z.T., Chumsky, R.J., Delano, K.C., Huang, X. et al. Journal of Geophysical Research (Planets), 123(12):3080–3087, 2018.
Draine, B.T. ApJS, 36:595–619, 1978.
Draine, B.T. and Bertoldi, F. ApJ, 468:269–+, 1996.
Draine, B.T. and McKee, C.F. ARA&A, 31:373–432, 1993.
Drążkowska, J. and Alibert, Y. A&A, 608:A92, 2017.
Drążkowska, J. and Szulágyi, J. ApJ, 866(2):142, 2018.
Dubrulle, B., Morfill, G. and Sterzik, M. Icarus, 114(2):237–246, 1995.
Dullemond, C.P. and Monnier, J.D. ARA&A, 48:205–239, 2010.
Durisen, R.H., Boss, A.P., Mayer, L., Nelson, A.F., Quinn, T. et al. Protostars and Planets V, pages 607–622, 2007.
Dwyer, C.A., Nimmo, F., Ogihara, M. and Ida, S. Icarus, 225(1):390–402, 2013.
Edgar, R.G., Quillen, A.C. and Park, J. MNRAS, 381(3):1280–1286, 2007.
Espaillat, C., Muzerolle, J., Najita, J., Andrews, S., Zhu, Z. et al. In Beuther, H., Klessen, R.S., Dullemond, C.P. and Henning, T., editors, Protostars and Planets VI, page 497, 2014.
Estrada, P.R., Mosqueira, I., Lissauer, J.J., D'Angelo, G. and Cruikshank, D.P. Formation of Jupiter and Conditions for Accretion of the Galilean Satellites. In Pappalardo, R.T., McKinnon, W.B. and Khurana, K.K., editors, Europa, page 27. 2009.
Fabrycky, D.C., Lissauer, J.J., Ragozzine, D., Rowe, J.F., Steffen, J.H. et al. ApJ, 790(2):146, 2014.
Fairlamb, J.R., Oudmaijer, R.D., Mendigutía, I., Ilee, J.D. and van den Ancker, M.E. MNRAS, 453(1): 976–1001, 2015.
Favre, C., Fedele, D., Semenov, D., Parfenov, S., Codella, C. et al. ApJ, 862(1):L2, 2018.
Fedele, D., Bruderer, S., van den Ancker, M.E. and Pascucci, I. ApJ, 800(1):23, 2015.
Fedele, D., Carney, M., Hogerheijde, M. R., Walsh, C., Miotello, A. et al. A&A, 600:A72, 2017.
Fedele, D., Tazzari, M., Booth, R., Testi, L., Clarke, C.J. et al. A&A, 610:A24, 2018.
Fedele, D., Toci, C., Maud, L. and Lodato, G. A&A, 651:A90, 2021.

Fedoseev, G., Ioppolo, S., Zhao, D., Lamberts, T. and Linnartz, H. MNRAS, 446(1):439–448, 2015.
Feigelson, E.D., Garmire, G.P. and Pravdo, S.H. ApJ, 572(1):335–349, 2002.
Fink, U., Dekkers, N.H. and Larson, H.P. ApJ, 179:L155, 1973.
Follette, K.B., Rameau, J., Dong, R., Pueyo, L., Close, L.M. et al. AJ, 153(6):264, 2017.
Fortney, J.J. and Nettelmann, N. Space Sci. Rev., 152:423–447, 2010.
Francis, L. and van der Marel, N. ApJ, 892(2):111, 2020.
Frank, J., King, A. and Raine, D.J. Accretion Power in Astrophysics: Third Edition. 2002.
Fressin, F., Torres, G., Charbonneau, D., Bryson, S.T., Christiansen, J. et al. ApJ, 766(2):81, 2013.
Fuchs, G.W., Cuppen, H.M., Ioppolo, S., Romanzin, C., Bisschop, S.E. et al. A&A, 505(2):629–639, 2009.
Fujii, Y.I., Okuzumi, S., Tanigawa, T. and Inutsuka, S.i. ApJ, 785:101, 2014.
Fujii, Y.I., Kobayashi, H., Takahashi, S.Z. and Gressel, O. AJ, 153(4):194, 2017.
Fujita, T., Ohtsuki, K., Tanigawa, T. and Suetsugu, R. AJ, 146(6):140, 2013.
Fulle, D., Hamann, H.F., Hippler, H. and Troe, J. The Journal of Chemical Physics, 105(3):983–1000, 1996.
Fuller, J., Luan, J. and Quataert, E. MNRAS, 458(4):3867–3879, 2016.
Fung, J. and Chiang, E. ApJ, 832(2):105, 2016.
Gaia Collaboration, Brown, A.G.A., Vallenari, A., Prusti, T., de Bruijne, J.H.J. et al. arXiv e-prints, art. arXiv:2012.01533, 2020.
Gaia Collaboration, Brown, A.G.A., Vallenari, A., Prusti, T., de Bruijne, J.H.J. et al. A&A, 649:A1, 2021.
Galilei, G. Sidereus nuncius magna, longeque admirabilia spectacula pandens lunae facie, fixis innumeris, lacteo circulo, stellis nebulosis, ... Galileo Galileo : nuper a se reperti beneficio sunt observata in apprime vero in quatuor planetis circa Iovis stellam disparibus intervallis, atque periodis, celeritate mirabili circumvolutis ... atque Medicea sidera nuncupandos decrevit. 1610. doi: 10.3931/e-rara-695.
Gálvez, O., Maté, B., Herrero, V.J. and Escribano, R. ApJ, 724(1):539–545, 2010.
Gammie, C.F. ApJ, 553(1):174–183, 2001.
Garrod, R., Park, I.H., Caselli, P. and Herbst, E. Faraday Discussions, 133:51, 2006.
Garrod, R.T. and Herbst, E. A&A, 457(3):927–936, 2006.
Garrod, R.T. and Pauly, T. ApJ, 735(1):15, 2011.
Garufi, A., Quanz, S.P., Avenhaus, H., Buenzli, E., Dominik, C. et al. A&A, 560:A105, 2013.
Garufi, A., Quanz, S. P., Schmid, H. M., Avenhaus, H., Buenzli, E. et al. A&A, 568:A40, 2014.
Gillon, M., Triaud, A.H.M.J., Demory, B.O., Jehin, E., Agol, E. et al. Nature, 542(7642):456–460, 2017.
Ginski, C., Benisty, M., van Holstein, R.G., Juhász, A., Schmidt, T.O.B. et al. A&A, 616:A79, 2018.
Gladstone, R., Retherford, K., Steffl, A., Eterno, J., Davis, M. et al. In AAS/Division for Planetary Sciences Meeting Abstracts #45, volume 45 of AAS/Division for Planetary Sciences Meeting Abstracts, page 211.04, 2013.
Glein, C.R. Icarus, 250:570–586, 2015.
Goldreich, P. and Schlichting, H.E. AJ, 147(2):32, 2014.
Goldreich, P. and Tremaine, S. ApJ, 241:425–441, 1980.
Goldreich, P., Murray, N., Longaretti, P.Y. and Banfield, D. Science, 245:500–504, 1989.
Gomes, R., Levison, H.F., Tsiganis, K. and Morbidelli, A. Nature, 435:466–469, 2005.
Gomez Casajus, L., Lainey, V., Fuller, J., Zannoni, M., Tortora, P. et al. In EPSC-DPS Joint Meeting 2019, volume 2019, pages EPSC–DPS2019–1685, 2019.
Gong, Y.X., Zhou, J.L., Xie, J.W. and Wu, X.M. ApJ, 769(1):L14, 2013.
Gonzalez, J.F., van der Plas, G., Pinte, C., Cuello, N., Nealon, R. et al. MNRAS, 499(3):3837–3856, 2020.
Gordon, S., Mulac, W. and Nangia, P. Journal of Physical Chemistry, 75:2087–2093, 1971.
Grady, C.A., Woodgate, B., Heap, S.R., Bowers, C., Nuth, J. A., I. et al. ApJ, 620(1):470–480, 2005.
Grady, C.A., Muto, T., Hashimoto, J., Fukagawa, M., Currie, T. et al. ApJ, 762(1):48, 2013.
Grasset, O., Sotin, C. and Deschamps, F. Planet. Space Sci., 48(7-8):617–636, 2000.
Grasset, O., Dougherty, M., Coustenis, A., Bunce, E., Erd, C. et al. Planet. Space Sci., 78:1–21, 2013.
Gratton, R., Ligi, R., Sissa, E., Desidera, S., Mesa, D. et al. A&A, 623:A140, 2019.
Gray, R.H. Astrobiology, 15(3):195–199, 2015.
Gray, R.O., Riggs, Q.S., Koen, C., Murphy, S.J., Newsome, I.M. et al. AJ, 154(1):31, 2017.
Gressel, O., Nelson, R.P., Turner, N.J. and Ziegler, U. ApJ, 779(1):59, 2013.
Gressel, O., Turner, N.J., Nelson, R.P. and McNally, C.P. ApJ, 801(2):84, 2015.

Grossman, A.S., Graboske, H., Pollack, J., Reynolds, R. and Summers, A. Physics of the Earth and Planetary Interiors, 6:91–98, 1972.
Guidi, G., Ruane, G., Williams, J.P., Mawet, D., Testi, L. et al. MNRAS, 479(2):1505–1513, 2018.
Gurnett, D.A., Kurth, W.S., Roux, A., Bolton, S.J. and Kennel, C.F. Nature, 384(6609):535–537, 1996.
Habing, H.J. Bull. Astron. Inst. Netherlands, 19:421, 1968.
Haffert, S.Y., Bohn, A.J., de Boer, J., Snellen, I.A.G., Brinchmann, J. et al. Nature Astronomy, 3:749–754, 2019.
Hahn, J., Krasnoperov, L., Luther, K. and Troe, J. Phys. Chem. Chem. Phys., 6:1997–1999, 2004.
Haisch, Karl E., J., Lada, E.A. and Lada, C.J. ApJ, 553:L153–L156, 2001.
Hammond, N.P., Parmenteir, E.M. and Barr, A.C. Journal of Geophysical Research: Planets, 123(12):3105–3118, 2018.
Haqq-Misra, J., Kopparapu, R.K. and Schwieterman, E. Astrobiology, 20(5):572–579, 2020.
Harris, A.W. and Kaula, W.M. Icarus, 24:516–523, 1975.
Harris, C.R., Millman, K.J., van der Walt, S.J., Gommers, R., Virtanen, P. et al. Nature, 585(7825):357–362, 2020.
Hart, M.H. Icarus, 37(1):351–357, 1979.
Hartmann, L., Ballesteros-Paredes, J. and Bergin, E.A. ApJ, 562(2):852–868, 2001.
Hartogh, P., Barabash, S., Beaudin, G., Börner, P., Bockeleé-Morvan, D. et al. In European Planetary Science Congress, pages EPSC2013–710, 2013.
Hasegawa, T.I. and Herbst, E. MNRAS, 261:83–102, 1993.
Hasegawa, T.I., Herbst, E. and Leung, C.M. ApJS, 82:167, 1992.
Hashimoto, J., Dong, R., Kudo, T., Honda, M., McClure, M.K. et al. ApJ, 758(1):L19, 2012.
Hawley, J.F., Gammie, C.F. and Balbus, S.A. ApJ, 440:742, 1995.
Hayashi, C. Progress of Theoretical Physics Supplement, 70:35–53, 1981.
Hayashi, C., Nakazawa, K. and Nakagawa, Y. In Black, D.C. and Matthews, M.S., editors, Protostars and Planets II, pages 1100–1153, 1985.
Hein Bertelsen, R.P., Kamp, I., van der Plas, G., van den Ancker, M.E., Waters, L.B.F.M. et al. A&A, 590: A98, 2016.
Heinzeller, D., Nomura, H., Walsh, C. and Millar, T.J. ApJ, 731(2):115, 2011.
Heller, R. and Pudritz, R. A&A, 578:A19, 2015.
Heller, R., Williams, D., Kipping, D., Limbach, M.A., Turner, E. et al. Astrobiology, 14(9):798–835, 2014.
Heller, R., Marleau, G.D. and Pudritz, R.E. A&A, 579:L4, 2015.
Helling, C., Dehn, M., Woitke, P. and Hauschildt, P.H. ApJ, 675(2):L105, 2008.
Helling, C., Woitke, P., Rimmer, P.B., Kamp, I., Thi, W.F. et al. Life, 4(2):142–173, 2014.
Herczeg, G.J. and Hillenbrand, L.A. ApJ, 786(2):97, 2014.
Hibbitts, C.A., Klemaszewski, J.E., McCord, T.B., Hansen, G.B. and Greeley, R. Journal of Geophysical Research: Planets, 107(E10):14–1–14–12, 2002.
Hibbitts, C.A., Pappalardo, R.T., Hansen, G.B. and McCord, T.B. Journal of Geophysical Research (Planets), 108(E5):5036, 2003.
Hidaka, H., Watanabe, N., Shiraki, T., Nagaoka, A. and Kouchi, A. ApJ, 614(2):1124–1131, 2004.
Hidaka, H., Watanabe, M., Kouchi, A. and Watanabe, N. Phys. Chem. Chem. Phys., 13:15798–15802, 2011.
Hidaka, Y., Takahashi, S., Kawano, H., Suga, M. and Gardiner, W.C. The Journal of Physical Chemistry, 86 (8):1429–1433, 1982.
Hill, G.W. On the part of the motion of the lunar perigee which is a function of the mean motions of the sun and moon. 1877.
Hill, M.L., Kane, S.R., Seperuelo Duarte, E., Kopparapu, R.K., Gelino, D.M. et al. ApJ, 860:67, 2018.
Hirama, M., Tokosumi, T., Ishida, T. and Aihara, J.i. Chemical Physics, 305(1):307–316, 2004.
Hiraoka, K., Ohashi, N., Kihara, Y., Yamamoto, K., Sato, T. et al. Chemical Physics Letters, 229(4):408–414, 1994.
Hiraoka, K., Yamashita, A., Yachi, Y., Aruga, K., Sato, T. et al. ApJ, 443:363, 1995.
Hirose, S. and Turner, N.J. ApJ, 732(2):L30, 2011.
Hoegh-Guldberg, O., Jacob, D., Taylor, M., Bindi, M., Brown, S. et al. Impacts of 1.5ºC global warming on natural and human systems. IPCC, 2018.
Hollenbach, D., Johnstone, D., Lizano, S. and Shu, F. ApJ, 428:654–669, 1994.

Homma, T., Ohtsuki, K., Maeda, N., Suetsugu, R., Machida, M.N. et al. ApJ, 903(2):98, 2020.
Honda, M., Maaskant, K., Okamoto, Y.K., Kataza, H., Fukagawa, M. et al. ApJ, 752(2):143, 2012.
Hong, Y.C., Raymond, S.N., Nicholson, P.D. and Lunine, J.I. ApJ, 852(2):85, 2018.
Hoogerwerf, R., de Bruijne, J.H.J. and de Zeeuw, P.T. A&A, 365:49–77, 2001.
Horowitz, A. J. Phys. Chem.; (United States), 89, 1985.
Hourigan, K. and Ward, W.R. Icarus, 60:29–39, 1984.
Hoyle, F. QJRAS, 1:28, 1960.
Huang, J., Andrews, S.M., Cleeves, L.I., Öberg, K.I., Wilner, D.J. et al. ApJ, 852(2):122, 2018.
Huang, J., Andrews, S.M., Dullemond, C.P., Isella, A., Pérez, L.M. et al. ApJ, 869:L42, 2018.
Hubickyj, O., Bodenheimer, P. and Lissauer, J.J. Icarus, 179(2):415–431, 2005.
Hudson, R.L. and Moore, M.H. Icarus, 140(2):451–461, 1999.
Hunter, J.D. Computing in Science & Engineering, 9(3):90–95, 2007.
Husser, T.O., Wende-von Berg, S., Dreizler, S., Homeier, D., Reiners, A. et al. A&A, 553:A6, 2013.
Hussmann, H. and Spohn, T. Icarus, 171(2):391–410, 2004.
Hussmann, H., Sohl, F. and Spohn, T. Icarus, 185(1):258–273, 2006.
Hussmann, H., Lingenauber, K., Kallenbach, R., Lüdicke, F., Enya, K. et al. In EGU General Assembly Conference Abstracts, EGU General Assembly Conference Abstracts, pages EGU22–12890, 2022.
Huynh, L.K. and Violi, A. The Journal of Organic Chemistry, 73(1):94–101, 2008.
Ikeda, M., Ohishi, M., Nummelin, A., Dickens, J.E., Bergman, P. et al. ApJ, 560(2):792–805, 2001.
Ikoma, M., Emori, H. and Nakazawa, K. ApJ, 553(2):999–1005, 2001.
Ioppolo, S., Cuppen, H.M., van Dishoeck, E.F. and Linnartz, H. MNRAS, 410(2):1089–1095, 2011.
Ireland, M.J., Kraus, A., Martinache, F., Law, N. and Hillenbrand, L.A. ApJ, 726(2):113, 2011.
Isella, A., Natta, A., Wilner, D., Carpenter, J.M. and Testi, L. ApJ, 725(2):1735–1741, 2010.
Isella, A., Pérez, L.M., Carpenter, J.M., Ricci, L., Andrews, S. et al. ApJ, 775(1):30, 2013.
Isella, A., Guidi, G., Testi, L., Liu, S., Li, H. et al. Phys. Rev. Lett., 117:251101, 2016.
Isella, A., Huang, J., Andrews, S.M., Dullemond, C.P., Birnstiel, T. et al. ApJ, 869(2):L49, 2018.
Isella, A., Benisty, M., Teague, R., Bae, J., Keppler, M. et al. ApJ, 879(2):L25, 2019.
Ishihara, D., Onaka, T., Kataza, H., Salama, A., Alfageme, C. et al. A&A, 514:A1, 2010.
Izidoro, A., Ogihara, M., Raymond, S.N., Morbidelli, A., Pierens, A. et al. MNRAS, 470(2):1750–1770, 2017.
Izidoro, A., Bitsch, B., Raymond, S.N., Johansen, A., Morbidelli, A. et al. arXiv e-prints, art. arXiv:1902.08772, 2019.
Izidoro, A., Bitsch, B., Raymond, S.N., Johansen, A., Morbidelli, A. et al. A&A, 650:A152, 2021.
Jamialahmadi, N., Ratzka, T., Panić, O., Fathivavsari, H., van Boekel, R. et al. ApJ, 865(2):137, 2018.
Javoy, S., Naudet, V., Abid, S. and Paillard, C. Experimental Thermal and Fluid Science, 27(4):371–377, 2003.
Jayawardhana, R., Fisher, R.S., Telesco, C.M., Piña, R.K., Barrado y Navascués, D. et al. AJ, 122(4):2047–2054, 2001.
Jeffreys, H. MNRAS, 83:350, 1923.
Joblin, C., Berné, O., Simon, A. and Mulas, G. In Henning, T., Grün, E. and Steinacker, J., editors, Cosmic Dust - Near and Far, volume 414 of Astronomical Society of the Pacific Conference Series, page 383, 2009.
Johansen, A. and Lambrechts, M. Annual Review of Earth and Planetary Sciences, 45(1):359–387, 2017.
Johansen, A., Oishi, J.S., Mac Low, M.M., Klahr, H., Henning, T. et al. Nature, 448(7157):1022–1025, 2007.
Johansen, A., Blum, J., Tanaka, H., Ormel, C., Bizzarro, M. et al. In Beuther, H., Klessen, R.S., Dullemond, C.P. and Henning, T., editors, Protostars and Planets VI, page 547, 2014.
Johnson, T.V. Annual Review of Earth and Planetary Sciences, 6:93–125, 1978.
Johnson, T.V., Mousis, O., Lunine, J.I. and Madhusudhan, N. ApJ, 757(2):192, 2012.
Johnstone, D., Hollenbach, D. and Bally, J. ApJ, 499(2):758–776, 1998.
Kamp, I., Tilling, I., Woitke, P., Thi, W.F. and Hogerheijde, M. Astronomy and Astrophysics, 510:A18, 2010a.
Kamp, I., Tilling, I., Woitke, P., Thi, W.F. and Hogerheijde, M. Astronomy and Astrophysics, 510:A18, 2010b.
Kamp, I., Thi, W.F., Woitke, P., Rab, C., Bouma, S. et al. A&A, 607:A41, 2017.

Kanagawa, K.D., Muto, T., Tanaka, H., Tanigawa, T., Takeuchi, T. et al. ApJ, 806(1):L15, 2015.
Kanagawa, K.D., Muto, T., Tanaka, H., Tanigawa, T., Takeuchi, T. et al. PASJ, 68(3):43, 2016.
Kane, S.R., Hinkel, N.R. and Raymond, S.N. AJ, 146(5):122, 2013.
Kargel, J.S. Icarus, 100(2):556–574, 1992.
Kargel, J.S., Kaye, J.Z., Head, J.W., Marion, G.M., Sassen, R. et al. Icarus, 148(1):226–265, 2000.
Kasper, M., Arsenault, R., Käufl, H.U., Jakob, G., Fuenteseca, E. et al. The Messenger, 169:16–20, 2017.
Keane, J.V., Tielens, A.G.G.M., Boogert, A.C.A., Schutte, W.A. and Whittet, D.C.B. A&A, 376:254–270, 2001.
Keppler, M., Benisty, M., Müller, A., Henning, T., van Boekel, R. et al. A&A, 617:A44, 2018.
Keppler, M., Teague, R., Bae, J., Benisty, M., Henning, T. et al. A&A, 625:A118, 2019.
Khalafinejad, S., Maaskant, K.M., Mariñas, N. and Tielens, A.G.G.M. A&A, 587:A62, 2016.
Khurana, K.K., Kivelson, M.G., Stevenson, D.J., Schubert, G., Russell, C.T. et al. Nature, 395(6704):777–780, 1998.
Kipping, D., Bryson, S., Burke, C., Christiansen, J., Hardegree-Ullman, K. et al. Nature Astronomy, 6: 367–380, 2022.
Kirk, R. and Stevenson, D. Icarus, 69(1):91–134, 1987.
Kivelson, M.G., Khurana, K.K., Russell, C.T., Walker, R.J., Warnecke, J. et al. Nature, 384(6609):537–541, 1996.
Kivelson, M.G., Khurana, K.K., Russell, C.T., Volwerk, M., Walker, R.J. et al. Science, 289(5483):1340–1343, 2000.
Kivelson, M.G., Khurana, K.K. and Volwerk, M. Icarus, 157(2):507–522, 2002.
Kley, W. MNRAS, 303:696–710, 1999.
Kley, W. and Nelson, R.P. ARA&A, 50:211–249, 2012.
Kley, W., D'Angelo, G. and Henning, T. ApJ, 547(1):457–464, 2001.
Kluska, J., Berger, J.P., Malbet, F., Lazareff, B., Benisty, M. et al. A&A, 636:A116, 2020.
Knez, C., Boogert, A.C.A., Pontoppidan, K.M., Kessler-Silacci, J., van Dishoeck, E.F. et al. ApJ, 635(2): L145–L148, 2005.
Kohler, S. Habitable Moons Instead of Habitable Planets? AAS Nova Highlight, 29 Aug 2018, id.4001, 2018.
Korycansky, D.G., Bodenheimer, P. and Pollack, J. Icarus, 92, 1991.
Kovalevsky, J. In Dollfus, A., editor, Surfaces and Interiors of Planets and Satellites, pages 1–44, 1970.
Kraus, A.L. and Ireland, M.J. ApJ, 745:5, 2012.
Kroupa, P. Science, 295:82–91, 2002.
Kruijer, T.S., Burkhardt, C., Budde, G. and Kleine, T. Proceedings of the National Academy of Sciences, 114 (26):6712–6716, 2017.
Kuiper, G.P. Proceedings of the National Academy of Science, 37:1–14, 1951.
Kuiper, G.P. AJ, 62:245–245, 1957.
Kuramoto, K. and Matsui, T. Journal of Geophysical Research: Planets, 99(E10):21183–21200, 1994.
Kurylo, M.J. The Journal of Physical Chemistry, 76(24):3518–3526, 1972.
Kuskov, O.L. and Kronrod, V.A. Icarus, 177(2):550–569, 2005.
Lagage, P.O., Pel, J.W., Authier, M., Belorgey, J., Claret, A. et al. The Messenger, 117:12–16, 2004.
Lagrange, A.M., Bonnefoy, M., Chauvin, G., Apai, D., Ehrenreich, D. et al. Science, 329:57, 2010.
Lainey, V., Jacobson, R.A., Tajeddine, R., Cooper, N.J., Murray, C. et al. Icarus, 281:286–296, 2017.
Lambrechts, M. and Johansen, A. A&A, 544:A32, 2012.
Lambrechts, M. and Johansen, A. A&A, 572:A107, 2014.
Lambrechts, M., Morbidelli, A., Jacobson, S.A., Johansen, A., Bitsch, B. et al. A&A, 627:A83, 2019.
Lari, G., Saillenfest, M. and Fenucci, M. In EPSC-DPS Joint Meeting 2019, volume 2019, pages EPSC–DPS2019–2017, 2019.
Lari, G., Saillenfest, M. and Fenucci, M. A&A, 639:A40, 2020.
Lee, T., Papanastassiou, D.A. and Wasserburg, G.J. Geophysical Research Letters, 3(2):109–112, 1976.
Leinert, C., van Boekel, R., Waters, L.B.F.M., Chesneau, O., Malbet, F. et al. A&A, 423:537–548, 2004.
Leleu, A., Alibert, Y., Hara, N.C., Hooton, M.J., Wilson, T.G. et al. A&A, 649:A26, 2021.
Leliwa-Kopystyński, J., Maruyama, M. and Nakajima, T. Icarus, 159(2):518–528, 2002.
Lewis, J.S. Icarus, 16:241–252, 1972.
Li, A. and Draine, B.T. ApJ, 554:778–802, 2001.

Li, D., Telesco, C.M., Zhang, H., Wright, C.M., Pantin, E. et al. MNRAS, 473(2):1427–1437, 2018.
Li, X., Heays, A.N., Visser, R., Ubachs, W., Lewis, B.R. et al. A&A, 555:A14, 2013.
Ligi, R., Vigan, A., Gratton, R., de Boer, J., Benisty, M. et al. MNRAS, 473(2):1774–1783, 2018.
Lin, D.N.C. and Papaloizou, J. ApJ, 309:846–857, 1986.
Lin, D.N.C. and Papaloizou, J.C.B. In Levy, E.H. and Lunine, J.I., editors, Protostars and Planets III, pages 749–835, 1993.
Lissauer, J.J., Ragozzine, D., Fabrycky, D.C., Steffen, J.H., Ford, E.B. et al. ApJS, 197(1):8, 2011.
Liu, B., Zhang, X., Lin, D.N.C. and Aarseth, S.J. ApJ, 798(1):62, 2015.
Liu, B., Raymond, S.N. and Jacobson, S.A. Nature, 604(7907):643–646, 2022.
Liu, S.F., Jin, S., Li, S., Isella, A. and Li, H. ApJ, 857(2):87, 2018.
Liu, W.M., Hinz, P.M., Meyer, M.R., Mamajek, E.E., Hoffmann, W.F. et al. ApJ, 598(2):L111–L114, 2003.
Liu, Y. and Sander, S. The journal of physical chemistry. A, 119, 2015.
Lodders, K. ApJ, 591(2):1220–1247, 2003.
Long, F., Pinilla, P., Herczeg, G.J., Harsono, D., Dipierro, G. et al. ApJ, 869(1):17, 2018.
Long, Z.C., Fernandes, R.B., Sitko, M., Wagner, K., Muto, T. et al. ApJ, 838(1):62, 2017.
Lopes, R.M., Kamp, L.W., Smythe, W.D., Mouginis-Mark, P., Kargel, J. et al. Icarus, 169(1):140–174, 2004.
Lubow, S.H. and D'Angelo, G. ApJ, 641(1):526–533, 2006.
Lubow, S.H. and Martin, R.G. ApJ, 749(2):L37, 2012.
Lubow, S.H., Seibert, M. and Artymowicz, P. ApJ, 526(2):1001–1012, 1999.
Lubow, S.H., Bate, M.R., Ogilvie, G.I. and Miller, K.A. In AAS/Division of Dynamical Astronomy Meeting #34, volume 34 of AAS/Division of Dynamical Astronomy Meeting, page 06.08, 2003.
Lucchitta, B.K. Icarus, 44(2):481–501, 1980.
Lunine, J.I. and Stevenson, D.J. Icarus, 52:14–39, 1982.
Lynden-Bell, D. and Pringle, J.E. MNRAS, 168:603–637, 1974.
Lynn, W.T. The Observatory, 26:254–256, 1903.
Lyot, B. L'Astronomie, 67:3, 1953.
Lyra, W. and Klahr, H. A&A, 527:A138, 2011.
Maaskant, K.M., Honda, M., Waters, L.B.F.M., Tielens, A.G.G.M., Dominik, C. et al. A&A, 555:A64, 2013.
Maaskant, K.M., Min, M., Waters, L.B.F.M. and Tielens, A.G.G.M. A&A, 563:A78, 2014.
MacDonald, M.G. and Dawson, R.I. AJ, 156(5):228, 2018.
Machida, M.N., Kokubo, E., Inutsuka, S.i. and Matsumoto, T. ApJ, 685(2):1220–1236, 2008.
Machida, M.N., Kokubo, E., Inutsuka, S.I. and Matsumoto, T. MNRAS, 405(2):1227–1243, 2010.
Macías, E., Anglada, G., Osorio, M., Torrelles, J.M., Carrasco-González, C. et al. ApJ, 838(2):97, 2017.
Madeira, G., Izidoro, A. and Giuliatti Winter, S.M. MNRAS, 504(2):1854–1872, 2021.
Magee, B. and Waite, J. In Lunar and planetary science conference, number 1964, page 2974, 2017.
Makalkin, A.B., Dorofeeva, V.A. and Ruskol, E.L. Solar System Research, 33:456, 1999.
Malfait, K., Waelkens, C., Waters, L.B.F.M., Vand enbussche, B., Huygen, E. et al. A&A, 332:L25–L28, 1998.
Mamajek, E.E. In T. Usuda, M. Tamura, & M. Ishii, editor, American Institute of Physics Conference Series, volume 1158 of American Institute of Physics Conference Series, pages 3–10, 2009.
Mamajek, E.E., Quillen, A.C., Pecaut, M.J., Moolekamp, F., Scott, E.L. et al. AJ, 143:72, 2012.
Mandt, K.E., Mousis, O., Lunine, J. and Gautier, D. ApJ, 788(2):L24, 2014.
Mariñas, N., Telesco, C.M., Fisher, R.S. and Packham, C. ApJ, 737(2):57, 2011.
Marius, S. Mundus Iovialis: anno MDCIX detectus ope perspicilli Belgici, hoc est, quatuor Jovialium planetarum, cum theoria, tum tabulæ ... Sumptibus & typis Iohannis Lauri, 1614.
Marley, M.S., Fortney, J.J., Hubickyj, O., Bodenheimer, P. and Lissauer, J.J. ApJ, 655(1):541–549, 2007.
Marois, C., Macintosh, B., Barman, T., Zuckerman, B., Song, I. et al. Science, 322:1348, 2008.
Marsh, K.A. and Mahoney, M.J. ApJ, 395:L115–L118, 1992.
Martí, J.G., Giuppone, C.A. and Beaugé, C. MNRAS, 433:928–934, 2013.
Martin, R.G. and Lubow, S.H. In AAS/Division for Extreme Solar Systems Abstracts, page 33.11, 2011.
Martin, R.G. and Lubow, S.H. MNRAS, 413(2):1447–1461, 2011.
Matsumoto, Y., Nagasawa, M. and Ida, S. Icarus, 221(2):624–631, 2012.
Mayor, M. and Queloz, D. Nature, 378(6555):355–359, 1995.
McCaughrean, M.J. and O'dell, C.R. AJ, 111:1977, 1996.

McCord, T.B., Carlson, R., Smythe, W., Hansen, G., Clark, R. et al. Science, 278:271–275, 1997.
McElroy, D., Walsh, C., Markwick, A.J., Cordiner, M.A., Smith, K. et al. A&A, 550:A36, 2013.
McGrath, M.A., Lellouch, E., Strobel, D.F., Feldman, P.D. and Johnson, R.E. Satellite atmospheres. In Bagenal, F., Dowling, T.E. and McKinnon, W.B., editors, Jupiter. The Planet, Satellites and Magnetosphere, volume 1, pages 457–483. 2004.
McKay, C.P., Scattergood, T.W., Pollack, J.B., Borucki, W.J. and van Ghyseghem, H.T. Nature, 332(6164): 520–522, 1988.
McKinnon, W.B. Icarus, 130(2):540 – 543, 1997.
McKinnon, W.B. Formation and early evolution of Io, pages 61–88. Springer Berlin Heidelberg, Berlin, Heidelberg, 2007. ISBN 978-3-540-48841-5. doi: 10.1007/978-3-540-48841-5_4. URL https://doi.org/10.1007/978-3-540-48841-5_4.
McNeil, D.S. and Nelson, R.P. MNRAS, 401(3):1691–1708, 2010.
Meeus, G., Waters, L.B.F.M., Bouwman, J., van den Ancker, M.E., Waelkens, C. et al. A&A, 365:476–490, 2001.
Meeus, G., Montesinos, B., Mendigutía, I., Kamp, I., Thi, W.F. et al. A&A, 544:A78, 2012.
Mendigutía, I., Oudmaijer, R.D., Garufi, A., Lumsden, S.L., Huélamo, N. et al. A&A, 608:A104, 2017.
Mennella, V., Hornekær, L., Thrower, J. and Accolla, M. ApJ, 745(1):L2, 2012.
Menu, J., van Boekel, R., Henning, T., Leinert, C., Waelkens, C. et al. A&A, 581:A107, 2015.
Mertens, J., Kalitan, D., Barrett, A. and Petersen, E. Proceedings of The Combustion Institute - PROC COMBUST INST, 32:295–303, 2009.
Mesa, D., Langlois, M., Garufi, A., Gratton, R., Desidera, S. et al. MNRAS, 488(1):37–46, 2019.
Miguel, Y. and Ida, S. Icarus, 266:1–14, 2016.
Miles, H. Journal of the British Astronomical Association, 83:192–195, 1973.
Miley, J.M., Panić, O., Haworth, T.J., Pascucci, I., Wyatt, M. et al. MNRAS, 485(1):739–752, 2019.
Mills, S.M., Clark Fabrycky, D., Migaszewski, C., Ford, E.B., Petigura, E. et al. In AAS/Division for Extreme Solar Systems Abstracts, volume 47 of AAS/Division for Extreme Solar Systems Abstracts, page 103.05, 2015.
Min, M., Dullemond, C.P., Kama, M. and Dominik, C. Icarus, 212(1):416–426, 2011.
Min, M., Rab, C., Woitke, P., Dominik, C. and Ménard, F. A&A, 585:A13, 2016a.
Min, M., Rab, C., Woitke, P., Dominik, C. and Ménard, F. A&A, 585:A13, 2016b.
Mitchell, T.R. and Stewart, G.R. AJ, 142(5):168, 2011.
Momose, M., Morita, A., Fukagawa, M., Muto, T., Takeuchi, T. et al. PASJ, 67(5):83, 2015.
Moore, J.M., Chapman, C.R., Bierhaus, E.B., Greeley, R., Chuang, F.C. et al. Callisto. In Bagenal, F., Dowling, T.E. and McKinnon, W.B., editors, Jupiter. The Planet, Satellites and Magnetosphere, volume 1, pages 397–426. 2004.
Moore, M., Ferrante, R., Hudson, R. and Stone, J. Icarus, 190(1):260–273, 2007.
Morabito, L.A., Synnott, S.P., Kupferman, P.N. and Collins, S.A. Science, 204:972, 1979.
Moraes, R.A., Kley, W. and Vieira Neto, E. MNRAS, 475(1):1347–1362, 2018.
Morbidelli, A. and Nesvorny, D. A&A, 546:A18, 2012.
Morbidelli, A., Szulágyi, J., Crida, A., Lega, E., Bitsch, B. et al. Icarus, 232:266–270, 2014.
Mordasini, C. A&A, 558:A113, 2013.
Mordasini, C., Alibert, Y., Klahr, H. and Henning, T. A&A, 547:A111, 2012.
Mordasini, C., Marleau, G.D. and Mollière, P. A&A, 608:A72, 2017.
Mori, S., Bai, X.N. and Okuzumi, S. ApJ, 872(1):98, 2019.
Morii, Y., Tsuboi, N., Koshi, M., Ogawa, H., Hayashi, A.K. et al. Science and Technology of Energetic Materials, 70:117–121, 2009.
Moroz, V.I. Soviet Ast., 9:999, 1966.
Morrison, D. Icarus, 19:1–14, 1973.
Mosqueira, I. and Estrada, P.R. Icarus, 163:198–231, 2003a.
Mosqueira, I. and Estrada, P.R. Icarus, 163:232–255, 2003b.
Mosqueira, I., Estrada, P. and Turrini, D. Space Sci. Rev., 153:431–446, 2010.
Moullet, A., Gurwell, M.A., Lellouch, E. and Moreno, R. Icarus, 208:353–365, 2010.
Mousis, O. and Alibert, Y. A&A, 448(2):771–778, 2006.
Mousis, O., Alibert, Y., Sekine, Y., Sugita, S. and Matsui, T. A&A, 459(3):965–968, 2006.

Mousis, O., Lunine, J.I., Thomas, C., Pasek, M., Marbœuf, U. et al. ApJ, 691(2):1780–1786, 2009.
Mousis, O., Ronnet, T. and Lunine, J.I. ApJ, 875(1):9, 2019.
Mulders, G.D., Paardekooper, S.J., Panić, O., Dominik, C., van Boekel, R. et al. A&A, 557:A68, 2013.
Müller, A., Keppler, M., Henning, T., Samland, M., Chauvin, G. et al. A&A, 617:L2, 2018.
Müller, J., Savvidou, S. and Bitsch, B. A&A, 650:A185, 2021.
Mumma, M.J., Hoban, S., Reuter, D.C. and Disanti, M. In AAS/DPS Meeting Abstracts #25, volume 25 of AAS/DPS Meeting Abstracts, page 14.10, 1993.
Muto, T., Grady, C.A., Hashimoto, J., Fukagawa, M., Hornbeck, J.B. et al. ApJ, 748(2):L22, 2012.
Namouni, F. ApJ, 719:L145–L147, 2010.
Naud, M.E., Artigau, É., Doyon, R., Malo, L., Gagné, J. et al. AJ, 154(3):129, 2017.
Nayakshin, S., Tsukagoshi, T., Hall, C., Vazan, A., Helled, R. et al. arXiv e-prints, art. arXiv:2004.10094, 2020.
Nealon, R., Cuello, N., Gonzalez, J.F., van der Plas, G., Pinte, C. et al. MNRAS, 499(3):3857–3867, 2020.
Neichel, B., Mouillet, D., Gendron, E., Correia, C., Sauvage, J.F. et al. In Di Matteo, P., Billebaud, F., Herpin, F., Lagarde, N., Marquette, J.B. et al, editors, SF2A-2018: Proceedings of the Annual meeting of the French Society of Astronomy and Astrophysics, page Di, 2018.
Neuhäuser, R., Guenther, E.W., Wuchterl, G., Mugrauer, M., Bedalov, A. et al. A&A, 435(1):L13–L16, 2005.
Nielsen, E.L., De Rosa, R.J., Macintosh, B., Wang, J.J., Ruffio, J.B. et al. AJ, 158(1):13, 2019.
Niemann, H.B., Atreya, S.K., Carignan, G.R., Donahue, T.M., Haberman, J.A. et al. Science, 272(5263): 846–849, 1996.
Nimmo, F. and Korycansky, D. Icarus, 219(1):508–510, 2012.
Nimmo, F. and Pappalardo, R.T. Journal of Geophysical Research: Planets, 121(8):1378–1399, 2016.
Nomura, H., Tsukagoshi, T., Kawabe, R., Ishimoto, D., Okuzumi, S. et al. ApJ, 819(1):L7, 2016.
Norfolk, B.J., Pinte, C., Calcino, J., Hammond, I., van der Marel, N. et al. ApJ, 936(1):L4, 2022.
Oba, Y., Watanabe, N., Kouchi, A., Hama, T. and Pirronello, V. ApJ, 712(2):L174–L178, 2010.
Öberg, K.I. and Wordsworth, R. AJ, 158(5):194, 2019.
Öberg, K.I., Garrod, R.T., van Dishoeck, E.F. and Linnartz, H. A&A, 504(3):891–913, 2009.
Oberg, N., Kamp, I., Cazaux, S. and Rab, C. A&A, 638:A135, 2020.
Oberg, N., Kamp, I., Cazaux, S., Rab, C. and Czoske, O. arXiv e-prints, art. arXiv:2212.03007, 2022a.
Oberg, N., Kamp, I., Cazaux, S., Woitke, P. and Thi, W.F. arXiv e-prints, art. arXiv:2208.11053, 2022b.
Ogihara, M. and Ida, S. ApJ, 699(1):824–838, 2009.
Ogihara, M. and Ida, S. ApJ, 753:60, 2012.
Ogihara, M., Kokubo, E., Suzuki, T.K. and Morbidelli, A. A&A, 615:A63, 2018.
Ohno, K. and Ueda, T. A&A, 651:L2, 2021.
Ojakangas, G.W. and Stevenson, D.J. Icarus, 81(2):220 – 241, 1989.
Okamoto, Y.K., Kataza, H., Honda, M., Yamashita, T., Fujiyoshi, T. et al. AJ, 154(1):16, 2017.
Ormel, C.W., Liu, B. and Schoonenberg, D. A&A, 604:A1, 2017a.
Ormel, C.W., Liu, B. and Schoonenberg, D. A&A, 604:A1, 2017b.
Osborn, H.P., Rodriguez, J.E., Kenworthy, M.A., Kennedy, G.M., Mamajek, E.E. et al. MNRAS, 471, 2017.
Osorio, M., Anglada, G., Carrasco-González, C., Torrelles, J.M., Macías, E. et al. ApJ, 791(2):L36, 2014.
Owen, J.E. and Menou, K. ApJ, 819(1):L14, 2016.
Owen, T., Mahaffy, P., Niemann, H.B., Atreya, S., Donahue, T. et al. Nature, 402(6759):269–270, 1999.
Owen, T.C. Planet. Space Sci., 48(7-8):747–752, 2000.
Paardekooper, S.J. A&A, 462(1):355–369, 2007.
Palla, F. and Stahler, S.W. ApJ, 540(1):255–270, 2000.
Panić, O., Hogerheijde, M.R., Wilner, D. and Qi, C. A&A, 491(1):219–227, 2008.
Panić, O., Ratzka, T., Mulders, G.D., Dominik, C., van Boekel, R. et al. A&A, 562:A101, 2014.
Pappalardo, R., McKinnon, W., Khurana, K. and Institute, L. Europa. Space Science Series. University of Arizona Press, 2009. ISBN 9780816528448.
Parisi, M., Finocchiaro, S. and Iess, L. In EGU General Assembly Conference Abstracts, EGU General Assembly Conference Abstracts, page 11912, 2012.
Pascucci, I. and Tachibana, S. The Clearing of Protoplanetary Disks and of the Protosolar Nebula, pages 263–298. 2010.
Peale, S.J. and Canup, R.M. The Origin of the Natural Satellites, pages 559–604. 2015.

Peale, S.J. and Lee, M.H. Science, 298(5593):593–597, 2002.
Peale, S.J., Cassen, P. and Reynolds, R.T. Science, 203(4383):892–894, 1979.
Pérez, L.M., Carpenter, J.M., Andrews, S.M., Ricci, L., Isella, A. et al. Science, 353(6307):1519–1521, 2016.
Pérez, S., Casassus, S., Baruteau, C., Dong, R., Hales, A. et al. The Astronomical Journal, 158(1):15, 2019.
Pérez, S., Casassus, S., Hales, A., Marino, S., Cheetham, A. et al. ApJ, 889(1):L24, 2020.
Perrone, G., Unpingco, J. and Lu, H.m. arXiv e-prints, art. arXiv:2006.04951, 2020.
Petigura, E.A., Howard, A.W. and Marcy, G.W. Proceedings of the National Academy of Science, 110(48): 19273–19278, 2013.
Petit dit de la Roche, D.J.M., van den Ancker, M.E., Kissler-Patig, M., Ivanov, V.D. and Fedele, D. MNRAS, 491(2):1795–1799, 2020.
Petit dit de la Roche, D.J.M., Oberg, N., van den Ancker, M.E., Kamp, I., van Boekel, R. et al. A&A, 648: A92, 2021.
Pfalzner, S. A&A, 549:A82, 2013.
Pfalzner, S., Steinhausen, M. and Menten, K. ApJ, 793(2):L34, 2014.
Piccioni, G., Langevin, Y., Filacchione, G., Poulet, F., Tosi, F. et al. In EGU General Assembly Conference Abstracts, EGU General Assembly Conference Abstracts, page 10925, 2014.
Pickering, W.H. and Shapley, H. Annals of Harvard College Observatory, 82:61–74, 1937.
Piétu, V., Dutrey, A., Guilloteau, S., Chapillon, E. and Pety, J. A&A, 460(3):L43–L47, 2006.
Pilcher, C.B., Ridgway, S.T. and McCord, T.B. Science, 178:1087–1089, 1972.
Pineda, J.E., Quanz, S.P., Meru, F., Mulders, G.D., Meyer, M.R. et al. ApJ, 788(2):L34, 2014.
Pineda, J.E., Szulágyi, J., Quanz, S.P., van Dishoeck, E.F., Garufi, A. et al. ApJ, 871(1):48, 2019.
Pinilla, P., Benisty, M. and Birnstiel, T. A&A, 545:A81, 2012.
Pinilla, P., Birnstiel, T., Benisty, M., Ricci, L., Natta, A. et al. A&A, 554:A95, 2013.
Pinilla, P., Birnstiel, T. and Walsh, C. A&A, 580:A105, 2015.
Pinte, C., Harries, T.J., Min, M., Watson, A.M., Dullemond, C.P. et al. A&A, 498:967–980, 2009.
Pinte, C., Price, D.J., Ménard, F., Duchêne, G., Dent, W.R.F. et al. ApJ, 860(1):L13, 2018.
Plummer, H.C. MNRAS, 71:460–470, 1911.
Pohl, A., Benisty, M., Pinilla, P., Ginski, C., de Boer, J. et al. ApJ, 850(1):52, 2017.
Pollack, J.B. and Fanale, F. In Satellites of Jupiter, pages 872–910, 1982.
Pollack, J.B. and Reynolds, R.T. Icarus, 21:248–253, 1974.
Pollack, J.B., Hubickyj, O., Bodenheimer, P., Lissauer, J.J., Podolak, M. et al. Icarus, 124(1):62–85, 1996.
Porco, C.C., Helfenstein, P., Thomas, P.C., Ingersoll, A.P., Wisdom, J. et al. Science, 311(5766):1393–1401, 2006.
Portegies Zwart, S. A&A, 622:A69, 2019.
Portegies Zwart, S., Pelupessy, I., van Elteren, A., Wijnen, T.P.G. and Lugaro, M. A&A, 616:A85, 2018.
Portegies Zwart, S.F. ApJ, 696:L13–L16, 2009.
Portilla-Revelo, B., Kamp, I., Rab, C., van Dishoeck, E.F., Keppler, M. et al. A&A, 658:A89, 2022.
Preibisch, T., Kim, Y.C., Favata, F., Feigelson, E.D., Flaccomio, E. et al. ApJS, 160(2):401–422, 2005.
Price-Whelan, A.M., Sipőcz, B.M., Günther, H.M., Lim, P.L., Crawford, S.M. et al. AJ, 156:123, 2018.
Pringle, J.E. ARA&A, 19:137–162, 1981.
Pyerin, M.A., Delage, T.N., Kurtovic, N.T., Gárate, M., Henning, T. et al. A&A, 656:A150, 2021.
Qasim, D., Lamberts, T., He, J., Chuang, K.J., Fedoseev, G. et al. A&A, 626:A118, 2019.
Quanz, S.P., Amara, A., Meyer, M.R., Kenworthy, M.A., Kasper, M. et al. ApJ, 766(1):L1, 2013a.
Quanz, S.P., Avenhaus, H., Buenzli, E., Garufi, A., Schmid, H.M. et al. ApJ, 766(1):L2, 2013b.
Quanz, S.P., Amara, A., Meyer, M.R., Girard, J.H., Kenworthy, M.A. et al. ApJ, 807(1):64, 2015.
Quillen, A.C. ApJ, 640(2):1078–1085, 2006.
Quillen, A.C. and Trilling, D.E. ApJ, 508(2):707–713, 1998.
Rab, C., Kamp, I., Ginski, C., Oberg, N., Muro-Arena, G.A. et al. A&A, 624:A16, 2019.
Rafikov, R.R. ApJ, 837(2):163, 2017.
Raman, A., Lisanti, M., Wilner, D.J., Qi, C. and Hogerheijde, M. AJ, 131(4):2290–2293, 2006.
Rameau, J., Follette, K.B., Pueyo, L., Marois, C., Macintosh, B. et al. AJ, 153(6):244, 2017.
Ramsay, S., Casali, M., Amico, P., Bezawada, N., Cirasuolo, M. et al. In Evans, C.J., Simard, L. and Takami, H., editors, Ground-based and Airborne Instrumentation for Astronomy VII, volume 10702 of Society of Photo-Optical Instrumentation Engineers (SPIE) Conference Series, page 107021P, 2018.

Ratzka, T., Leinert, C., Henning, T., Bouwman, J., Dullemond, C.P. et al. A&A, 471(1):173–185, 2007.
Rauls, E. and Hornekær, L. ApJ, 679(1):531–536, 2008.
Raymond, S.N., Barnes, R. and Mandell, A.M. MNRAS, 384(2):663–674, 2008.
Reboussin, L., Wakelam, V., Guilloteau, S. and Hersant, F. MNRAS, 440(4):3557–3567, 2014.
Reggiani, M., Quanz, S.P., Meyer, M.R., Pueyo, L., Absil, O. et al. ApJ, 792(1):L23, 2014.
Reggiani, M., Christiaens, V., Absil, O., Mawet, D., Huby, E. et al. A&A, 611:A74, 2018.
Rein, H. and Liu, S.F. A&A, 537:A128, 2012.
Remus, F., Mathis, S., Zahn, J.P. and Lainey, V. A&A, 541:A165, 2012.
Ribas, I., Guinan, E.F., Güdel, M. and Audard, M. ApJ, 622:680–694, 2005.
Rice, W.K.M., Armitage, P.J., Wood, K. and Lodato, G. MNRAS, 373(4):1619–1626, 2006a.
Rice, W.K.M., Armitage, P.J., Wood, K. and Lodato, G. MNRAS, 373(4):1619–1626, 2006b.
Richling, S. and Yorke, H.W. ApJ, 539:258–272, 2000.
Rivier, G., Crida, A., Morbidelli, A. and Brouet, Y. A&A, 548:A116, 2012.
Röllig, M., Abel, N.P., Bell, T., Bensch, F., Black, J. et al. A&A, 467(1):187–206, 2007.
Rømer, O.C. Philosophical Transactions of the Royal Society of London Series I, 12:893–894, 1677.
Ronnet, T. and Johansen, A. arXiv e-prints, art. arXiv:1912.04765, 2019.
Ronnet, T. and Johansen, A. A&A, 633:A93, 2020.
Ronnet, T., Mousis, O. and Vernazza, P. ApJ, 845(2):92, 2017.
Ronnet, T., Mousis, O., Vernazza, P., Lunine, J.I. and Crida, A. AJ, 155:224, 2018.
Rosotti, G.P., Benisty, M., Juhász, A., Teague, R., Clarke, C. et al. MNRAS, 491(1):1335–1347, 2020.
Roth, L., Ivchenko, N., Gladstone, G.R., Saur, J., Grodent, D. et al. Nature Astronomy, 5:1043–1051, 2021.
Ruaud, M., Loison, J.C., Hickson, K.M., Gratier, P., Hersant, F. et al. MNRAS, 447(4):4004–4017, 2015.
Ruaud, M., Wakelam, V. and Hersant, F. MNRAS, 459(4):3756–3767, 2016.
Ruelle, P., Kesselring, U.W. and Nam-Tran, H. Journal of the American Chemical Society, 108(3):371–375, 1986.
Ruffle, D.P., Hartquist, T.W., Caselli, P. and Williams, D.A. MNRAS, 306(3):691–695, 1999.
Ruskol, E.L. Soviet Ast., 4:657, 1961.
Safronov, V.S. Evolution of the protoplanetary cloud and formation of the earth and planets. 1972.
Sagan, C. Pale Blue Dot: A Vision of the Human Future in Space. Random House, 1994. ISBN 9780679438410.
Sakai, N., Saruwatari, O., Sakai, T., Takano, S. and Yamamoto, S. A&A, 512:A31, 2010.
Salaris, M. and Cassisi, S. Evolution of Stars and Stellar Populations. Wiley, 2005. ISBN 9780470092224.
Sánchez, M.B., de Elía, G.C. and Downes, J.J. A&A, 663:A20, 2022.
Sasaki, T., Stewart, G.R. and Ida, S. ApJ, 714(2):1052–1064, 2010.
Saur, J., Duling, S., Roth, L., Jia, X., Strobel, D.F. et al. Journal of Geophysical Research (Space Physics), 120(3):1715–1737, 2015.
Savage, B.D. and Sembach, K.R. ARA&A, 34:279–330, 1996.
Schaller, G., Schaerer, D., Meynet, G. and Maeder, A. A&AS, 96:269, 1992.
Schindhelm, E., France, K., Herczeg, G.J., Bergin, E., Yang, H. et al. ApJ, 756(1):L23, 2012.
Schneider, P.C., Dougados, C., Whelan, E.T., Eislöffel, J., Günther, H.M. et al. arXiv e-prints, art. arXiv:2006.00573, 2020.
Schoonenberg, D., Liu, B., Ormel, C.W. and Dorn, C. A&A, 627:A149, 2019.
Schubert, G., Anderson, J.D., Spohn, T. and McKinnon, W.B. Interior composition, structure and dynamics of the Galilean satellites, pages 281–306. 2004.
Schulik, M., Johansen, A., Bitsch, B., Lega, E. and Lambrechts, M. A&A, 642:A187, 2020.
Schutte, W.A., Boogert, A.C.A., Tielens, A.G.G.M., Whittet, D.C.B., Gerakines, P.A. et al. A&A, 343: 966–976, 1999.
Sekine, Y., Genda, H., Sugita, S., Kadono, T. and Matsui, T. Nature Geoscience, 4(6):359–362, 2011.
Sekine, Y., Genda, H., Muto, Y., Sugita, S., Kadono, T. et al. Icarus, 243:39–47, 2014.
Sellevag, S.R., Georgievskii, Y. and Miller, J.A. The Journal of Physical Chemistry A, 112(23):5085–5095, 2008.
Shabram, M. and Boley, A.C. ApJ, 767(1):63, 2013.
Shakura, N.I. and Sunyaev, R.A. A&A, 24:337–355, 1973.
Shibaike, Y., Okuzumi, S., Sasaki, T. and Ida, S. ApJ, 846(1):81, 2017.

Shibaike, Y., Ormel, C.W., Ida, S., Okuzumi, S. and Sasaki, T. ApJ, 885(1):79, 2019.
Showman, A.P. and Malhotra, R. Icarus, 127(1):93–111, 1997.
Showman, A.P. and Malhotra, R. Science, 296(5437):77–84, 1999.
Showman, A.P., Stevenson, D.J. and Malhotra, R. Icarus, 129(2):367 – 383, 1997.
Showman, A.P., Mosqueira, I. and Head, J.W. Icarus, 172(2):625–640, 2004.
Siebenmorgen, R. and Heymann, F. A&A, 539:A20, 2012.
Siess, L., Dufour, E. and Forestini, M. A&A, 358:593–599, 2000.
Sissa, E., Gratton, R., Garufi, A., Rigliaco, E., Zurlo, A. et al. A&A, 619:A160, 2018.
Slade, R. Global warming of 1.5 c. Technical report, 2018. URL https://www.ipcc.ch/sr15/chapter/summary-for-policy-makers/.
Smith, B.A., Soderblom, L.A., Johnson, T.V., Ingersoll, A.P., Collins, S.A. et al. Science, 204(4396):951–957, 1979.
Smith, I.W.M., Herbst, E. and Chang, Q. MNRAS, 350(1):323–330, 2004.
Sohl, F., Spohn, T., Breuer, D. and Nagel, K. Icarus, 157(1):104–119, 2002.
Sohl, F., Choukroun, M., Kargel, J., Kimura, J., Pappalardo, R. et al. Space Sci. Rev., 153(1-4):485–510, 2010.
Sokal, K.R., Deen, C.P., Mace, G.N., Lee, J.J., Oh, H. et al. ApJ, 853(2):120, 2018.
Song, L., Balakrishnan, N., van der Avoird, A., Karman, T. and Groenenboom, G.C. The Journal of Chemical Physics, 142(20):204303, 2015.
Spahn, F., Schmidt, J., Albers, N., Hörning, M., Makuch, M. et al. Science, 311(5766):1416–1418, 2006.
Spiegel, D.S. and Burrows, A. ApJ, 745:174, 2012.
Spohn, T. and Schubert, G. Icarus, 161(2):456–467, 2003.
Squyres, S.W., Reynolds, R.T., Cassen, P.M. and Peale, S.J. In Bulletin of the American Astronomical Society, volume 14 of BAAS, page 737, 1982.
Strom, K.M., Strom, S.E., Edwards, S., Cabrit, S. and Skrutskie, M.F. AJ, 97:1451, 1989.
Subbotin, M.T. Matematicheskii Sbornik, 31:296–301, 1923.
Suetsugu, R. and Ohtsuki, K. ApJ, 839:66, 2017.
Suutarinen, A., Geppert, W.D., Harju, J., Heikkilä, A., Hotzel, S. et al. A&A, 531:A121, 2011.
Szulágyi, J. ApJ, 842(2):103, 2017.
Szulágyi, J. and Mordasini, C. MNRAS, 465(1):L64–L68, 2017.
Szulágyi, J., Morbidelli, A., Crida, A. and Masset, F. ApJ, 782:65, 2014.
Szulágyi, J., Masset, F., Lega, E., Crida, A., Morbidelli, A. et al. MNRAS, 460(3):2853–2861, 2016.
Szulágyi, J., Mayer, L. and Quinn, T. MNRAS, 464(3):3158–3168, 2017.
Szulágyi, J., Cilibrasi, M. and Mayer, L. ApJ, 868:L13, 2018.
Szulágyi, J., Binkert, F. and Surville, C. ApJ, 924(1):1, 2022.
Takasao, S., Aoyama, Y. and Ikoma, M. arXiv e-prints, art. arXiv:2106.16113, 2021.
Takata, T. and Stevenson, D.J. Icarus, 123(2):404–421, 1996.
Tamayo, D., Rein, H., Petrovich, C. and Murray, N. ApJ, 840(2):L19, 2017.
Tanaka, H. and Ward, W.R. ApJ, 602(1):388–395, 2004.
Tang, H. and Dauphas, N. Earth and Planetary Science Letters, 359:248–263, 2012.
Tanigawa, T., Ohtsuki, K. and Machida, M.N. ApJ, 747:47, 2012.
Tatulli, E., Benisty, M., Ménard, F., Varnière, P., Martin-Zaïdi, C. et al. A&A, 531:A1, 2011.
Teachey, A. and Kipping, D.M. Science Advances, 4(10), 2018.
Teachey, A., Kipping, D.M. and Schmitt, A.R. AJ, 155:36, 2018.
Teague, R., Bae, J., Bergin, E.A., Birnstiel, T. and Foreman-Mackey, D. ApJ, 860(1):L12, 2018.
Teague, R., Bae, J. and Bergin, E.A. Nature, 574(7778):378–381, 2019.
Terquem, C. and Papaloizou, J.C.B. ApJ, 654(2):1110–1120, 2007.
Thanathibodee, T., Calvet, N., Bae, J., Muzerolle, J. and Hernández, R.F. ApJ, 885(1):94, 2019.
Thi, W.F., Woitke, P. and Kamp, I. MNRAS, 412(2):711–726, 2011.
Thi, W.F., Kamp, I., Woitke, P., van der Plas, G., Bertelsen, R. et al. A&A, 551:A49, 2013.
Thi, W.F., Hocuk, S., Kamp, I., Woitke, P., Rab, C. et al. A&A, 634:A42, 2020a.
Thi, W.F., Hocuk, S., Kamp, I., Woitke, P., Rab, C. et al. A&A, 635:A16, 2020b.
Thomas, P.C. Icarus, 208:395–401, 2010.
Thomas, P.C., Tajeddine, R., Tiscareno, M.S., Burns, J.A., Joseph, J. et al. Icarus, 264:37–47, 2016.

Throop, H.B. and Bally, J. ApJ, 623(2):L149–L152, 2005.
Thrower, J.D., Collings, M.P., Rutten, F.J.M. and McCoustra, M.R.S. MNRAS, 394(3):1510–1518, 2009.
Thrower, J.D., Jørgensen, B., Friis, E.E., Baouche, S., Mennella, V. et al. ApJ, 752(1):3, 2012.
Tielens, A. Molecular Astrophysics. Cambridge University Press, 2021. ISBN 9781316761779.
Tielens, A.G.G.M. The Physics and Chemistry of the Interstellar Medium. Cambridge University Press, ISBN 0521826349, 2005.
Tittemore, W.C. Science, 250(4978):263–267, 1990.
Toomre, A. ApJ, 139:1217–1238, 1964.
Trumbo, S.K., Brown, M.E. and Hand, K.P. Science Advances, 5(6):aaw7123, 2019.
Tsang, W. and Hampson, R.F. Journal of Physical and Chemical Reference Data, 15(3):1087–1279, 1986.
Tsiganis, K., Gomes, R., Morbidelli, A. and Levison, H.F. Nature, 435:459–461, 2005.
Tsukagoshi, T., Nomura, H., Muto, T., Kawabe, R., Ishimoto, D. et al. ApJ, 829(2):L35, 2016.
Tsukagoshi, T., Muto, T., Nomura, H., Kawabe, R., Kanagawa, K.D. et al. ApJ, 878(1):L8, 2019.
Turner, N.J., Lee, M.H. and Sano, T. In AAS/Division for Planetary Sciences Meeting Abstracts #42, volume 42 of AAS/Division for Planetary Sciences Meeting Abstracts, page 24.08, 2010.
Turner, N.J., Choukroun, M., Castillo-Rogez, J. and Bryden, G. ApJ, 748(2):92, 2012.
Turner, N.J., Fromang, S., Gammie, C., Klahr, H., Lesur, G. et al. In Beuther, H., Klessen, R.S., Dullemond, C.P. and Henning, T., editors, Protostars and Planets VI, page 411, 2014.
Ubeira Gabellini, M.G., Miotello, A., Facchini, S., Ragusa, E., Lodato, G. et al. MNRAS, 486(4):4638–4654, 2019.
Unterborn, C.T., Desch, S.J., Hinkel, N.R. and Lorenzo, A. Nature Astronomy, 2:297–302, 2018.
Vacca, W.D. and Sandell, G. ApJ, 732(1):8, 2011.
van Boekel, R., Waters, L.B.F.M., Dominik, C., Dullemond, C.P., Tielens, A.G.G.M. et al. A&A, 418:177–184, 2004.
van Boekel, R., Min, M., Waters, L.B.F.M., de Koter, A., Dominik, C. et al. A&A, 437(1):189–208, 2005.
van Boekel, R., Henning, T., Menu, J., de Boer, J., Langlois, M. et al. ApJ, 837(2):132, 2017.
van den Ancker, M.E., The, P.S., Tjin A Djie, H.R.E., Catala, C., de Winter, D. et al. A&A, 324:L33–L36, 1997.
van der Marel, N., van Dishoeck, E.F., Bruderer, S., Birnstiel, T., Pinilla, P. et al. Science, 340(6137):1199–1202, 2013.
van der Marel, N., van Dishoeck, E.F., Bruderer, S., Andrews, S.M., Pontoppidan, K.M. et al. A&A, 585:A58, 2016.
van der Marel, N., Williams, J.P. and Bruderer, S. ApJ, 867(1):L14, 2018.
van der Plas, G., Ménard, F., Canovas, H., Avenhaus, H., Casassus, S. et al. A&A, 607:A55, 2017a.
van der Plas, G., Wright, C.M., Ménard, F., Casassus, S., Canovas, H. et al. A&A, 597:A32, 2017b.
van der Plas, G., Ménard, F., Gonzalez, J.-F., Perez, S., Rodet, L. et al. A&A, 624:A33, 2019.
van Dishoeck, E.F. and Blake, G.A. ARA&A, 36:317–368, 1998.
van Dishoeck, E.F., Jonkheid, B. and van Hemert, M.C. Faraday Discuss., 133:231–243, 2006.
Vance, S.D., Panning, M.P., Stähler, S., Cammarano, F., Bills, B.G. et al. Journal of Geophysical Research: Planets, 123(1):180–205, 2018.
Verhoeff, A. Dusty Disks around Young Stars. PhD thesis, Sterrenkundig Instituuut “Anton Pannekoek”, University of Amsterdam, 2009.
Vigan, A., Bonavita, M., Biller, B., Forgan, D., Rice, K. et al. A&A, 603:A3, 2017.
Villenave, M., Stapelfeldt, K.R., Duchêne, G., Ménard, F., Lambrechts, M. et al. ApJ, 930(1):11, 2022.
Vioque, M., Oudmaijer, R.D., Baines, D., Mendigutía, I. and Pérez-Martínez, R. A&A, 620:A128, 2018.
Virtanen, P., Gommers, R., Oliphant, T.E., Haberland, M., Reddy, T. et al. Nature Methods, 17:261–272, 2020.
Vorobyov, E.I. A&A, 552:A129, 2013.
Wagner, K., Apai, D., Kasper, M. and Robberto, M. ApJ, 813(1):L2, 2015.
Wagner, K., Follete, K.B., Close, L.M., Apai, D., Gibbs, A. et al. ApJ, 863(1):L8, 2018.
Wagner, K., Stone, J.M., Spalding, E., Apai, D., Dong, R. et al. ApJ, 882(1):20, 2019.
Wahlberg Jansson, K. and Johansen, A. A&A, 570:A47, 2014.
Waite, J. H., J., Lewis, W.S., Magee, B.A., Lunine, J.I., McKinnon, W.B. et al. Nature, 460(7254):487–490, 2009.

Waite, J.H., Combi, M.R., Ip, W.H., Cravens, T.E., McNutt, R.L. et al. Science, 311(5766):1419–1422, 2006.
Wakelam, V., Bron, E., Cazaux, S., Dulieu, F., Gry, C. et al. Molecular Astrophysics, 9:1–36, 2017.
Walsh, C., Harada, N., Herbst, E. and Millar, T.J. ApJ, 700(1):752–761, 2009.
Walsh, C., Juhász, A., Pinilla, P., Harsono, D., Mathews, G.S. et al. ApJ, 791(1):L6, 2014.
Walsh, C., Loomis, R.A., Öberg, K.I., Kama, M., van 't Hoff, M.L.R. et al. ApJ, 823(1):L10, 2016.
Walsh, C., Daley, C., Facchini, S. and Juhász, A. A&A, 607:A114, 2017.
Walsh, K.J., Morbidelli, A., Raymond, S.N., O'Brien, D.P. and Mandell, A.M. Nature, 475:206–209, 2011.
Wardle, M. Ap&SS, 311(1-3):35–45, 2007.
Watanabe, N. and Kouchi, A. ApJ, 571(2):L173–L176, 2002.
Weidenschilling, S.J. MNRAS, 180:57–70, 1977.
Weidner, C. and Kroupa, P. MNRAS, 365:1333–1347, 2006.
Weinberger, A.J., Anglada-Escudé, G. and Boss, A.P. ApJ, 762(2):118, 2013.
Weiss, B.P. and Bottke, W.F. AGU Advances, 2(2):e2020AV000376, 2021.
Wen-sai, D. Chinese Astronomy, 2(2):279 – 291, 1978.
Whipple, F.L. In Elvius, A., editor, From Plasma to Planet, page 211, 1972.
Wichittanakom, C., Oudmaijer, R.D., Fairlamb, J.R., Mendigutía, I., Vioque, M. et al. MNRAS, 493(1): 234–249, 2020.
Williams, D.M., Kasting, J.F. and Wade, R.A. Nature, 385(6613):234–236, 1997.
Winn, J.N. Planet Occurrence: Doppler and Transit Surveys, page 195. 2018. doi: 10.1007/978-3-319-55333-7_195.
Winn, J.N. and Fabrycky, D.C. ARA&A, 53:409–447, 2015.
Witasse, O. In European Planetary Science Congress, pages EPSC2022–645, 2022.
Woitke, P., Dominik, C. and Sedlmayr, E. A&A, 274:451, 1993.
Woitke, P., Kamp, I. and Thi, W. A&A, 501:383–406, 2009.
Woitke, P., Min, M., Pinte, C., Thi, W.F., Kamp, I. et al. A&A, 586:A103, 2016.
Woitke, P., Kamp, I., Antonellini, S., Anthonioz, F., Baldovin-Saveedra, C. et al. PASP, 131(1000):064301, 2019.
Woodall, J., Agúndez, M., Markwick-Kemper, A.J. and Millar, T.J. A&A, 466(3):1197–1204, 2007.
Wootton, D. The Invention of Science: A New History of the Scientific Revolution. Allen Lane, 2015. ISBN 9781846142109.
Yang, H., Herczeg, G.J., Linsky, J.L., Brown, A., Johns-Krull, C.M. et al. ApJ, 744(2):121, 2012.
Yoder, C.F. Nature, 279(5716):767–770, 1979.
Yoder, C.F. and Peale, S.J. Icarus, 47(1):1–35, 1981.
Youdin, A.N. and Goodman, J. ApJ, 620(1):459–469, 2005.
Yu, J. and Savage, P.E. Industrial & Engineering Chemistry Research, 37(1):2–10, 1998.
Yu, S.Y., Ho, L.C. and Zhu, Z. ApJ, 877(2):100, 2019.
Zahnle, K., Dones, L. and Levison, H.F. Icarus, 136(2):202 – 222, 1998.
Zahnle, K., Schenk, P., Levison, H. and Dones, L. Icarus, 163(2):263–289, 2003.
Zahnle, K.J. and Walker, J.C.G. Reviews of Geophysics and Space Physics, 20:280–292, 1982.
Zangi, R. and Mark, A.E. Phys. Rev. Lett., 91:025502, 2003.
Zhang, K., Blake, G.A. and Bergin, E.A. ApJ, 806(1):L7, 2015.
Zhang, K., Bergin, E.A., Schwarz, K., Krijt, S. and Ciesla, F. ApJ, 883(1):98, 2019.
Zhang, S., Zhu, Z., Huang, J., Guzmán, V.V., Andrews, S.M. et al. ApJ, 869(2):L47, 2018.
Zhou, Y., Bowler, B.P., Wagner, K.R., Schneider, G., Apai, D. et al. AJ, 161(5):244, 2021.
Zhu, W. and Dong, S. ARA&A, 59:291–336, 2021.
Zhu, Z. ApJ, 799(1):16, 2015.
Zhu, Z., Nelson, R.P., Hartmann, L., Espaillat, C. and Calvet, N. ApJ, 729(1):47, 2011.
Zhu, Z., Nelson, R.P., Dong, R., Espaillat, C. and Hartmann, L. ApJ, 755(1):6, 2012.
Zhu, Z., Andrews, S.M. and Isella, A. MNRAS, 479(2):1850–1865, 2018.
Zolotov, M.Y. and Shock, E.L. J. Geophys. Res., 106(E12):32815–32828, 2001.
Zubko, V.G., Mennella, V., Colangeli, L. and Bussoletti, E. MNRAS, 282(4):1321–1329, 1996.